Theses and Dissertations

2011

Iron-based nanoparticles: Investigating the microstructure, surface chemistry, and reactions with environmental contaminants

WEILE YAN
Lehigh University

Follow this and additional works at: http://preserve.lehigh.edu/etd

IRON-BASED NANOPARTICLES: INVESTIGATING THE NANOSTRUCTURE, SURFACE CHEMISTRY, AND REACTIONS WITH ENVIRONMENTAL CONTAMINANTS

Weile Yan

A Dissertation
Presented to the Graduate and Research Committee
of Lehigh University
in Candidacy for the Degree of
Doctor of Philosophy

in

Environmental Engineering
Lehigh University

May 2011

IRON-BASED NANOPARTICLES: INVESTIGATING THE NANOSTRUCTURE, SURFACE CHEMISTRY, AND REACTIONS WITH ENVIRONMENTAL CONTAMINANTS

Approved and recommended for acceptance as a dissertation in partial fulfillment of the requirements for the degree of Doctor of Philosophy.

_____

Date

_____

Accepted Date

_____

Dr. Wei-xian Zhang
(Dissertation Advisor)

Committee Members:

_____

Dr. Derick G. Brown

_____

Dr. Arup K. SenGupta

_____

Dr. Christopher J. Kiely

_____

Dr. Bruce E. Koel

_____

Dr. Chin-Pao Huang

Acknowledgement

I would like to thank my advsior, Dr. Wei-xian Zhang, for letting me pursue what I find interesting and for his continuous support, guidance, and patience during my entire PhD study. My sincere appreciation goes to my other committee members, Dr. Derick G. Brown, Dr. Arup K. SenGupta, Dr. Chris J. Kiely, Dr. Bruce E. Koel, and Dr. Chin-Pao Huang, for committing their precious time and providing insightful feedback at various stages of my research.

I would like to thank my collaborators, Dr. Chris J. Kiely and Dr. Bruce E. Koel for sharing their knowledge and making my study at Lehigh a truly rewarding learning experience. My sincere thanks to Dr. Kiely for lending me objective and helpful advice and being a kind mentor. I am grateful for the help from Dr. Al Miller and Bill Mushock, who were extremely helpful in setting up instrument analysis. Many thanks to Dr. Xiao-qin Li, Dr. Andrew A. Herzing, and Mauricio A. V. Ramos for spending a great amount of effort working on and improving our joint work.

Lastly, I would like to thank my parents and sister for being a constant source of understanding, love, and encouragement. I am most grateful to my husband for giving me endless support and being my close companion in yet another journey we made together.

Table of Contents

List of Tables

List of Figures

which was used to prepare the As(III) solutions used in these experiments. The vertical scale of the two spectra from the nZVI sample is enlarged five-fold.

Abstract

Nanoscale zero-valent iron (nZVI) is one of the most extensively applied nanomaterials for groundwater and hazardous waste treatment. Despite its high potential for environmental applications, there is limited knowledge about the fundamental properties of nZVI, particularly, its structure, surface composition, and changes in these characteristics in the aqueous media as the nanoparticles interact with aqueous contaminants. This research aims to investigate the structure and surface chemistry of nZVI and to understand how these attributes influence the material's reactivity towards various water contaminants. This work first involved a detailed examination of the metallic-core-oxide-shell structure using a variety of microscopic and spectroscopic tools. It was found that the polycrystalline metallic iron nuclei are spontaneously enclosed by a disordered layer of iron oxide that is 2-3 nm thick. Using a group of water contaminants (Hg(II), Zn(II) and hydrogen sulfide) as molecular probes, it was shown that the nanoparticles were able to utilize multiple pathways including adsorption, precipitation, reduction and surface mineralization to effectively immobilize these contaminants. The observed multiplexed reactivity is imparted by the particular core-shell configuration allowing both the oxide and metal components to exert their reactive tendency without undue kinetic hindrance. The second theme of this research was to examine the structural changes experienced by Pd-doped nZVI during exposure to aqueous media. With scanning-TEM X-ray energy-dispersive spectroscopy (STEM-

XEDS), the translocation of Pd from the surface to regions underneath the oxide layer and the rapid loss of the Fe(0) core due to accelerated aqueous corrosion were observed. The morphological changes resulted in a severe reduction in the reductive dechlorination rate of trichloroethylene (TCE), suggesting that the activity of Pd-doped nZVI is a dynamic function of time and particle structure. The close relationship between the structure and reactivity of nZVI is further illustrated by reactions with aqueous arsenite (As(III)). Notably, nZVI caused simultaneous oxidation and reduction of arsenite in the solid phase. Using depth-resolved high-resolution X-ray photoelectron spectroscopy (HR-XPS), multi-layered distributions of different arsenic valence states in the nanoparticles were observed, where the oxidized arsenic (As(V)) was predominantly present at the surface and the reduced form (As(0)) was located at the oxide/metal interface. The observed dual redox capability is therefore enabled by the metal core and oxide layer independently. The findings presented in this work establish that nZVI possesses more complex functionality than bulk-scale ZVI or iron oxides. The improved understanding of sequestration mechanisms studied here may inform optimal design of nZVI treatment systems and aid development of materials and new applications.

Chapter 1

Introduction

1.1 Background and motivation

Nanotechnology is the science of understanding and control of matter at dimensions between approximately 1 and 100 nanometers (National Nanotechnology Initiative, 2009). Since the term was first mentioned by the prophetic physicist Richard Reyman in 1959, nanotechnology has evolved into a prominent research field that profoundly influences major science and engineering disciplines, where the unusual properties of nanomaterials are harnessed in applications impacting virtually all aspects of the modern society: energy production, chemical synthesis, electronics, lighting, biotechnology, and health care. Among these, nanotechnology for environmental remediation is a highly anticipated frontier, as the growing demand for limited supply of clean water places an urgent need on technologies that can deliver faster, cleaner and more affordable clean-up measures.

The field of engineered nanomaterials for environmental clean-up emerged when a small amount of nanosized iron particles, or zero valent iron nanoparticles (nZVI), were used to rapidly destroy a group of recalcitrant groundwater contaminants including tricholoroethylene (TCE) and polychlorinated biphenyls (PCBs) (Wang & Zhang, 2007).

This seminal work has stimulated an intense interest in nZVI to degrade a variety of water or groundwater contaminants, as reflected in the sharp increase in publications related to nZVI in recent years. For example, over three hundred publications can be identified by searching the keywords "zero-valent iron" and "nano" in the ISI database. The subjects of interest of these publications can be broadly categorized by the types of contaminants treated and the various properties and engineering aspects of nZVI being investigated (Figure 1.1). The size of each segment reflects the relative number of publications in the respective area, which conveys a sense about the breadth of scope covered by this multidisciplinary topic and the focuses of recent research efforts. In addition to the well-studied halogenated organic compounds, the list of contaminants amenable to nZVI treatment encompasses many inorganic contaminants such as nitrate, Cr(VI), arsenic, heavy metals, and radionuclides. With an increasing number of field applications being conducted with nZVI for *in situ* groundwater and soil treatment, engineering aspects related to the stability, mobility and long-term eco-toxicological impact of nZVI have gained more attention.

The development of nZVI technology builds upon earlier studies by Gillham and O'Hannesin (1994), who discovered that bulk zero-valent iron (ZVI) was able to reduce a group of halogenated organic aliphatic compounds in groundwater. This property of iron led to the conceptualization of iron permeable reactive barriers (PRBs), which involves placing a vertical trench filled with granular ZVI materials in the flow path of an underground contaminant plume (Scherer *et al*., 2000).

Examples:

- Nitrate, Nitrite
- Perchlorate
- Bromate

- Cr(VI)
- As(III), As(V)
- U(VI)
- Pd(II)
- Cu(II)

- Dyes
- Explosives
- Pesticides

Non-metal inorganic species

Metals

Other organic compounds

(a)
Types of contaminants treated

Halogenated aliphatics

Halogenated aromatics

- Chlorinated methanes
- Brominated methanes
- Chlorinated ethenes

- Chlorinated benzenes
- Chlorinated phenols
- Chlorinated biphenyls

Examples:

- Polymer-coated nZVI
- Effect of magnetic interactions on aggregation
- NOM-enhanced transport

Stabilization & transport

Oxidative properties

Eco-toxicity

(b)
Properties and engineering modifications

Synthesis, characteriza-tion & aging

Supported nZVI

- Green synthesis
- Micro-structure & surface chemistry analysis
- Effect of aging on reactivity & fate / transport

- nZVI-support composite materials
- Functionalized sorbents & membranes

Figure 1.1 Overview of nZVI-related publications. (a) Breakdown by the type of contaminants treated and (b) various properties and engineering aspects of nZVI

5

investigated in the literature (size of the segments reflects the number of publications in the respective area based on an open search in the ISI database using the keywords "zero-valent iron" and "nano").

Well over one hundred PRB structures have been commissioned in the United States in the past two decades to remediate groundwater contaminated with halogenated organics, heavy metals, and radionuclides (Sacre, 1997; Gavaskar *et al.*, 1998). This technology is considered an attractive alternative to the conventional pump-and-treat approaches, which are inherently expensive and operation intensive (EPA, 2001). Although ZVI-PRBs were shown to be effective for many sites, the limitations have been noted with an increasing amount of field data becoming available. The effectiveness of PRBs varies with site-specific hydraulic and geochemical conditions. Decreased permeability due to precipitation of secondary mineral products and microbial growth is a critical concern for the long-term effectiveness of PRB installations (Battelle, 1999; Liang *et al.*, 2000). Furthermore, costs associated with construction limit the use of PRBs for treating deep aquifers and localized pollution hot spots. In this context, nanoscale ZVI (nZVI), or iron particles with diameters below 100 nm, is regarded as a complementary treatment technology (Theron *et al.*, 2008; Karn *et al.*, 2009). Because of their diminutive sizes, iron nanoparticles can be directly injected into groundwater by gravity or pressurized feed (e.g. via Geoprobe^{TM} method), rendering it a more flexible treatment option and adaptable for localized source zones and sites with complex hydro-geological characteristics (Li *et al.*, 2006). Over 50 pilot or large-scale field applications of nZVI have been conducted over the last decade and the target contaminants in these

6

projects have included TCE and other chlorinated compounds, pesticides and chromium (Project on Emerging Nanotechnologies, 2009).

Despite the engineering merits of nZVI technology and the intense research interest directed at this topic, fundamental knowledge of the nanoparticles, particularly their nanostructures, chemistry of their surfaces where contaminant degradation occurs, and changes in these properties in environmental media over time have not been systematically investigated. For example, while a huge volume of publications is available on the reactions of bimetallic nZVI with chlorinated compounds (Figure 1.1), the dynamic changes in reactivity of nZVI towards TCE due to changes in the surface properties of the catalytic metal with respect to the iron substrate were barely discussed in the literature (Muftikian *et al*., 1996; Zhu & Lim, 2007). As a result, many uncertainties remain concerning the fundamental features of this technology and its strengths and challenges compared to PRB-based remediation (Tratnyek & Johnson, 2006).

In early nZVI studies, the nanoparticles were viewed as a homogeneous entity of zero-valent iron, whereas more recent studies suggest that the passivating oxide layer present on the nanoparticle surface bears important implications for the particle stability and reactivity (Liu *et al*., 2005; Li & Zhang, 2006). The oxide layer is not only capable of adsorbing contaminants and forming coordinative bonds, but is also permeable to electron and mass transport. This core-shell structure of nZVI thus imparts the nanoparticles with a dual functionality of oxide and metallic iron, and the sequestered

contaminants may distribute differentially in the nanoparticles depending on their chemical properties. Therefore, reactions enabled by nZVI must be evaluated in terms of the core-shell structure. This aspect, however, has not been systematically examined. Majority of the studies consider nZVI as a simple reductant (e.g. in reductive dechlorination reactions) or surface sorbents similar to iron oxide materials (e.g. in sequestration of metal pollutants).

The research for this thesis was to investigate the basic properties of nZVI, namely, the structural and chemical nature of the nanoparticles, placing emphasis on characterizing their core-shell structure and the surface chemistry in order to understand how these properties affect or shape the interactions between nZVI and water pollutants. Due to the interdisciplinary nature of nanoparticle research that involves broad fields of material science, chemistry, and chemical engineering, a comprehensive investigation of iron nanoparticles requires methodologies developed in those fields. Therefore, a multi-disciplinary approach was adopted here. The structural and surface chemical properties of iron nanoparticles were examined with a suite of microscopic and spectroscopic techniques including scanning and transmission electron microscopes (SEM and TEM), and high-resolution X-ray photoelectron spectroscopy (HR-XPS). The findings were integrated with results from conventional solution chemistry experiments in order to form a more complete and accurate understanding of the reactivity of nanoparticles in environmental treatment systems. Results from this work help to advance the understanding of reaction mechanisms and kinetics, improve the design of remediation

systems, and inform the long-term impacts of this technology on the receiving ecosystems. This grand scheme is illustrated schematically in Figure 1.2.
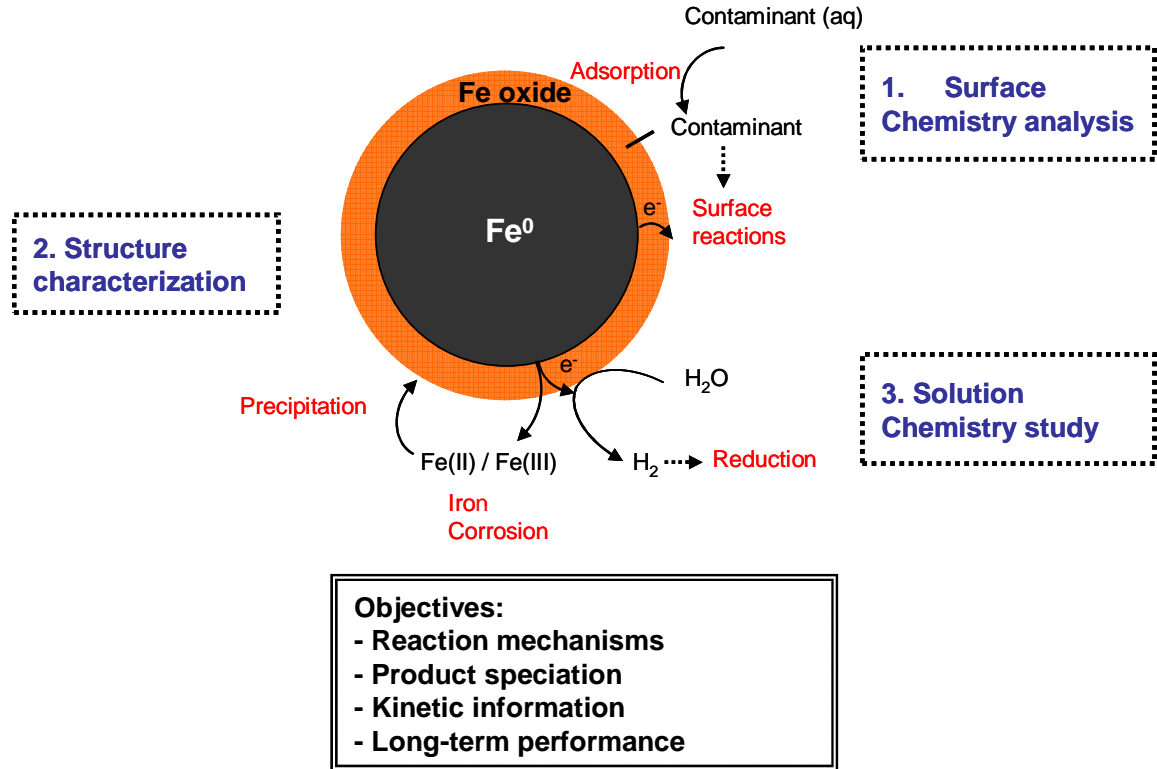
Figure 1.2 Proposed research objectives and methods to investigate the reactions between nZVI and aqueous contaminants (reaction schemes are for illustration purpose and are not definitive).

1.2 Research objectives

Specifically, this research aimed to accomplish the following objectives:

- Evaluate the microstructure of nZVI using a variety of microscopic (SEM/

TEM/STEM-XEDS), spectroscopic (HR-XPS), and chemical reduction methods. Of particular interest was the nature of the core-shell structure of nZVI.

- Characterize the changes in structure and phase distribution of nZVI materials in aqueous environment at different time stages.

- Measure the solution chemistry, including pH and E_h profiles and the changes in contaminant concentrations, through laboratory batch experiments. The latter will provide the efficiency of nZVI in sequestering water contaminants. Candidate contaminants studied here are of vital environmental concerns, for example, copper, mercury, arsenic, and trichloroethylene (TCE).

- Examine the products of reactions between nZVI and the above contaminants with surface analysis techniques (HR-XPS). Time-dependent analysis can be employed to characterize the distributions of reaction intermediates and products at different stages. Depth-resolved XPS techniques can be used to investigate the spatial distributions of contaminants immobilized by nZVI.

- Integrate results from the above components, and propose improved or new models of reaction mechanisms and kinetics.

1.3 Dissertation overview

This section provides an overview of the dissertation and highlights the focus and interconnections of later chapters. The sequence of presentation is as follows:

- Chapter 2 gives a literature review of nZVI technology for water remediation, the current state-of-knowledge regarding the underlying mechanisms, and engineering experiences from *in situ* field applications.

- Chapter 3 describes the methodology adopted in this study with detailed descriptions of experimental set-ups and instrument analysis procedures.

- Chapter 4 examines the structural and chemical properties of nZVI using a suite of advanced spectroscopic and microscopic techniques, and proposes the core-shell model of nZVI. The size of the oxide shell is quantified reliably by three independent methods, which provides a basis for later discussion on the unique role of the oxide shell in mediating reactions between the nanoparticles and environmental contaminants.

- Chapter 5 examines the non-specific oxidation behavior of palladium-impregnated nZVI in aqueous environments (dubbed 'aging') and the dynamic changes of nZVI structure that results from such aging processes. These changes bear important implications for the particle reactivity as reflected through a series of trichloroethylene dechlorination experiments.

- Chapters 6 and 7 investigate the reactivity of nZVI towards a group of well-chosen inorganic contaminants with varying coordinative, electrochemical and

redox properties. These contaminants are selected as molecular probes to evaluate the multi-faceted functionality of nZVI imparted by its core-shell composite structure. Specifically, Chapter 6 focuses on the role of adsorption, reduction, surface precipitation and mineralization processes in the sequestration of Hg(II), Zn(II) and hydrogen sulfide. Chapter 7 concentrates on one particular contaminant of great concern - arsenic, and shows how the internal structure of nZVI imparts a dual redox capability causing concurrent oxidation and reduction of arsenite species in the nanoparticles, as well as how these reactions determine the locations and chemical states of the solid-bound arsenic species.

- Chapter 8 summarizes the major findings of this research, identifies new questions or research areas arising from these findings, and proposes future efforts to address these topics.

References

1. National Nanotechnology Initiative. 2009. What Is Nanotechnology? (http://www.nano.gov/html/facts/whatIsNano.html)

2. Feynman, R. There is plenty of room at the bottom, Caltech Institute Archives, 1959. (http://www.zyvex.com/nanotech/feynman.html)

3.   Wang, C. B.; Zhang, W. X., Synthesizing nanoscale iron particles for rapid and complete dechlorination of TCE and PCBs. *Environ. Sci. Technol.* **1997,** *31* (7), 2154-2156.

4.   Gillham, R. W.; Ohannesin, S. F., Enhanced Degradation of Halogenated Alphatics by Zero-Valent Iron. *Ground Water* **1994,** *32* (6), 958-967.

5.   Scherer, M. M.; Richter, S.; Valentine, R. L.; Alvarez, P. J. J., Chemistry and microbiology of permeable reactive barriers for *in situ* groundwater clean up. *Crit. Rev. Microbiol.* **2000**, *26*(4), 221-264.

6.   Sacre, J. A. Treatment walls: a status update. Ground-water remediation technologies analysis center, TP-97-02, Pittsburgh, PA, 1997.

7.   Gavaskar, A. R.; Sass, N. N. M.; Janoy, R. J.; O'Sullivan, D. Permeable Barriers for Goundwater Remediation—Design, Construction, and Monitoring, Battelle Memorial Institute, Columbus, OH, 1998.

8.   U.S. EPA. Cost analysis for selected groundwater cleanup projects: Pump and treat systems and permeable reactive barriers. U.S. EPA 542-R-00-013. Washington, D.C., 2001.

   (http://www.epa.gov/tio/download/remed/542r00013.pdf)

9.   Liang, L. Y.; Korte, N.; Gu, B. H.; Puls, R.; Reeter, C., Geochemical and microbial reactions affecting the long-term performance of *in situ* 'iron barriers'. *Adv. Environ. Res.* **2000,** *4* (4), 273-286.

10.   Battelle, 1999. Monitoring plan for permeable reactive barriers at Department of Defense sites. Prepared for Naval Facilities Engineering Service Center, Port Hueneme, CA. 1999.

11.   Li, X. Q.; Elliott, D. W.; Zhang, W. X., Zero-valent iron nanoparticles for abatement of environmental pollutants: Materials and engineering aspects. *Crit. Rev. Sol. State* **2006,** *31* (4), 111-122.

12.   Karn, B.; Kuiken, T.; Otto, M., Nanotechnology and *in Situ* Remediation: A Review of the Benefits and Potential Risks. *Environ. Health Persp.* **2009,** *117* (12), 1823-1831.

13.   Project on Emerging Nanotechnologies, 2009. Nanoremediation map. (http://www.nanotechproject.org/inventories/remediation_map)

14.   Theron, J.; Walker, J. A.; Cloete, T. E., Nanotechnology and water treatment: Applications and emerging opportunities. *Crit. Rev. Microbiol.* **2008,** *34* (1), 43-69.

15.   Muftikian, R.; Nebesny, K.; Fernando, Q.; Korte, N., X-ray photoelectron spectra of the palladium-iron bimetallic surface used for the rapid dechlorination of chlorinated organic environmental contaminants. *Environ. Sci. Technol.* **1996,** *30*, 3593-3596.

16.   Zhu, B. W.; Lim, T. T., Catalytic reduction of chlorobenzenes with Pd/Fe nanoparticles: reactive sites, catalyst stability, particle aging, and regeneration. *Environ. Sci. Technol.* **2007,** *41*, 7523-7529.

17.   Tratnyek, P. G.; Johnson, R. L., Nanotechnologies for environmental cleanup. *Nano Today* **2006,** *1* (2), 44-48.

18.   Liu, Y. Q.; Choi, H.; Dionysiou, D.; Lowry, G. V., Trichloroethene hydrodechlorination in water by highly disordered monometallic nanoiron. *Chem. Mater.* **2005,** *17* (21), 5315-5322.

19.   Li, X. Q.; Zhang, W. X., Iron nanoparticles: the core-shell structure and unique properties for Ni(II) sequestration. *Langmuir* **2006,** 22, (10), 4638-4642.

Chapter 2

Literature Review

2.1 Overview of ZVI technology development

Nanotechnology has revolutionized the science of controlling materials at the atomic and molecular level since the visionary physicist Richard Feynman predicted that "There is plenty of room at the bottom" in 1959 (Feynman, 1959). Collectively, the term nanomaterials refer to all engineered or natural materials with a characteristic dimension below 100 nm (National Nanotechnology Initiative, 2009). At dimensions below 10 nm, materials exhibit novel chemical/photochemical, mechanical, electrical, and optical properties due to quantum size effects. More generally, nanomaterials exhibit increased chemical reactivity, which is thought to be brought about by a greater proportion of surface atoms, especially the more active edge and corner atoms, and distinct localized environments created by intermixing of atomic species (Mulvaney, 2001; Campbell & Parker, 2002). In environmental studies, nanomaterials do not come as an entirely new concept. Many naturally-occurring particulate or colloidal materials with sizes in the range of a few to several hundred nanometers have been studied by environmental scientists, the most well-known examples being iron oxides and alumina silicates, which have been extensively studied for their adsorptive properties for aqueous ionic species (Stumm, 1992; Morel & Hering, 1993).

16

Zero-valent iron (Fe(0)) is a moderately strong reducing agent and electron donor. It reacts favorably with a large group of chemicals that have more positive electrochemical potential than iron (Gillham & O'hannesin, 1994). In the realm of environmental remediation, ZVI has been applied to the decontamination of halogenated hydrocarbons, azo dyes, munitions, nitrate, hexavalent chromium, arsenic, and heavy metals by transforming the contaminants into substances less harmful and more degradable (Matheson & Tratnyek, 1994; Johnson *et al*., 1996; Hundal *et al*., 1997; Gavaskar *et al*., 1998; Gu *et al*., 1998; Cao *et al*., 1999; Alowitz & Scherer, 2002; Wilkin *et al*., 2005).

Since early 1990s, granular ZVI has been employed in a type of engineering fixture known as permeable reactive barrier (PRB) for *in situ* remediation of groundwater contaminated with chlorinated solvents or hexavalent chromium (Gavaskar *et al*., 1998; Gu *et al*., 1998; Wilkin *et al*., 2005). In essence, a PRB is a vertical wall in a funnel or gate design installed below the ground in the path of a contaminant plume. The funnel design directs a contaminant plume to the reactive barrier ('gate'), where the contaminants react with granular iron in a manner similar to a plug-flow reactor. The effluent from a PRB typically has contaminants reduced to concentrations below the applicable USEPA regulatory levels. Several excellent review papers are available in the literature on the design, operation, and long-term assessment of PRB structures (Sacre 1997; Gavaskar *et al*., 1998; Scherer *et al*., 2000).

17

Nanoscale zero-valent iron (nZVI) can be regarded as an extension of zero-valent iron (ZVI) technology. The nanoparticles were first synthesized in our lab at Lehigh University and received widespread attention because of their greatly enhanced reactivity towards TCE and PCBs compared to conventional macro-sized ZVI particles (Wang & Zhang, 1997). The same group also synthesized a modified nZVI by doping the iron nanoparticles with a second metal, typically Pd, Pt, Cu or Ni, which proved even more effective for the degradation of halogenated hydrocarbons owing to the catalytic effect introduced by the second metal (Zhang *et al*., 1998; Lien & Zhang, 1999; Xu & Zhang, 2000). Concerted research efforts have been made since then and a wide range of contaminants are now identified as amenable to nZVI remediation (Table 2.1).

Pilot or large-scale field applications of nZVI have been conducted since early 2000, where nZVI was directly injected into the remediation site by gravity flow or under pressure into underground contaminant plumes (Elliott & Zhang, 2001) (Figure 2.1). More recently, a field test using nZVI in an emulsified state, produced by blending nZVI with stabilizing agents such as vegetable oil, has shown this form of nZVI to be effective for dehalogenation of a dense non-aqueous phase liquid (DNAPL) site. Compared to aqueous suspensions, emulsified nZVI can remain suspended in the liquid phase for a longer time, thereby enabling better penetration of the nanoparticles to the source zones and increasing the contact time (Quinn *et al*., 2005).

Table 2.1: Environmental contaminants amenable to degradation by nZVI (adapted from Li *et al*., 2006).

Chlorinated Methanes	Trihalomethanes
Carbon tetrachloride (CCl_4) Chloroform ($CHCl_3$) Dichloromethane (CH_2Cl_2) Chloromethane (CH_3Cl)	Bromoform ($CHBr_3$) Dibromochloromethane ($CHBr_2Cl$) Dichlorobromomethane ($CHBrCl_2$)
Chlorinated Benzenes	Chlorinated Ethenes
Hexachlorobenzene (C_6Cl_6) Pentachlorobenzene (C_6HCl_5) Tetrachlorobenzenes ($C_6H_2Cl_4$) Trichlorobenzenes ($C_6H_3Cl_3$) Dichlorobenzenes ($C_6H_4Cl_2$) Chlorobenzene (C_6H_5Cl)	Tetrachloroethene (C_2Cl_4) Trichloroethene (C_2HCl_3) *cis*-Dichloroethene ($C_2H_2Cl_2$) *trans*-Dichloroethene ($C_2H_2Cl_2$) 1,1-Dichloroethene ($C_2H_2Cl_2$) Vinyl Chloride (C_2H_3Cl)
Pesticides	Other Polychlorinated Hydrocarbons
DDT ($C_{14}H_9Cl_5$) Lindane ($C_6H_6Cl_6$)	PCBs Pentachlorophenol (C_6HCl_5O) 1,1,1-trichloroethane ($C_2H_3Cl_3$)
Organic Dyes	Other Organic Contaminants
Orange II ($C_{16}H_{11}N_2NaO_4S$) Chrysoidin ($C_{12}H_{13}ClN_4$) Tropaeolin O ($C_{12}H_9N_2NaO_5S$)	N-nitrosodiumethylamine ($C_4H_{10}N_2O$) TNT ($C_7H_5N_3O_6$)
Heavy Metals	Other Inorganic Anions
Mercury (Hg^{2+}) Nickel (Ni^{2+}) Cadium (Cd^{2+}) Lead (Pb^{2+})	Perchlorate (ClO_4^-) Nitrate (NO_3^-) Dichromate ($Cr_2O_7^{2-}$) Arsenate (AsO_4^{3-})
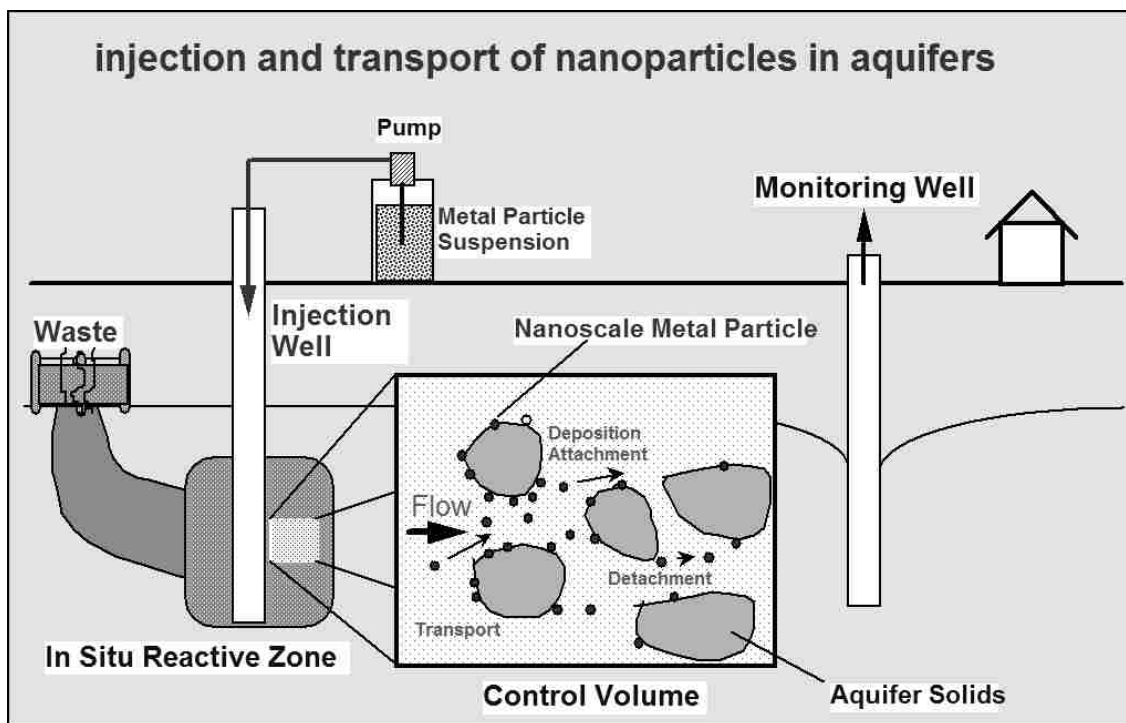
Figure 2.1 Schematic drawing of a field application of iron nanoparticles for underground contaminant remediation (adapted from PARS Environmental Inc, 2005)

2.2 Preparation of nZVI and bimetallic nZVI

Preparation methods can be categorized into two classes: top-down and bottom-up approaches. The latter entails piecing together iron atoms to form Fe(0) clusters at the nanometer scale. Typically, this is done by chemical reduction of ferrous (Fe(II)) or ferric (Fe(III)) salts (Glavee *et al*., 1995), or by vapor condensation in a vacuum or inert gas (Hahn, 1997). Various chemical reduction schemes have been used, among which the most widely adopted one is the borohydride reduction approach, where ferric

or ferrous ions react with sodium borohydride in water under intensive mixing (Wang & Zhang, 1997). The reaction is shown in Eq. 2.1:

$$4Fe^{3+} + 3BH_4^- + 9H_2O \rightarrow 4Fe^0(s) + 3H_2BO_3^- + 12H^+ + 6H_2 \text{ (g)} \qquad (2.1)$$
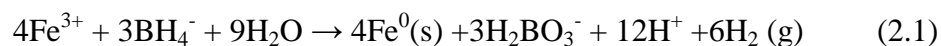
This method, conducted under ambient temperature and pressure, can be routinely performed in common wet chemistry laboratories. However, the unit cost of wet chemistry synthesis is rather expensive (over \$200/kg nZVI) due to the high cost of sodium borohydride and the labor required. This method is also difficult to scale up to an industrial scale due to the several separation steps involved and the large amount of wastewater produced (Li *et al*., 2009).

Other bottom-up approaches, such as decomposition of iron pentacarbonyl ($Fe(CO)_5$) in organic solvents, or reduction of goethite (α-FeOOH) or hematite (α-Fe$_2$O$_3$) by H$_2$ at high temperature, have also been reported (Capek, 2004; Nurmi *et al*., 2005, Majewski & Thierry, 2007). However, chemical reactions often consume expensive and toxic reagents, and produce not only nZVI but also byproducts such as $B(OH)_3$. For example, thermal decomposition of iron pentacarbonyl ($Fe(CO)_5$) generates small (10-20 nm) and uniform-sized nZVI (Suslick *et al*., 1991), but iron pentacarbonyl is a highly toxic reagent and thus raises critical safety concerns.

Top-down approaches start with bulk-sized iron materials, such as granular iron, and achieve size reduction through mechanical means. A precision ball-milling technique has recently been proposed, which uses stainless steel balls as the grinding media to

fragment the starting iron materials into pieces less than 100 nm in diameter in approximately 3 hours. Laboratory batch experiments using such milled nZVI particles and several well-studied chlorinated contaminants confirm the milled nZVI (8-hour milling time) has slightly higher chemical reactivity over the chemically made nZVI (Li *et al*., 2009). Thus, precision ball-milling offers an attractive route to green manufacturing of iron nanoparticles at quantities sufficient for full-scale remediation. Currently, this method has been adopted for routine manufacturing of nZVI by PARS Environmental, Inc.

Preparation of bimetallic nZVI involves reductive plating of the as-synthesized nZVI in a salt solution of the metal to be added. Because the standard reduction potential of these metals (e.g., Pd, Pt, Ni, Cu, and Ag) are more positive than that of Fe(0), they are reduced by Fe(0) via classical metal replacement reactions and deposit as solid metals onto the nZVI surface (Zhang *et al*., 1998; Lien & Zhang, 1999; Zhu & Lim, 2007; Choi *et al*., 2008). The salt precursors of these metals can be in chloride (e.g., $PdCl_2$ or K_2PdCl_6) or acetate (e.g., $Pd(CH_3COO)_2$) form. Generally, bimetallic nZVI from a chloride precursor is prepared in aqueous solutions, whereas those from acetate salts are done in ethanol or an ethanol/water mixture.

2.3 Characterizing physico-chemical properties of nZVI

2.3.1 Morphology, size, and crystallinity

In SEM or TEM, nZVI appears as spherical particles typically in an aggregated form due to chemical and magnetic interactions (Sun *et al*., 2006). It has been mentioned in several studies that nZVI morphology and crystallinity are dependent on the synthesis methods. In a study by Nurmi *et al*., (2005), the morphology and crystallinity of the nZVI produced by borohydride reduction method (nZVI^{BH}) and those by reduction of goethite or hematite by H_2 (nZVI^{H2}) were compared. nZVI^{BH} are spherical in shape and tend to form chain-like aggregates; both attributes are likely associated with the synthesis medium being a solution phase. nZVI^{H2} is composed of irregular-shaped particles and large faceted plates, the latter likely to be iron oxides (Nurmi *et al*., 2005).

In terms of crystallinity, nZVI^{BH} and nZVI^{H2} exhibit distinct properties. The electron diffraction pattern of nZVI^{BH} is comprised of diffuse rings, indicating the metal phase is *bcc* polycrystalline iron with individual crystal grain sizes of < 1.5 nm (Liu *et al*., 2004). At this scale, the distinction between amorphous and polycrystalline iron is ambiguous. The lack of lattice fringes in HR-TEM micrographs suggests that the oxide phase is amorphous and disordered. In contrast, nZVI^{H2} exists mainly as single-crystal Fe(0) particles, and a highly crystalline iron oxide phase is evident from the faceted surfaces and the appearance of periodic lattice fringes (Nurmi *et al*., 2005).

Similar conclusions have been drawn from XRD studies. The broad peak at 45° 2Ө corresponding to *bcc* Fe^0 for $nZVI^{BH}$ indicates a highly disordered Fe^0 core (Liu *et al.*, 2004). No peaks corresponding to iron oxide were noticed in the XRD spectrum, consistent with its amorphous nature. To analyze the fine structure of the oxide layer, Mossbauer spectroscopy has been conducted on $nZVI^{BH}$ with the results showing the presence of mixed ferrous (Fe(II)) oxide and superparamagnetic ferric (Fe(III)) oxide (Kanel *et al.*, 2006).

Liu *et al.* (2004) evaluated the effect of crystallinity on TCE reduction rate for freshly synthesized $nZVI^{BH}$ and compared to those that had undergone air oxidation ($nZVI^{ox}$) and annealing ($nZVI^{cr}$). The fresh nZVI particles had disordered Fe(0) and amorphous oxide phases as evident in HR-TEM images and XRD patterns. After three days of air exposure at ambient temperature, the oxidized nanoparticles underwent partial oxidation, although TEM analysis could not differentiate a significant change in the thickness of the oxide layer. Subsequent annealing of the oxidized particles produced nanoparticles with significantly more crystalline Fe(0) as *bcc*-Fe(0). TCE reduction tests showed that the fresh and partially oxidized particles were able to activate H_2 to reduce TCE, while the annealed particles do not have such chemical reactivity. It was suggested in this study that disorder in the Fe(0) phase and the oxide layer were key to the reactivity of iron nanoparticles.

Size and size distribution are important parameters for nZVI because they determine the effective surface area and relative amount of Fe(0) and oxide in the nanoparticles,

which have a direct influence on the total number of surface reactive sites and reactive capacity of the particles. The size distribution may be obtained by examining a large quantity of particles using TEM or by an ultrasound method. A characterization study dedicated to nZVI^{BH} produced in our laboratory showed that the particles were polydisperse (median diameter 60 nm with a relatively broad standard deviation of 42%) (Sun *et al*., 2006). In addition to microscopic or acoustic means, the nZVI size can be quantified indirectly by BET surface area measurements using the geometric correlation between the surface area and size of the nanoparticles (Li *et al*., 2009).

2.3.2 Electrochemistry

In applications of iron materials for reduction of chlorinated hydrocarbons and other contaminants, the formation of the surface oxide layer may pose long-term problems by reducing the activity of the metal surface, clogging pores, and reducing the permeability of a PRB structure (Odziemkowski, *et al*., 1997). In an aqueous medium, iron inevitably reacts with water and releases Fe^{2+} (Eq. 3.2), and in aerobic conditions, it also reacts with dissolved oxygen (Eq. 3.3). A portion of Fe^{2+} may further react with dissolved oxygen to produce Fe^{3+} (Eq. 3.4).

$$Fe^0 + 2H_2O \rightarrow Fe^{2+} + H_2 + 2OH^- \text{ (aerobic / anaerobic conditions)} \quad (3.2)$$

$$2Fe^0 + O_2 + 2H_2O \rightarrow 2Fe^{2+} + 4OH^- \text{ (aerobic conditions)} \quad (3.3)$$

$$4Fe^{2+} + O_2 \rightarrow 4Fe^{3+} + 4OH^- \text{ (aerobic conditions)} \qquad (3.4)$$
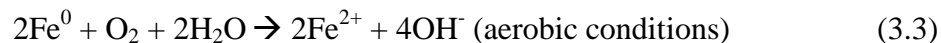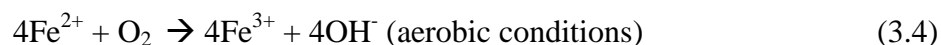
All of the above reactions can lead to increased pH due to production of hydroxyl ions (Eq. 3.2-4). However, the pH increase is most prominent in aerobic systems due to much higher iron corrosion rates (Matheson & Tratnyek, 1994). In alkaline pH, Fe^{2+} will precipitate as $Fe(OH)_2$, which may eventually form a surface layer to inhibit further iron dissolution (Gillham & O'Hannesin, 1994). Formation of other oxide phases has also been suggested, for example, goethite, green rust, and siderite ($FeCO_3$) (Agrawal, *et al.*, 2002; Su & Puls, 2004; Kanel *et al.*, 2006). Odziemkowski *et al*. (1997) used Raman spectroscopy to identify the oxide phase formed as a result of granular iron corrosion in a simulated groundwater solution. It was found that under anaerobic conditions, ferrous hydroxide ($Fe(OH)_2$) was formed during the initial stage of corrosion, which gradually transformed to magnetite (Fe_3O_4) as a more stable product regardless of the composition of the groundwater. Green rust was not identified in the Raman spectra, although other studies had found it in arsenic-contaminated water based on FTIR analysis (Su & Puls, 2004).

A classical technique to examine the corrosion behavior of a metal is to use an anodic polarization voltammogram obtained with a rotating disk electrode (RDE) submersed in an electrolyte solution or amperometric measurements using a powder-disk electrode (PDE). In a PDE test, the electrodes are constructed in such a way that a small amount of nZVI is exposed to the electrode-solution interface. During the test, the potential is varied and the currents passed are recorded. A graph is made that plots the log of the

current (log(I)) as a function of the electrode potential (Ponder *et al*., 2001). An important feature of the graph is the singularity point where the net current drops to zero. The potential at this point is known as the corrosion potential, E_{corr}. In the Bulter-Volmer Equation (Eq. 3.5), E_{corr} is the potential when the cathodic reaction rate (water reduction) equals the anodic reaction rate (iron corrosion) (Farrell *et al*., 2001):

$$i = i_{corr}(\underbrace{e^{-\beta_c(E-Ecorr)}} - \underbrace{e^{-\beta_a(E-Ecorr)}}) \qquad (3.5)$$

Rate of cathodic   Rate of anodic
reactions   reactions

where i is the net current; i_{corr} is the corrosion current, E is the electrode potential, and β_c and β_a are the cathodic and anodic Tafel slopes, respectively.

E_{corr} is sensitive to the oxidation state of the iron material and the tendency of the material to corrode in the test medium. Oxidized iron gives a more anodic E_{corr} (i.e., more positive E_{corr} values) than Fe^0, and similarly, iron covered by a surface-passivating oxide has E_{corr} shifted to more positive values. Nurmi *et al*. (2005) compared the polarization curves of $nZVI^{BH}$ and $nZVI^{H2}$ versus bulk iron or iron oxides. They noticed that the E_{corr} values for both nZVI materials shifted significantly to lower potential (cathodic shift) compared to bulk Fe^0. Between the two nZVI materials, E_{corr} values were similar. The results suggested nano-sized iron corrodes faster than bulk iron, which may be due to higher surface areas of nZVI materials or higher surface

27

concentrations of defect sites that are able to facilitate electron passage and accelerate Fe(0) oxidation (Nurmi *et al*., 2005).

Polarization curves have proven useful in the study of Cr(VI) sequestration by ZVI, because the product formed, Cr(III) hydroxide or oxide, is an excellent corrosion inhibition agent. Its accumulation on the iron surface results in a shift in E_{corr} in the voltammogram and a decrease in exchange current (Melitas *et al*. 2001).

2.3.3 Surface chemistry

The nature of the nZVI-water interface plays a key role in the reactivity and stability of the nanoparticles because the interface is where various processes, including corrosion, precipitation, contaminant adsorption and degradation, take place. Knowledge of the chemical composition and structure of the interface is indispensable in order to understand molecular-level mechanisms underlying the environmental applications. The techniques employed to investigate surface chemistry are many, for example, X-ray photoelectron spectroscopy (XPS), Auger electron spectroscopy (AES), extended X-ray absorption fine structure (EXAFS) or X-ray absorption near-edge fine structure (XANES), ion scattering spectroscopy (ISS), attenuated total reflection Fourier transform infrared spectroscopy (ATR-FTIR), Raman spectroscopy, and atomic force spectroscopy (AFM). Table 2.2 summarizes the working principles of these techniques and their analytical capabilities and limitations. Each approach has its own strengths and limitations, such as a vacuum requirement and or low detection limits, and a

comprehensive understanding of nZVI surface chemistry and how it changes with reactions in water requires using more than one technique. Meaningful interpretation of these data should also take into account the aqueous phase chemistry to gain a holistic picture of the overall system containing both solid and liquid phases.

A few studies have been published examining the surfaces of ZVI after reactions with contaminants. For example, AES was used to map the spatial distribution of Pd on a Pd-Fe surface by McGuire *et al*. (2003). The bimetallic particles prepared in a neutral solution had Pd mainly at the surface and the Pd distribution was highly heterogeneous with distinct domains of Pd-rich and Fe-rich phases. In contrast, Pd-Fe prepared in an acidic solution had an intermediate Pd layer buried by an iron oxide surface layer. Such structural information may be useful to interpret the reactivity of the bimetallic particles because the availability of surface Pd, which are believed to act as catalytic sites for the intended reactions, directly influences the key mechanistic steps involved in dehalohydrogenation of organic halides.

In studying nZVI-mediated heavy metal sequestration, XPS is frequently used to identify the chemical states of the surface-bound metal species in order to decipher the processes responsible for their removal. Li *et al*. (2007) reported that the actual mechanism of metal ion removal by nZVI depends on the redox potential of the metal relative to Fe(0) (E^0_h = -0.44 mV). Species with redox potential more negative than or close to that of Fe^0, e.g., Zn(II) and Cd(II), are sequestrated by adsorption. Those with more positive redox potentials, e.g., Cu(II) and Ag(I), are entirely reduced to their metal

states on nZVI. For Ni(II) and Pb(II), which have redox potential slightly more positive than that of iron, both adsorption and reduction contribute to their removal.

EXAFS and XANES are able to provide information on the local atomic environment and interatomic distances, which are particularly useful for elucidating the surface complexes formed between nZVI and inorganic ions. For example, XANES analysis of the mineral products extracted from a Cr(VI) site remediated by an iron PRB revealed that the chromium is converted to Cr(III) and it bonds in part with iron sulfide minerals formed as a consequence of microbially mediated sulfate reduction around the PRB area (Wilkin *et al.*, 2005). Similar studies on Fe materials reacted with As(III) and As(V) have generated insights into the chemical states of the immobilized As species and the chelating structure formed by arsenic and iron corrosion products, and this will be the topic of discussion in a later section (Section 2.5).

Table 2.2: Analytical techniques for surface chemistry studies (all instruments, except for EXAFS and XANES, are available at Lehigh University).

Technique	Working principle	Information generated	Probing depth (typical)	Detection capability	Sample requirement
AES	Near surface core-hole excitations stimulated by 1-10 keV incident electrons. Auger electrons with characteristic energies are emitted and analyzed.	Elemental composition	2 nm	0.1%	Inorganic solids, vacuum env.
AFM	Bending of the probe due to Van der Waals forces between the surface and the probe. Probe deflection measured by various means.	Surface morphology, magnetic and chemical properties	Sub A	NA	All solid surfaces
EELS	Energy loss of surface scattered electron measured	Surface electronic structure, coordination environment of surface atoms	20 nm	Few %	<30 nm thick solids, vacuum env.
ATR-FTIR	FTIR spectrum of surface layer	Identity and bonding geometry of surface molecules	NA	NA	All solid surfaces
ISS	Surface bombarded by incident ions, whose momentum is transferred to surface atoms. The scattered ions are analyzed.	Surface composition	3A	50 ppm – 1%	All solid surfaces, vacuum env.

Table 2.2 Cont'd

Technique	Working principle	Information generated	Probing depth (typical)	Detection capability	Sample requirement
EXAFS	Monoenergetic photons excite a core hole. The change in the absorption cross section above the excitation threshold yields information on radial distances to neighboring atoms.	Surface fine structure (note: the technique applies to bulk materials as well)	Bulk	Few %	All solid
XANES	X-ray absorption within ~30 eV of the excitation threshold is measured, which is more sensitive to local 3-D geometry.	Surface fine structure	Bulk	Few %	All solid
Raman	Raman shift of the scattered photons measured. Yields complementary information to FTIR.	Identification and bonding geometry of surface molecules	Few μm	Few %	All solid surfaces
XPS (a.k.a. ESCA)	Excitation of atoms by incident X-ray photons generates photoelectrons. Energy of the emitted photoelectrons measured.	Surface composition, oxidation state	~3 nm	1 %	All solid surfaces, vacuum env.

Note: adapted from reference 46-48.

32

2.4 Reactions with chlorinated hydrocarbons

Halogenated organic compounds are the most prevalent organic contaminants in groundwater due to their extensive use as industrial solvents, insulating fluids in electronic components, and dry cleaning agents in the past (Urbano & Marinas, 2001; Wong *et al*., 2009). The ability of zero-valent iron (ZVI) to reductively transform aqueous chlorinated solvents to less chlorinated compounds was first noted by Gillham and O'Hannesin (1994). From a historical perspective, reduction of organic halides by zero-valent metals has been in use for over a century in chemical industry for organic synthesis (Urbano & Marinas, 2001). It is generally agreed that there are two types of reduction at a metal surface: the "indirect reduction" reduces organic halides via hydrogen species adsorbed on the metal surface. The metals here do not supply electrons, rather, they act as catalytic surfaces for absorption of atomic hydrogen species. Many noble metals, e.g. Pd and Pt, are known to mediate reduction through this mechanism. The other reduction pathway, "direct reduction", involves direct electron transfer between the adsorbed organic substrate and the metal surface. This mechanism applies to reduction at metals with high hydrogen overpotential, such as iron and zinc (Brewster, 1954), where the metals are corroded to provide electrons, hence the name "dissolving metal reductions".

2.4.1 Monometallic nZVI

Micron-sized or bulk metallic iron powder is a moderately strong reductant for reductive dechlorination of chlorinated aliphatics (Gillham & O'Hannesin, 1994):

$$Fe^0 + RCl + H^+ \rightarrow Fe^{2+} + RH + Cl^- \tag{3.6}$$
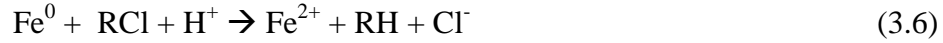
Equation 3.6 is actually the net reaction of two electrochemical half reactions, shown in Eq. 3.7-3.8.

$$Fe^0 \rightarrow Fe^{2+} + 2e^- \qquad\qquad E^0 = -0.44V \tag{3.7}$$

$$RCl + 2e^- + H^+ \rightarrow RH + Cl^- \qquad E^0 = 0.5 \sim 1.5 \text{ V at pH 7} \tag{3.8}$$
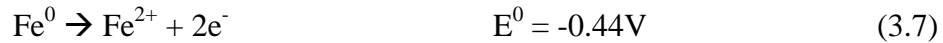
The half reaction of aliphatic chlorinated compounds in Eq. 3.8 has a standard reduction potential ranging form +0.5 to +1.5V (Matheson & Tratnyek, 1994). Thus, the reduction of chlorinated hydrocarbons by iron metal is thermodynamically favorable.

Matheson & Tratnyek (1994) proposed three possible pathways of reductive dehalogenation:

Pathway 1: direct reduction at exposed Fe(0) surface (e.g. corrosion pits) by electron transfer from the Fe(0) surface to the surface attached alkyl halide.

Pathway 2: reduction by aqueous Fe^{2+} produced from iron corrosion (Eq. 3.2 & 3.3).

Pathway 3: reduction by H_2 from anaerobic corrosion (Eq. 3.2).

It is shown by subsequent studies that direct reduction at Fe(0) surface is a minor process since the iron surface is inherently enclosed by an oxide layer in a core-shell configuration and the particles are continuously deposited with precipitates of corrosion

products (Liu *et al*., 2005; Reardon *et al*, 2008; Sarathy *et al*., 2008). Although ferrous ions can mediate the reduction of some contaminants such as hexavalent chromium (Eary & Rai, 1988), no reduction of carbon tetrachloride was observed in the presence of Fe(II) alone (Matheson & Tratneyk, 1994). However, this does not rule out the possibility that surface adsorbed Fe(II) may have reduction capability not present in aqueous free Fe(II) ions. Pathway 3 is regarded as being kinetically slow in the absence of a surface catalyst (e.g. Pd, Pt).

In an elegant study designed by Weber (1996) using 4-aminoazobenzene as a probe molecule, it is confirmed that reduction is mediated by the surface of iron and not occurring in the aqueous phase. This study, combined with the above discussion, indicates that *reductive dehalogenation is a process occurring at the iron surface involving electron transfer mediated by the iron oxide layer*. Three possible mechanisms for such electron transfer were proposed by Scherer *et al*. (1998), which are depicted in Figure 2.2. The first mechanism involves direct electron transfer from exposed Fe(0) surface (e.g. corrosion pits) to the adsorbed contaminants. In the second mechanism, the oxide layer acts as semiconductor mediating electron passage. The third mechanism suggests the oxide behaves as a coordinative surface with surface Fe(II) participating in the reduction of the organohalides.
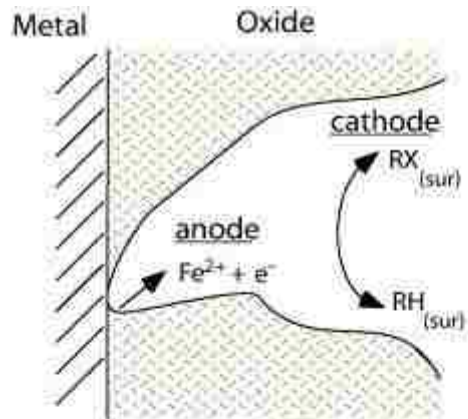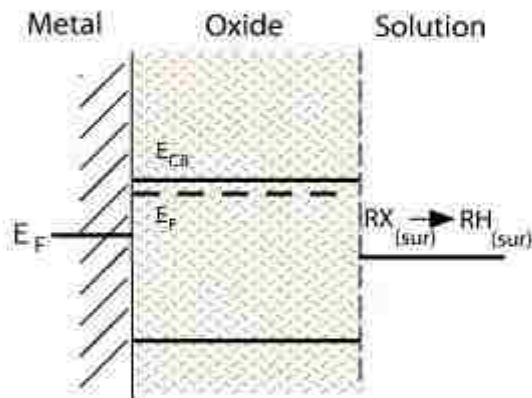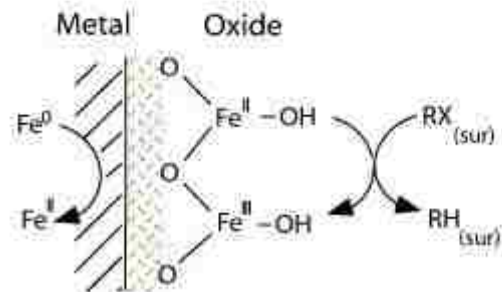
Figure 2.2 Possible roles of surface oxides in mediating reduction of chlorinated contaminants in water (from Scherer *et al*., 1998).

2.4.2 Bimetallic nZVI

Bimetallic nZVI nanoparticles refer to a class of nZVI material produced by depositing a second metal, such as Pd, Pt, Ni, Cu or Ag, on iron nanoparticles. Among many transitional metals studied for catalytic dehalogenation reactions, Pd is the most commonly used heterogeneous catalyst for its optimal structural and chemical properties to generate hydrogen species and to cleavage the carbon-halogen bond (Alonso *et al*., 2002). Pd-based catalysts in gas phase hydrogenation reactions are well-established, most well known examples are dehalogenation of CFC compounds, NO_x reduction in selective catalytic conversion units in electrical power plants, and in catalytic converter of automobiles (Wong *et al*., 2009). Pd catalyst for ground water remediation is a relatively new field. Early studies used Pd and hydrogen gas to dehalogenate simple aliphatic hydrocarbons. Lowry & Reinhard (1999) studied dechlorination of tetrachloroethene (PCE) and trichloroethene (TCE) with Pd on Al_2O_3 support in the presence of hydrogen gas. Other than alumina, other supports, such as carbon, aluminosilicates, clay materials and various metal oxides have been evaluated for Pd catalysts as well (Alonso *et al*., 2002).

Another form of Pd catalysts is produced by depositing Pd on top of a second metal, such as Fe, Ni, Mg, Au and others. In particular, Pd-Fe bimetallic system has become a fast growing field for groundwater remediation studies (a crude search using "Palladium" and "Iron" as the key words among leading environmental journals comes up with >200 references). Early studies on tetrachloroethene (PCE), trichloroethene (TCE) and

dichloroethene (DCE) reduction with Pd-Fe particles suggest that palladized iron is able to degrade these simple organic halides at much higher rates than monometallic iron. Furthermore, Pd-Fe systems give off more saturated products and produce less chlorinated intermediates compared to iron alone (Muftikian *et al.*, 1995; Lowry & Reinhard, 1999). A series of steps were proposed by Cheng *et al.* (1997) to account for the reductive dehalogenation mechanism in Pd-Fe systems, which is illustrated schematically in Figure 2.3: step 1) rapid iron corrosion and water reduction resulting in hydrogen gas evolution; step 2) adsorption and intercalation of hydrogen gas into the elemental palladium lattice, forming highly active hydrogen species; step 3) reduction of organic halides at the Pd surface or Pd-Fe interface. The role of Pd therefore lies essentially in its catalytic ability to adsorb and form dissociated hydrogen species as the active reducing agent.

Catalyzed Reduction (fast)

Direct Reduction (slow)

$R\text{-}H + Cl^-$

$R\text{-}H + Cl^-$

H_2

H_2O

H

$R\text{-}Cl$

H^+

$R\text{-}Cl$

Fe^{2+}

e^-

e^-

Fe^0

Pd^0

Iron oxide
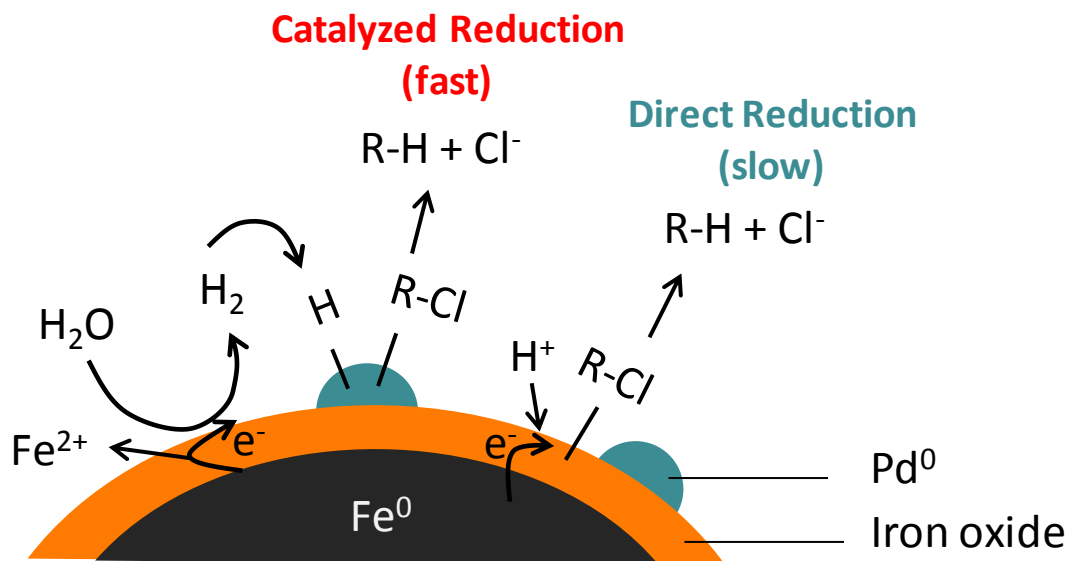
Figure 2.3 Mechanisms of reductive dechlorination by Pd-nZVI particles (adapted from Cheng *et al*., 1997).

More recent studies support the catalytic model proposed by Cheng *et al*. (1997), i.e. the enhanced reaction rates and the product distribution advantage of Pd-Fe systems are resulted from the synergistic effect between Pd and Fe, where Pd serves as the hydrodehalogenation and hydrogenation catalyst and Fe provides the hydrogen source through water reduction (Cwiertny *et al*., 2006; Bransfield *et al*., 2006; Schrick *et al*., 2002; Nutt *et al*., 2005; Song & Carraway, 2008). Cwiertny *et al*. (2006) compared the activity of Pd to other metals (e.g., Cu, Ni, Pt, and Au) on metallic iron for 1,1,1-trichloroethane reduction. At the same metal loading, Pd exhibited the highest activity relative to others, and the reaction rate constants of different bimetallic particles correlate very well with the theoretical solubility of atomic hydrogen in each additive metal. Another important clue in favor of the catalytic model is that organics with less

number of halogenated atoms in the molecule are more easily reduced by Pd, where as the opposite trend is followed if the reduction is mediated by iron surface (Alonso *et al*., 2002; Song & Carraway, 2008). Since Pd-Fe systems are known to have minimal build-up of partially chlorinated intermediates, the trend confirms the vital role played by Pd in dehalogenation reactions.

Other mechanisms explaining the enhanced reactivity of Pd-Fe system have been proposed, such as galvanic effect, in which the presence of Pd forms a galvanic couple with Fe causing accelerated Fe corrosion and hydrogen evolution (Cwiertny *et al*., 2007).

Despite the reactivity enhancement offered by the bimetallic particles, there is a lack of systematic studies to characterize the microstructure and surface chemistry of bimetallic nZVI materials. Main reason for this is that the additive metal is present at a very small quantity relative to iron (typical loading < 5 wt.%) and its distribution on nZVI is often non-uniform with feature dimension less than 10 nm, which challenge both the detection limits and the resolution power of common analytical instruments. Among a handful studies available on bimetallic ZVI material characterizations, majority focus on additive metal distribution on iron surface in an attempt to correlate with their reactivity data. Using AES elemental mapping or SEM-EDS technique, it is showed that the distribution of the additive metal on iron surface is highly heterogeneous, forming patches of Fe-rich and additive metal-rich regions (Kim & Carraway, 2003; McGuire *et al*., 2003; Xu *et al*., 2005; Bransfield *et al*., 2006; Cwiertny *et al*., 2006 & 2007). Using

XRD, formation of additive Pd nano-islands in the iron matrix has been observed with Pd grain size estimated to be 3-4 nm (Lien & Zhang, 2007).

All characterization works mentioned above were done on the freshly made bimetallic materials, and there is an underlying assumption in these studies that the properties measured do not change with reactions, while in actual conditions structural and surface-chemical changes are likely to occur. Very limited studies have attempted to evaluate this aspect. Muftikian *et al*. (1996) examined the changes in surface chemistry of a Pd-on-Fe film after reaction with TCE in aqueous phase. With XPS analysis, they noticed a significant decrease in surface Pd/Fe ratio after prolonged exposure to TCE solution. The Pd signal was recovered after the surface washed with hydrochloric acid. The authors proposed that Pd was buried underneath an iron hydroxide film resulted from iron corrosion over time, and cleaning with HCl re-expose the Pd surface by dissolving the hydroxide layer.

2.5 Reactions with metal contaminants

Recent studies show that nZVI is capable of sequestering a variety of metal contaminants including Cu(II), Zn(II), Pd(II), Cd(II), Ni(II), U(VI), Cr(VI) and Arsenic species (Shokes & Moller, 1999; Ponder *et al*., 2000; Su & Puls, 2001; Miehr *et al*., 2004; Cao & Zhang, 2006; Li & Zhang, 2006 & 2007). Invariably, these studies observed significantly higher apparent removal rates with nanoscale iron particles

compared to micron-sized particles. Ponder *et al*. (2000) reported that the apparent rates of Cr(VI) and Pd(II) removal by nZVI immobilized on a Ferrogel are up to 30 times faster than those of iron filings on an equal molar basis. The enhanced reaction rate is primarily attributed to the increase in surface area because the surface-area normalized reaction rate constants are similar between bulk iron (iron powder or filings) and nZVI (Miehr *et al*., 2004). Since metal contaminants are eventually bound to the solid phase, a greater surface area represents a potentially more voluminous capacity for metal uptake. For instance, Cao & Zhang (2006) reported that the capacity for Cr(VI) sequestration of nZVI is 50-70 times higher than a commercial micron-scale iron powder.

The mechanisms of metal removal have recently been elucidated with HR-XPS analysis. Li & Zhang (2006) have invoked a core-shell model for Ni(II) removal, whereby aqueous Ni(II) ions are first bound to the oxide surface via outer or inner-sphere complex formation, a portion of which are subsequently reduced to elemental nickel by accepting electrons transferred across the oxide layer from Fe(0) core (Li & Zhang, 2006). In a follow-up study, the core-shell model is extended to a variety of metal species with different electrochemical properties (Li & Zhang, 2007). It is shown that the final states of the metal species are dictated by the reduction potentials of the metal with respect to that of iron. Species with E^0 (standard reduction potential) more positive than iron, such as Cu(II) and Ag(I), are predominantly sequestered in their reduced states. Species close to or more negative than the E^0 of iron (-0.44 V) (e.g. Zn(II) and

Cd(II)) are removed by surface adsorption. Metals with E^0 slightly higher than iron, for instance, Ni(II) and Pd(II), are removed by a combination of adsorption and reduction mechanisms (Li & Zhang, 2007). The reactions of nZVI with Cr(VI) and Arsenic species are more complex. They are addressed separately in the following discussion.

2.5.1 Cr(VI)

The stable forms of chromium in the environment are trivalent, Cr(III), and hexavalent chromium (Cr(VI), CrO_4^{2-} or $HCrO_4^-$) (Patterson, 1985; Nriagu, 1988). At low concentrations, Cr(III) is non-toxic while Cr(VI) is a potent carcinogen. At present, the maximum concentration of total chromium in drinking water by USEPA regulation is 100 µg/L (USEPA, ref 81). Cr(III) is sparingly soluble at circumneutral pH (pH of 5.5– 7.4), whereas Cr(VI) is highly soluble and mobile in the environment (Palmer & Wittbrodt, 1991).

Within pH 2-10, it is shown that chromate ion is a stronger oxidant than water and reaction between iron and chromate (Eq. 3.9) dominates over aqueous corrosion (Eq. 3.2-3.3) (Eary & Rai, 1988; Powell *et al*., 1995).

$$Fe^0 + CrO_4^{2-} + 2H_2O + 2H^+ \rightarrow Fe(OH)_3(s) + Cr(OH)_3(s) \qquad (3.9)$$
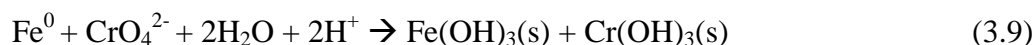
Blowes *et al*. (1997) conducted surface analysis using XPS and XANES (X-ray adsorption near-edge spectroscopy), and they confirm that the products of iron

43

oxidation and Cr(VI) reduction are Fe(III) hydroxide and Cr(III) hydroxide as in Eq. 3.9.

They form a layer of precipitates on the surface of iron materials. Mixed Fe(III)/Cr(III)

hydroxide solids have also been identified on the iron surface (Manning *et al.*, 2007),

which may be represented as $Fe_xCr_{1-x}OH_3$. Furthermore, Blowes *et al.* (1997) observed

through SEM X-ray mapping that Cr(III) was not homogeneously distributed in the iron

hydroxide phase. The goethite phase attracted the highest concentration of Cr(III) while

other phases such as maghemite and lepidocrocite were low in chromium.

Li *et al.* (2008) investigated the reaction products of Cr(VI) and nZVI using HR-XPS.

Their reaction model, shown in Figure 2.4, suggests that aqueous Cr(VI) is initially

removed from the solution by sorption and reduction as enabled by the oxide shell and

the Fe(0) core, respectively. The reduced Cr(III) species is incorporated into the

growing surface oxide phase by forming mixed Fe(III)/Cr(III) hydroxide in an

approximate stoichiometry of $Cr_{0.67}Fe_{0.33}O(OH)$ or $Cr_{0.67}Fe_{0.33}(OH)_3$.
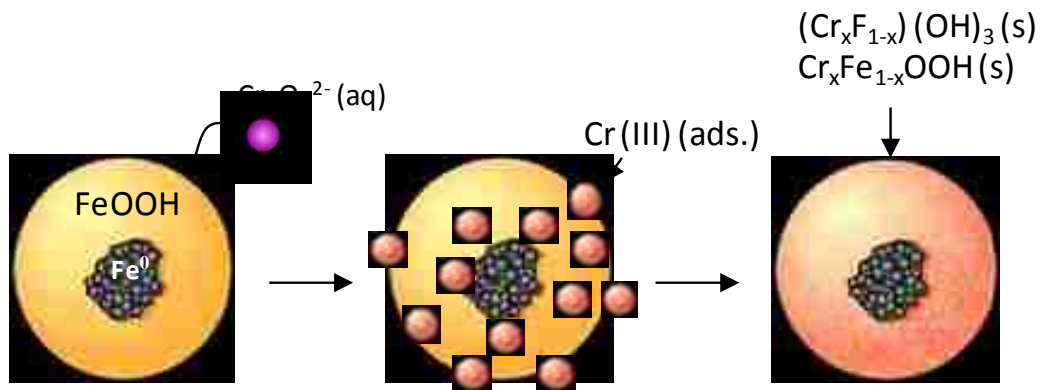
Figure 2.4 Proposed reaction model of nZVI and Cr(VI) (adapted from Li *et al.*, 2008).

Similar to other heterogeneous reactions, reaction rate of ZVI with Cr(VI) is a function of the surface concentration of Fe(0), ρ_A, and the aqueous Cr(VI) concentration. When abundant Fe(0) surface is present relative to Cr(VI), the rate can be simplified into a pseudo- first-order equation (refer to Section 2.6). However, several studies report that iron loses reactivity as Cr(VI) concentration increases (Ponder *et al.*, 2000; Melitas *et al.*, 2001). In a column study by Melitas *et al.* (2001), a Cr(VI) feed concentration below 5 mg/L resulted in complete chromium removal for over 100 days. Increasing Cr(VI) concentration in the feed stream to 10 mg/L led to breakthrough within a few days, indicating a loss in iron reactivity. The phenomenon was attributed to the passivating effect of Cr(III) hydroxide and mixed hydroxides deposited on the iron surface, with the hydroxides acting as an barrier layer inhibiting electron release from Fe(0) surface. Interestingly, the same chemistry is applied in metal corrosion prevention and accounts for the largest industrial use of chromate in the past. Increasing Cr(VI) concentration exacerbates the passivation effect. However, such effect has not been observed in field-scale remediation (Wilkin *et al.*, 2005), possibly due to the Cr(VI) concentrations there being generally below 10 mg/L.

It is found that the surface properties of ZVI exert a profound impact on the reaction rate and reduction capacity. Cao *et al.* (2006) reported that the reduction capacity of nano-ZVI particles was 50-70 times greater than that of iron powder under the same experiment conditions. The increased capacity was attributed to the larger surface area of nano-ZVI particles. In addition to surface area effect, metal surface structure is

known to affect its reduction potential significantly. It has been reported that iron filings by different manufacturers display varying degrees of performance in Cr(VI) removal ranging from extremely fast to essentially no effect (Powell *et al*., 1995). Impurities on the iron surface, particularly partially oxidized iron phase, may have caused accelerated corrosion of some iron filings as they form additional redox couples with Fe^0 surface.

2.5.2 Arsenic

High levels of arsenic in groundwater pose a serious health threat to millions of people around the world (Nordstrom, 2002; Smedley & Kinniburgh, 2002). The most important anthropogenic sources of arsenic are from smelter operations and fossil fuel combustion (Smedley & Kinniburgh, 2002). The principal forms of arsenic in the aqueous environment are arsenite (predominantly as H_3AsO_3) and arsenate (as $H_2AsO_4^-$ or $HAsO_4^{2-}$) (Korte & Fernando, 1991; Dixit & Hering, 2003). Unlike chromium or selenium, which are more readily adsorbed in their reduced forms, arsenic is relatively more mobile in the reduced trivalent state (Smedley & Kinniburgh, 2002). This distinct property of arsenic explains its higher concentrations in groundwater than in surface waters. The heavy dependence on arsenic-contaminated groundwater as the primary source of water for drinking and irrigation uses place developing countries such as Bangladesh, India, Vietnam, and Cambodia in a particularly vulnerable situation (Meharg & Rahman, 2003; Dittmar *et al*., 2010), where there is no centralized water

treatment facility to remove arsenic to below the WHO guideline of 10 μg/L (WHO, 2008).

Many options have been explored for arsenic removal and these include coagulation, adsorption, ion exchange, and membrane processes. Edwards (1994) studied the efficiency of arsenate (As(V)) removal using alum and ferric ions as coagulants. It is found that below pH 7.5, aluminum hydroxides are as effective as ferric hydroxides for As(V) removal. Ferric salts are more effective at higher pH and for As(III) removal. Adsorption of arsenic by naturally occurring metal oxides have been extensively studied. Both As(III) and As(V) can adsorb on a wide variety of adsorbents, most notably aluminum oxides and iron oxides (Manceau, 1995; Manning & Goldberg, 1997; Manning *et al*., 1998; Goldberg & Johnson, 2001). Adsorption takes place by ligand exchange with surface OH_2 and/or OH^- sites. Many other forms of adsorbents have been developed to remove As(III) and As(V), such as surface-treated activated carbon and materials prepared from industrial or agricultural by-products, have shown promising potentials for low-cost As(V) removal (Huang & Fu, 1984; Huang & Vane, 1989; Mohan & Pittman, 2007).

Raven *et al*., (1998) studied As(III) and As(V) adsorption on ferrihydrite at different pH. At the same arsenic initial concentration and metal oxide loading, the adsorption envelope of As(III) has a flat top over a broad pH range (pH 6-10), while adsorption maximum of As(V) occurs at pH 4-7. *The authors point out that, contrary to the misconception that As(III) is less adsorbable, As(III) can be retained at much higher*

quantity than As(V) at higher pH (>7.5) or high As concentrations. This point is confirmed by other groups (Manning *et al.*, 1998; Dixit & Hering, 2003). Dixit & Hering (2003) compared As(III) and As(V) adsorption among amorphous iron oxides (HFO), goethite, and magnetite. It is found that HFO has similar densities of sorption sites as the crystalline goethite (Table 2.3), but HFO possesses much higher adsorption capacity due to its higher specific surface area (600 m^2/g vs. 54 m^2/g for goethite). In the presence of phosphate ions, adsorption of both As(III) and As(V) adsorption are strongly affected, nevertheless, As(III) is still more adsorbable than As(V) over a wide range of pH.

Table 2.3: Adsorption site densities of iron oxide materials (based on Dixit & Hering, 2003).

Sites/nm^2	HFO	Goethite	Magnetite
As(V)	2.6	2.0	n/a
As(III)	3.5	2.0	2.2

The implications of these results are multi-fold: since As(III) is adsorbed to a greater extent than As(V) over a broad pH, microbial reduction of As(V) in natural waters would not necessarily increase arsenic mobility. However, in iron reducing conditions occurring in deep aquifers, arsenic release may take place with iron mobilization (Sullivan & Aller, 1996). Another potential release mechanism is that, iron oxides initially formed in natural waters are amorphous in nature and have high surface areas,

however, the amorphous oxides may undergo crystalline transformation over time, which will cause decrease in sorption sites and release of solid bound arsenic.

The molecular-level structures of As(V) or As(III) surface complexes on iron oxides have been studied using various spectroscopic techniques (Manceau, 1995; Manning & Goldberg, 1997; Manning *et al*., 1998; Goldberg & Johnson, 2001). Using shift in point of zero charge (PZC) as an indicator of inner-sphere complex formation and together with FTIR spectroscopic analysis, Goldberg & Johnson (2001) suggest that As(V) forms predominantly inner-sphere complexes with iron oxides, while As(III) forms both inner and outer-sphere complexes with iron oxides. Using EXAFS technique, Manning *et al*. (1998) and Fendorf *et al*. (1997) conclude that As(III) forms a single bidentate binuclear As(III) surface complex, whereas As(V) forms both bidentate binuclear and monodentate mononuclear structures (Figure 7.1 in chapter 7). Other structures, such as a bidentate mononuclear structure, have been reported by Ona-Nguema *et al*. (2005) for As(III) adsorption on ferrihydrite and hematite. The detailed structure and their relative distributions on the surfaces are found to vary with arsenic surface loading and the type of the iron oxide studied.

Recently, zero-valent iron has been applied to the remediation of arsenic contaminated groundwater (Lackovic *et al*., 2000; Manning *et al*., 2002; Hussam & Munir, 2007). There is a generally accepted notion that the interaction between arsenic and zero-valent iron materials are predominantly via surface adsorption onto the oxide layer present on the metal iron surface (Lackovic *et al*., 2000; Farrell *et al*. 2001). Melitas *et al*. (2002)

suggest that As(V) reduction did not occur in solutions equilibrated with Fe(0)-corroding surface (based on Tafel diagrams of iron wire electrodes in As(V) solutions), thus As(V) was mainly retained by surface adsorption. Similarly, Lackovic *et al.* (2000) found no evidence of As(V) reduction in leachates from ZVI-sand columns. Instead, they proposed that arsenate was retained by surface sorption and co-precipitation with sulfur species present in the ZVI material. These notions are largely based on aqueous analysis only and they are not backed by direct evidence from careful analysis of the solid phase.

More recent spectroscopic investigations of arsenic speciation in ZVI materials reveal that the immobilized arsenic is converted to different oxidation states from their aqueous forms, suggesting arsenic redox transformations have played an active part in the remediation. X-ray photoelectron spectroscopy (XPS) analysis by Su & Puls (2001) detected no reduction of As(III) by ZVI filings but partial oxidation of As(III) to As(V). Manning *et al.* (2002) reported similar findings with X-ray absorption spectroscopy (XANES and EXAFS) for ZVI powders reacted under aerobic conditions, where they proposed the oxidation of As(III) might be mediated by iron corrosion products such as magnetite/maghemite or lepidocrocite. On the other hand, Bang *et al.* (2005) found a fraction of As(III) being reduced to As(0) on an acid-pretreated iron coupon under anoxic conditions. Table 2.4 summarizes findings presented by recent ZVI-arsenic studies. The discrepancies in these studies cannot be simply explained due to limited spectroscopic data sets available and variations in experimental conditions.

Table 2.4: Summary of results of recent arsenic-ZVI studies.

Iron material used	Initial As state	As speciation in the solid phase	As state in the solution	Reaction conditions	ZVI corrosion products	Proposed reaction mechanisms	Reference
Iron fillings	As(III)	As(III) + As(V)	As(III) + As(V)	oxic batch reactor		Sorption, surface oxidation	Su & Puls, 2001,
Iron fillings	As(III)	As(III) + As(V)	As(III) + As(V)	Oxic batch reactor	Magnetite, maghemite, lepidocrocite	Sorption, surface or homogeneous oxidation	Manning *et al.*, 2002
Iron filings	As(III)	NA	NA	Iron/sand mixed column		Sorption, precipitation	Nikolaidis *et al.*, 2003
Nanoscale iron particles	As(III)	As(III) + As(V)	NA	Oxic batch reactor	amorphous iron hydroxide (short-term), Magnetite, maghemite, lepidocrocite,	Sorption, surface oxidation	Kanel *et al.*, 2005
Polished and acid-treated iron coupon	As(III)	As(III) + As(0)	NA	Anoxic batch reactor	Iron hydroxide	Sorption, reduction	Bang *et al.*, 2005
Iron powder	As(III)	NA	As(III) + As(V)	Oxic batch reactor		Sorption, oxidation	Hug *et al.*, 2008
Iron powder	As(III)	As(III) + As(V)	NA	Oxic batch reactor, column	Carbonate green rust	Sorption, co-precipitation, oxidation	Lien & Wilkin, 2005

The oxidative capability of zero-valent iron is generally considered to be a result of Fenton Chemistry involving Fe(II) and H_2O_2 produced from aerobic ZVI corrosion (Joo et al., 2004; Katsoyiannis et al., 2008). The production of Fe(II) and H_2O_2 follows two-electron transfer from Fe(0) (Eq. 3.10). H_2O_2 can be reduced to water with another two-electron transfer from Fe(0) (Eq. 3.11), alternately, it can react with Fe(II) to produce a potent oxidant, OH· radical, under acidic conditions or Fe(IV) species at neutral to alkaline pH (Joo et al., 2004; Lee & Sedlak, 2008), as shown in Eq. 3.12-3.13.

$$O_2 + Fe^0 \rightarrow Fe^{2+} + H_2O_2 \tag{3.10}$$

$$H_2O_2 + Fe^0 \rightarrow Fe^{2+} + H_2O \tag{3.11}$$

$$H_2O_2 + Fe^{2+} \rightarrow Fe^{3+} + OH· + OH^- \quad \text{(acidic pH)} \tag{3.12}$$

$$H_2O_2 + Fe^{2+} \rightarrow Fe(IV) \quad \text{(pH > 5)} \tag{3.13}$$

Under neutral pH conditions, Fe(II) may react with O_2 directly to produce $O_2·^-$ radicals.

$$Fe^{2+} + O_2 \rightarrow Fe^{2+} + O_2·^- \quad \text{(pH ~ 7)} \tag{3.14}$$

Compared to bulk iron, nanoscale ZVI yields more H_2O_2 and Fe(II) due to more rapid and continual iron corrosion (Joo et al., 2004). Thus, formation of oxidants such as H_2O_2, OH·, ferryl species, and $O_2·^-$ is more significant. Higher yield of oxidants per mole of nZVI added is observed at lower doses of nZVI. This may be related to the increase in Fe(II) ion concentration at higher nZVI doses, which serves as a competitive scavenger of OH· radicals. It is noted that pH plays a large role in the type and quantity

of oxidants formed (Katsoyiannis *et al*., 2008). It is suggested that at pH less than 5, OH· radicals are the dominant oxidant responsible for As(III) oxidation (Hug & Leupin, 2003). At neutral pH, a different but weaker oxidant accounts for As(III) oxidation. The identity of this weaker oxidant is subject to intense debate, with several species, e.g. Fe(IV), HO_2·, and O_2·⁻, being the possible candidates (Hug & Leupin, 2003; Katsoyiannis *et al*., 2008; Lee & Sedlak, 2008). These reactions are given in Eq. 3.15-3.16.

$$As(III) + OH· \rightarrow As(V) \qquad \text{(acidic pH)} \qquad (3.15)$$

$$As(III) + Fe(IV) / HO_2· / O_2·⁻ \rightarrow As(V) \qquad \text{(neutral pH)} \qquad (3.16)$$
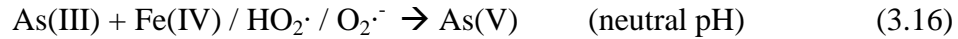
The facile oxidation of As(III) by Fe(0) in the presence of O_2 may be one of the most important abiotic pathway for arsenic oxidation, and may explain rapid oxidation of As(III) in groundwater to As(V) when pumped to surface (Hug & Leupin, 2003)

2.6 Kinetic models of nZVI treatment

It is generally observed that the reaction rates of iron nanoparticles follow pseudo-first-order kinetics. The apparent rate constant, k_{obs}, is proportional to the reactive sites on iron surface, which is equivalent to the product of the surface-area-normalized specific reaction rate constant, k_{SA}, surface area of iron, α_s, and the mass concentration of iron in solution, ρ_m (Johnson *et al*., 1996), as in Eq. 3.17.

$$-dC/dt = k_{obs}C = k_{SA}\alpha_s\rho_mC \qquad (3.17)$$

Eq. 3.17 suggests that $k_{obs} = k_{SA}\alpha_s\rho_m$, thus plotting k_{obs} by $\alpha_s\rho_m$ should give k_{SA}, which is an intrinsic property of the iron material and is independent of the mass of iron dosed or the volume of the system. By comparing the k_{obs} and k_{SA} data of benzoquinone (BQ) and carbon tetrachloride (CT), Nurmi *et al*. (2005) conclude that the intrinsic reactivity of nanoscale-ZVI particles is comparable to that of bulk iron. The enhanced rates are simply the result of increased specific surface areas.

Pseudo-first-order kinetic model shown above has been observed during degradation of carbon tetrachloride, TCE, nitrobenzene, and chromate with Fe(0) particles (Matheson & Tratnyek, 1994; Gillham & O'Hannesin, 1994; Johnson *et al*., 1996; Miehr *et al*., 2004). This model has been shown to be particularly applicable to aliphatic chlorinated compounds based on extensive kinetics data obtained using different types of iron particles (Miehr *et al*., 2004). Eq. 3.17 is a simplistic model assuming that there is no loss of reactivity of the metal surface over prolonged exposure to contaminant media. In practical scenarios, reductions in reaction rate constants have been observed. For instance, at elevated Cr(VI) concentrations, iron particles are deactivated due to strong passivation effect of Cr(III) hydroxide and mixed oxides formed on the iron surface (Ponder *et al*., 2000; Melitas *et al*., 2001).

Another type of deviation from Eq. 3.17 is that the reaction rate constants are found to vary with the initial contaminant concentrations. For example, Johnson *et al*. (1996) discovered that carbon tetrachloride degradation rate increased with CT concentrations until it reached a saturated value at relatively high concentration. This kind of kinetic

behavior is attributed to surface saturation effect. Mixed-order reaction rate model is proposed to account for this effect (Eq. 3.18).

$$- \text{dC/dt} = \frac{K_0 C}{K_{1/2} + C}$$ (3.18)

Where k_0 can be interpreted as the maximum reaction rate, and $k_{1/2}$ as a parameter indicating the affinity of contaminants for the surface sites. Eq. 3.18 is in close analogy to the well-known Michaelis-Menten Equation.

2.7 Improving nZVI transport in subsurface media

The potential of nZVI as an *in situ* remediation agent hinges on the ability of the nanoparticles to migrate in subsurface porous media. Early studies reported that bare nZVI travelled limited distance in packed sand columns, which was primarily attributed to the aggregation of nZVI as commonly noted in many characterization studies (Nurmi *et al*., 2005; Sun *et al*., 2006). Such aggregation behavior cannot be accounted for by the classical Derjaguin-Landau-Verwey-Overbeek (DLVO) theory, which predicts that the colloidal stability of charged particles is controlled by the attractive Van der Waals force and the repulsive electrostatic interactions, thus the net result of the two forces would create an energy barrier preventing particle aggregation at low ionic concentrations (Elimelech *et al*., 1995). Latest results indicate that an attractive magnetic interaction among nZVI particles may play a crucial role in particle

agglomeration, particularly at high particle concentrations. A modified DLVO model has been developed which yields potential curves without energy barriers and predicts rapid association of the particles in reasonable agreement with the experimental observations (Phenrat *et al.*, 2007; Phenrat *et al.*, 2009).

A variety of engineering approaches have been explored to modify the particle surfaces to mitigate particle agglomeration. Many commercially available, non-toxic polymers such as polyacrylic acid (PAA), guar gum, and carboxymethylcellulose (CMC) have achieved varying degrees of success in improving particle stability (He *et al.*, 2007; Tiraferri *et al.*, 2008). There are generally two approaches to introduce a polymeric coating onto nZVI surface: by mixing the polymers with pre-formed nanoparticles and by synthesizing nZVI in polymeric solutions (He & Zhao, 2005; Phenrat *et al.*, 2009). By similar mechanisms, naturally occurring macromolecules such as fulvic acids and humic acids can act as stabilizers to retard the aggregation of nanoparticles (Johnson & Tratnyek, 2009; Fatisson *et al.*, 2010). Recent modeling efforts show that the presence of natural organic matter can carry pressure-injected nZVI slurry for distances up to several meters (Johnson & Tratnyek, 2009), and conceivably the migration length can be further improved with the amendment of engineered polymeric coatings.

Improved mobility of the surface-modified nZVI has been confirmed *in situ* in recent field applications, among which, direct treatment of an underground TCE DNAPL phase was documented using a type of emulsified nZVI (Quinn *et al.*, 2005). In this study, the nanoparticles were trapped in oil-in-water droplets for better contact with the

DNAPL plume and were delivered by a pressure pulse injection method. Short-term reductions in TCE concentrations indicative of abiotic degradation were recorded. Data from a more recent field study using CMC-stabilized Pd-nZVI for PCE and TCE remediation suggests that nZVI amendment may invoke rapid abiotic degradation within a few weeks after injection and stimulate slower but persistent biodegradation processes spanning over several years. In the latter case, iron and surfactant molecules served as excellent stimulating agents for the indigenous anaerobic microbial populations (He *et al*., 2010).

References

1. Feynman, R. There is plenty of room at the bottom, Caltech Institute Archives, 1959. (http://www.zyvex.com/nanotech/feynman.html)

2. National Nanotechnology Initiative. 2009. What Is Nanotechnology? (http://www.nano.gov/html/facts/whatIsNano.html)

3. Mulvaney, P. Metal nanoparticles: double layers, optical properties, and electrochemistry. In *Nanoscale Materials in Chemistry*; Klabunde, K. J., Ed.; Wiley: NewYork, 2001, pp 121-167.

4. Campbell, C. T.; Parker, S. C. The effect of size-dependent nanoparticle energetics on catalyst sintering. *Science* **2002**, *298*, 811-814.

5. Stumm, W., Chemistry of the solid-water interface: Processes at the mineral-water and particle-water interface in natural systems. John Wiley & Sons, New York, 1992.

6. Morel F. M. M.; Hering, J., Principles and applications of aquatic chemistry. John Wiley & Sons, New York, 1993.

7. Masciangioli, T.; Zhang, W. X., Environmental technologies at the nanoscale. *Environ. Sci. Technol.* **2003,** *37* (5), 102A-108A.

8. Gillham, R. W.; Ohannesin, S. F., Enhanced Degradation of Halogenated Alphatics by Zero-Valent Iron. *Ground Water* **1994,** *32* (6), 958-967.

9. Matheson, L. J.; Tratnyek, P. G., Reductive Dehalogenation of Chlorinated Methanes by Iron Metal. *Environ. Sci. Technol.* **1994,** *28* (12), 2045-2053.

10. Johnson, T. L.; Scherer, M. M.; Tratnyek, P. G., Kinetics of halogenated organic compound degradation by iron metal. *Environ. Sci. Technol*. **1996,** *30* (8), 2634-2640.

11. Hundal, L. S.; Singh, J.; Bier, E. L.; Shea, P. J.; Comfort, S. D.; Powers, W. L., Removal of TNT and RDX from water and soil using iron metal. *Environ. Pollut.* **1997,** *97* (1-2), 55-64.

12. Gavaskar, A. R.; Sass, N. N. M.; Janoy, R. J.; O'Sullivan, D. Permeable Barriers for Goundwater Remediation—Design, Construction, and Monitoring, Battelle Memorial Institute, Columbus, OH, 1998.

13. Gu, B.; Liang, L.; Dickey, M. J.; Yin, X.; Dai, S., Reductive precipitation of

uranium(VI) by zero-valent iron. *Environ. Sci. Technol*. **1998,** *32* (21), 3366-3373.

14. Cao, J. S.; Wei, L. P.; Huang, Q. G.; Wang, L. S.; Han, S. K., Reducing degradation of azo dye by zero-valent iron in aqueous solution. *Chemosphere* **1999,** *38* (3), 565-571.

15. Alowitz, M. J.; Scherer, M. M., Kinetics of nitrate, nitrite, and Cr(VI) reduction by iron metal. *Environ. Sci. Technol*. **2002,** *36* (3), 299-306.

16. Wilkin, R. T.; Su, C. M.; Ford, R. G.; Paul, C. J., Chromium-removal processes during groundwater remediation by a zerovalent iron permeable reactive barrier. *Environ. Sci. Technol*. **2005,** *39* (12), 4599-4605.

17. Wang, C. B.; Zhang, W. X., Synthesizing nanoscale iron particles for rapid and complete dechlorination of TCE and PCBs. *Environ. Sci. Technol*. **1997,** *31* (7), 2154-2156.

18. Zhang, W. X.; Wang, C. B.; Lien, H. L., Treatment of chlorinated organic contaminants with nanoscale bimetallic particles. *Catal. Today* **1998,** *40* (4), 387-395.

19. Lien, H. L.; Zhang, W. X., Transformation of chlorinated methanes by nanoscale iron particles. *J. Environ. Eng.-ASCE* **1999,** *125* (11), 1042-1047.

20. Xu, Y.; Zhang, W. X., Subcolloidal Fe/Ag particles for reductive dehalogenation of chlorinated benzenes. *Ind. Eng. Chem. Res.* **2000,** *39* (7), 2238-2244.

21. Li, X. Q.; Elliott, D. W.; Zhang, W. X., Zero-valent iron nanoparticles for abatement of environmental pollutants: Materials and engineering aspects. *Crit. Rev. Sol. State* **2006,** *31* (4), 111-122.

22. Sacre, J. A. Treatment walls: a status update. Ground-water remediation technologies analysis center, TP-97-02, Pittsburgh, PA, 1997.

23. Scherer, M. M.; Richter, S.; Valentine, R. L.; Alvarez, P. J. J., Chemistry and microbiology of permeable reactive barriers for *in situ* groundwater clean up. *Crit. Rev. Microbiol* **2000**, *26*(4), 221-264.

24. Elliott, D. W.; Zhang, W. X., Field assessment of nanoscale biometallic particles for groundwater treatment. *Environ. Sci. Technol.* **2001,** *35* (24), 4922-4926.

25. Quinn, J.; Geiger, C.; Clausen, C.; Brooks, K.; Coon, C.; O'Hara, S.; Krug, T.; Major, D.; Yoon, W. S.; Gavaskar, A.; Holdsworth, T., Field demonstration of DNAPL dehalogenation using emulsified zero-valent iron. *Environ. Sci. Technol.* **2005,** *39* (5), 1309-1318.

26. Glavee, G. N.; Klabunde, K. J.; Sorensen, C. M.; Hadjipanayis, G. C., Chemistry of borohydride reduction of iron(II) and iron(III) ions in aqueous and nonaqueous media – Formation of nanoscale Fe, FeB, and Fe_2B powders. *Inorg. Chem.* **1995,** *34* (1), 28-35.

27. Hahn, H., Gas phase synthesis of nanocrystalline materials. *Nanostructured Materials* **1997,** *9* (1-8), 3-12.

28. Nurmi, J. T.; Tratnyek, P. G.; Sarathy, V.; Baer, D. R.; Amonette, J. E.; Pecher, K.; Wang, C. M.; Linehan, J. C.; Matson, D. W.; Penn, R. L.; Driessen, M. D., Characterization and properties of metallic iron nanoparticles: Spectroscopy, electrochemistry, and kinetics. *Environ. Sci. Technol.* **2005,** *39* (5), 1221-1230.

29. Li, S. L.; Yan, W. L.; Zhang, W. X., Solvent-free production of nanoscale zero-valent iron (nZVI) with precision milling. *Green Chem.* **2009,** *11* (10), 1618-1626.

30. Capek, I. Preparation of metal nanoparticles in water-in-oil (W/O) microemulsions. *Adv. Colloid Interface Sci.* **2004,** *110*, 49-47.

31. Majewski, P.; Thierry, B. Functionalized magnetiten—synthesis, properties, and bio-applications. *Crit. Rev. Sol. State Mater. Sci.* **2007,** *32*(3), 203-215.

32. Suslick, K. S.; Choe, S. B.; Chichowias, A. A.; Grinstaff, M. W. Sonochemical synthesis of amorphous iron. *Nature* **1991,** *353*, 414-416.

33. Zhu, B. W.; Lim, T. T., Catalytic reduction of Chlorobenzenes with Pd/Fe nanoparticles: reactive sites, catalyst stability, particle aging, and regeneration. *Environ. Sci. Technol.* **2007,** *41* (21), 7523-7529.

34. Choi, H.; Al-Abed, S. R.; Agarwal, S.; Dionysiou, D. D., Synthesis of reactive nano-Fe/Pd bimetallic system-impregnated activated carbon for the simultaneous adsorption and dechlorination of PCBs. *Chem. Mater.* **2008,** *20* (11), 3649-3655.

35.   Sun, Y. P.; Li, X. Q.; Cao, J. S.; Zhang, W. X.; Wang, H. P., Characterization of zero-valent iron nanoparticles. *Adv. Colloid Interfac.* **2006,** *120* (1-3), 47-56.

36.   Liu, Y. Q.; Choi, H.; Dionysiou, D.; Lowry, G. V., Trichloroethene hydrodechlorination in water by highly disordered monometallic nanoiron. *Chem. Mater.* **2005,** *17* (21), 5315-5322.

37.   Kanel, S. R.; Greneche, J. M.; Choi, H., Arsenic(V) removal kom groundwater using nano scale zero-valent iron as a colloidal reactive barrier material. *Environ. Sci. Technol.* **2006,** *40* (6), 2045-2050.

38.   Odziemkowski, M. S.; Schuhmacher, T. T.; Gillham, R. W.; Reardon, E. J., Mechanism of oxide film formation on iron in simulating groundwater solutions: Raman spectroscopic studies. *Corrosion Sci.* **1998,** *40* (2-3), 371-389.

39.   Agrawal, A.; Ferguson, W. J.; Gardner, B. O.; Christ, J. A.; Bandstra, J. Z.; Tratnyek, P. G., Effects of carbonate species on the kinetics of dechlorination of 1,1,1-trichloroethane by zero-valent iron. *Environ. Sci. Technol.* **2002,** *36* (20), 4326-4333.

40.   Su, C. M.; Puls, R. W., Significance of iron(II,III) hydroxycarbonate green rust in arsenic remediation using zerovalent him in laboratory column tests. *Environ. Sci. Technol.* **2004,** *38* (19), 5224-5231.

41.   Ponder, S. M.; Darab, J. G.; Bucher, J.; Caulder, D.; Craig, I.; Davis, L.; Edelstein, N.; Lukens, W.; Nitsche, H.; Rao, L. F.; Shuh, D. K.; Mallouk, T. E., Surface chemistry and electrochemistry of supported zerovalent iron

nanoparticles in the remediation of aqueous metal contaminants. *Chem. Mater.* **2001,** *13* (2), 479-486.

42. Melitas, N.; Chuffe-Moscoso, O.; Farrell, J., Kinetics of soluble chromium removal from contaminated water by zerovalent iron media: Corrosion inhibition and passive oxide effects. *Environ. Sci. Technol.* **2001,** *35* (19), 3948-3953.

43. Morris, J. C.; Stumm, W. Redox equilibria and measurements of potentials in the aquatic environment. In Equilibrium Concepts in Natural Water Systems; American Chemical Society: Washington, DC, 1967, pp 270-285.

44. Whitfield, M. Thermodynamic limitations on the use of the platinum electrode in Eh measurements. *Limnol. Oceanogr.* **1974**, *19*, 857–865.

45. Farrell, J.; Wang, J.; O'Day, P.; Conklin, M., Electrochemical and spectroscopic study of arsenate removal from water using zero-valent iron media. *Environ. Sci. Technol*. **2001**, *35*, 2026-2032.

46. Somorja, G. A. Introduction to Surface Chemistry and Catalysis, John Wiley & Sons: New York, 1994.

47. McGuire, M. M.; Carlson, D. L.; Vikesland, P. J.; Kohn, T.; Grenier, A. C.; Langley, L. A.; Roberts, A. L.; Fairbrother, D. H., Applications of surface analysis in the environmental sciences: dehalogenation of chlorocarbons with zero-valent iron and iron-containing mineral surfaces. *Analytica Chimica Acta* **2003,** *496* (1-2), 301-313.

48. Class notes, ChE 398 Environmental Catalysis, Lehigh University.

49. Sarathy, V.; Tratnyek, P. G.; Nurmi, J. T.; Baer, D. R.; Amonette, J. E.; Chun, C. L.; Penn, R. L.; Reardon, E. J., Aging of iron nanoparticles in aqueous solution: Effects on structure and reactivity. *J. Phys. Chem. C* **2008,** *112* (7), 2286-2293.

50. Reardon, E. J.; Fagan, R.; Vogan, J. L.; Przepiora, A., Anaerobic corrosion reaction kinetics of nanosized iron. *Environ. Sci. Technol.* **2008,** *42* (7), 2420-2425.

51. Eary, L. E.; Rai, D., Chromate removal from aqueous wastes by reduction with ferrous ion. *Environ. Sci. Technol.* **1988,** *22* (8), 972-977.

52. Scherer, M. M.; Balko B. A., Tratnyek, P., in Kinetics and Mechanisms of Reactions at the Mineral-Water Interface, Sparks, D., Grundl, T., Eds., ACS Symp. Ser. No. 715, pp. 301-322.

53. Wong, M. S.; Alvarez, P. J. J.; Fang, Y. I.; Akcin, N.; Nutt, M. O.; Miller, J. T.; Heck, K. N., Cleaner water using bimetallic nanoparticle catalysts. *J. Chem. Technol. Biot.* **2009,** *84* (2), 158-166.

54. Urbano, F. J.; Marinas, J. M., Hydrogenolysis of organohalogen compounds over palladium supported catalysts. *J. Mol. Catal. A-Chem.* **2001,** *173* (1-2), 329-345.

55. Brewster, J. H. Mechanisms of reduction at metal surfaces. I. A general working hypothesis. *J. Am. Chem. Soc.* **1954**, 76, 6361-6363.

56. Alonso, F.; Beletskaya, I. P.; Yus, M., Metal-mediated reductive hydrodehalogenation of organic halides. *Chem. Rev.* **2002,** *102* (11), 4009-4091.

57. Lowry, G. V.; Reinhard, M., Hydrodehalogenation of 1-to 3-carbon halogenated organic compounds in water using a palladium catalyst and hydrogen gas. *Environ. Sci. Technol.* **1999,** *33* (11), 1905-1910.

58. Muftikian, R.; Fernando, Q.; Korte, N., A method for the rapid dechlorination of low-molecular-weight chlorinated hydrocarbons in water. *Water Res.* **1995,** *29* (10), 2434-2439.

59. Cheng, I. F.; Fernando, Q.; Korte, N., Electrochemical dechlorination of 4-chlorophenol to phenol. *Environ. Sci. Technol.* **1997,** *31* (4), 1074-1078.

60. Cwiertny, D. M.; Bransfield, S. J.; Roberts, A. L., Influence of the oxidizing species on the reactivity of iron-based bimetallic reductants. *Environ. Sci. Technol.* **2007,** *41* (10), 3734-3740.

61. Cwiertny, D. M.; Bransfield, S. J.; Livi, K. J. T.; Fairbrother, D. H.; Roberts, A. L., Exploring the influence of granular iron additives on 1,1,1-trichloroethane reduction. *Environ. Sci. Technol.* **2006,** *40* (21), 6837-6843.

62. Bransfield, S. J.; Cwiertny, D. M.; Roberts, A. L.; Fairbrother, D. H., Influence of copper loading and surface coverage on the reactivity of granular iron toward 1,1,1-trichloroethane. *Environ. Sci. Technol.* **2006,** *40* (5), 1485-1490.

63. Schrick, B.; Blough, J. L.; Jones, A. D.; Mallouk, T. E., Hydrodechlorination of trichloroethylene to hydrocarbons using bimetallic nickel-iron nanoparticles.

Chem. Mater. **2002,** *14* (12), 5140-5147.

64. Nutt, M. O.; Hughes, J. B.; Wong, M. S., Designing Pd-on-Au bimetallic nanoparticle catalysts for trichloroethene hydrodechlorination. *Environ. Sci. Technol.* **2005,** *39* (5), 1346-1353.

65. Song, H.; Carraway, E. R., Catalytic hydrodechlorination of chlorinated ethenes bly nanoscale zero-valent iron. *Appl. Catal. B-Environ.* **2008,** *78* (1-2), 53-60.

66. Kim, Y. H.; Carraway, E. R., Dechlorination of chlorinated ethenes and acetylenes by palladized iron. *Environ. Technol.* **2003,** *24* (7), 809-819.

67. Xu, J.; Dozier, A.; Bhattacharyya, D., Synthesis of nanoscale bimetallic particles in polyelectrolyte membrane matrix for reductive transformation of halogenated organic compounds. *J. Nanopart. Res.* **2005,** *7* (4-5), 449-467.

68. Bransfield, S. J.; Cwiertny, D. M.; Livi, K.; Fairbrother, D. H., Influence of transition metal additives and temperature on the rate of organohalide reduction by granular iron: Implications for reaction mechanisms. *Appl. Catal. B-Environ.* **2007,** *76* (3-4), 348-356.

69. Lien, H. L.; Zhang, W. X., Nanoscale Pd/Fe bimetallic particles: Catalytic effects of palladium on hydrodechlorination. *Appl. Catal. B-Environ.* **2007,** *77* (1-2), 110-116.

70. Muftikian, R.; Nebesny, K.; Fernando, Q.; Korte, N., X-ray photoelectron spectra of the palladium-iron bimetallic surface used for the rapid dechlorination of chlorinated organic environmental contaminants. *Environ. Sci. Technol.* **1996,**

30 (12), 3593-3596.

71.   Shokes, T. E.; Moller, G., Removal of dissolved heavy metals from acid rock drainage using iron metal. *Environ. Sci. Technol.* **1999,** 33, (2), 282-287.

72.   Rangsivek, R.; Jekel, M. R., Removal of dissolved metals by zero-valent iron (ZVI): Kinetics, equilibria, processes and implications for stormwater runoff treatment. *Water Res.* **2005,** 39, (17), 4153-4163.

73.   Miehr, R.; Tratnyek, P. G.; Bandstra, J. Z.; Scherer, M. M.; Alowitz, M. J.; Bylaska, E. J., Diversity of contaminant reduction reactions by zerovalent iron: Role of the reductate. *Environ. Sci. Technol.* **2004,** 38, (1), 139-147.

74.   Su, C. M.; Puls, R. W., Arsenate and arsenite removal by zerovalent iron: Kinetics, redox transformation, and implications for *in situ* groundwater remediation. *Environ. Sci. Technol.* **2001,** 35, (7), 1487-1492.

75.   Li, X. Q.; Zhang, W. X., Iron nanoparticles: the core-shell structure and unique properties for Ni(II) sequestration. *Langmuir* **2006,** 22, (10), 4638-4642.

76.   Li, X. Q.; Zhang, W. X., Sequestration of metal cations with zerovalent iron nanoparticles - A study with high resolution X-ray photoelectron spectroscopy (HR-XPS). *J. Phys. Chem. C* **2007,** 111, (19), 6939-6946.

77.   Ponder, S. M.; Darab, J. G.; Mallouk, T. E., Remediation of Cr(VI) and Pb(II) aqueous solutions using supported, nanoscale zero-valent iron. *Environ. Sci. Technol.* **2000,** 34, (12), 2564-2569.

78.   Cao, J. S.; Zhang, W. X., Stabilization of chromium ore processing residue

(COPR) with nanoscale iron particles. *J. Haz. Mater.* **2006,** *132* (2-3), 213-219.

79. Nriagu, J., Production and Uses of Chromium, in "Chromium in the Natural and Human Environments", John Wiley & Sons: New York, 1988.

80. Patterson, J., Hexavalent Chromium. In Industrial Wastewater Treatment Technology, Butterworth Publishers, Stoneham, 1985.

81. U. S. Environmental Protection Agency, "Hazardous Waste Clean-Up Information (CLU-IN). Contaminant Focus: ChromiumVI", (http://www.cluin.org/contaminantfocus/default.focus/sec/ chromium_VI/cat/Overview)

82. Palmer, C.D. and Wittbrodt, P.R. "Processes Affecting the Remediation of Chromium-Contaminated Sites", *Environ. Health Persp.*, 1991, 92, 25-40.

83. Abdel-Samad, H.; Watson, P. R., "An XPS Study of the Adsorption of Chromate on goethite (α-FeOOH)", *Appl. Surf. Sci.,* 1997, 108, 371-377.

84. Powell, R. M.; Puls, R. W.; Hightower, S. K.; Sabatini, D. A., Coupled iron corrosion and chromate reduction − mechanisms for subsurface remediation. *Environ. Sci. Technol.* **1995,** *29* (8), 1913-1922.

85. Blowes, D. W.; Ptacek, C. J.; Jambor, J. L., In-situ remediation of Cr(VI)-contaminated groundwater using permeable reactive walls: Laboratory studies. *Environ. Sci. Technol.* **1997,** *31* (12), 3348-3357.

86.   Manning, B. A.; Kiser, J. R.; Kwon, H.; Kanel, S. R., Spectroscopic investigation of Cr(III)- and Cr(VI)-treated nanoscale zerovalent iron. *Environ. Sci. Technol.* **2007,** *41* (2), 586-592.

87.   Nordstrom, D. K., Public health - Worldwide occurrences of arsenic in ground water. *Science* **2002,** *296*, 2143-2145.

88.   Smedley, P. L.; Kinniburgh, D. G., A review of the source, behaviour and distribution of arsenic in natural waters. *Appl. Geochem.* **2002,** *17*, 517-568.

89.   Dixit, S.; Hering, J. G., Comparison of arsenic(V) and arsenic(III) sorption onto iron oxide minerals: Implications for arsenic mobility. *Environ. Sci. Technol.* **2003,** *37*, 4182-4189.

90.   Korte, N. E.; Fernando, Q., A review of Arsenc(III) in groundwater. *Crit. Rev. Env. Control* **1991,** *21*, 1-39.

91.   Meharg, A. A.; Rahman, M., Arsenic contamination of Bangladesh paddy field soils: Implications for rice contribution to arsenic consumption. *Environ. Sci. Technol.* **2003,** *37*, 229-234.

92.   Dittmar, J.; Voegelin, A.; Roberts, L. C.; Hug, S. J.; Saha, G. C.; Ali, M. A.; Badruzzaman, A. B. M.; Kretzschmar, R., Arsenic Accumulation in a Paddy Field in Bangladesh: Seasonal Dynamics and Trends over a Three-Year Monitoring Period. *Environ. Sci. Technol.* **2010,** *44*, 2925-2931.

93.   WHO guidelines for drinking-water quality, 3rd edition, 2008. (http://www.who.int/water_sanitation_health/dwq/gdwq3rev/en/index.html)

94. Edwards, M., Chemistry of arsenic removal during coagulation and Fe-Mn oxidation. *J. Am. Water Works Assn.* **1994,** *86*, 64-78.

95. Manceau, A., The mechanism of anion adsorption on iron-oxides - Evidence for the bonding of arsenate tetrahedra on free Fe(O,OH)(6) edges. *Geochim. Cosmochim. Acta* **1995,** *59*, 3647-3653.

96. Manning, B. A.; Goldberg, S., Adsorption and stability of As(III) at the clay mineral-water interface. *Environ. Sci. Technol.* **1997,** *31*, 2005-2011.

97. Manning, B. A.; Fendorf, S. E.; Goldberg, S., Surface structures and stability of arsenic(III) on goethite: Spectroscopic evidence for inner-sphere complexes. *Environ. Sci. Technol.* **1998,** *32*, 2383-2388.

98. Huang, C. P.; Fu, P. L. K., Treatment of arsenic (V)-containing water by the activated carbon process. *J. Water Pollut. Con. Fed.* **1984,** *56* (3), 233-242.

99. Huang, C. P.; Vane, L. M., Enhancing As^{5+} removal by a Fe^{2+}-treated activated carbon. *J. Water Pollut. Con. Fed.* **1989,** *61* (9-10), 1596-1603.

100. Mohan, D.; Pittman, C. U., Arsenic removal from water/wastewater using adsorbents - A critical review. *J. Haz. Mater.* **2007**, *142* (1-2), 1-53.

101. Raven, K. P.; Jain, A.; Loeppert, R. H., Arsenite and arsenate adsorption on ferrihydrite: Kinetics, equilibrium, and adsorption envelopes. *Environ. Sci. Technol.* **1998,** *32*, 344-349.

102. Goldberg, S.; Johnston, C. T., Mechanisms of arsenic adsorption on amorphous oxides evaluated using macroscopic measurements, vibrational spectroscopy,

and surface complexation modeling. *J. Colloid Interface Sci.* **2001,** *234*, 204-216.

103. Sullivan, K. A.; Aller, R. C., Diagenetic cycling of arsenic in amazon shelf sediments. *Geochimica et Cosmochimica Acta.* **1996**, *60*, 1465-1477.

104. Fendorf S., Matthew, J. E.; Grossl, P.; Sparks, D. L., Arsenate and chromate retention mechanisms on goethite. 1. surface structure. *Environ. Sci. Technol.* **1997,** *31*, 315-320.

105. Ona-Nguema, G.; Morin, G.; Juillot, F.; Calas, G.; Brown, G. E., EXAFS analysis of arsenite adsorption onto two-line ferrihydrite, hematite, goethite, and lepidocrocite. *Environ. Sci. Technol.* **2005,** *39*, 9147-9155.

106. Manning, B. A.; Hunt, M. L.; Amrhein, C.; Yarmoff, J. A., Arsenic(III) and Arsenic(V) reactions with zerovalent iron corrosion products. *Environ. Sci. Technol.* **2002,** *36*, 5455-5461.

107. Lackovic, J. A.; Nikolaidis, N. P.; Dobbs, G. M., Inorganic arsenic removal by zero-valent iron. *Environ. Eng. Sci.* **2000,** *17*, 29-39.

108. Hussam, A.; Munir, A. K. M., A simple and effective arsenic filter based on composite iron matrix: Development and deployment studies for groundwater of Bangladesh. *J. Environ. Sci. Health. Part A Toxic/Hazard. Subst. Environ. Eng.* **2007,** *42*, 1869-1878.

109. Nikolaidis, N. P.; Dobbs, G. M.; Lackovic, J. A., Arsenic removal by zero-valent iron: field, laboratory and modeling studies. *Water Res.*, **2003**, *37*, 1417-

1425.

110. Kanel, S. R.; Manning, B.; Charlet, L.; Choi, H., Removal of arsenic(III) from groundwater by nanoscale zero-valent iron. *Environ. Sci. Technol.* **2005,** *39*, 1291-1298.

111. Bang, S.; Johnson, M. D.; Korfiatis, G. P.; Meng, X. G., Chemical reactions between arsenic and zero-valent iron in water. *Water Res.* **2005,** *39*, 763-770.

112. Lien, H. L.; Wilkin, R. T., High-level arsenite removal from groundwater by zero-valent iron. *Chemosphere* **2005,** *59*, 377-386.

113. Katsoyiannis, I. A.; Ruettimann, T.; Hug, S. J., pH dependence of Fenton reagent generation and As(III) oxidation and removal by corrosion of zero valent iron in aerated water. *Environ. Sci. Technol.* **2008,** *42*, 7424-7430.

114. Melitas, N.; Conklin, M.; Farrell, J., Electrochemical study of arsenate and water reduction on iron media used for arsenic removal from potable water. *Environ. Sci. Technol.* **2002,** *36*, 3188-3193.

115. Hug, S. J.; Leupin, O., Iron-catalyzed oxidation of arsenic(III) by oxygen and by hydrogen peroxide: pH-dependent formation of oxidants in the Fenton reaction. *Environ. Sci. Technol.* **2003,** *37*, 2734-2742.

116. Joo., S. H.; Feitz, A. J.; Waite, T. D., Oxidative degradation of the carbothioate herbicide, molinate, using nanoscale-zerovalent iron. *Environ. Sci. Technol.* **2005,** *38*, 2242-2247.

117. Lee, C.; Sedlak, D. L., Enhanced formation of oxidants from bimetallic Nickel-

Iron nanoparticles in the presence of oxygen. *Environ. Sci. Technol.* **2008,** *42*, 8528-8533.

118. Elimelech, M, Gregory, J, Jia, X, Williams, RA: Particle deposition and aggregation: Measurement, modeling and simulation. Butterworth-Heinemann, Oxford, UK, 1995.

119. Fatisson, J.; Ghoshal, S.; Tufenkji, N., Deposition of carboxymethylcellulose-coated zero-valent iron nanoparticles onto silica: Roles of solution chemistry and organic molecules. *Langmuir* **2010**, *26* (15), 12832-12840.

120. He, F.; Zhao, D. Y., Preparation and characterization of a new class of starch-stabilized bimetallic nanoparticles for degradation of chlorinated hydrocarbons in water. *Environ. Sci. Technol.* **2005**, *39* (9), 3314-3320.

121. He, F.; Zhao, D. Y.; Liu, J. C.; Roberts, C. B., Stabilization of Fe-Pd nanoparticles with sodium carboxymethyl cellulose for enhanced transport and dechlorination of trichloroethylene in soil and groundwater. *Ind. Eng. Chem. Res.* **2007**, *46* (1), 29-34.

122. He, F.; Zhao, D. Y.; Paul, C., Field assessment of carboxymethyl cellulose stabilized iron nanoparticles for in situ destruction of chlorinated solvents in source zones. *Water Res.* **2010**, *44* (7), 2360-2370.

123. Johnson, R. L.; Johnson, G. O.; Nurmi, J. T.; Tratnyek, P. G., Natural organic matter enhanced mobility of nano zerovalent iron. Environmental *Environ. Sci. Technol.* **2009**, *43* (14), 5455-5460.

124. Phenrat, T.; Kim, H. J.; Fagerlund, F.; Illangasekare, T.; Tilton, R. D.; Lowry, G. V., Particle size distribution, concentration, and magnetic attraction affect transport of polymer-modified Fe-0 nanoparticles in sand columns. *Environ. Sci. Technol.* **2009**, *43* (13), 5079-5085.

125. Phenrat, T.; Saleh, N.; Sirk, K.; Tilton, R. D.; Lowry, G. V., Aggregation and sedimentation of aqueous nanoscale zerovalent iron dispersions. *Environ. Sci. Technol.* **2007**, *41* (1), 284-290.

126. Tiraferri, A.; Chen, K. L.; Sethi, R.; Elimelech, M., Reduced aggregation and sedimentation of zero-valent iron nanoparticles in the presence of guar gum. *J. Coll. Interf. Sci.* **2008**, *324* (1-2), 71-79.

Chapter 3

Experimental Methodology

This chapter describes in details the materials and methods used in nZVI experiments. The iron nanoparticles used in this study were prepared in the laboratory and were not from commercial providers. All chemicals were of reagent grade and were used as purchased without further purification. Instrument analyses, unless otherwise noted, were performed in the Department of Civil and Environmental Engineering and the Center for Advanced Materials and Nanotechnology (CAMN) at Lehigh University.

3.1 Synthesis of nanoparticles

3.1.1 Iron nanoparticles

Iron nananoparticles were prepared in batch of ~ 10 g by slowly introducing sodium borohydride solution ($NaBH_4$, Finnish Chemicals, 0.2M) into ferric chloride solution ($FeCl_3 \cdot 6H_2O$, Alfa Aesar, 0.05M) until reaching a volume ratio of 1:1. During the process, the aqueous mixture was intensely mixed with a rotary mechanical mixer at a speed of 650 rpm at room temperature. The fluid turned from brownish clear solution to

jet-black slurry as ferric ions being reduced to metallic iron according to the following reaction (Glavee *et al.*, 1995):

$$4Fe^{3+} + 3BH_4^- + 9H_2O \rightarrow 4Fe^0 (s) + 3H_2BO_3^- + 12H^+ + 6H_2 (g) \qquad (3.1)$$
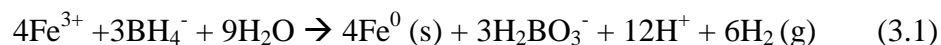
Note that sodium borohydride in excess of the stoichiometry (Eq. 3.1) was used to accelerate the reduction and to control the size distributions of the resultant nanoparticles.

Upon mixing, the suspension was allowed to settle for 30 min before the particles were harvested by vacuum filtration. The efficient separation was based upon the fact that the nanoparticles, despite having an average diameter of ~ 60 nm (Sun *et al.*, 2006), are loosely aggregated to form clusters in the size range of a few hundred nanometers to several microns (refer to Chap 4 on characterization of particle sizes). The collected particles were rinsed three times with 95% ethanol (Farmco-AAPER) and stored in a sealed PTFE container at $4\,^{o}C$ prior to use.

3.1.2 Bimetallic nanoparticles

Pd-Fe bimetallic nanoparticles (Pd-nZVI) were prepared by mixing the freshly prepared iron nanoparticles with an ethanol/water (vol. ratio 1:1) solution containing palladium chloride (PdCl$_2$, 99.9 %, Alfa Aesar) at a concentration of 200 mg/L (Figure 3.1). The

mixture was sonicated for 10 min, during which Pd(II) ions were reduced and deposited on the nZVI surface following the classical metal replacement reaction (Eq. 3.2).

$$Pd^{2+} + Fe^0 (s) \rightarrow Pd^0 (s) + Fe^{2+} \tag{3.2}$$

The resulting particles were collected by vacuum filtration. In this study, the nominal loading of Pd with respect to iron was fixed at a mass fraction of 1.5 %, a value which was confirmed by measuring the initial and final concentrations of Pd(II) in the solutions using inductively coupled plasma-optical emission spectrometry (ICP-OES, Perkin-Elmer Optimal 2100DV).
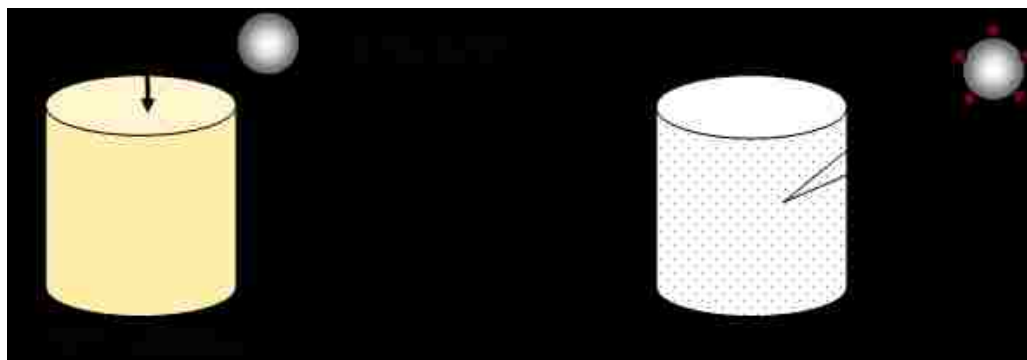
Figure 3.1 Synthesis of palladium-doped bimetallic iron nanoparticles.

3.2 Experiment procedures

3.2.1 Batch equilibrium experiments

Equilibrium tests were performed in closed, 120-ml glass serum bottles in which the solution volume was 100 ml. The following stock solutions were prepared using the indicated chemicals (Table 3.1)

Table 3.1: List of reagents used to prepare stock solutions for batch experiments.

Stock solution	Chemical formula	Manufacturer
Inorganic		
Hg(II)	$Hg(CH_3COO)_2$	Fisher
Cu(II)	$CuCl_2$	Fisher
Zn(II)	$ZnCl_2$	Fisher
H_2S	Saturated H_2S solution	Ricca Chemical
As(III)	$NaAsO_2$	Fluka
As(V)	$Na_2HAsO_4 \cdot 7H_2O$	Fluka
Organic		
TCE	C_2HCl_3	Fisher

An appropriate volume of the stock solution was diluted with de-ionized water to 100 ml. The solutions were deoxygenated by purging with high purity nitrogen (>99.9%) for 30 min. After a pre-determined amount of nZVI was loaded into the bottle, it was closed and the cap was sealed with a teflon liner to prevent air leakage. The bottles were agitated on a mechanical shaker at 250 rpm at 25 ^{0}C. After a suitable time interval (typically 24 hours for reactions with metal species), the reaction was stopped by separating the solution and the particles with vacuum filtration. The particles were dried and stored in N_2-filled glove box before solid phase analysis, and the solution was acidified with HNO_3 to pH less than two and stored at 4 ^{0}C before solution analysis. For

each set of experiments, a control was performed under identical conditions in parallel except there was no iron nanoparticles added.

For experiments involving volatile compounds (e.g. H_2S and TCE), 250-ml serum bottles containing 100-ml aqueous solutions were used. After charging a small amount of nZVI, the bottles were capped with Teflon Mininert valves and placed on a mechanical shaker at 250 rpm at 25 ^{o}C. Sampling of TCE concentration was done by drawing 25-μL aliquot of headspace gas using a gas-tight syringe. Particles were collected and dried following the same procedure as described above.

3.2.2 Batch kinetic experiments

Kinetic experiments of reactions with metal species were performed in a set-up illustrated in Figure 3.2. The system consists of a 500-ml three-necked flask equipped with mechanical rotating paddle. The remaining necks are connected to N_2 gas supply, a pH probe and an ORP probe, respectively. Anaerobic conditions were created by purging the reaction flask with pure N_2 continuously. This allows real-time tracking of pH and E_h changes in the solution phase without interrupting the reaction media. Periodically, a small volume of the solution ($\sim$ 5 ml) was sampled, filtered immediately, acidified, and stored at 4 ^{o}C prior to analysis.

For volatile compounds, kinetic experiments were performed following similar procedures as in 3.2.1. Sampling was conducted periodically by withdrawing 25-µL of headspace gas through the Mininert valve.
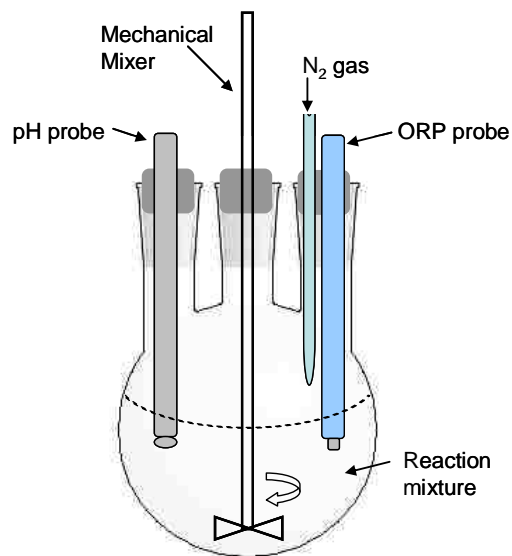
Figure 3.2 Experimental set-up for kinetic experiments involving inorganic contaminants.

3.3 Aqueous analysis

3.3.1 Atomic absorption

Total aqueous concentrations of Fe, Cu, Ni, Fe, and Zn were measured with a Perkin Elmer atomic absorption (AA) spectrometer (AAnalyst 200). For analysis of each

species, a four-point calibration curve was obtained with solutions prepared from the respective AA standards (1000 mg/L standards purchased from Fisher). Three replicate readings were taken for each analysis. Sample concentrations exceeding linear concentration range of the respective wavelength were diluted accordingly. Samples with Fe concentration below 3 mg/L were measured with ICP-OES (3.3.2). Mercury concentration was analyzed with the same AA spectrometer equipped with a FIAS 100 flow injection system for cold vapor AA analysis. The procedure employs stannous chloride as the reductant and a 'purge and trap' design to capture and concentrate elemental mercury vapor generated. This system offers a mercury detection limit of 0.1 µg/L and has a linear response up to 1 mg/L. Occasionally for samples with mercury above 1 mg/L, the measurement was confirmed by ICP-OES analysis.

3.3.2 Inductively-coupled plasma optical emission spectroscopy

Total aqueous concentration of Fe, As, and Pd were analyzed with a Perkin Elmer Optima 2100 DV inductively-coupled plasma optical emission spectroscopy (ICP-OES). A radial plasma view was utilized for concentrations below 1 mg/L and an axial view for higher concentrations. Four-point calibration curves were obtained using reference solutions prepared from ICP multi-reagent standards (Fisher). Three replicate readings were taken for each analysis.

3.3.3 Gas chromatography

The concentrations of TCE were measured by a Shimatzu GC analyzer (GC-17A) equipped with a flame ionization detector (FID) and a SUPELCO SPB 624 capillary column. The injection port temperature was set at 180 ^{o}C. The oven temperature was set to 50 ^{o}C and ramped to 200 ^{o}C at 20 ^{o}C/min. The detector temperature was 300 ^{o}C. The concentration of headspace H_2S was analyzed with the same GC analyzer installed with a SPB^{TM}-1 sulfur capillary column (Supelco).

3.3.4 pH, DO, and ORP measurements

Solution pH was measured with a Orion 420A+ bench top pH/ISE analyzer. Three-point calibration was performed daily using pH 4.0, 7.0, and 10.0 standard pH buffers (Fisher). Oxidation-reduction potential (ORP) was measured using the same analyzer equipped with an ORP electrode (Pt band with Ag/AgCl/Saturated KCl reference cell). One-point ORP calibration was performed using a Zobel standard solution (Sigma), which gives a reading of ~ +230 mV at 25 ^{o}C. ORP reading can be converted to the standard hydrogen electrode potential (E_h) by adding +197 mV at 25 ^{o}C. Dissolved oxygen (DO) was measured using a HACH HQ20 luminescent DO meter. The sensor cap was replaced yearly as directed by the manufacturer and calibration was performed using air-saturated water before each use.

3.4 Solid phase analysis

The nature of this study requires extensive characterizations of the morphology, internal structure, composition, and surface chemistry of the solid phase, which consists of the nanoparticles and the solid products formed after reacting with various contaminants. This section presents an overview of the techniques used to conduct these solid-phases analyses. Detailed operating parameters used in different sets of experiments can be found in the Materials and Methods section of later chapters. Figure 3.3 below summarizes sample preparation protocols adopted in this study.
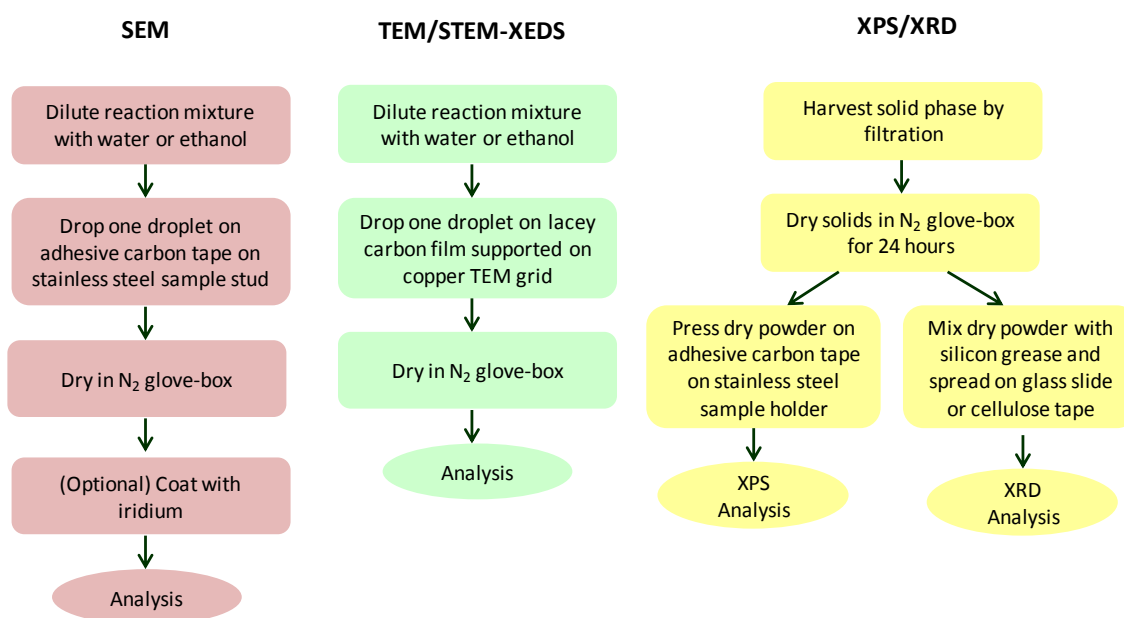
Figure 3.3 Sample preparation protocols for solid phase characterization.

3.4.1 Scanning electron microscopy

Morphology characterization of nZVI was carried out using a field-emission scanning electron microscope (FE-SEM) (Hitachi 4300). The popularity of SEM for characterizing nanomaterials stems from its capability of obtaining 3-dimensional-like topographical images in secondary electron (SE) imaging mode, Z-contrast imaging using back-scattered electrons (BSE), and quantitative elemental mapping with energy-dispersive X-ray spectrometer (XEDS) (Goldstein, *et al*., 2003). Imaging under SE mode was typically conducted at 5 kV accelerating voltage. Samples with poor electron conductivity (e.g. severely oxidized surfaces) were coated with a thin layer of iridium to minimize surface charging.

3.4.2 Transmission electron microscopy

Various transmission electron microscopy (TEM) techniques were used in this study. Bright field TEM imaging was conducted using JOEL 2000FX at 200 kV for microstructure characterization and selected area electron diffraction pattern. Phase contrast TEM imaging was obtained with a JOEL 2200FS at 220 kV. High angle annular dark field imaging (HAADF) and chemical mapping were carried out at Lehigh University using a dedicated Cs-aberration-corrected scanning transmission electron microscope-XEDS system (Philips, VG HB603) and an FEI Titan 80-300 STEM-XEDS system equipped with a Cs-aberration corrector (CEOS GmbH) at the National Institute

of Standards and Technology (NIST). The STEM-XEDS imaging was conducted at 300 kV.

While conventional and phase contrast TEM imaging techniques have been extensively applied to the characterization of nanoparticulate materials, relatively few applications of STEM-XEDS analysis have been reported in the literature. The challenges of STEM-XEDS analysis lie in the fact that X-ray fluorescence by a single nanoparticle at high spatial resolution is extremely low. This can be improved by optimizing detector configuration and the solid angle of collection. Additionally, to enhance beam current without compromising spatial resolution, the electron beam has to be intensively corrected for spherical aberration (Cs). Only a limited number of STEM in the world that have been equipped with the sophisticated C_s aberration corrector, and instruments at Lehigh and NIST are fortunately among the best in terms of spatial resolution and detection limit. The procedure of STEM-XEDS analysis is as follows: first, an HAADF image of the area of interest is acquired. The image is divided into an array of pixels (typically 128 x 128). The STEM probe then scans across the above area and stopping at each pixel for a fixed amount of time (100-200 ms), during which an X-ray spectrum from 0- 20 keV is collected by XEDS detector. A collection of X-ray spectra over the entire area is called a spectrum image 'data cube' (Figure 3.4) (Herzing, *et al*., 2008). The name implies that each data point in the data cube is uniquely defined by three coordinates: the first two coordinates for the spatial location (x and y) and the third one for the energy of the emitted X-ray photons (E). E is characteristics of the elements

present in the pixel, therefore, 2-dimensional maps of elements can be extracted from the data cube. Superimposing individual elemental maps gives an overlay image that depicts the chemical composition inside a nanoparticle at sub-nanometer resolution.

3.4.3 X-ray photoelectron spectroscopy (XPS)

X-ray photoelectron spectroscopy (XPS), also known as ESCA (Electron spectroscopy for chemical analysis), is a well established technique for quantitative analysis of surface composition and oxidation states (Somorjai, 1994). An XPS spectrum is obtained by irradiating a specimen with an X-ray beam generated by an aluminum or magnesium anode (Figure 3.5a). The incident X-ray photons expel electrons from atomic core-levels, and the emitted electrons are detected by a detector as a function of their kinetic energy (E_k) (Figure 3.5b). The kinetic energy is used to calculate the binding energy (E_B) following the equation first proposed by Rutherford (Briggs & Seah, 1990) (Eq. 3.3)

$$E_B \approx h\upsilon - E_K \qquad (3.3)$$

Where hυ is the energy of an incident photon.

Fe k$_\alpha$

O k$_\alpha$

Pd L$_\alpha$

Data Extraction

Overlay

(a) Data cube

(b) Elemental maps

(c) Overlay image
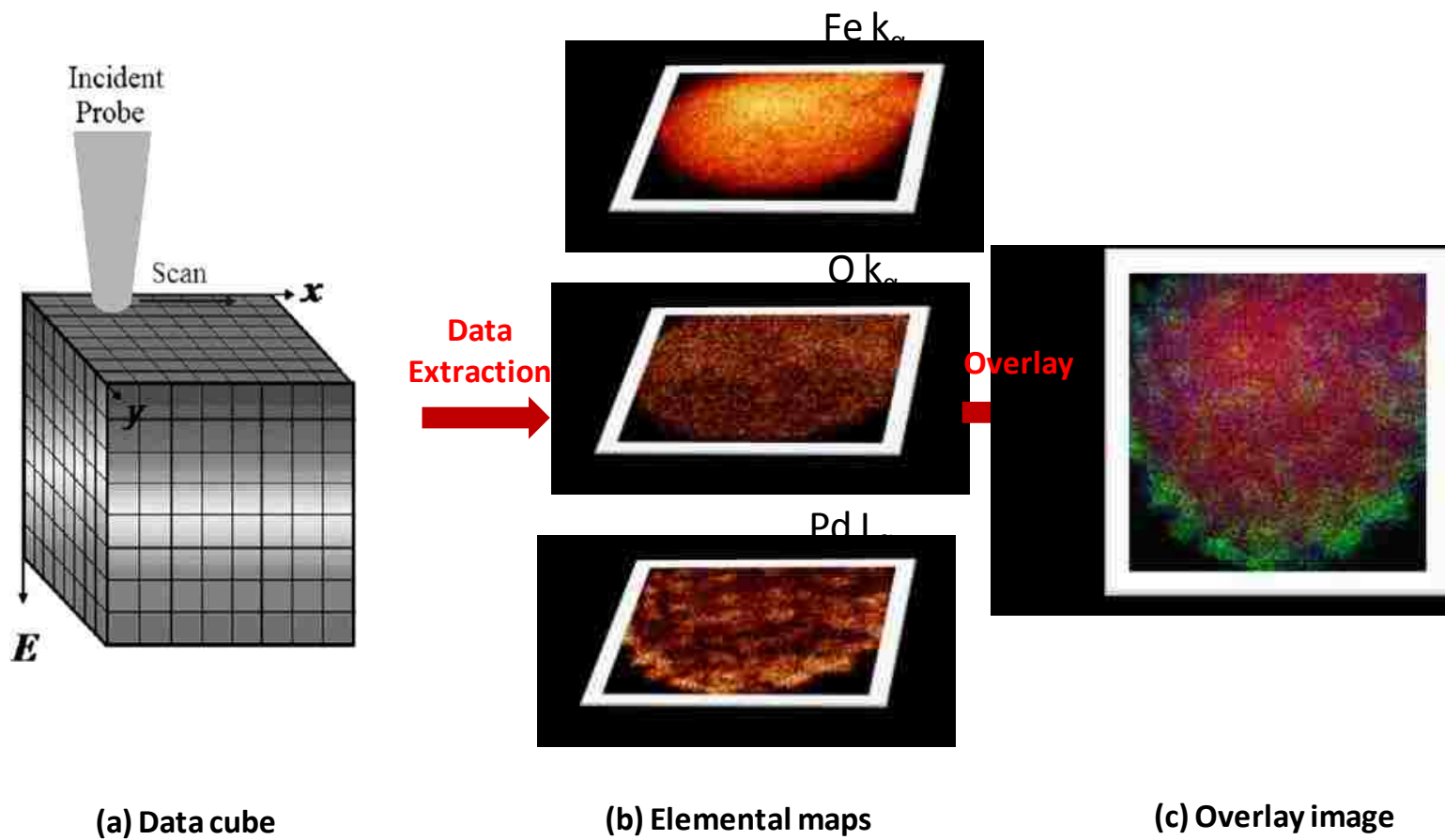
Figure 3.4 Schematic diagram illustrating the process underlying a STEM-XEDS analysis (adapted from Herzing *et al*., 2008).

XPS is a surface sensitive technique. The sampling depth (defined as 3 times the length of electron inelastic mean free path, IMFP) is a function of the incident X-ray, the analysis angle and the surface electron states (Briggs & Seah, 1990). Several empirical formula have been proposed to estimate electron IMFP, such as the CS2 Equation (Cumpson & Seah, 1997) in Eq. 3.4. Other models to estimate IMFP are available in the literature (Mohai, 2005). Typical sampling depth of XPS is approximately 2-10 nm.

$$\lambda_{IMFP} = 0.316a^{\frac{3}{2}}\left(\frac{E_k}{Z^{0.45}\left(\frac{lnE_k}{27}\right)+3} + 4\right) \qquad (3.4)$$

Where a is the lattice parameter or average monolayer thickness, E_k is the electron kinetic energy, and Z is the average atomic number.

XPS is a quantitative technique, implying that the intensity of photoelectrons from a chemical species is a function of its atomic concentration. For a homogenous sample, the relationship is simply (Mohai, 2005):

$$I^{\infty} = \Phi\sigma Nk\lambda_{IMFP}\cos\theta \qquad (3.5)$$

Where I^{∞} is the photoelectron intensity from an infinitely thick homogeneous sample, Φ is the incident X-ray flux, σ is the photo-ionization cross section, N is the number of atoms per unit area, k is an instrument dependent factor, and θ is the angle between the ejected electrons and the surface normal (Figure 3.5a).

The shifts of core-level binding energies in XPS spectra provide information on the chemical environment of the atoms. This ability to distinguish and quantify chemical states of the detected elements, e.g. oxidized iron (Fe(III)) from metallic iron (Fe(0)), is a unique advantage of XPS compared to other spectroscopic techniques that provide elemental information only.

The XPS used in this work is a ESCA 300, which is regarded as among the best XPS with regards to energy resolution and analysis throughput. Several features of this instrument are worth mentioning here (Figure 3.6). Al Kα x-rays (1486.7eV) are generated from a *rotating anode* which can operate at power levels of up to 7.5 kW. The *monochromator* is a collection of seven α-quartz crystals mounted on three Rowland circles, which collects the X-rays from the rotating anode and subsequently projects them onto the surface of the sample. A prominent feature of this instrument is the *hemispherical electron energy analyzer* (HMA). It has an average radius of 300 mm which allows a high energy resolution and efficient electron detection over a large energy window at high speed. The *electron detector* is a CCD camera combined with multi-channel micro-channel plates. The nominal analyzed area is rectangular with approximate dimensions of 4 mm x 0.2 mm. The analysis chamber operates in ultra-high vacuum conditions (UHV) at 5.0×10^{-9} Torr.

Spectra are typically collected using a takeoff angle (90^0 - Ө) of 90° with respect to the surface plane of the samples. The hemispherical analyzer pass energy was set at 150 eV, which yields an optimized resolution of the analyzer of ~0.1 eV. The opening of the slit

is 0.8 mm. A typical analysis was conducted by pressing N_2-dried solids onto an adhesive carbon tape mounted on a stainless steel sample bar. The sample was immediately sent to the fast-entry chamber, pumped down to low 10^{-8} Torr, and parked at preparation chamber prior to analysis. A typical analysis proceeds by collecting a survey spectrum (300 eV pass energy) from 0-1200 eV followed by detailed region scans using 150 eV pass energy. In most cases, spectra at the following regions were collected: C1s, O1s, Fe2p, and the appropriate transitions of contaminants involved (e.g. As3d and Cu2p). Spectra were calibrated against the binding energy of adventitious carbon detected in the C1s region (284.6 eV). Curve fitting was carried out using the CASA XPS MFC application software (version 2.3.12.8).

(a)
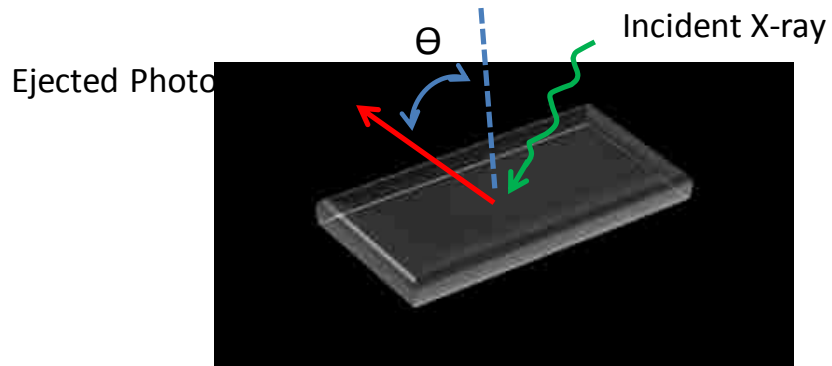
(b)
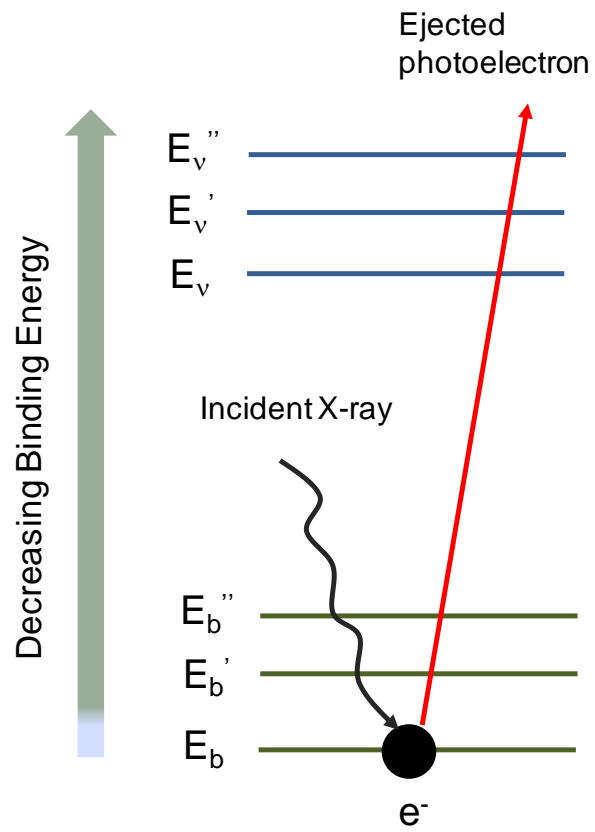
Figure 3.5 schematic illustrations of the XPS process: (a) irradiation of a sample surface generates photoelectrons; (b) processes occurring at atomic level.
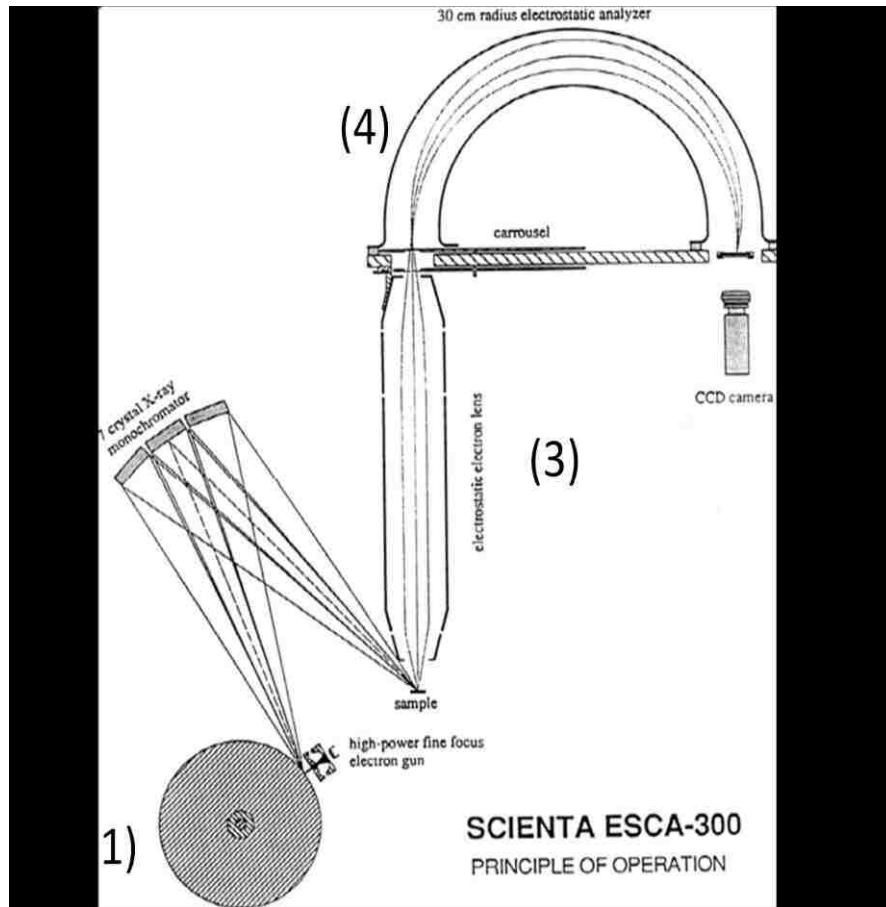
Figure 3.6 Main components of a Scienta ESCA-300 system.

3.4.4 X-ray diffraction

X-Ray diffractogram was obtained with a Rigaku diffractometer (Rigaku, Japan) with Cu Kα (λ = 1.5418 A) radiation generated at 40 kV. Bragg Equation (Eq. 3.6) was used to convert from diffraction angel (θ) to the lattice spacing (d):

$$n\lambda = 2d \sin\theta \tag{3.6}$$

Samples were scanned from a 2 θ range of 10° to 80° with a stepping size of 0.1^0 and a scanning rate of 60 second per step. The crystalline phase was identified by comparing with XRD diffraction patterns in the literature (JCPDS, 1998).

3.4.5 BET surface area

Specific surface area of the iron particles was measured using a Micrometrics Flowsorb 2305 following the classic Brunauer-Emmett-Teller (BET) method (Bruauer *et al.*, 1938). Dried samples were first degassed at 170°C for 40 minutes. Adsorption of pure nitrogen by iron sample was done in a sample tube at liquid nitrogen temperature followed by desorption of nitrogen as temperature ramps up to room conditions. The amounts of nitrogen adsorbed and desorbed by the iron particles were measured by a potentiometer and were used to calculate the total surface area.

References

1. Glavee, G. N.; Klabunde, K. J.; Sorensen, C. M.; Hadjipanayis, G. C., Chemistry of borohydride reduction of iron(II) and iron(III) ions in aqueous and nonaqueous media – Formation of nanoscale Fe, FeB, and Fe_2B powders. *Inorg. Chem.* **1995,** *34* (1), 28-35.

2. Sun, Y. P.; Li, X. Q.; Cao, J. S.; Zhang, W. X.; Wang, H. P., Characterization of zero-valent iron nanoparticles. *Adv. Colloid Interfac.***2006,** *120*, 47-56.

3. Goldstein, J. I.; Lyman, C. E.; Newbury, D. E.; Lifshin, E.; Echlin, P.; Sawyer, L.; Joy, D. C.; Michael, J. R. Scanning electron microscopy and X-ray microanalysis, Springer, 2003.

4. Herzing, A. A.; Watanabe, M.; Edwards, J. K.; Conte, M.; Tang, Z. R.; Hutchings, G. J.; Kiely, C. J., Energy dispersive X-ray spectroscopy of bimetallic nanoparticles in an aberration corrected scanning transmission electron microscope. *Faraday Discuss.* **2008,** *138*, 337-351.

5. Joint Committee on Powder Diffraction Standards (JCPDS) (1998) Selected powder diffraction data for minerals. International Center for Diffraction Data, Newtown Square, PA, USA.

6. S. Brunauer, P. H. Emmett and E. Teller, Adsorption of Gases in Multimolecular Layers. *J. Am. Chem. Soc.*, **1938**, *60*, 309.

7. Briggs, D.; Seah, M. P. (Ed) Practical Surface Analysis Vol 1 - Auger and X-ray photoelectron spectroscopy, 2nd Ed., John Wiley & Sons, 1990.

8. Somorjai, G. A. Introduction to surface chemistry and catalysis, Wiley-Interscience, 1994.

9. P. J. Cumpson and M. P. Seah, *Surf. Interface Anal.* 1997, **25**, 430.

10. Mohai, M. *XPS Multiquant Users Manual* **2005**.

Chapter 4

Characterizing the Core-Shell Structure of nZVI

4.0 Abstract

This study presents a detailed characterization of the morphology, structure, and chemical composition of iron nanoparticles (nZVI). Scanning electron microscopy (SEM) images show that the size of individual particles is within a range of 20-100 nm and particles are aggregated into necklace-like formation due to magnetic interactions. The internal structure and elemental distribution of nZVI were characterized by X-ray energy-dispersive spectroscopy (XEDS) with nanometer-scale spatial resolution in an aberration-corrected scanning transmission electron microscope (STEM). The analysis provides unequivocal evidence of a layered structure of nZVI consisting of a metallic iron core encapsulated by a thin amorphous oxide shell. The thickness of the oxide shell was determined using three independent methods. High resolution TEM analysis indicates that the shell thickness of fresh nZVI is predominantly in the range of 2-4 nm. High-resolution X-ray photoelectron spectroscopy (HR-XPS) analysis through comparison of the relative integrated intensities of metallic and oxidized iron with a topographic correction to account for the curved overlayer yield an average shell thickness in the range of 2.3-2.8 nm. Finally, the complete oxidation reaction of the nZVI particles

95

by Cu(II) was used as an indication of the zero-valent iron content of the particles, which correlates with the oxide thickness through direct geometric correlations. The three methods yield remarkably similar results, providing a reliable determination of the shell thickness. The results presented here fill an essential gap in our knowledge about the nZVI structure and have direct implications for the reactivity of nZVI in environmental systems.

4.1 Introduction

Zero-valent iron (ZVI) has been widely used as a reductant in hazardous waste treatment and environmental remediation. Over the past two decades, numerous studies have shown that ZVI can effectively degrade a wide array of environmental contaminants, such as halogenated hydrocarbons, azo dyes, munitions, pesticides, hexavalent chromium, and nitrate by reductively transforming the contaminants into benign or less harmful forms (Gillham & Ohannesin, 1994; Matheson & Tratnyek, 1994; Johnson *et al*., 1996; Cao *et al*., 1999; Hundal *et al*., 1997; Huang *et al*. 1998; Alowitz & Scherer, 2002). More recently, the use of nanoscale zero-valent iron (nZVI) has attracted increasing attention because of its enhanced reactivity compared to conventional bulk ZVI materials (Lien & Zhang, 1999; Kanel *et al*., 2006; Sohn *et al*., 2006), which studies attribute to the substantial increase in surface-to-volume ratio as the particle size shrinks to the nanometer scale (Nurmi *et al*., 2005).

It is generally accepted that nZVI has a core-shell structure with a zero-valent iron core surrounded by an iron oxide/hydroxide shell, which grows thicker with the progress of iron oxidation. However, it is difficult to measure the exact thickness of the shell due to the high reactivity of iron, which reacts very rapidly with both oxygen and water and may even oxidize in air. Traditionally, the shell thickness is estimated based upon measurement of the zero valent iron content, which is determined from its corrosion rate and/or production of hydrogen gas (Hydutsky *et al*., 2007). However, such experiments are tedious, time consuming, and often use hazardous chemicals.

Detailed structural characterization is essential to understand how the structure of nZVI relates to its activity. The nZVI structure depends on how the nanoparticles are synthesized (Huber, 2005; Li & Zhang, 2007), and in this work we focus on fresh nZVI produced chemically by the reduction of iron salts. This method was previously shown by x-ray photoelectron spectroscopy (XPS) to produce core-shell particles (Li & Zhang, 2006). These particles were also analyzed by transmission electron microscopy (TEM) and acoustic spectrometric methods, and found to be polydisperse with an average diameter of approximately 60 nm and a standard deviation of 15 nm (Sun *et al*., 2006). TEM analysis also indicated that the shell thickness varied significantly, however, a full statistical determination of the thickness has not yet been carried out.

XPS is a powerful tool for probing surface and near-surface elemental composition and chemical oxidation state. Quantitatively, the sampling depth of a photoelectron can be defined based on the inelastic mean free path for electron scattering, or the attenuation

length, λ, which is the thickness of material through which electrons may pass with a probability e^{-1} that they survive without inelastic scattering and thus are detected at their characteristic energies (Seah & Dench, 1979). Knowledge of these attenuation lengths can be used with XPS data to provide information on the concentration variations with depth in the near surface region for non-homogenous distributions within the sample. Analysis often requires a model to be assumed for this distribution, but it is common to analyze flat, planar films and layers by comparing the relative intensity of signals characteristic of the bulk and film or overlayer (Fadley, 1978). Effects such as surface roughness can also be accounted for by geometrical corrections (Gunter & Niemantsverdriet, 1995 ; Mohai & Bertoli, 2004; Gillet & Meunier, 2005).

In this study, a variety of characterization methods were employed to analyze the physicochemical properties of nZVI and the thickness of the oxide shell. Specifically, the morphology, size distribution, and surface area of nZVI particles were determined by Scanning Electron Microscopy (SEM) and Brunauer-Emmett-Teller (BET) method. The micro-structure of nZVI was characterized by advanced TEM techniques including bright-Field TEM, phase-contrast TEM and a state-of-the-art scanning transmission electron microscope (STEM) equipped with an X-ray energy-dispersive spectrometer (XEDS). The instrument employs a sub-nanometer probe afforded by a C_s-aberration corrector to perform XEDS spectrum imaging, which is able to map out the elemental compositions at a nanometer-scale spatial resolution, thus enabling for the first time direct visualization of the core-shell structure.

The thickness of the nZVI oxide shell was determined by three independent methods: (i) high-resolution TEM imaging, (ii) high-resolution XPS, and (iii) chemical oxidation of ZVI. TEM analysis provides direct images of the core-shell structure, the dimension and variation of the shell thickness in the area analyzed. However, TEM technique inherently suffers the drawback of limited sampling statistics. HR-XPS analysis, by comparing the intensities of metallic versus oxidized iron core-level peaks, was applied in order to calculate the mean and standard deviation of the distribution of shell thicknesses by using a geometrical correction to account for the spherical structure of the nanoparticles (Mohai & Bertoli, 2004). This thickness determination was compared with a magic angle analysis where topographical effects are limited (Kappen *et al.*, 2000). Furthermore, the average shell thickness can be estimated independently based on the sample total mass and iron content of the sample determined by using stoichiometric oxidation of iron by Cu(II).

4.2 Materials and methods

nZVI Synthesis. Nanoscale zero valent iron particles were prepared as previously reported (Chapter 3).

BET Surface Area. Specific surface area of nZVI was measured following the classic Brunauer-Emmett-Teller (BET) method as described in Chapter 3.

Electron microscopy characterization. SEM imaging was performed using a field-emission SEM (Hitachi S-4300) operating at 5-10 kV. Samples for transmission electron microscopy (TEM) and scanning transmission electron microscopy (STEM) analysis were prepared by allowing a drop of the nZVI in ethanol solution to dry on a lacey-carbon film supported on a 300-mesh copper grid. Conventional bright-field imaging was carried out using a JEOL 2000FX TEM equipped with a LaB_6 filament operating at 200 kV. High-resolution lattice imaging was performed using a JEOL 2200FS TEM with a field-emission gun operating at 200 kV. Chemical microanalysis and annular dark-field (ADF) imaging were performed using a 300kV VG HB603 dedicated STEM equipped with a Nion spherical aberration corrector and an Oxford Instruments INCA 300 system for energy dispersive X-ray spectrometry (XEDS). X-ray spectrum images were acquired by first collecting an ADF image of the area of interest, which was then divided into an array of 128 x 128 pixels. The electron probe was then scanned over this array, stopping at each pixel for 200 ms during which an entire x-ray spectrum from 0 to 20 keV was collected with a resolution of 20 eV/channel. In this fashion, a data cube is created with dimensions defined by the position coordinates of the image pixels (x and y) and the x-ray energy spectrum (z). This type of data set is highly-redundant and thus lends itself particularly well to data processing techniques such as multi-variate statistical analysis (MSA), which allows for the isolation of the principal components within the data cube. The overall noise in the data cube was significantly reduced by reconstructing the dataset using only the principal components

100

identified as independently varying by the MSA technique (MSAXESP v0.6) (Watanabe *et al.*, 2006). After this reconstruction process, elemental maps of the constituent elements were extracted from the data cubes in the Gatan Digital Micrograph software environment. Further details regarding this technique have been published elsewhere (Herzing *et al.*, 2008; Watanabe *et al.*, 2006).

XPS Measurements. High-resolution X-ray photoelectron spectroscopy (HR-XPS) was carried out on nZVI material using a Scienta ESCA-300 instrument. Detailed procedures of XPS analysis are provided in Chapter 3.

Estimation of oxide-layer thickness by reduction of Cu (II). When ZVI is in contact with Cu(II) ion in solution, a galvanic cell is established. At the anode, Fe^0 is oxidized to Fe(II), and the electrons are taken up by the Cu(II) ion at the cathode to form Cu^0 as shown in the following equation:

$$Cu^{2+}(aq) + Fe^0(s) \rightarrow Cu^0(s) + Fe^{2+}(aq) \qquad\qquad (4.1)$$
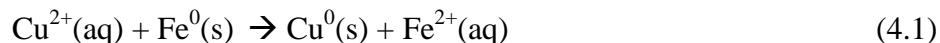
In an oxygen-free solution at near-neutral pH, the reduction of water by nZVI is relatively slow and reaction 4.1 predominates in the solution (Speller, 1951). The kinetics of the above reaction have been studied and the rate scales with the surface area of iron metal (Khudenko & Gould, 1991). In addition, it has been demonstrated that nano-scale iron particles, with a surface area on the order of 20-30 m^2/g, are able to reduce copper ions rapidly (Li & Zhang, 2007). From the quantity of copper reduced, the amount of Fe^0 originally present in the nanoparticles can be estimated and thereby

the thickness of the oxide layer can be deduced by a simple calculation involving the total mass of the nanoparticle sample.

To carry out this measurement, aqueous Cu(II) solutions were prepared from cupric chloride salt. The solution was purged with nitrogen for 30 minutes prior to addition of ZVI nanoparticles to remove dissolved oxygen. A set of experiments were conducted at various initial concentrations of Cu(II) with the iron nanoparticle concentration fixed at 0.25 g/L. The bottles were capped, tape-sealed, and agitated for 1 hour. After the reaction, the solutions were filtered and the concentrations of Cu(II) remaining in the aqueous phase were analyzed by an atomic absorption spectrometer (Perkin-Elmer AAnalyst200).

4.3 Results and discussion

4.3.1 Morphology, size distribution and surface area of nZVI

The surface morphology of nZVI is shown in Figure 4.1. SEM images show that the fresh nZVI particles are generally spherical in shape with the majority in the size range of 50-100 nm. A close-up image (Figure 4.1b) reveals that the particles are connected in chains due to magnetic dipole interactions and chemical aggregation. A few large flaky materials are oxidized products of nZVI. Figure 4.1c shows a bright field TEM micrograph of a typical nZVI cluster. In the absence of stabilizing agents such as

polyacrylic acid (PAA), the nanoparticles appear agglomerated, forming chain-like formation due to magnetic and electrostatic interactions. It is clearly shown in the image that a single particle comprises of a dense core surrounded by a thin shell exhibiting markedly less contrast than the interior core. Selected area electron diffraction (SAED) of the core region shows diffused ring patterns (Figure 4.1e) that are characteristic of very fine crystallites (or nanocrystalline) body-centered cubic (*bcc*) iron metal as evidenced by the the presence of {110}, {200} and {211} rings. The thickness of the shell was found to vary significantly among different nZVI particles and within each individual particle. Typically, the oxide layers were in the range of 2-4 nm, although shells as thick as 25 nm and as thin as 1 nm were occasionally observed. It is noticed that the chains of connected nanoparticles have a continuous oxide shell, but the individual metallic cores are separated from each other by a thinner (~1 nm) interfacial oxide layer. Phase-contrast TEM image (Figure 4.1d) shows the oxide shell has a speckly contrast and lacks periodic lattice-fringes, suggesting the oxide layer is amorphous in character. The disordered oxide layer can be explained by the extremely small radii of the nanoparticles and the curvature of the oxide shell, which impose considerable stress hindering crystalline formation. Moreover, the presence of a small amount of boron in the oxide film from borohydride precursor used in the synthesis step may contribute to defective sites and alter the oxide structure as well. (Carpenter *et al.*, 2003; Ponder *et al.*, 2001).
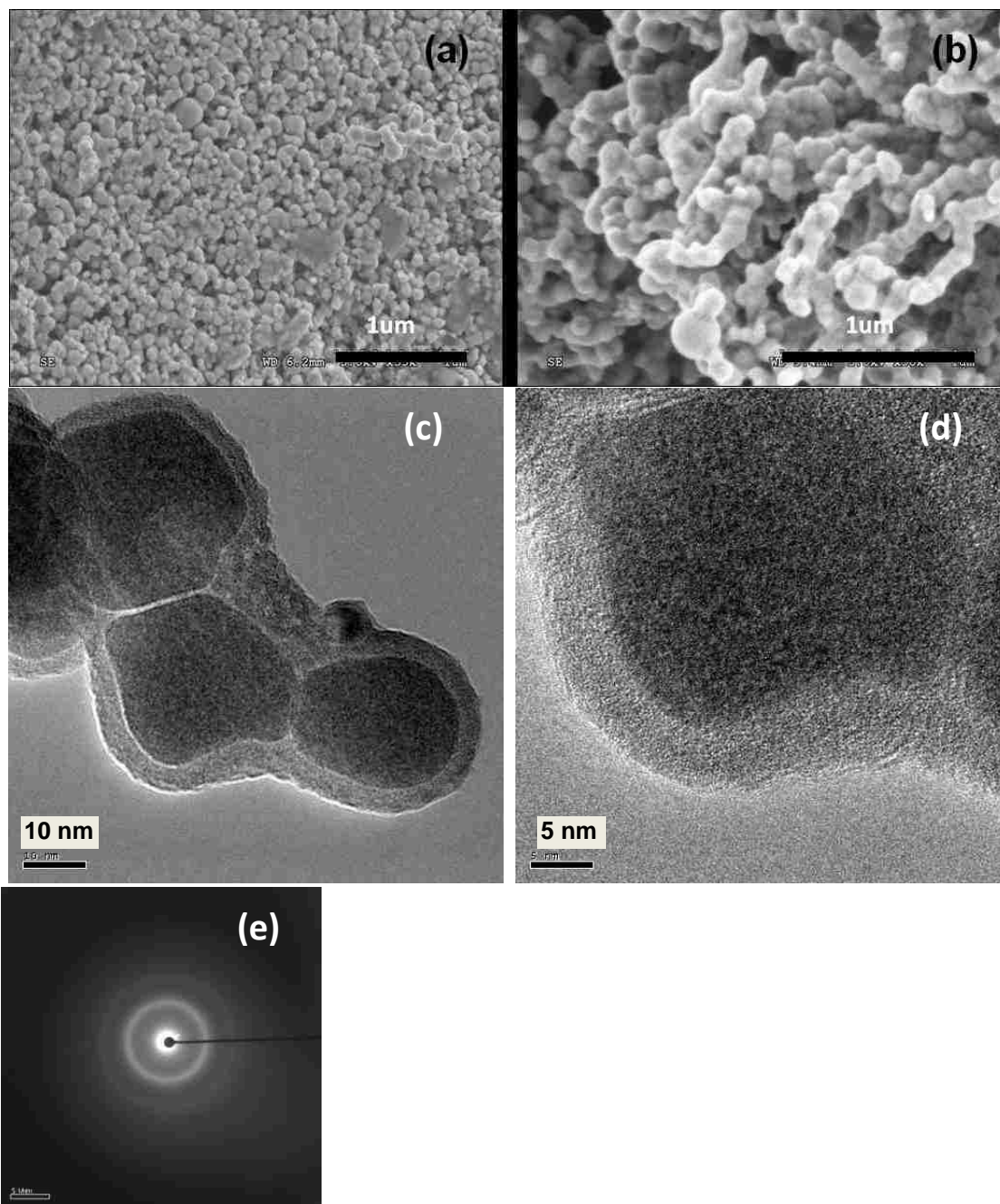
Figure 4.1 (a) & (b) SEM images of freshly-made nZVI particles. (c) Bright-field TEM micrograph of a nanoparticle agglomerate. (d) Phase contrast TEM image showing a continuous surface amorphous layer that encapsulates the agglomerate. (e) Selected-area electron diffraction (SAED) pattern of fresh nZVI particles characteristic of polycrystalline *bcc* iron.

Although SEM & TEM imaging provides direct visual evidence of the particle size, it cannot quantify the size with high statistical confidence due to limited number of iron particles sampled during analysis. An indirect but more reliable approach to gauge the particle size is to measure the surface area. In this study, BET specific surface area (a_s) of fresh nZVI was measured to be 29 m^2/g. Assuming a spherical geometry, specific surface area (a_s) of a particle is directly related to the particle diameter (D) as in Eq. 4.2:

$$Specific\ \ Surface\ \ Area = a_s = \frac{Surface}{Mass} = \frac{\pi D^2}{\frac{1}{6}\pi D^3 \rho} = \frac{6}{\rho D} \tag{4.2}$$

where ρ represents the density of metallic iron (7,800 kg m^{-3}). Given the specific surface area, an equivalent sphere diameter (D) of iron particles can be calculated from Eq. 4.2.

Eq. 4.2 yields an average particle diameter of 26 nm, which is significantly smaller than the size measured by the acoustic spectrometer method reported by Sun *et al*., (Sun *et al*., 2007), which indicates a median size of 60 nm, and it is also smaller than the size range shown in SEM images (Figure 4.1). The discrepancy can be explained by acknowledging that the particles tend to agglomerate into chain-like structures due to magnetic or chemical interactions, thus the assumption of well-separated particles in Eq.4.2 does not hold. As particle size increases to micron-scale, it is noticed that the SSA is a fairly accurate indicator of the average particle size (Li *et al*., 2009). Since

acoustic spectrometry is a more appropriate method for estimating nanoparticle size, the diameter measured by this method (median diameter 60nm) is adopted in subsequent discussions.

4.3.2 Direct visualization of core-shell structure by STEM-XEDS

Figure 4.2a shows an annular dark-field (ADF) image and the corresponding STEM-XEDS elemental maps (Figure 4.2b-d) from a typical agglomerate of the nZVI particles. As shown in Figure 4.2b, the Fe K_α map exhibits strong intensity in the bulk of the agglomerate, but depicts a clear decrease in intensity at the edge region corresponding to the amorphous shell. By comparison, the O K_α map (Figure 4.2c) has a fairly flat contrast level across the centre of the agglomerate but is much brighter at the edge in the amorphous region. Overlay of the elemental maps, shown in Figure 4.2d where red and green represent O and Fe respectively, clearly illustrates the presence of the amorphous oxide phase both at the agglomerate surface and between the individual particles. While the structure of nZVI has been characterized by various microscopic, spectroscopic and chemical reduction methods in recent publications (Cao *et al*., 2008; Martin *et al*., 2008; Nurmi *et al*., 2005; Sun *et al*., 2006), direct visual presentation of the chemical composition and the micro-structure of the nanoparticles were not attainable in those studies. The STEM-XEDS technique employed in this study is able to unambiguously map out elemental distribution at a nanometer-scale spatial solution,

and thereby provides direct evidence of a core-shell layered structure existing in these
nZVI materials.
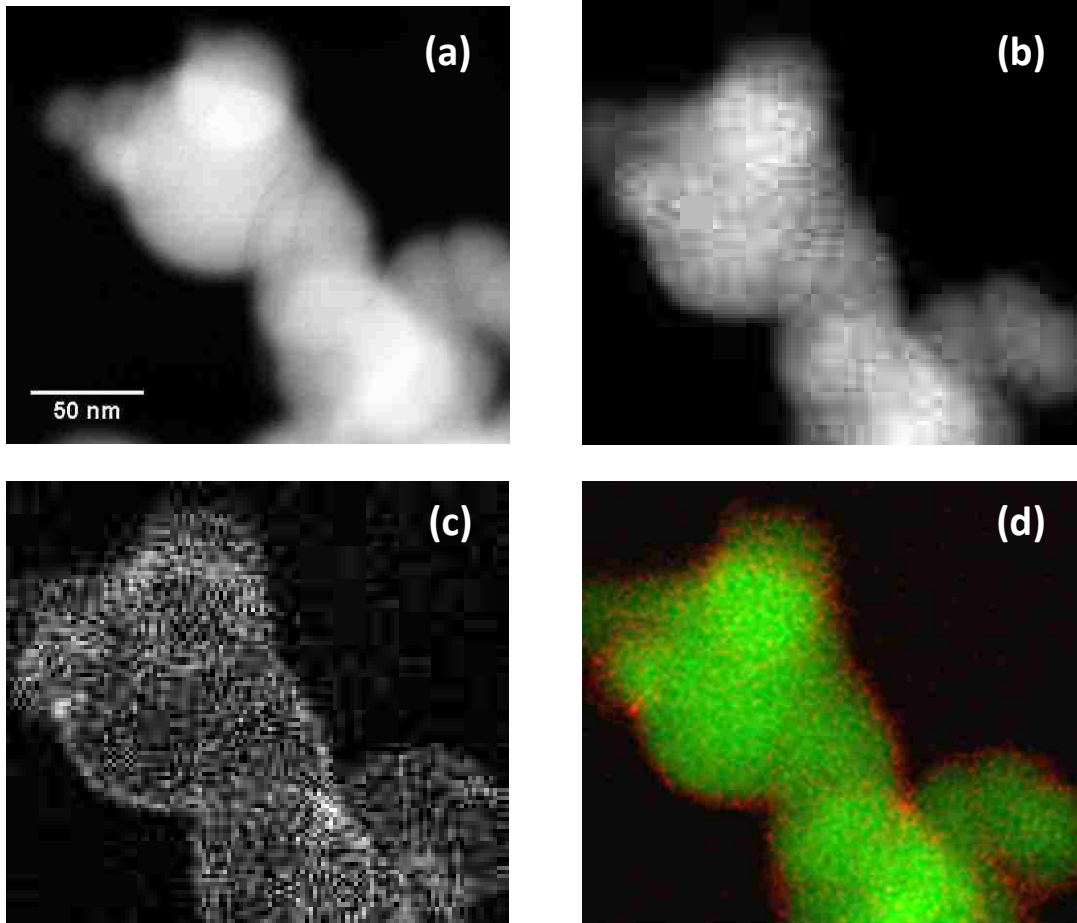
Figure 4.2 (a) ADF image and corresponding (b) Fe K_α, and (c) O K_α STEM-XEDS
elemental maps of an nZVI agglomerate. The color image in (d) is an overlay of the
elemental maps (red-O; green-Fe), which emphasizes the presence of an oxide layer
both at the agglomerate surface and between the individual particles.

4.3.3 Estimation of oxide-shell thickness by HR-XPS

An XPS survey scan from 0-1100 eV BE was acquired for the as-prepared nZVI sample, as shown in Figure 4.3a. This broad, low resolution scan indicates the predominate elements present in the near-surface region of the sample. It shows the presence of principally iron and oxygen, as indicated by the Fe $2p_{3/2}$ peaks at 715 eV BE and the O 1s peak at 530 eV BE. In addition, adventitious carbon on the sample is indicated by a peak at 284.6 eV BE, and peaks at 1071 and 182 eV BE from Na 1s and B 1s, respectively, which are believed to be from residual $NaBH_4$ from the synthesis process.
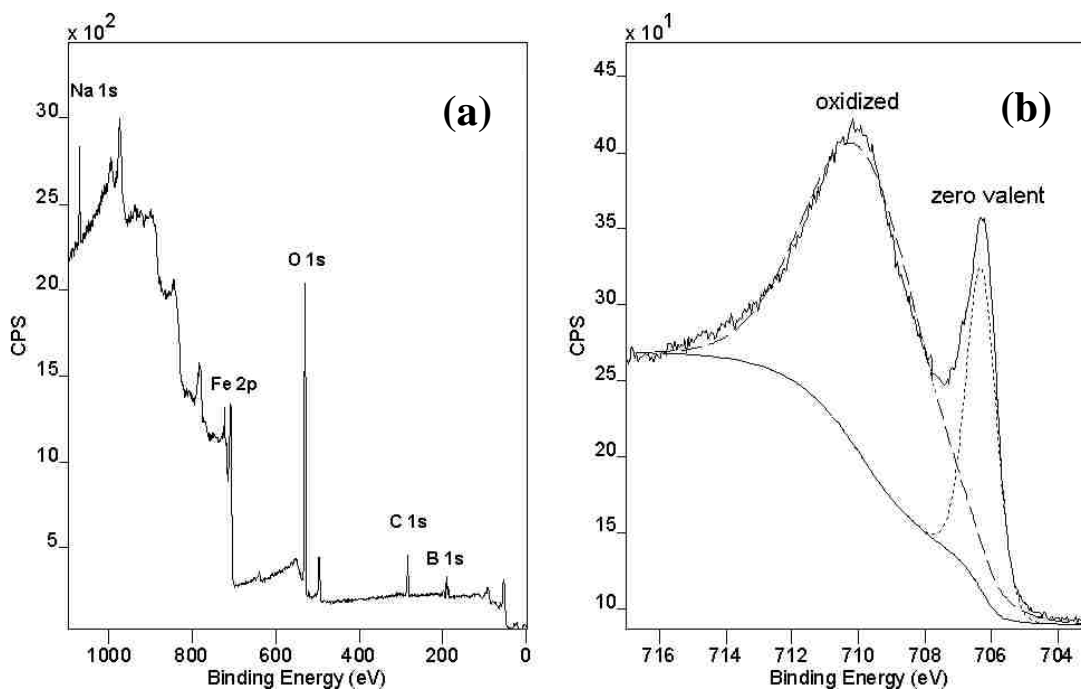
Figure 4.3 (a) Broad survey scan in XPS of the nZVI sample. (b) High-resolution XPS scan of the Fe2p$_{3/2}$ region.

Iron detected in this survey scan can be attributed to metallic iron within the core of the particles as well as iron oxides and iron oxyhydroxide, FeOOH, within the shell (Li & Zhang, 2006; Li & Zhang, 2007; Sun *et al*., 2006). To delineate the different iron chemical (oxidation) states present in the particles, a high resolution scan of the Fe 2p region was performed. Because the Fe $2p_{1/2}$ and $2p_{3/2}$ spin-orbit split peaks in XPS reveal the same chemical information, we show only the more intense Fe $2p_{3/2}$ region in Figure 4.3b. As expected, we observed chemically shifted peaks due to metallic iron, Fe^0, and from oxidized iron, (a combination of Fe^{2+} and Fe^{3+}) . Figure 4.3b establishes clearly that some metallic iron remains in the nZVI, in the core of the particles, however it is not obvious by inspection how much metallic iron is present and, in particular, what is the thickness of the oxidized iron shell. XPS is a quantitative analytical technique, and the intensity of the Fe 2p signal in XPS is proportional to the number of Fe atoms in the sampled near-surface region. This relationship is independent of the Fe atom environment, i.e., independent of the Fe oxidation state, and so in principle the relative amount of oxidized iron and metallic iron in the sample can be calculated by analysis of a spectrum such as that shown in Figure 4.3b. In this analysis, a Shirley-type background subtraction was applied to distinguish the Fe 2p photoelectron peaks from an inelastic scattering background. The $2p_{1/2}$ and $2p_{3/2}$ peaks for both oxidized iron and Fe^0 were assigned individual Gaussian-Laurentian components for deconvolution and the area under each peak was integrated. A relative intensity ratio, 0.233, was

109

determined as the sum of the $2p_{1/2}$ and $2p_{3/2}$ areas for Fe^0 divided by the corresponding areas of the $2p_{1/2}$ and $2p_{3/2}$ signals for the oxidized iron component.

The nZVI shell thickness was calculated with XPS Multiquant software using a geometric correction to compensate for spherical topography (Mohai & Bertoli, 2004 ; Mohai, 2004 ; Mohai, 2005). For a metal covered by a metal oxide layer with a flat topography, the relative intensity of zero-valent to oxidized metal is defined by (Mohai, 2005):

$$\frac{I_{me}}{I_{ox}} = \frac{N_{me}\lambda_{me}}{N_{ox}\lambda_{ox}} \cdot \frac{\exp\left(-d/\lambda_{ox}\cos\theta\right)}{1-\exp\left(-d/\lambda_{ox}\cos\theta\right)} \tag{4.3}$$

where I_{me} is the photoelectron intensity of the metal, I_{ox} is the intensity of the oxidized metal, N is the number of atoms per unit volume, λ is the inelastic mean free path, d is the oxide layer thickness, and θ is the detection angle. For normal take-off angle ($\theta = 90^0$), the layer thickness can be calculated as (Mohai, 2005):

$$d = \lambda_{ox}\ln\left(\frac{N_{me}\lambda_{me}}{N_{ox}\lambda_{ox}} \cdot \frac{I_{ox}}{I_{me}} + 1\right) \tag{4.4}$$

However, for a spherical nanoparticle, the curved surface of the nanoparticle causes changes in the relative intensity of photoelectrons originating from the core or shell. For a detector placed above the sample surface, photoelectrons escaping from the edge of a nanoparticle will originate predominantly from the shell while those photoelectrons escaping from the apex will more likely emanate from both the core and shell.

110

Although the shell thickness may be constant around the particle, the effective thickness, d^{eff}, will vary at different positions across the diameter of the nanoparticle (Mohai, 2005). This topology effect is corrected by dividing the particle into many slides at different angles and assigning different weightage for the overlayer (shell) and substrat (core) components at these angles. Since the nanoparticles were analyzed in powder form, a second correction was applied to account for signals originating from lower layers of spheres. These calculation can be routinely performed by the XPS multiquant software (Mohai, 2005; Martin *et al*., 2008).

The inelastic mean free path was calculated using the CS2 semi-empirical method (Cumpson & Seah, 1997). This is based on calculations of the attenuation length, λ_{AL} :

$$\lambda_{AL} = 0.316a^{3/2}\left\{\frac{E}{Z^{0.45}\left[\ln(E/27)+3\right]}+4\right\} \tag{4.5}$$

where *a* is the lattice parameter or monolayer thickness in nm, E is the kinetic energy, and Z is the average atomic number. Since the relative intensities are from the same element, corrections for sensitivity factors or contamination need not be applied.

For Fe photoelectrons moving through the metallic core and oxide shell, $\lambda_{me} = 1.10$ nm and $\lambda_{ox} = 1.42$ nm. One limitation of this model is that the thickness can only be determined if the layer is within a certain range. This range is governed by the sampling depth of the photoelectrons analyzed, with a maximum sampling depth of

approximately several multiples of λ. Therefore, the XPS technique is most accurate for measurements of oxide layers less than 5-10 nm in thickness.

The density of bulk iron, 7.87 g/cm^3, and bulk goethite (FeOOH), 4.28 gm/cm^3 (Yang *et al*., 2006) , were utilized to approximate the density of the core and shell layers. It has been shown by TEM and acoustic spectrometry method that the median nanoparticle diameter was 60 nm (Sun *et al*., 2006). Based on this particle size, the calculated average shell thickness was 2.4 nm. The effect of varying diameter was assessed because these nanoparticles are very polydisperse, possessing a broad range of sizes. Since the distribution of particle diameters was mainly between 10 and 200 nm, the thickness was calculated at intervals within this range (Table 4.1).

Table 4.1: Thickness determination for varying average particle diameters.

Diameter (nm)	10	20	30	40	50	60	100	200
Oxide-shell thickness (nm)	2.85	2.57	2.49	2.45	2.42	2.40	2.38	2.36

Based on these values, the maximum error due to polydispersity was calculated. For a constant intensity, a nanoparticle of 10-nm diameter has a thickness of 2.85 nm, and a particle of 200-nm diameter a thickness of 2.36 nm. This provides a maximum error of ± 0.25 nm. Based on this model, most of the error is attributed to the smaller nanoparticles. This is because the effects of the edge are slightly more exaggerated for smaller particles. The relatively narrow range of the average shell thickness reflects the

nature of the shell formation in that the thickness is controlled by the rate of mass or electron transfer across the oxide layer.

4.3.4 Estimation of oxide-shell thickness by Cu(II) reduction

Another approach to estimate the shell thickness is to experimentally measure the content of zero-valent iron in the particles, which can be done in a number of ways. For example, some researchers have measured the amount of hydrogen gas produced from iron reactions with water (Nurmi *et al*., 2005). The facile reaction of nZVI with Cu(II) aqueous solution is exploited for the fast measurement of the zero-valent iron content. We tested the rapid and complete reduction of Cu(II) with nZVI to independently verify the results obtained by both TEM and XPS analysis.

Figure 4.4a shows the XPS spectrum of the Cu 2p3/2 region for the nZVI particles after the particles were reacted with copper. A peak at 932.4 eV BE arises from Cu(0), suggesting that Cu(II) was reduced and immobilized on nZVI. To exclude the possibility that the Cu signal is from precipitation of copper hydroxide, the solution pH was measured after reaction and found to be in the range of 4-5, thus ensuring that the Cu was indeed reduced to elemental copper on the nZVI particles. To further confirm the product is metallic copper, X-ray analysis was performed on the reacted particles and the result is shown in Figure 4.4b. The diffraction pattern corresponds well to that of Cu(0) in (111), (200) and (220) directions. There is no peak indicative of the

(a)

(b)
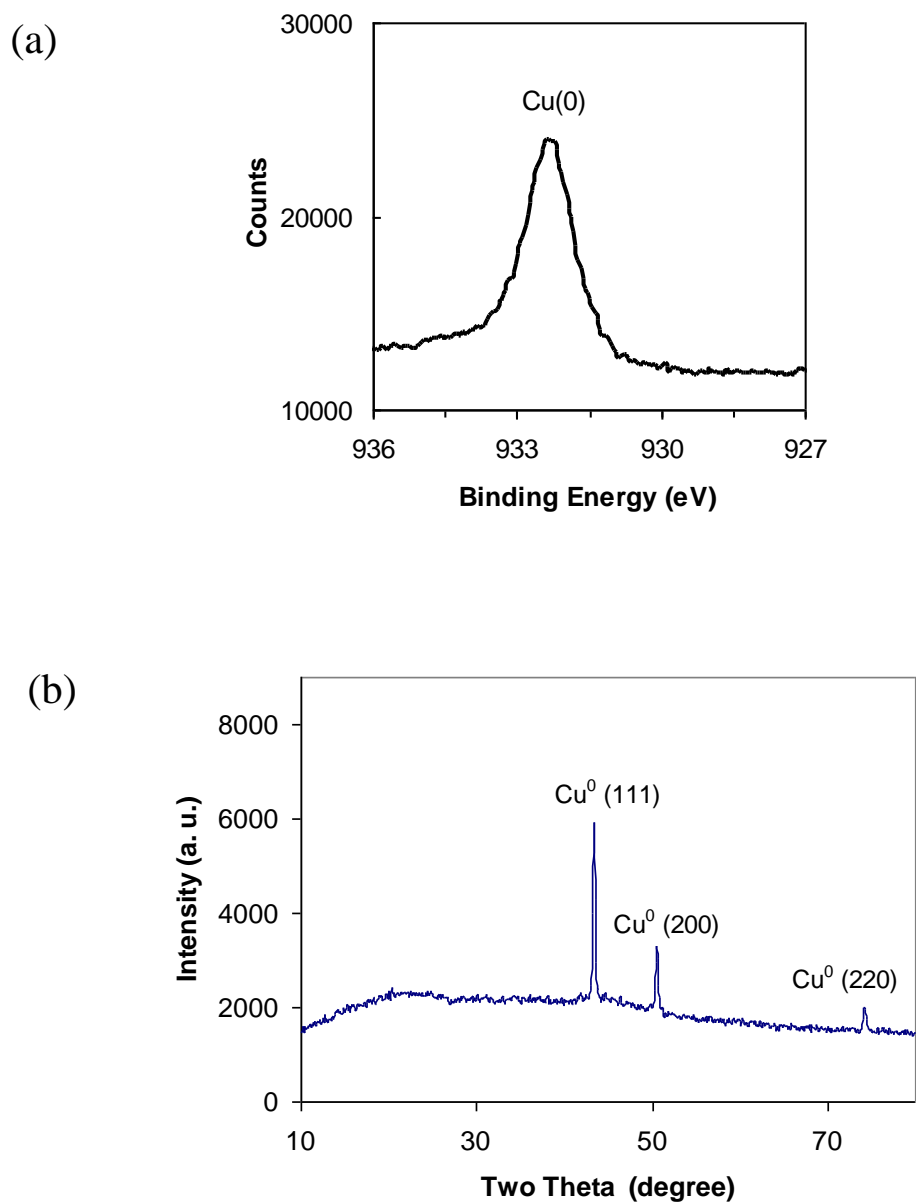
Figure 4.4 (a) High-resolution XPS scan of the Cu2p$_{3/2}$ region showing the presence of a peak at 932.4 eV BE indicative of Cu^0. (b) XRD diffractogram confirms the formation of crystalline Cu^0 after reaction with nZVI.

presence of CuO or Cu_2O phase. The sharp peaks observed imply the metallic copper is crystalline in character, which agrees with SEM observations (results not shown).

Given that essentially all sequestrated copper is converted to Cu(0) by nZVI, the ideal stoichiometry of Cu(II) sequestration by nZVI is 1:1 on a mole basis (Eq. 4.1). In reality, the actual stoichiometry deviates from 1: 1 ratio primarily because iron nanoparticles are not made of pure Fe(0) but a composite of metallic iron enclosed by an iron oxide shell. Thus the amount of Cu(II) being reduced is related to the metallic iron content in the nanoparticles. To evaluate the iron concent, a set of experiments were performed with a fixed dose of nZVI particles while varying the Cu(II) concentration. The results were plotted in terms of copper removal per unit mass of nZVI added as a function of the initial Cu(II) to nZVI ratio (Figure 4.5). Two auxiliary lines are plotted on the figure to assist the interpretation of the data. The dashed line with a slope of unity represents the hypothetical scenario of 100% Cu(II) removal when Cu(II) is the limiting species. The horizontal line indicates the maximum Cu(II) sequestration capacity (mM-Cu/g-nZVI) when metal iron is limiting. As shown in Figure 4.5, the experimental data exhibits a clear "crank" shape revealing two distinct domains. At low initial Cu(II) concentration, the Cu(II) being removed per gram of iron nanoparticles increases with the initial copper concentration. The match of the experimental data to the unit-slope line, which represents the scenario for complete removal of the Cu(II), indicates all Cu(II) is sequestrated when iron is present in excess. At higher Cu/Fe mass ratios, iron became the limiting reagent. The curve bends sharply and approaches a plateau

corresponding to a maximum removal capacity of 14.5 mM-Cu/g-nZVI, or 0.922 g-Cu/g-nZVI.

As shown in Figure 4.5, the total reduction is approximately 0.922 g-Cu(II)/g-iron nanoparticles. Since 1 mole of Fe^0 is consumed for every mole of Cu^{2+} reduced, the mass fraction of Fe^0 in the nanoparticles is calculated as 0.810 g-Fe^0/g-nanoparticles. Using a median particle diameter of 60 nm and the bulk densities of Fe^0 and FeOOH given earlier, the thickness of the oxide shell is estimated to be 3.4 nm. This is in fairly good agreement with the TEM and XPS results considering that the calculation of shell thickness from mass fraction is sensitive to the size of the nanoparticles. If compared on the basis of reduction capacity, the values obtained by XPS analysis and Cu(II) reduction experiments are in close agreement with a discrepancy of less than 7% (Table 4.2). The slightly lower reduction capacity obtained by the copper reduction experiments is to be expected because a small quantity of Fe^0 is inevitably consumed by reaction with water.
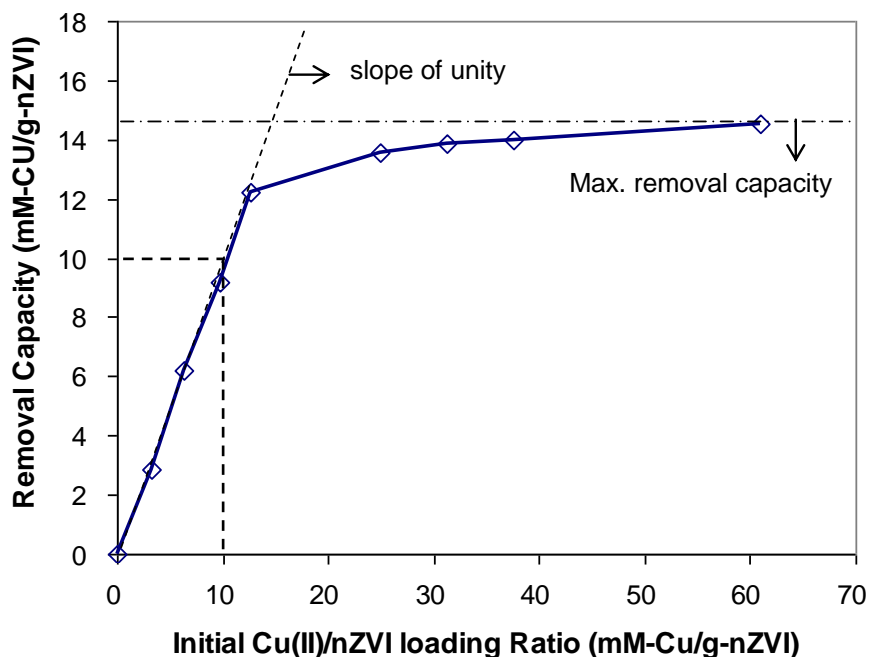
Figure 4.5 Cu(II) removal capacity at different Cu(II)/nZVI loading ratios showing two behavioral domains. The initial concentration of Cu(II) varied from 50 to 1000 mg/L, with the concentration of iron nanoparticles fixed at 0.25g/L. The auxiliary lines represent the ideal cases where i) Cu(II) is completely removed by nZVI when Cu(II) is limiting; or ii) nZVI is exhausted when Fe(0) is limiting.

Table 4.2: Shell thickness and reductive capacity of iron nanoparticles predicted by XPS measurements and Cu(II) reduction experiments.

	Cu(II) reduction experiments	XPS analysis
Oxide shell thickness (nm)	~ 3.4*	~ 2.4
Mass fraction of Fe^0 in nZVI ($g-Fe^0$/g-nanoparticles)	0.810	0.866*
Cu(II) reduction capacity (meq/g-nanoparticles)	29.0	31.0*

* Calculated based on an average nanoparticle diameter of 60 nm.

117

4.4 Conclusion

In summary, a series of detailed characterizations of iron nanoparticles were presented here using a variety of microscopic and spectroscopic characterization tools. SEM imaging clearly shows the agglomeration of individual nanoparticles due to magnetic and chemical interactions. Bright field and phase contrast TEM methods indicate the polycrystalline metal iron core is surrounded by a continuous oxide layer. Advanced STEM-XEDS imaging technique provide for the first time direct evidence of the core-shell structure. Additionally, phase contrast TEM suggests the oxide layer lacks long-range order and is amorphous in character. This property may have significant implications for particle adsorptive and redox activity as will be examined in details in later chapters. The thickness of the oxide shell was determined using three independent methods. High-resolution TEM images indicate that fresh nZVI nanoparticles have the shell thickness vary from region to region, predominantly within 2-4 nm. High-resolution XPS analysis, using the relative integrated intensities of metallic and oxidized iron with a geometric correction applied to account for the curved overlayer, yield an average shell thickness in the range of 2.3-2.8 nm. Thirdly, the complete oxidation reaction of the nZVI particles by Cu(II) indicated a shell thickness (3.4 nm) consistent with these analyses. The three methods yielded very similar results and thus we have made a reliable determination of the shell thickness for fresh nZVI nanoparticles. This information fills an essential gap in our knowledge about the nZVI structure. In addition, we note that the methods presented in this work can also be

applied to the study of the aging process of nZVI and may also prove useful for the measurement and characterization of other metallic nanoparticles.

References

1.   Gillham, R. W.; Ohannesin, S. F., Enhanced Degradation of Halogenated Alphatics by Zero-Valent Iron. *Ground Water* **1994,** *32* (6), 958-967.

2.   Matheson, L. J.; Tratnyek, P. G., Reductive Dehalogenation of Chlorinated Methanes by Iron Metal. *Environ. Sci. Technol.* **1994,** 28, (12), 2045-2053.

3.   Alowitz, M. J.; Scherer, M. M., Kinetics of nitrate, nitrite, and Cr(VI) reduction by iron metal. *Environ. Sci. Technol.* **2002,** 36, (3), 299-306.

4.   Johnson, T. L.; Scherer, M. M.; Tratnyek, P. G., Kinetics of halogenated organic compound degradation by iron metal. *Environ. Sci. Technol.* **1996,** 30, (8), 2634-2640.

5.   Cao, J. S.; Wei, L. P.; Huang, Q. G.; Wang, L. S.; Han, S. K., Reducing degradation of azo dye by zero-valent iron in aqueous solution. *Chemosphere* **1999,** 38, (3), 565-571.

6.   Hundal, L. S.; Singh, J.; Bier, E. L.; Shea, P. J.; Comfort, S. D.; Powers, W. L., Removal of TNT and RDX from water and soil using iron metal. *Environ. Pollut.* **1997,** 97, (1-2), 55-64.

7.   C. P. Huang, H. W. Wang and P. C. Chiu, Nitrate reduction by metallic iron.

Water Res., 1998, **32**, 2257-2264.

8.   Lien, H. L.; Zhang, W. X., Transformation of chlorinated methanes by nanoscale iron particles. *J. Environ. Eng.-ASCE* **1999,** *125* (11), 1042-1047.

9.   Kanel, S. R.; Greneche, J. M.; Choi, H., Arsenic(V) removal kom groundwater using nano scale zero-valent iron as a colloidal reactive barrier material. *Environ. Sci. Technol.* **2006,** *40* (6), 2045-2050.

10.   Sohn, K.; Kang, S. W.; Ahn, S.; Woo, M.; Yang, S. K., Fe(0) nanoparticles for nitrate reduction: Stability, reactivity, and transformation. *Environ. Sci. Technol.* **2006,** 40, (17), 5514-5519.

11.   Nurmi, J. T.; Tratnyek, P. G.; Sarathy, V.; Baer, D. R.; Amonette, J. E.; Pecher, K.; Wang, C. M.; Linehan, J. C.; Matson, D. W.; Penn, R. L.; Driessen, M. D., Characterization and properties of metallic iron nanoparticles: Spectroscopy, electrochemistry, and kinetics. *Environ. Sci. Technol.* **2005,** *39* (5), 1221-1230.

12.   Hydutsky BW, Mack EJ, Beckerman BB, Skluzacek JM, Mallouk TE. Optimizatin of nano- and microiron transport through sand columns using polyelectrolyte mixtures. *Environ. Sci. Technol*. **2007**. 41 (18): 6418-6424.

13.   Huber, D. L. Synthesis, properties and applications of iron nanoparticles. *Small* **2005**, 5, 482-501.

14.   Li, X. Q.; Zhang, W. X., Sequestration of metal cations with zerovalent iron nanoparticles - A study with high resolution X-ray photoelectron spectroscopy (HR-XPS). *J. Phys. Chem. C* **2007,** 111, (19), 6939-6946.

15. Li, X. Q.; Zhang, W. X., Iron nanoparticles: the core-shell structure and unique properties for Ni(II) sequestration. *Langmuir* **2006,** 22, (10), 4638-4642.

16. Sun, Y. P.; Li, X. Q.; Cao, J. S.; Zhang, W. X.; Wang, H. P., Characterization of zero-valent iron nanoparticles. *Adv. Colloid Interfac.* **2006,** *120* (1-3), 47-56.

17. Seah, M.; Dench, W. *Surf. Interface Anal.* **1979**, **1**, 2–11.

18. Fadley, C.; in *Basic Concepts of X-ray Photoelectron Spectroscopy*; Brundle, C.; Baker, A. (Eds.) Electron Spectroscopy: Theory Techniques and Applications Vol. 2, Academic Press, New York, 1978, p.1.

19. Gunter, P.; Niemantsverdriet, J., Thickness determination of uniform overlayers on rough substrates by angle-dependent XPS *Appl. Surf. Sci.* **1995**, 89, 69-76.

20. Mohai, M.; Bertoli, I., Calculation of overlayer thickness of curved surfaces based on XPS intensities. *Surf. Interface Anal.* **2004**, 36**,** 805-808.

21. Gillet, J. ; Meunier, M. General equation for size nanocharacterization of the core-shell nanoparticles by X-ray photoelectron spectroscopy. *J. Phys. Chem. B* **2005**, 109**,** 8733-8737.

22. Kappen, P.; Reihs, K.; Seidel, C.; Voetz, M.; Fuchs, H. Overlayer thickness determination by angular dependent X-ray photoelectron spectroscopy (ADXPS) of rough surfaces with a spherical topology. *Surf. Sci.* **2000**, 465, 40-50.

23. Watanabe, M.; Ackland, D.W.; Burrows, A.; Kiely, C. J.; Williams, D. B.; Krivanek, O. L.; Dellby, N.; Murfitt, M. F.; Szilagyi, Z., Improvements in the X-ray analytical capabilities of a scanning transmission electron microscope by

spherical-aberration correction. *Microsc. Microanal.* **2006**, *12*, 515-526.

24. Herzing, A.A.; Watanabe, M.; Edwards, J. K.; Conte, M.; Tang, Z. R.; Hutchings, G. J.; Kiely, C. J.; Energy dispersive X-ray spectroscopy of bimetallic nanoparticles in an aberration corrected scanning transmission electron microscope. *Faraday Discuss.* **2008**, *138*, 337-351.

25. Speller, F. N.; Corrosion, Causes and Prevention, 3rd ed.; McGraw-Hill: New York, 1951.

26. Khudenko, B. M.; Gould, J. P., Specifics of Cementation Processes for Metal Removal. *Water Sci. Technol.* **1991,** 24, (7), 235-246.

27. Sun, Y. P.; Li, X. Q.; Zhang, W. X.; Wang, H. P., A method for the preparation of stable dispersion of zero-valent iron nanoparticles. *Colloid Surface A-Physicochem. Eng. Aspects* **2007,** *308* (1-3), 60-66.

28. Carpenter, E. E.; Calvin, S.; Stroud, R. M.; Harris, V. G., Passivated iron as core-shell nanoparticles. *Chem. Mater.* **2003**, *15*, 3245-3246.

29. Ponder, S. M.; Darab, J. G.; Bucher, J.; Caulder, D.; Craig, I.; Davis, L.; Edelstein, N.; Lukens, W.; Nitsche, H.; Rao, L. F.; Shuh, D. K.; Mallouk, T. E., Surface chemistry and electrochemistry of supported zerovalent iron nanoparticles in the remediation of aqueous metal contaminants. *Chem. Mater.* **2001,** *13* (2), 479-486.

30. Cao, J. S.; Li, X. Q.; Tavakoli, J.; Zhang, W. X., Temperature programmed reduction for measurement of oxygen content in nanoscale zero-valent iron.

Environ. Sci. Technol. **2008**, *42*, 3780-3785.

31.   Martin, J. E.; Herzing, A. A.; Yan, W. L.; Li, X. Q.; Koel, B. E.; Kiely, C. J.; Zhang, W. X., Determination of the oxide layer thickness in core-shell zerovalent iron nanoparticles. *Langmuir* **2008**, *24*, 4329-4334.

32.   Mohai, M. XPS multiquant: Multimodel XPS quantification software. *Surf. Interface Anal.* **2004,** 36, 828-832.

33.   Mohai, M. *XPS Multiquant Users Manual* **2005**.

34.   Cumpson, P.; Seah, M. Elastic scattering corrections in AES and XPS. 2. Estimating attenuation lengths and conditons required for their valid use in overlayer/substrate experiments. *Surf. Interface Anal.* **1997**, 25, 430-446.

35.   Yang, H.; Lu, R.; Downs, R.; Costin, G. Goethite, alpha-FeO(OH) from single-crystal data. *Acta Crystallographica, Section E: Structure Reports Online* **2006**, E62(12), i250-i252.

Chapter 5

Aging of nZVI in Aqueous Media and Implications for Particle Reactivity

---

5.0 Abstract

Iron nanoparticles have been extensively employed to degrade halogenated organic compounds in lab and field studies, yet the structure, especially the distribution of a second metal additive, which serves as a catalyst of reductive dehalogenation reactions, within the nanoparticles have not been specifically examined due to the resolution challenge imposed by the nanoscale particles. In this work, the structural evolution of palladized nanoscale iron particles (Pd-nZVI, with a mass fraction of Pd of 1.5%) was examined using X-ray photoelectron spectroscopy (XPS), scanning transmission electron microscopy (STEM), and X-ray energy dispersive spectroscopy (XEDS) techniques. For a freshly made Pd-nZVI sample, the particles consist of a metallic iron core and a thin amorphous oxide shell, and Pd is observed to form 2 to 5 nm islands decorating the outer surface of the nanoparticles. Upon exposure to water, Pd-nZVI undergoes substantial morphological and compositional changes. STEM-XEDS elemental maps show that Pd infiltrates through the oxide layer to the metallic iron interface, which is accompanied by oxidation and outward diffusion of the iron species. Within a 24 h period, Pd is completely buried underneath a growing iron oxide matrix,

and a fraction of the nanoparticles exhibits a hollowed-out morphology with no metallic iron remaining. The microstructural variations observed concur with the reactivity data, which shows the aged bimetallic particles display an 80% decrease in dechlorination rate of trichloroethene (TCE) compared to the fresh particles. These findings shed new insight into the function of palladium in hydrodechlorination reactions, nZVI particle aging and deactivation, and the longevity of Pd-nZVI for *in-situ* remediation applications.

5.1 Introduction

Nanoscale zero-valent iron (nZVI) represents one of the most widely studied engineered nanomaterials in environmental remediation and toxic waste treatment. The reactivity of nZVI can be substantially improved by impregnating with a second metal, typically Pd, Pt, Ni, Ag or Cu, to form so-called bimetallic nanoparticles. Among these transition metal additives, Pd-doped nZVI (Pd-nZVI) is known to exhibit higher reactivity than the other reported bimetallic systems (Alonso *et al*., 2002; Cwiertny *et al*., 2006). For treatment of chlorinated organic compounds (e.g., trichloroethene and tetrachloroethene), Pd-Fe bimetallic materials yield more-saturated products (*i.e.,* C_2H_6) and generate less toxic intermediates, such as dichloroethenes and vinyl chloride, which are often produced with monometallic iron (Alonso *et al*., 2002; Lien & Zhang, 2007). Ample literature exists on reductive dehalogenation using Pd-Fe bimetallic materials,

and Table 5.1 summarizes some of the most frequently-cited laboratory and field studies.

Table 5.1: Common halogenated contaminants treated by Pd-Fe bimetallic nanoparticles in recent studies.

Contaminant	Pd-Fe materials	Reference
Chlorinated methane	As synthesized Pd(0.05-1 % by mass)-Fe nanoparticles	Lien & Zhang, 1999
Carbon tetrachloride	Palladized iron cathode in flow through cell	Li & Farrell, 2000
Tetrachloroethene (PCE), Trichloroethene (TCE), Dichloroethene (DCE), Vinyl chloride (VC)	As-synthesized Pd-Fe nanoparticles	Zhang *et al*., 1998
Trichloroethene (TCE)	Pd(11 % by mass)-Fe nanoparticles embedded in polymer matrix	Xu *et al*., 2005
Trichloroethene (TCE)	Starch stabilized Pd(0.1 % by mass)-Fe nanoparticles	He *et al*., 2007
Trichloroethene (TCE)	As synthesized Pd(0.3 % by mass)-Fe nanoparticles for field evaluation	Korte *et al*., 2000; Elliott & Zhang, 2001
Chlorophenols	Encapsulated Pd-Fe in magnetic stabilized fluid bed reactor	Graham & Jovanovic, 1999
Polychlorinated biphenyls (PCB)	As-synthesized Pd-Fe nanoparticles	Wang & Zhang, 1997
Polychlorinated biphenyls (PCB)	As-synthesized Pd-Fe on granular activated carbon support	Choi *et al*., 2008
Chlorobenzenes	As-synthesized and regenerated Pd(0.1 % by mass)-Fe nanoparticles	Zhu & Lim, 2007

Palladium metal is a well-known heterogeneous catalyst for gas phase dehalogenation and hydrogenation reactions (Alonso *et al*., 2002; Wong *et al*., 2009). The use of Pd-impregnated iron (Pd-Fe) for groundwater remediation is a relatively recent application. Mechanistic studies of the degradation of simple aliphatic chlorinated compounds in water suggest that the iron component of the Pd-Fe material serves as the source of electrons, which reduces water and produces H_2 via aqueous corrosion. On the other hand, palladium behaves as a catalytic surface for hydrogen adsorption, activation, and the subsequent formation of dissociated hydrogen species, which in turn act as the reducing agents responsible for the dechlorination and hydrogenation of the contaminants (Kim & Carraway, 2003; Cwiertny *et al*., 2006; Lien & Zhang, 2007).

In contrast to gas phase reactions, the use of iron materials in water remediation applications inevitably requires that they sustain prolonged contact with the aqueous environment and undergo reactions with water. Moreover, in the presence of Pd, iron reaction with water is accelerated due to the galvanic effect between iron and palladium in addition to the well known ability of the latter to catalytically promote the reduction of water and hydrogen generation (Uhlig, 1971; Cwiertny *et al*., 2006). Because of the large excess of water molecules relative to those contaminants of concern, the interaction of the Pd-Fe particles with water determines the longevity of these materials and their long-term effectiveness for contaminant remediation applications. Stability in water is particularly important for nanoscale, Fe-based materials due to the enhanced reactivity imparted by their high surface area. Despite the popular use of doped nZVI

127

materials in water research, only a few studies have been conducted to investigate the effect of aqueous exposure on the structure and composition of these bimetallic nanoparticles (Muftikian *et al*., 1996; Zhu & Lim, 2007).

In this work, state-of-the-art X-ray energy dispersive spectroscopy (XEDS) spectrum imaging in an aberration-corrected scanning transmission electron microscope (STEM) (Burke *et al*., 2006; Watanabe *et al*., 2006; Herzing *et al*., 2008) is utilized for high resolution elemental mapping of Pd-nZVI bimetallic nanoparticles. The STEM-XEDS technique enables direct visualization of the nanoscale structural and compositional changes of the bimetallic particles induced by their aging in water. These findings are correlated with the results from X-ray photoelectron spectroscopy (XPS) and batch experiments with trichloroethene (TCE) in an effort to generate a more complete understanding of the reactivity and stability of Pd-nZVI particles in aqueous media over time. Implications of these results for water treatment and remediation are discussed.

5.2 Materials and methods

Preparation of nanoparticles. Iron nanoparticles (nZVI) were prepared using a sodium borohydride reduction method as described previously (Chapter 3). The nanoparticles were previously characterized and found to have a median diameter of 60 nm with more than 80 % of the particles being smaller than 100 nm (Sun *et al*., 2006). The BET

surface area was found to be 29 m^2/g. Pd-Fe bimetallic nanoparticles (Pd-nZVI) were prepared following the procedure described in Chapter 3.

Aging Experiments. The aging experiment was performed in 120 mL serum bottles containing 100 mL of de-ionized water. An appropriate amount of freshly made nZVI or Pd-nZVI nanoparticles were added into 100 mL DI water to reach a concentration of 5 g/L. The bottles were sealed with crimp caps having a Teflon-lined septum, and placed on a mechanical shaker at 25 ^{o}C for 24 h. The solid residues were harvested by vacuum filtration and dried in a glove bag containing high purity N_2.

XPS and XRD analysis. High-resolution X-ray photoelectron spectroscopy (HR-XPS) analysis was performed on a Scienta ESCA 300 spectrometer. Samples were placed in the HR-XPS analysis chamber held at 6.7×10^{-7} Pa (5×10^{-9} Torr) where general survey spectra and detailed spectra for the C 1s, O 1s, Fe 2p and Pd 3d regions were acquired. Detailed spectrum analysis and curve-fitting procedures are described in Chapter 3. XRD analysis was performed on a Rigaku diffractometer with Cu K_α radiation ($\lambda = 0.15406$ nm). Samples were scanned over a 2θ angular range from $10°$ to $80°$ with a step size of $0.1°$ and a scanning rate of 30 s per step.

Electron Microscopy Analysis. Samples for transmission electron microscopy (TEM) and scanning transmission electron microscopy (STEM) analysis were prepared by allowing a drop of a dilute ethanol suspension of the nanoparticles to dry on a lacey-carbon film supported on a 300-mesh copper TEM grid. Conventional bright-field and

phase contrast imaging experiments were carried out using a JEOL 2200FS FEG-TEM operating at 200 kV. High-angle annular dark-field (HAADF) imaging and XEDS spectrum imaging were performed using an FEI Titan 80-300 TEM/STEM operating at 300 kV in scanning (STEM) mode. This instrument is equipped with a double-hexapole spherical aberration (C_s) corrector (CEOS GmbH) and an EDAX r-TEM system for XEDS analysis.

The details of XEDS spectrum imaging have been described elsewhere (Burke *et al*., 2006; Watanabe *et al*., 2006; Herzing *et al*., 2008). Briefly, the electron probe is slowly scanned over a two-dimensional area of interest, collecting an entire X-ray fluorescence spectrum at each pixel. Because the aberration-corrected STEM probe is only about 100 pm in diameter, this type of analysis can be carried out at very high spatial resolution. In the present case, the data was collected using the Titan Image and Analysis (TIA) software package (FEI Co.) with a pixel size of 1 nm^2 or less and a spectrum collection time of 200 ms per pixel. The spectra were collected from 0 keV to 40 keV at 10 eV/channel, and drift-correction was carried out periodically during the acquisition by cross-correlation of the STEM-HAADF image intensity with a static reference image. The end result of this acquisition is a spectrum image data cube, the dimensions of which are defined by the spatial coordinates of the pixels (x and y) and the energy channels of the XEDS spectra (E). In order to analyze the information contained in the resulting data cube and extract background-subtracted elemental maps, post-processing was carried out using Lispix (ref. 22). Background subtraction was carried out using a

three-window method for the Fe and Pd signals, while only two windows were utilized for O due to the difficulty in background modeling of low energy X-rays.

Batch Experiments. TCE dechlorination experiments were conducted to compare the reactivity of fresh and aged Pd-nZVI particles. To remove hydrogen species accumulated in the solid phase during the aging process, which may contribute to TCE dechlorination, the aged nZVI suspension was sonicated for 10 min in air before collection by vacuum filtration and use in the subsequent TCE batch experiments. At the beginning of each experiment, a 100-mL of aqueous TCE solution (50 mg/L) was charged into a 250-mL serum bottle containing 0.25 g Pd-nZVI. The bottle was capped with a Teflon Mininert valve and mixed on a mechanical shaker at 250 rpm at room temperature (25 ^{o}C). Periodically, a 25-uL aliquot of headspace gas was withdrawn using a gastight syringe for gas chromatography (GC) analysis. Concentration of TCE was measured by a Shimatzu GC analyzer (GC-17A) equipped with a flame ionization detector and a SUPELCO SPB 624 capillary column. Each experiment was repeated and data shown were the average of two runs. A blank experiment was performed in parallel under the identical conditions but without the addition of Pd-nZVI particles.

5.3 Results and discussion

5.3.1 Surface chemistry analysis with XPS

Figures 5.1a and 5.1b show the Fe 2p XPS spectra of the nZVI and Pd-nZVI materials, respectively. The two spectra displayed for each type of nanoparticle correspond to the freshly made nanoparticles and those aged in water for one day. The Fe $2p_{3/2}$ photoelectron peaks at 706.6 eV and 710.8 eV can be assigned to metallic iron (Fe(0)) and oxidized iron (Fe(III)) based on the binding energies (B.E.) (Martin *et al.*, 2008).

For the freshly made nZVI and Pd-nZVI particles, a strong Fe(III) peak was present along with a relatively small Fe(0) peak. Considering that the typical sampling depth of the XPS technique is less than 10 nm, the iron XPS spectra agree with the core-shell model described in the literature, in which a metallic iron core is surrounded by a thin layer of oxidized iron. The overlayer is thought to form spontaneously upon synthesis and serves to prevent the underlying metallic iron core from rapid oxidation (Carpenter *et al.*, 2003; Li & Zhang, 2007). Prior analysis of O 1s spectra of freshly made nZVI suggests that the oxide phase has a stoichiometry of iron oxyhydroxide (FeOOH) (Li & Zhang, 2007). The relative abundance of Fe(0) to Fe(III) are comparable for the nZVI and Pd-nZVI materials, suggesting that the Pd impregnation process does not cause a significant alteration to the core-shell structure.

(a)
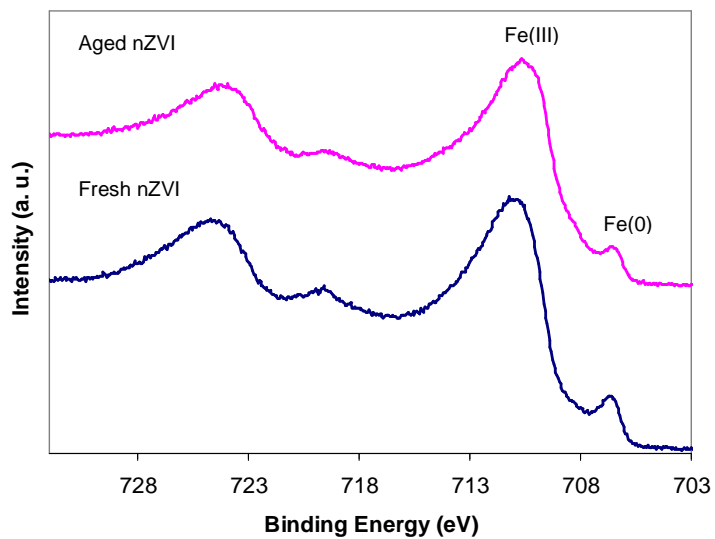
(b)
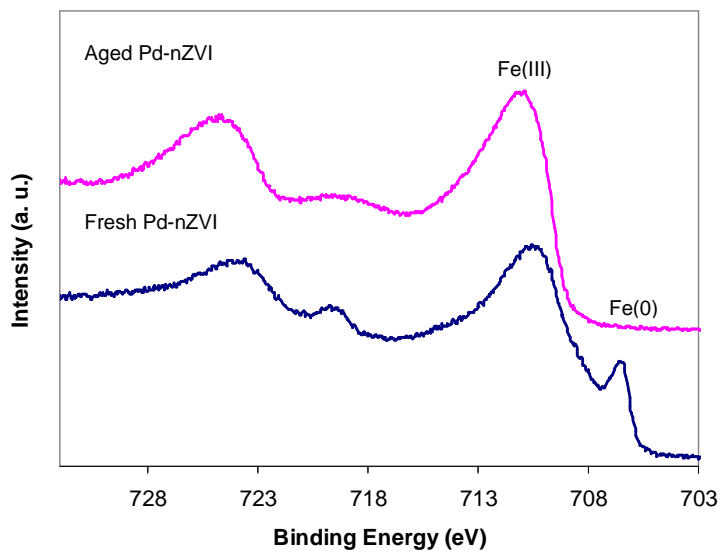
(c)
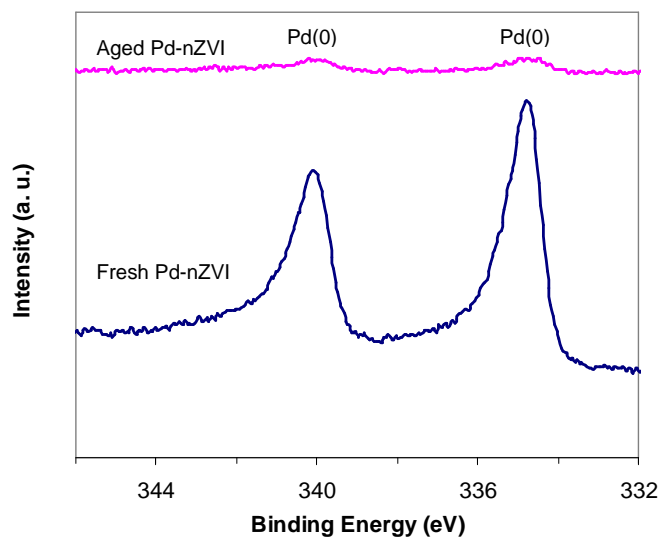
Figure 5.1 Fe2p XPS spectra of (a) monometallic iron nanoparticles (nZVI) and (b) Pd-impregnated iron nanoparticles (Pd-nZVI). Figure (c) Pd3d spectra of Pd-nZVI. The spectra in blue represent freshly made nanoparticles, and those in pink are for particles aged in aqueous media for 24 h.

After aging in water for one day, the Fe(0) peak remains detectable for the undoped Fe nanoparticles (Figure 5.1a). However, the intensity is markedly reduced, which indicates that surface corrosion may have occurred effectively increasing the shell thickness during the aging process. In contrast, the Pd-nZVI nanoparticles immersed in water for one day did not exhibit any metallic iron component in the XPS spectrum (Figure 5.1b), implying that the particles had undergone severe oxidation during the aging period. Figure 5.1c overlays the Pd 3d XPS spectra of the freshly made and the aged Pd-nZVI materials. The fresh Pd-nZVI exhibits two prominent peaks with binding

energies of 334.7 eV and 340.0 eV, respectively, which can be assigned to the $3d_{5/2}$ and $3d_{3/2}$ components for Pd(0) (Muftikian *et al*., 1996). No other Pd valence state was observed, thus confirming that the impregnated Pd was completely reduced to Pd(0) via a Pd(II)-Fe(0) replacement reaction:

$$Pd^{2+}(aq.) + Fe^0 \ (s) = Pd^0 \ (s) + Fe^{2+} \ (aq.) \qquad\qquad (5.1)$$
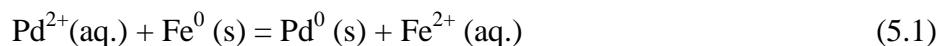
However, after a one-day exposure to an aqueous environment, the Pd $3d_{5/2}$ and $3d_{3/2}$ signals were severely attenuated and barely discernible from the background noise. Analysis of the solution in which Pd-nZVI particles were suspended showed no elution of Pd ions into the aqueous phase, suggesting Pd may have become effectively buried underneath a growing layer of iron corrosion products during the aging test period. The combined results of Fe 2p and Pd 3d XPS analysis imply that the bimetallic particles experienced much more rapid corrosion in water than the monometallic iron nanoparticles.

5.3.2 XRD characterization

The structures of the fresh and aged Pd-nZVI particles were also examined using XRD. The reflections in the XRD patterns of both the fresh and aged samples are broad (Figure 5.2), indicating that the particles under examination are nanocrystalline in nature. While several of the expected XRD peaks for *bcc* Fe, *fcc* Pd and iron oxide

phases are within close proximity and therefore have overlaps, there is clear evidence of

an overall increase in 6-line ferrihydrite phase after aging.
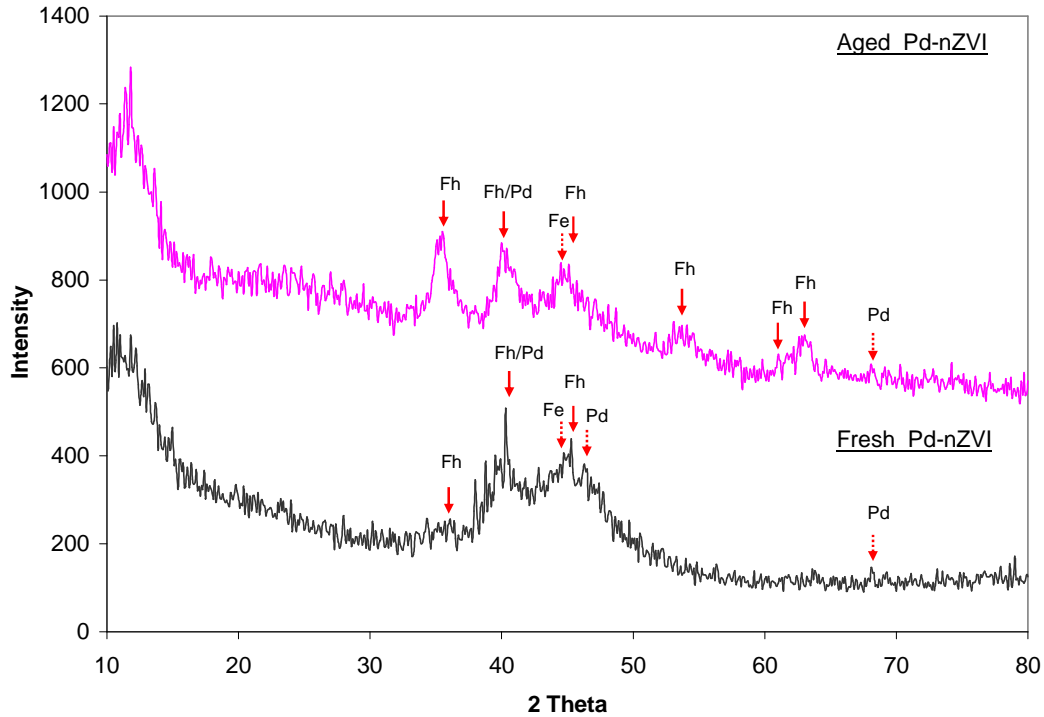
Figure 5.2 X-ray diffractograms acquired from the as-synthesized Pd-impregnated nZVI sample (black line) and the n-ZVI sample aged in water for 24 hours (pink line). While several of the diffraction peaks in question overlap, there is a clear increase in 6-line ferrihydrite (Fh) content upon aging, suggesting accelerated oxidation of the sample in water.

5.3.3 TEM, HAADF and STEM-XEDS characterization

Figure 5.3a shows a high-angle annular dark field (HAADF) image of a typical fresh undoped nZVI spherical particle. The signal collected via this technique is sensitive to atomic number, with the heavier elements scattering more effectively to the high collection angles employed. Thus, the locations of the specimen with greater average through-thickness atomic number will appear brighter, and compositional information can, to a certain extent, be garnered directly from the images.
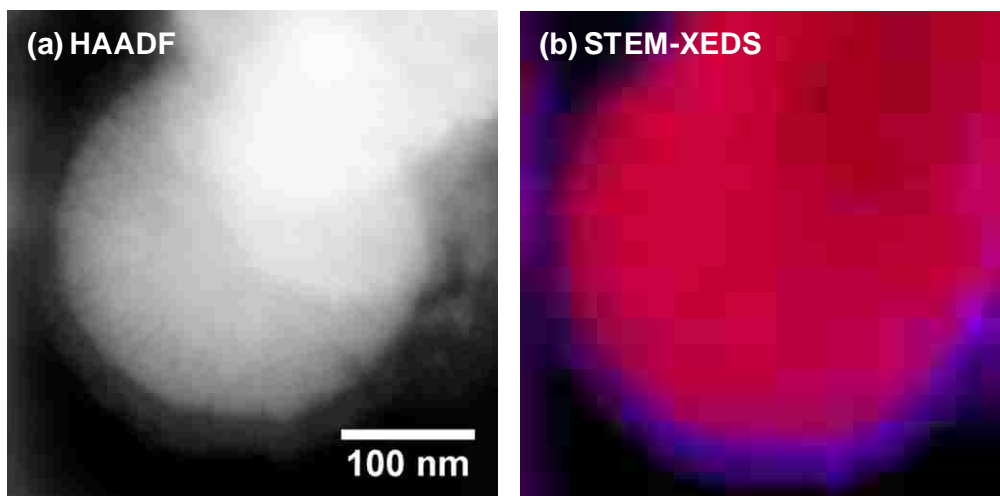
Figure 5.3 (a) HAADF image of an undoped nZVI particle showing the Fe-core/iron oxide-shell morphology. (b) a color overlay of STEM-XEDS elemental maps generated from the Fe K_α and the O K_α X-ray peaks (Red = Fe, Blue = O).

The particle in Figure 5.3a consists of a bright core, corresponding to metallic iron, enclosed by a ~5 nm thick shell, which is thought to be iron oxide. Previous combined TEM and XPS studies (Chapter 4) have identified the core of the n-ZVI particle to

consist of nanocrystalline (*bcc*) metallic Fe, while the shell is a highly disordered oxide layer resembling iron oxyhydroxide (FeOOH) in stoichiometry (Li & Zhang, 2007). This structural identification is further verified by the STEM-XEDS compositional maps shown in Figure 5.3b, which is produced by overlaying Fe K_α (red) and O K_α (blue) elemental maps, respectively. Notably, there is a reduced intensity in Fe signals and much enhanced O signals in the oxide shell region. The physical extent of the oxide layer relative to the nanoparticle is readily visualized using the STEM-XEDS mapping technique.

Figure 5.4a and Figure 5.4b show corresponding HAADF images of two typical particle morphologies found in the freshly prepared Pd-nZVI material. When compared to the HAADF images of the undoped nZVI (Figure 5.3a), the fresh Pd-nZVI particles have a considerably rougher surface profile, and, in the case of the particle shown in Figure 5.4b, the surface is decorated with 2 nm to 5 nm particles. After exposure to water for 24 h the Pd-nZVI particles undergo gross morphological changes as evidenced in the three HAADF images presented in Figures 5.4c - 5.4e. The starting Pd-nZVI structures and the three co-existing 'water-aged' morphologies (labeled X, Y and Z) can be interpreted more fully when considered in conjunction with their corresponding STEM-XEDS elemental maps, which are presented in Figure 5.5 & 5.6. Each set of STEM-XEDS maps consists of individual elemental maps for Fe K_α, O K_α, and Pd L_α, and a color overlay map of the three elements.

(a) fresh

25 nm

(b) fresh

50 nm

(c) aged *type-X*

50 nm

(d) aged *type-Y*

150 nm

(e) aged *type-Z*

50 nm
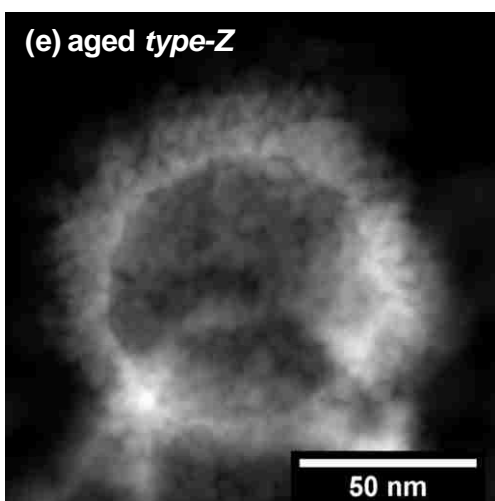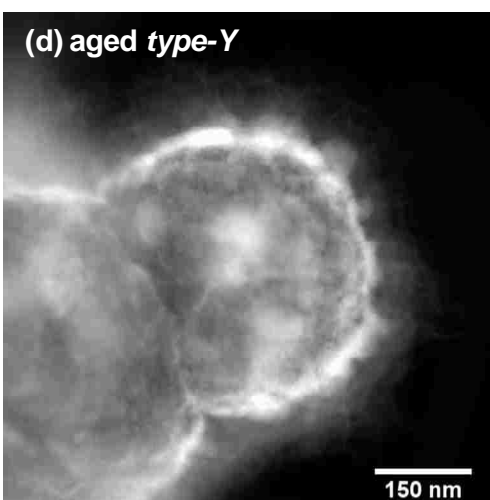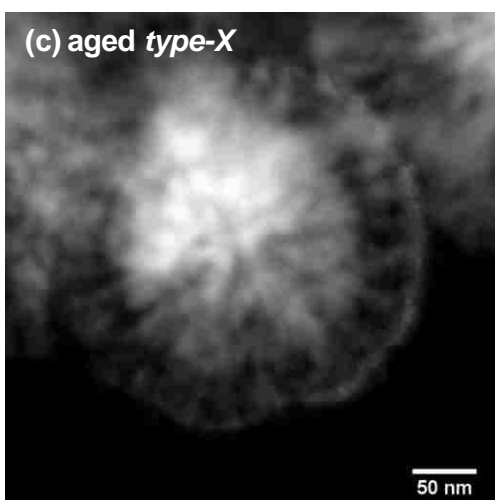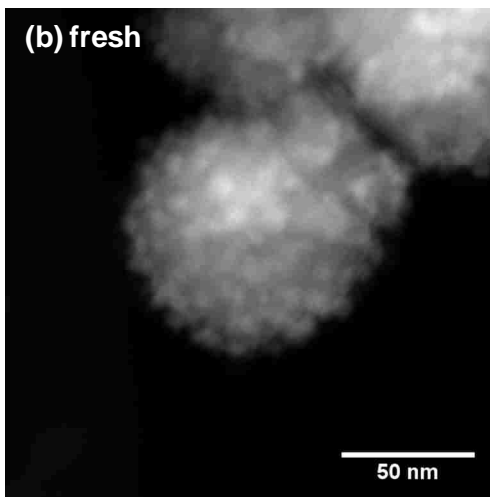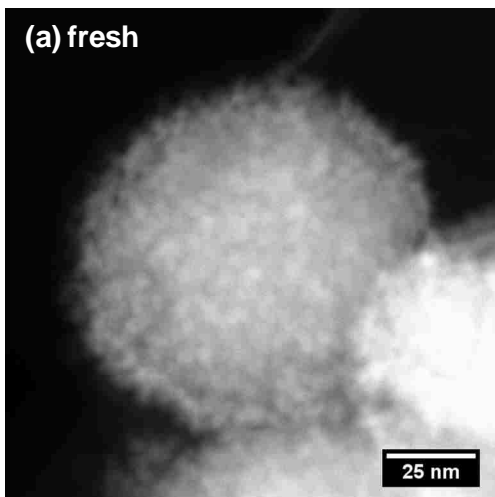
Figure 5.4 (previous page) HAADF images of Pd-nZVI material. (a) & (b) freshly made Pd-nZVI. (c) - (e) Pd-nZVI after aqueous aging for 24 h.

STEM-XEDS mapping data of the two main morphologies found in the fresh Pd-nZVI sample are shown in Figure 5.5. Figures 5.5a shows the Fe K_α, O K_α and Pd L_α elemental maps acquired from the cluster of particles shown previously in Figure 5.4a, where the Pd forms an almost continuous layer over the surface of the Fe/oxide core-shell particle. The color overlay map (last column of Figure 5.5a), where the elemental distribution of Pd is represented in green, clearly highlights the nearly continuous Pd layer on the exterior surface. However, the vast majority of the particles found in the fresh Pd-nZVI sample are more like that shown in Figure 5.5b. The corresponding elemental maps from this type of particle clearly show that there are discrete (green) Pd nanoparticles decorating the surface of the n-ZVI species. The XPS spectra acquired from these fresh samples Pd-nZVI samples (Figure 5.1c) suggest that these are metallic rather than oxidized Pd nanoparticles.

Figure 5.6 shows the Fe K_α, O K_α and Pd L_α STEM-XEDS elemental maps from the 'after–aging' morphologies, which are denoted as Type-X, Type-Y, and Type-Z morphology, respectively, in Figure 5.4. Close examination of the Type-X morphology (Figure 5.6a) suggests that Pd is beginning to penetrate through the less dense oxide outerlayer towards the metallic Fe core.

STEM-XEDS mapping of fresh Pd-nZVI nanoparticles

Fe Kα   O Kα   Pd Lα   Overlay

(a)

(b)
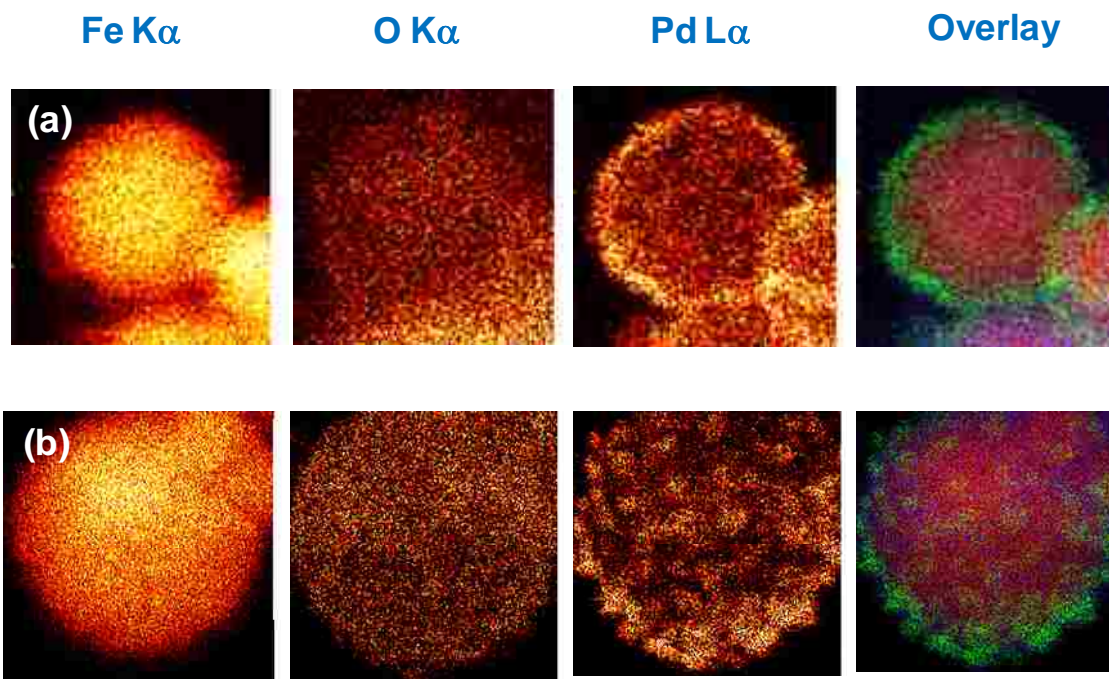
Figure 5.5 STEM-XEDS elemental maps of the Fe K$_\alpha$, O K$_\alpha$, Pd L$_\alpha$ X-ray signals and a color overlay (Red = Fe, Blue = O, and Green = Pd) of the fresh Pd-nZVI particles shown in Figure 5.4a (corresponding to 5.5a) and 5.4b (corresponding to 5.5b).
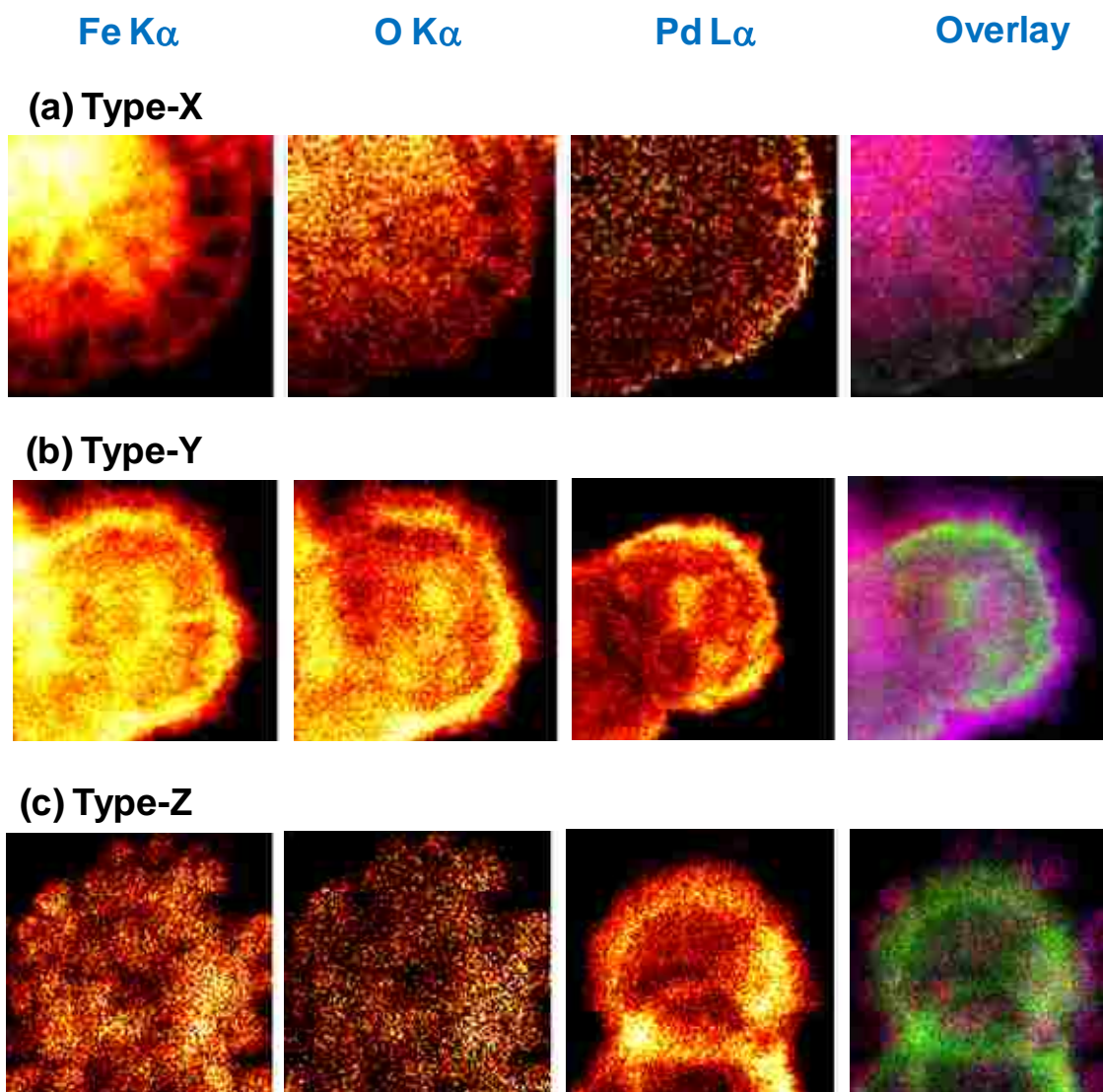
Figure 5.6 STEM-XEDS elemental maps of the Fe K_α, O K_α , Pd L_α X-ray signals and a color overlay (Red = Fe, Blue = O, and Green = Pd) of the aged Pd-nZVI particles shown in Figure 5.4c-5.4e. (a) - (c) correspond to the aged Type-X, Y, and Z morphology, respectively.

The elemental maps corresponding to the 'after–aging' morphology denoted as type-Y in Figure 5.4d are presented in Figure 5.6b. The spatial extent of the Pd signal is found to be considerably smaller than that of the Fe signal, suggesting that the Pd in this particle is now all sub-surface. The color overlay of elemental maps demonstrates the situation where all Pd is accumulating as a buried (green) layer at the metallic Fe/oxide interface. This observation of a buried interfacial layer of Pd is consistent with the XPS data, where a dramatic decrease in overall surface Pd signal was noted for the samples aged in water (Figure 5.1c).

The third distinct (type-Z) morphology of aged Pd-nZVI particle shows a characteristic low level of contrast at its center in HAADF images (Figure 5.4e), suggesting that it may in fact have a hollow core. Figure 5.6c shows the corresponding STEM-XEDS elemental data for this particle type. The Fe K_α and O K_α elemental maps show a very close correspondence, suggesting that complete oxidation of metallic iron has occurred, and both display an intensity decrease at the particle center indicative of the presence of a central void. The Pd distribution shown in Figure 5.6c indicates that the Pd is located under the oxide layer, seemingly defining the interior surface of the pore. We believe that while the Pd is diffusing inward to the Fe/oxide interface, the metallic Fe associated with the core simultaneously diffuses outward, oxidizes and contributes to the oxide shell, which then grows in thickness until eventually all the metallic Fe is consumed. This oxidation process could be controlled by several factors, such as the particle surface area, exposure of different surface facets, etc. Therefore, the microstructural

heterogeneities in the system cause the reaction rate to vary from particle to particle, and we observe multiple types of microstructure (X, Y and Z) in the aged sample. The progression from one morphology to the next cannot be unequivocally addressed in this study, since our structural characterization was carried out at only one aging interval (24 h). However, our interpretation of the data is that during exposure to water, nZVI particles, which originally have Pd on their outer surfaces, sequentially transform though the X, Y and Z microstructures that have been identified in this study (Figure 5.7).
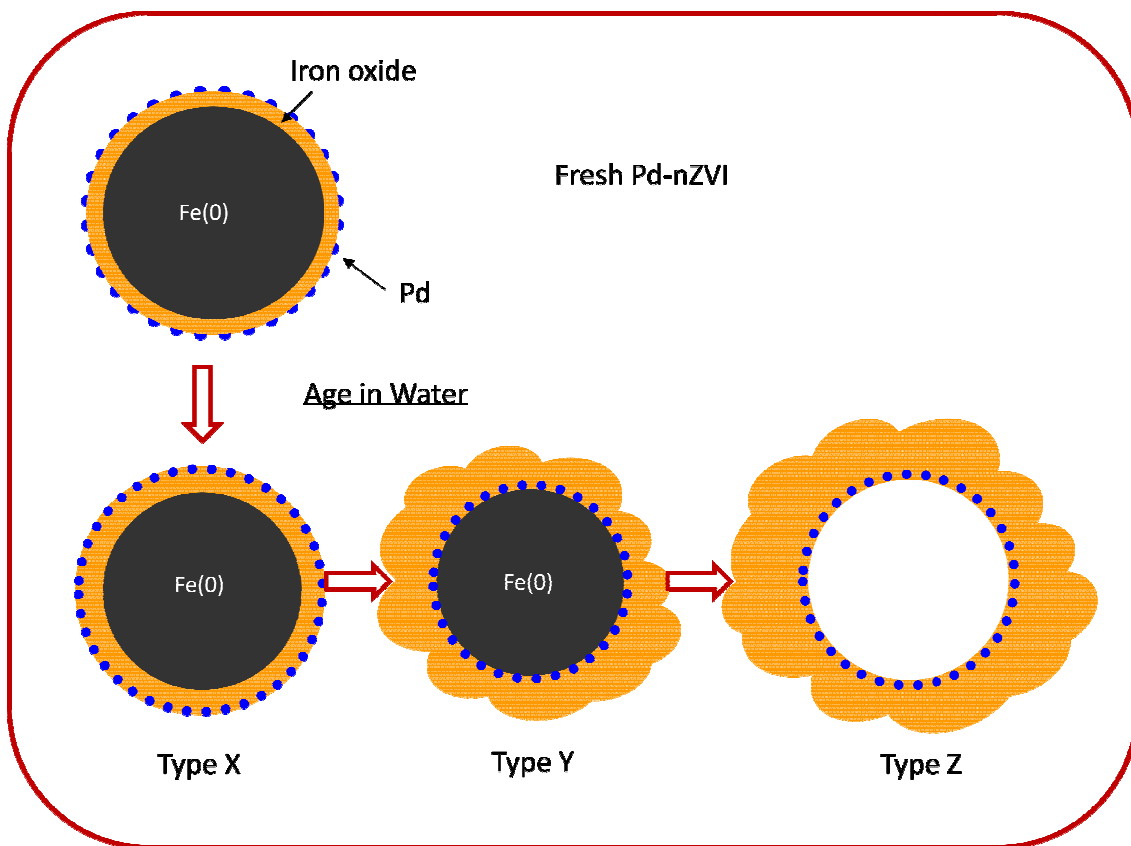
Figure 5.7 Schematic illustration of the progressive transformation of Pd-nZVI nanoparticles during immersion in aqueous media.

144

5.3.4 Interpretation of the observed structural transformations

The structural changes observed due to aging, namely, the increase in oxide layer thickness, the enclosure of the initial surface Pd by the oxide layer, and in some cases the evacuation of the metallic iron core to give a characteristic "hollowed-out" structure, may result from several processes. The growth of the oxide layer is the net result of iron oxidation, outward diffusion of Fe(II), and oxidation and precipitation of Fe(II) upon reactions with water, dissolved oxygen and other potential oxidants in the solution phase (Wang *et al*., 2005; Reardon *et al*., 2008). Similar phenomena including the outward diffusion of the metal species and the growth of an oxide shell have been observed previously during the oxidation of iron and cobalt nanoparticles in gas or aqueous media (Wang *et al*., 2005; Yin *et al*., 2004). The inward migration of palladium metal is also favored thermodynamically since the core region has the highest concentration of metallic iron, which reduces Pd(II) and stabilizes elemental palladium. Due to the very large surface-area-to-volume ratio and short diffusion distances associated with these nanoscale particles, the mass transport could easily result in void formation and eventually a hollow structure within reasonably short time frames.

In the case of Pd-nZVI, the process of iron oxidation is significantly accelerated compared to the undoped nZVI particles. The effect is attributed to the galvanic contact between palladium and iron, which creates a large electrochemical potential difference ($\Delta E^o = 1.355$ V) (Bard *et al*., 1985) driving iron oxidation. In addition, palladium is also a well-known hydrogenation catalyst (Alonso *et al*., 2002; Wong *et al*., 2009) for water

reduction to hydrogen. Both effects result in enhanced iron corrosion. Indeed, we conducted experiments to evaluate the hydrogen generation rate by nZVI and Pd-nZVI in water, and the results confirm there is a more than 30-fold increase in hydrogen evolution rate by doping the nanoparticles with mass fraction of 1% of palladium (Table 5.2). The experiments were performed in 1 L of deoxygenated DI water with varying doses of iron-based nanoparticles. The suspension was mixed with a magnet stirrer at 400 rpm. Rotating stirring paddle, which was commonly used in batch kinetic experiments, was not employed here due to concern over possible gas leakage through the rotating fixture. The pressure of the headspace inside the reactor was monitored by a pressure sensor. Reaction time was 20 h for Pd-nZVI and ranged from 100 to 250 h for nZVI.

We observed that the curves of hydrogen generation vs. time can be reasonably fitted using a straight line (data not shown), thus a simple linear hydrogen evolution rate is assumed in life-span estimations. The following reaction stoichiometry is used (Reardon *et al*., 2008):

$$3Fe(s) + 4H_2O \rightarrow Fe_3O_4 + 4H_2 (g) \hspace{2cm} (5.2)$$

By approximating with a linear model of hydrogen generation with time, the life span of our Pd-nZVI nanoparticles is estimated to be approximately 38 h (Table 5.2). This number is in good agreement with the observation that a sizable proportion of the aged Pd-nZVI had their metallic iron interior hollowed out after 24 h of aging in water. It

should be noted that the estimated life span of undoped nZVI is extrapolated from H_2 evolution experiments that lasted for up to 250 h, thus it is assumed herein that Fe(0) corrodes at a constant rate until complete exhaustion. However, previous studies have reported that the rate of iron corrosion declines with time (Reardon *et al*., 2008), so the actual longevity of nZVI may be substantially higher than the value estimated here.

Table 5.2: Laboratory evaluated hydrogen evolution rates for nZVI and Pd-nZVI and the estimated life-spans of the nanoparticles.

Nanoparticles	*Dose (g)*	*H_2 evolution rate (mg-H_2/g-Fe/h)*	*Estimated life-span of the nanoparticles before complete oxidation*
nZVI	0.1	2.27×10^{-2}	87 d
	0.25	4.82×10^{-2}	41 d
	0.5	4.09×10^{-2}	49 d
Pd-nZVI (Pd at 1wt%)	0.5	1.24	38 h

5.3.5 Implications for water remediation applications

nZVI-based bimetallic materials have been extensively studied for their enhanced reactivity and the generation of more benign end-products in the reductive dehalogenation of organic halides (Table 5.1). However, most studies have not considered the possibility of dynamic structural changes of the bimetallic nanoparticles in the aqueous reaction media. Structural characterization studies are typically

performed on the fresh material, and it is assumed that the nanostructure and elemental distribution remain unchanged during the course of the remediation treatment. The observation that the Pd-Fe bimetallic nanoparticles can undergo massive structural and compositional changes in water over a time-frame comparable to that of the contaminant transformation process calls for a significant modification of the reaction models of bimetallic nanoparticles. Enclosure of Pd by an extensive iron oxide layer due to aqueous aging clearly requires the contaminants (*e.g.,* TCE) to penetrate into the particle and the products (*e.g.,* ethane) to diffuse out through the oxide layer, which may affect reaction kinetics, alter the rate-limiting steps, and influence final product distributions. No detailed study has been performed yet on these aspects, but the apparent loss of reactivity for Pd-Fe materials after aging in water is observed in TCE batch experiments (Figure 5.8). The apparent reaction rate constant based on a pseudo-first-order reaction rate model decreased from 5.7 h^{-1} for the fresh particles to 0.96 h^{-1} upon 24 h aging. Decreased reaction rates have also been reported in prior studies over repeated use of Pd-Fe particles in aqueous solutions (Zhu & Lim, 2007), and these findings are consistent with the rapid enclosure of surface Pd sites by a growing iron oxide shell as illustrated in Figure 5.7.

Prior studies have attempted to correlate the reactivity of the bimetallic particles with the mass loading of the additive metal. Instead of following a monotonically increasing trend, it has been observed that an optimal dosage exists and the reactivity declines with a further increase in the additive metal loading (Nutt *et al*., 2005; Cwiertny *et al*., 2006;

Lien & Zhang, 2007). The behavior may conceivably be attributable to accelerated particle aging and more rapid surface deactivation with increasing Pd dopant level. This hypothesis needs to be confirmed by systematically extending this study to Pd-Fe nanoparticles with different Pd contents. Differences in the initial structure of nZVI, the doping procedure, and the aging medium (for instance, in solvent/water mixture) may also affect the reactivity and aging of the bimetallic nanoparticles.
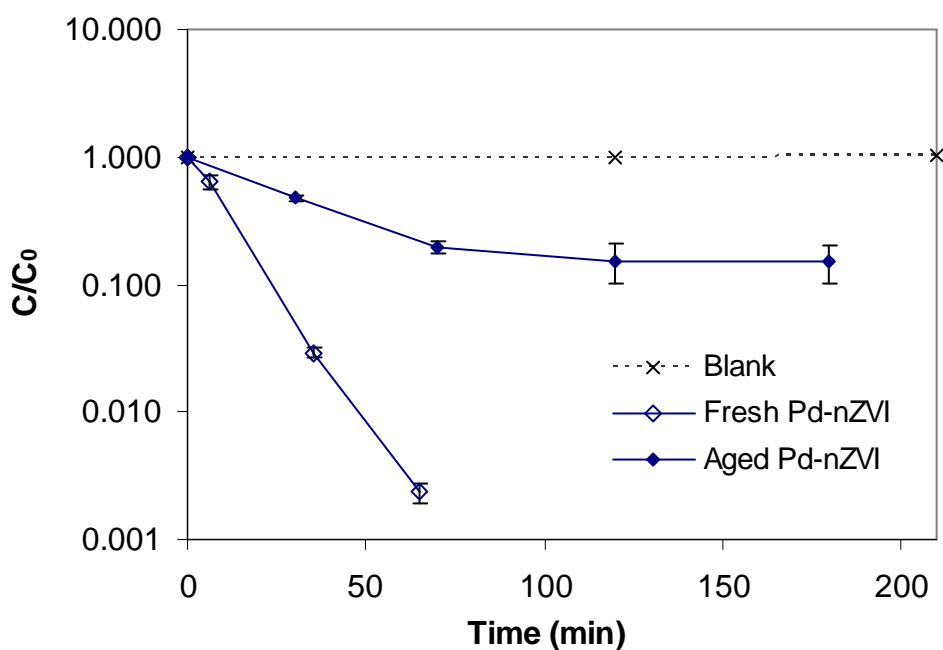
Figure 5.8 TCE removal by fresh and aged Pd-nZVI particles. Initial TCE concentration was 50 mg/L, and particle dose was 2.5 g/L. The error bars represent the results of duplicate runs.

With regards to the potential application of bimetallic nanoparticles for *in-situ* treatment of halogenated contaminants, our results imply that particle age and storage environment will play a critical role in determining the effectiveness of the remediation. For field applications of the palladized nZVI, palladium should be introduced onto the nZVI at the time of use due to the high reactivity and limited life span of Pd-nZVI. It has been noted that the presence of dissolved silica may impede iron corrosion by adsorbing to the anodic surface (Reardon *et al*., 2008). It may be the case that, in actual field applications, the life span of Pd-nZVI in a soil matrix containing silica and other corrosion inhibitors may be longer as compared to the life times in pure water studied here. On the other hand, Pd in the aged particles is embedded in the growing oxide phase and there is no dislodging of Pd metal or elution of Pd(II) ions into the aqueous phase. This attribute is highly favorable for the collection and recycling of palladium material and for addressing concerns regarding possible palladium leaching into the environment.

References

1. Alonso, F.; Beletskaya, I. P.; Yus, M., Metal-mediated reductive hydrodehalogenation of organic halides. *Chem. Rev.* **2002,** *102*, 4009-4091.

2.   Cwiertny, D. M.; Bransfield, S. J.; Livi, K. J. T.; Fairbrother, D. H.; Roberts, A. L., Exploring the influence of granular iron additives on 1,1,1-trichloroethane reduction. *Environ. Sci. Technol.* **2006,** *40*, 6837-6843.

3.   Lien, H. L.; Zhang, W. X., Nanoscale Pd/Fe bimetallic particles: Catalytic effects of palladium on hydrodechlorination. *Appl. Catal. B-Environ.* **2007,** *77*, 110-116.

4.   Lien, H. L.; Zhang, W. X., Transformation of chlorinated methanes by nanoscale iron particles. *J. Environ. Eng.-ASCE* **1999,** *125*, 1042-1047.

5.   Li, T.; Farrell, J., Reductive dechlorination of trichloroethene and carbon tetrachloride using iron and palladized-iron cathodes. *Environ. Sci. Technol.* **2000,** *34*, 173-179.

6.   Zhang, W. X.; Wang, C. B.; Lien, H. L., Treatment of chlorinated organic contaminants with nanoscale bimetallic particles. *Catal. Today* **1998,** *40*, 387-395.

7.   Xu, J.; Dozier, A.; Bhattacharyya, D., Synthesis of nanoscale bimetallic particles in polyelectrolyte membrane matrix for reductive transformation of halogenated organic compounds. *J. Nanopart. Res.* **2005,** *7*, 449-467.

8.   He, F.; Zhao, D. Y.; Liu, J. C.; Roberts, C. B., Stabilization of Fe-Pd nanoparticles with sodium carboxymethyl cellulose for enhanced transport and dechlorination of trichloroethylene in soil and groundwater. *Ind. Eng. Chem. Res.* **2007,** *46*, 29-34.

9.   Korte, N. E.; Zutman, J. L.; Schlosser, R. M.; Liang, L.; Gu, B.; Fernando, Q., Field application of palladized iron for the dechlorination of trichloroethene. *Waste Management* **2000,** *20*, 687-694.

10. Elliott, D. W.; Zhang, W. X., Field assessment of nanoscale biometallic particles for groundwater treatment. *Environ. Sci. Technol.* **2001,** *35*, 4922-4926.

11. Graham, L. J., and Jovanovic, G., Dechlorination of p-chlorophenol on a Pd/Fe catalyst in a magnetically stabilized fluidized bed; Implications for sludge and liquid remediation. *Chem. Eng. Sci.* **1999***, 54*, 3085-3093.

12. Wang, C. B.; Zhang, W. X., Synthesizing nanoscale iron particles for rapid and complete dechlorination of TCE and PCBs. *Environ. Sci. Technol.* **1997,** *31*, 2154-2156.

13. Choi, H.; Al-Abed, S. R.; Agarwal, S.; Dionysiou, D. D., Synthesis of reactive nano-Fe/Pd bimetallic system-impregnated activated carbon for the simultaneous adsorption and dechlorination of PCBs. *Chem. Mater.* **2008,** *20*, 3649-3655.

14. Zhu, B. W.; Lim, T. T., Catalytic reduction of chlorobenzenes with Pd/Fe nanoparticles: reactive sites, catalyst stability, particle aging, and regeneration. *Environ. Sci. Technol.* **2007,** *41*, 7523-7529.

15. Wong, M. S.; Alvarez, P. J. J.; Fang, Y. I.; Akcin, N.; Nutt, M. O.; Miller, J. T.; Heck, K. N., Cleaner water using bimetallic nanoparticle catalysts. *J. Chem. Technol. Biot.* **2009,** *84* (2), 158-166.

16. Kim, Y. H.; Carraway, E. R., Dechlorination of chlorinated ethenes and acetylenes by palladized iron. *Environ. Technol.* **2003,** *24*, 809-819.

17. Uhlig, H. H., Corrosion and Corrosion Control*,* 2[nd]edition, John Wiley & Sons, Inc., New York, 1971.

18. Muftikian, R.; Nebesny, K.; Fernando, Q.; Korte, N., X-ray photoelectron spectra of the palladium-iron bimetallic surface used for the rapid dechlorination of chlorinated organic environmental contaminants. *Environ. Sci. Technol.* **1996,** *30*, 3593-3596.

19. Burke, M. G.; Watanabe, M.; Williams, D. B.; Hyde, J. M., Quantitative characterization of nanoprecipitates in irradiated low-alloy steels: advances in the application of FEG-STEM quantitative microanalysis to real materials. *J. Mater. Sci.* **2006,** *41*, 4512-4522.

20. Herzing, A. A.; Watanabe, M.; Edwards, J. K.; Conte, M.; Tang, Z. R.; Hutchings, G. J.; Kiely, C. J., Energy dispersive X-ray spectroscopy of bimetallic nanoparticles in an aberration corrected scanning transmission electron microscope. *Faraday Discuss.* **2008,** *138*, 337-351.

21. Watanabe, M.; Ackland, D. W.; Burrows, A.; Kiely, C. J.; Williams, D. B.; Krivanek, O. L.; Dellby, N.; Murfitt, M. F.; Szilagyi, Z., Improvements in the X-ray analytical capabilities of a scanning transmission electron microscope by spherical-aberration correction. *Microsc. Microanal.* **2006,** *12*, 515-526.

22. Available from http://www.nist.gov/lispix/.

23. Martin, J. E.; Herzing, A. A.; Yan, W. L.; Li, X. Q.; Koel, B. E.; Kiely, C. J.; Zhang, W. X., Determination of the oxide layer thickness in core-shell zerovalent iron nanoparticles. *Langmuir* **2008,** *24*, 4329-4334.

24.   Sun, Y. P.; Li, X. Q.; Cao, J. S.; Zhang, W. X.; Wang, H. P., Characterization of zero-valent iron nanoparticles. *Adv. Colloid Interface Sci.* **2006,** *120*, 47-56.

25.   Li, X. Q.; Zhang, W. X., Sequestration of metal cations with zerovalent iron nanoparticles - A study with high resolution X-ray photoelectron spectroscopy (HR-XPS). *J. Phys. Chem. C* **2007,** *111*, 6939-6946.

26.   Carpenter, E. E.; Calvin, S.; Stroud, R. M.; Harris, V. G., Passivated iron as core-shell nanoparticles. *Chem. Mater.* **2003,** *15*, 3245-3246.

27.   Brewster, J. H., Mechanisms of reduction at metal surfaces. I. A general working hypothesis. *J. Am. Chem. Soc.* **1954**, *76*, 6361-6363.

28.   Wang, C. M.; Baer, D. R.; Thomas, L. E.; Amonette, J. E.; Antony, J.; Qiang, Y.; Duscher, G., Void formation during early stages of passivation: Initial oxidation of iron nanoparticles at room temperature. *J. Appl. Phys.* **2005,** *98*, 094308.

29.   Yin, Y. D.; Rioux, R. M.; Erdonmez, C. K.; Hughes, S.; Somorjai, G. A.; Alivisatos, A. P., Formation of hollow nanocrystals through the nanoscale Kirkendall effect. *Science* **2004,** *304*, 711-714.

30.   Bard, A. J.; Parsons, R.; Jordan, J.; Eds. Standard Potentials in Aqueous Solution; M. Dekker: New York, 1985.

31.   Nutt, M. O.; Hughes, J. B.; Wong, M. S., Designing Pd-on-Au bimetallic nanoparticle catalysts for trichloroethene hydrodechlorination. *Environ. Sci. Technol.* **2005,** *39*, 1346-1353.

32. Reardon, E. J.; Fagan, R.; Vogan, J. L.; Przepiora, A., Anaerobic corrosion reaction kinetics of nanosized iron. *Environ. Sci. Technol.* **2008,** *42*, 2420-2425.

Chapter 6

Reactions of Inorganic Pollutants with nZVI: Role of the Core-shell Structure

6.0 Abstract

Aspects of the core-shell model of nanoscale zero-valent iron (nZVI) and their environmental implications were examined in this work. The structure of the nanoparticles and the chemical nature of the oxide coating and the highly reducing Fe(0) nuclei revealed by previous microscopic and spectroscopic characterizations were summarized herein, which provides a basis for understanding the structure-reactivity relationship of nZVI material and exploring new environmental abatement applications. Three aqueous environmental contaminants, namely Hg(II), Zn(II) and hydrogen sulfide, were used to probe the reactive properties of nZVI. High-resolution X-ray photoelectron spectroscopy (HR-XPS) analysis of the reacted particles indicated that Hg(II) was sequestrated via chemical reduction to elemental mercury. On the other hand, Zn(II) removal was achieved via sorption to the iron oxide shell followed by zinc hydroxide precipitation. Hydrogen sulfide was immobilized on the nZVI surface as disulfide (S_2^{2-}) and monosulfide (S^{2-}) species. Their relative abundance in the final products suggests that the retention of hydrogen sulfide occurs via reactions with the oxide shell to form iron sulfide (FeS)

and subsequent conversion to iron disulfide (FeS_2). The results presented herein highlight the multiple reactive pathways permissible with nZVI owing to its two functional constituents. The core-shell structure imparts nZVI with manifold functional properties previously unexamined and grants the material with potentially new applications.

6.1 Introduction

Engineered nanomaterials have found increasing applications in environmental technologies, including water and wastewater treatment, air, water and soil remediation, and hazardous waste treatment, owing to their superior reactivity towards a variety of recalcitrant contaminants and their enhanced capacities for contaminant abatement (Li *et al*., 2006; Tratnyek & Johnson, 2006; Karn *et al*., 2009). Amongst this promising class of remediation agents, nanoscale zero-valent iron (nZVI) perhaps has received the most attention and has been shown to effectively degrade a wide spectrum of water contaminants, such as halogenated hydrocarbons, nitroaromatic compounds, azo dyes, perchlorate, nitrate, hexavalent chromium and various heavy metal ions (Kanel *et al*., 2005; Li & Zhang, 2006, 2007; Lowry & Johnson, 2004; Ponder *et al*., 2000; Ponder *et al*. 2001; Tee *et al*., 2005).

Microscopic and spectroscopic studies have suggested that nZVI in the aqueous environment consists mainly of zero-valent iron and a surface layer of iron oxide

(Martin *et al*., 2008; Nurmi et al., 2005; Sun *et al*., 2006). The oxide layer is thought to comprise of mixed Fe(II)/Fe(III) oxides near the interface with Fe^0 and mostly Fe(III) oxide near the oxide/water interface (Signorini *et al*., 2003; Wang *et al*., 2009). This core-shell structure has important implications for the chemical properties of nZVI. The defective and disordered nature of the oxide shell renders it potentially more reactive than a simple passive oxide layer formed on bulk iron materials (Wang *et al*., 2009). The relative composition of the oxide and the metal in nZVI is also markedly different from that of bulk ZVI. These considerations make the core-shell structure a highly important aspect to consider when studying the activity of nZVI for various remediation processes. The presence of two nano-constituents in the core-shell structure may impart combinational properties for contaminant removal: the metallic iron acts as the electron source and exerts a reducing character, while the oxide shell facilitates sorption of contaminants via electrostatic interactions and surface complexation, and at the same time, permits electron passage from the metal core. Figure 6.1 proposes conceptually a structural model of nZVI and its reactions with several contaminants that are examined in this work.

So far, the majority of published work have focused on the reductive properties of nZVI, *e.g.*, reductive dehalogenation of organic compounds and reductive precipitation of hexavalent chromium (Lowry & Johnson, 2004; Ponder *et al*., 2001), There is no study that has examined the specific functions of the metal-core and the oxide-shell in different remediation systems. More information on the core-shell structure and the

surface chemistry of nZVI materials can accelerate the development of new applications, especially in the dealing of inorganic contaminants, whose treatment typically involves surface-mediated complexation and/or redox transformations (Stumm, 1992). Another aspect which has received less attention in the literature is the inevitable reaction of nZVI with water and its effect on the solution and surface chemistry. This is of particular relevance to the treatment of ionic species including heavy metal ions, because their speciation and reactivity are profoundly dependent on the solution as well as the surface pH.
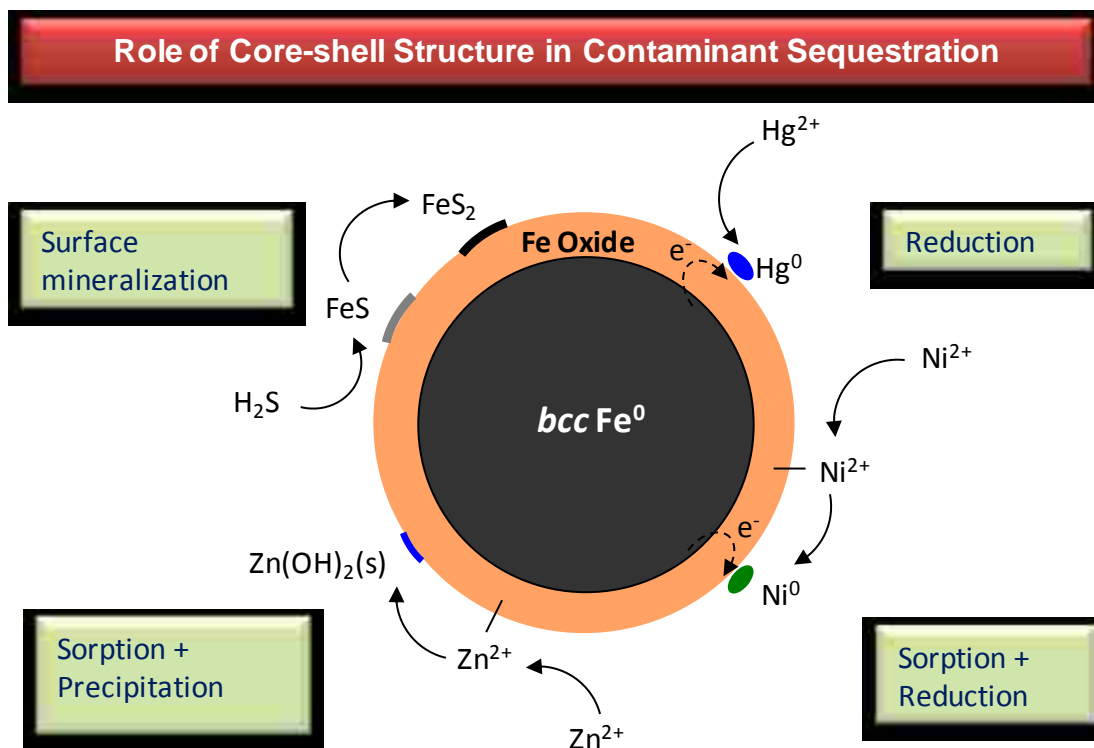
Figure 6.1 The core-shell model of nZVI and schematic representations of the reaction mechanisms for the removal of Hg(II), Ni(II), Zn(II) and H_2S investigated in this study.

The objective of this work is to demonstrate the multi-faceted reactivity of nZVI towards different contaminants on the basis of its nanostructure. The study proceeds with a discussion about the nature of the core-shell structure confirmed by the recently available microscopic and spectroscopic evidence and the pertinent properties of the oxide shell and the metallic core components. Experimental studies involving three common aqueous contaminants, *viz.,* Hg(II), Zn(II), and hydrogen sulfide (H$_2$S), are then presented. These contaminants are markedly different from one another in terms of electrochemical or coordinative properties and are used as probe molecules to emphasize various reactive pathways permissible with nZVI treatment. For each contaminant studied, aspects related to reaction kinetics, sequestration efficiency, and the proposed reaction mechanism(s) based on spectroscopic and solution phase evidence are discussed. The distinct reaction pathways and the remarkable reactivity and capacity demonstrated by nZVI in these systems underline the notion that nZVI has manifold functions in addition to reductive-transformations, and has potential applications in treating a diverse group of environmental contaminants.

6.2 Materials and methods

Synthesis of iron nanoparticles. nZVI was prepared following procedures reported previously (Chapter 3). Our previous characterization work (Sun *et al*., 2006) showed that the median diameter of single nanoparticles was approximately 60 nm, although in

the absence of stabilizers, individual nanoparticles readily form chain-like aggregates of several hundreds of nanometers in size due to magnetic interactions. The tendency to form larger aggregates permit facile separation of the nanoparticles from aqueous solutions via conventional filtration method. The Brunauer-Emmett-Teller (BET) surface area was found to be 29 m^2/g (Chapter 4).

X-ray Photoelectron Spectroscopy. The surface chemistry of nZVI samples before and after reaction was analyzed with a Scienta ESCA-300 high-resolution X-ray photoelectron spectrometer (HR-XPS). Detailed procedures of XPS analysis are available in Chapter 3.

Batch experiments. In all experiments, deoxygenated water was used, which was prepared by purging the deionized (DI) water with nitrogen (>99.8% purity) for 30 minutes prior to use. Hg(II) and Zn(II) solutions were prepared from mercury acetate ($Hg(CH_3COO)_2$, Fisher) and zinc chloride ($ZnCl_2$, Fisher), respectively. Hydrogen sulfide water (a saturated solution prepared from > 99.5% purity H_2S) was obtained from Ricca Chemical. All chemicals used were of ACS reagent grade. A typical batch experiment entails adding a pre-determined amount of nZVI into a solution containing one of the above species and allowing the mixture to undergo mechanical agitation at 250 rpm and 25^0C. Mercury and zinc removal experiments were performed in 200-mL serum bottles sealed with PTFE-lined caps and a small volume of solution sample was taken at selected time intervals. Hydrogen sulfide experiments were carried out in 100-mL serum bottles capped with a Teflon Mininert valve and sampling was performed

periodically by withdrawing 20 μl of headspace gas using a gas-tight syringe for GC analysis. For comparative purposes, a commercial grade micro-scale iron powder (from BASF, mean agglomerate diameter 4.1 μm) was studied in some experiments. Dilute acid treatment of the BASF iron powder refers to soaking the iron particles in 0.1 N HCl for 10 min followed by rinsing with DI water just prior to performing the respective experiments.

Analytical Methods. All solution samples were filtered with 0.2-μm PTFE syringe filters before analysis. Solution samples with mercury concentration > 1 mg/L were analyzed using inductively coupled plasma-optical emission spectrometry (ICP-OES, Perkin-Elmer Optimal 2100DV). Samples with mercury below 1 mg/L were analyzed by cold vapor atomic absorption using an atomic absorption (AA) spectrometer equipped with a flow injection system (Perkin-Elmer AAnalyst 200-FIAS 100), which offers a detection limit of 0.1 μg/L. Zinc concentrations in the aqueous solutions were determined using an atomic absorption spectrometer (Perkin-Elmer AAnalyst200, detection limit 0.1 mg/L). Concentrations of hydrogen sulfide in the headspace were analyzed with a Shimadzu Model 17A Gas Chromatograph (GC) equipped with a flame ionization detector (FID) and a SPB^{TM}-1 sulfur capillary column (Supelco).

6.3 Results and discussion

6.3.1 The core-structure of nZVI revisited

Chapter 4 presents a detailed characterization of microstructure of nZVI. Bright-field transmission electron microscope (TEM) images of freshly synthesized nZV reveal that the electron-dense metallic iron nuclei aggregate into chain-like structures, which is enclosed by a continuous, smooth oxide outer-layer varying in thickness from 2-20 nm. Using high-resolution X-ray photoelectron spectroscopy (HR-XPS) analysis of the metallic and oxidized iron signals, we estimated an average oxide thickness to be ~ 2-3 nm (Martin *et al*., 2008). Thickness estimation obtained by chemical reduction method yields results in good agreement with the HR-XPS method. Close-examination of the oxide layer with phase-contrast TEM shows the oxide shell does not contain orderly structure and appears to be amorphous in character (Chapter 4). Similar findings are noted via X-ray diffraction pattern as no distinct patterns corresponding to crystalline forms of iron oxides (e.g. lepidocrocite γ-FeOOH, goethite α-FeOOH, or magnetite Fe_3O_4) were observed. The disordered structure may result from a large curvature caused by the small radii of the particles, imposing difficulty in lattice alignment. Additionally, detailed XPS analysis of the oxide surface indicates there is a significant level of impurities such as boron from synthesis precursor (sodium borohydride) in the oxide layer, which may contribute to its glassy, amorphous nature (Figure 4.3a).

The chemical composition of the oxide layer has been analyzed in previous studies. It is reported that the oxide layer consists of a mixed Fe(II)/Fe(III) phase in proximity to the metallic core and a predominantly Fe(III) oxide phase at the surface of the nanoparticles (Signorini *et al*., 2003; Wang *et al*., 2009). The detailed arrangement of the oxide

structure depends on the synthesis process, particle size, and storage conditions (Wang *et al*., 2009; Wang *et al*. 2010). XPS analysis of our freshly made nZVI particles reveals that the surface of the oxide is attached with a layer of hydroxide groups (OH⁻) (Figure 6.2), which is consistent with the origin of the particles from aqueous-based synthesis process (Baer *et al*., 2010). By analyzing O1s (Figure 6.2) and Fe2p XPS spectra, an apparent stoichiometry close to FeOOH is proposed (Li & Zhang, 2006). We wish to emphasize that this is just an apparent formula based on the XPS measurement and it does not suggests resemblance in structure to the commonly known iron oxy-hydroxides (e.g. lepidocrocite γ-FeOOH, goethite α-FeOOH).
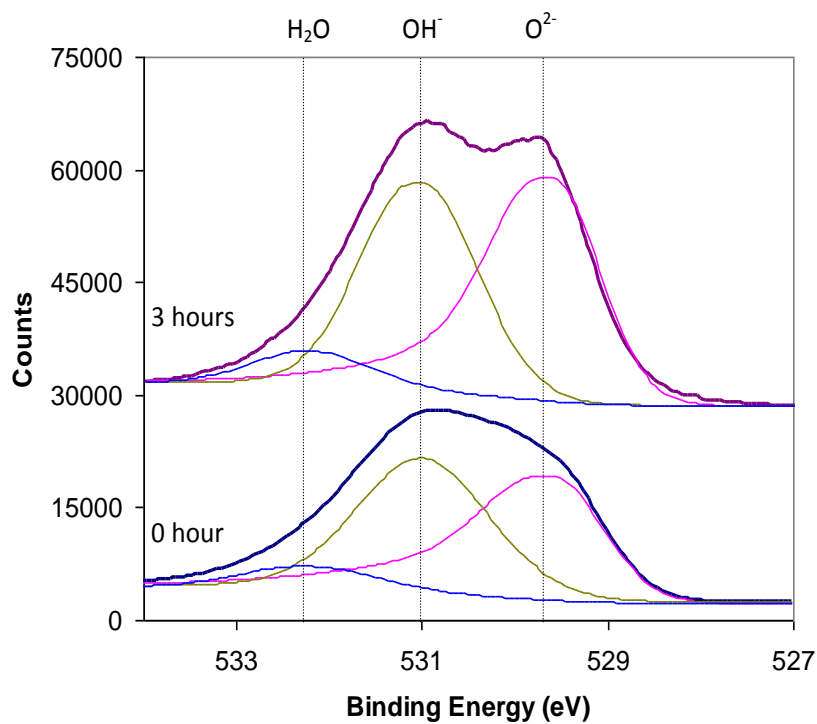
Figure 6.2 XPS spectra at O1s region of freshly made nZVI and those exposed to water for 3 hours.

The surface ≡Fe-OH groups may function as reactive sites to bind with contaminants in the solution, in a mode similar to surface adsorption on iron (oxyhydro)oxide. At the same time, the oxide layer is known to possess semiconductor properties (Balko and Tratnyek, 1998; Wang *et al*., 2009), where charge transfer is a relatively facile process owing to its exceedingly small thickness and the presence of defective sites, allowing rapid reduction of contaminants to occur. This implies that nZVI may exhibit the combined reactivity of iron oxides and the metallic iron. Since the actual processes at work likely vary with the contaminants of interest and the reaction conditions, three specific cases are discussed in the following sections to demonstrate the possible roles played by the core-shell structure in different remediation systems.

6.3.2 Reduction property of nZVI - Removal of Hg(II)

Mercury is among the most notorious metal contaminants released from many industrial activities including mining and coal burning. In water, mercury exists predominantly as Hg(II). Sequestration of Hg(II) in aqueous solution was investigated here at different iron doses. To attain sufficient (> 0.1 at.%) mercury on nZVI surface for unambiguous XPS characterization, an initial Hg(II) concentration of 40 mg/L was used in the experiments. As shown in Figure 6.3a, the addition of 2 g/L nZVI particles resulted in a removal of 98% of the Hg(II) initially present in the aqueous phase in 2 minutes. At a

lower nZVI loading (0.5 g/L), the sequestration kinetics is still considerably rapid with greater than 97% Hg(II) removal in 10 minutes.

The reacted nZVI particles were collected for XPS analysis to determine the chemical state of mercury on the nZVI surface. As shown in Figure 6.3b, Hg $4f_{7/2}$ XPS spectrum has a single peak at ca. 99.7 eV, which matches with the binding energy of Hg(0) (Behra et al., 2001; Ehrhardt et al., 2000). There was no peak occurring between 100.6-100.7 eV that would otherwise have implied the presence of Hg(I) or Hg(II) on the surface, hence we conclude that the immobilized mercury was completely reduced to elemental mercury.

Reduction of Hg(II) by Fe(0) is energetically favorable given the large difference between the standard redox potential of iron (E^0_h = -0.44 V) and mercury (E^0_h = +0.86 V) (Eq. 6.1) (Bard et al., 1985). With excess Hg(II), ferrous ions can be further oxidized to ferric ions via reaction in Eq. 6.2 (O'Loughlin et al., 2003).

$$Hg^{2+} (aq.) + Fe^0 (s) \rightarrow Hg^0 (l) + Fe^{2+} (aq.) \qquad \Delta E^0 = 1.30V \qquad (6.1)$$

$$Hg^{2+} (aq.) + 2Fe^{2+} (aq.) \rightarrow Hg^0 (l) + 2Fe^{3+} (aq.) \quad \Delta E^0 = 0.09V \qquad (6.2)$$
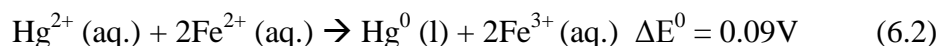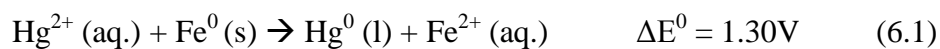
Although XPS reveals only the presence of elemental mercury on the surface of nZVI, we cannot exclude sorption of Hg(II) to nZVI prior to its reduction since the oxide layer on nZVI has high affinity for heavy metal ions. For example, we proposed in a prior study that sorption of Ni(II) onto nZVI is a proceeding step of surface reduction based

on the observed surface speciation of Ni(II) at different reaction times (Li & Zhang, 2006).

The reactivity of nZVI was compared to a commercial grade micro-scale iron powder (denoted as 'mZVI' with a mean diameter of 4.1 μm). As shown in Figure 6.3a, no appreciable Hg(II) uptake was observed during the first 1 hour sampling period for the mZVI while nearly all Hg(II) ions were sequestrated by nZVI at the same mass loading (0.5 g/L). It is suspected that the reactivity of mZVI was hindered by the presence of a surface passivation layer of iron oxide. Pre-treatment of mZVI in dilute HCl was conducted to remove the surface passivation layer. However, the reactivity of the pre-treated mZVI was still considerably lower than that of nZVI, and approximately 77% of the Hg(II) originally present in the solution remained after the reaction. The results demonstrate that the large surface area possessed by nZVI imparts significant advantages in reaction rate and sequestration efficiency compared to the bulk-scale iron materials. Similar findings have been reported for the remediation of hexavalent chromium and Ni(II) with ZVI materials (Li & Zhang, 2006; Shokes & Moller, 1999).

(a)

(b)
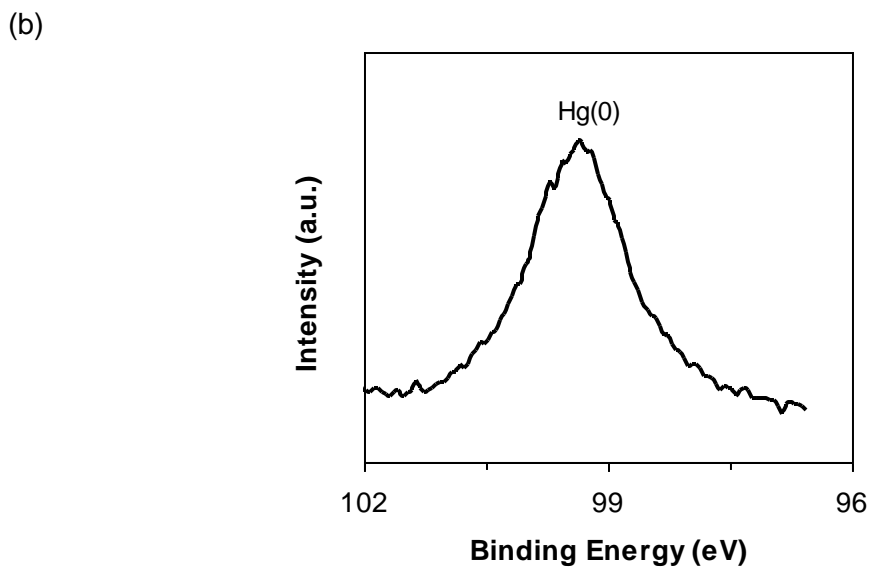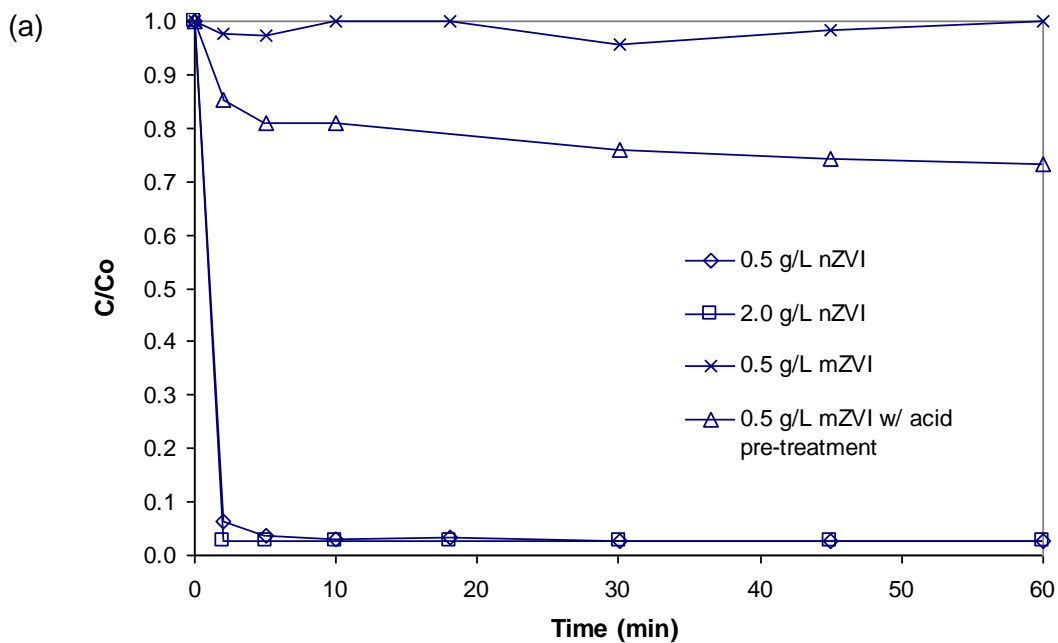
Figure 6.3 (a) Hg(II) removal from solutions containing various doses of nZVI (Hg(II) initial concentration was 40 mg/L; mZVI refers to microscale zero-valent iron; solution pH of nZVI systems varied from 5.9 to 6.9). (b) Hg4f$_{7/2}$ XPS spectrum of nZVI particles reacted with Hg(II) for 1 hour.

To fully assess the potential of nZVI for mercury abatement, the stability of the reaction products needs to be considered as elemental mercury tends to revert back to its ionic state via biological or chemical processes (Lalonde *et al*., 2004; Siciliano *et al*., 2002). By doping fresh nZVI with a small amount of noble metal, such as Cu, Ag or Pd, which are known to form stable amalgam with mercury (Huttenloch *et al*., 2003), the elemental mercury can be securely retained in the solid phase. Figure 6.4 compares the Hg(II) sequestration performance of nZVI and two bimetallic nanoparticles (nZVI-Ag and nZVI-Pd). The second metal (Ag or Pd) was impregnated on nZVI surface at a mass fraction of 1%. It is evident in Figure 6.4 that the presence of a small amount of silver or palladium on nZVI improves remarkably the mercury retention efficiency. The residue mercury concentrations in the solution were below 5 µg/L, whereas treatment with pure nZVI can only achieve a final mercury concentration of approximately 50 µg/L. Further studies to systematically evaluate the performance of bimetallic nZVI for mercury abatement applications are underway.
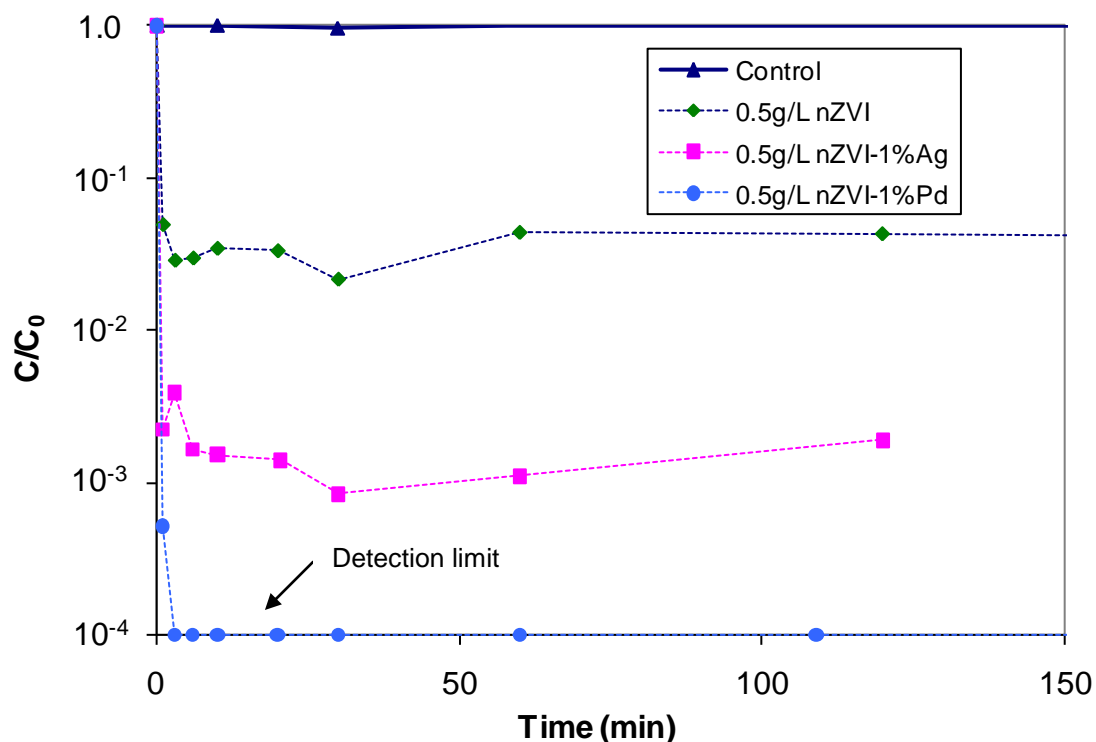
Figure 6.4 Removal of Hg(II) by nZVI and bimetallic nZVI (nZVI-1%Ag or nZVI-1%Pd). Initial Hg(II) concentration was 1000 µg/L. nZVI or bimetallic nZVI dose was 0.5 g/L. Initial pH was 5. Final pH varied from 5 to 6.4. Mass fraction of the second metal (Ag or Pd) was 1% of the mass of nZVI.

6.3.3 Sorption and precipitation - Removal of Zn(II)

The removal of Zn(II) ions from aqueous solutions with nZVI is shown in Figure 6.5a. The batch reactors were loaded with 2 g/L of nZVI with initial Zn(II) concentrations varied between 100 and 800 mg/L. Despite this large variation in initial concentrations, the final concentrations of Zn(II) after 168 hr were less than 1 mg/L in all experiments except at 800 mg/L, in which case the final concentration was 15 mg/L. The maximum

170

Zn(II) removal capacity, obtained at a initial concentration of 800 mg/L, was 393 mg-Zn/g-nZVI. The value is more than one order of magnitude higher than the theoretical uptake capacity afforded by surface adsorption, considering that nZVI has a BET surface area of 30 m^2/g (Sun *et al*., 2006) and the surface co-ordination site density of the oxide shell is 2-3 sites/nm^2 (Smith, 1996). The discrepancy implies that additional mechanisms other than adsorption are responsible for the highly effective Zn(II) removal.

Figure 6.5b shows the XPS spectrum of the reacted particles. The Zn $2p_{3/2}$ spectrum exhibits a single peak at 1022 eV, consistent with the binding energy reported for Zn(II) oxide (Herbert, 2003). Additional auger electron analysis confirms that zinc is bound in its oxide state, thus no reduction was involved in the sequestration process, as would be expected from the more negative standard redox potential of zinc (E^0_{Zn} = -0.76 V) compared to iron (E^0_{Fe} = -0.44 V) (Bard *et al*., 1985). Solution chemistry measurement recorded that the removal of Zn(II) ions was accompanied by a concurrent pH increase as revealed in Figure 6.5a. In all experiments, the solutions registered steep pH increases in the first few hours. In the subsequent period of 4 days, pH continued to rise, albeit at much slower rates, gradually approaching a common plateau with a final pH in the vicinity of 8. These pH trends are attributed to spontaneous reaction between nZVI and water, which, owing to the relatively high concentration (~56 M) of water molecules, predominates other reactions in the solution and controls the pH of the solution. In anaerobic conditions, this reaction is described as (Reardon, 1995):

$$Fe^0(s) + 2H_2O \rightarrow Fe^{2+} + H_2 \text{ (g)}+ 2OH^- \text{ (aq.)} \tag{6.3}$$
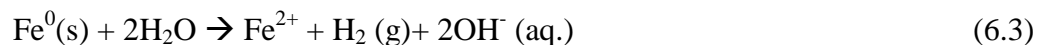
Fresh nZVI tends to experience a rapid oxidation phase upon entering into the aqueous phase (Reardon, 1995), thus contributing to the initial pH surge. As hydroxyl ions accumulate on the particles, a passivating oxyhydroxide coating is formed, slowing down further oxidation (and pH increase) until a meta-stable equilibrium is established between the oxide and the solution.

Zn(II) adsorption is known to be strongly influenced by solution pH. Multi-layer sorption of Zn(II) could lead to surface precipitation, and at elevated pH, bulk precipitation of zinc hydroxide may take place (Farley *et al*., 1985). Figure 6.5c overlays the solution pH and aqueous zinc concentrations recorded at different stages of the experiments onto the theoretical zinc predominance diagram. Carbonate species are not shown because they are deemed to be effectively stripped out of the system due to the pre-purging step. The dashed line in Figure 6.5c represents the theoretical boundary between soluble Zn(II) species and zinc hydroxide solid phase. The figure shows that, at the early stage of the reaction (< 5 hour), zinc predominately exists as aqueous Zn(II) species. Zn(II) uptake in this early stage was likely brought about by non-specific sorption or surface complexation with the iron oxide shell. With the changes in pH due to nZVI-water reaction in Eq. 6.3, the solution conditions shifted towards the phase boundary. After 5 hours, the solutions were observed to cluster around the contour line of the phase boundary, indicating zinc removal at this stage was governed by the precipitation of zinc hydroxide. Taken together, the remarkable capacity of nZVI for Zn

removal is a result of a combination of sorption and precipitation. Although the actual contributions of sorption and precipitation may vary with the initial Zn(II) concentration, nZVI dosage and solution conditions, this study demonstrates that for cationic species amenable to adsorption and/or precipitation (e.g. Zn(II)), nZVI corrosion in water will foster an alkaline condition that fortuitously promotes both processes.

(a)

(b)

(c)
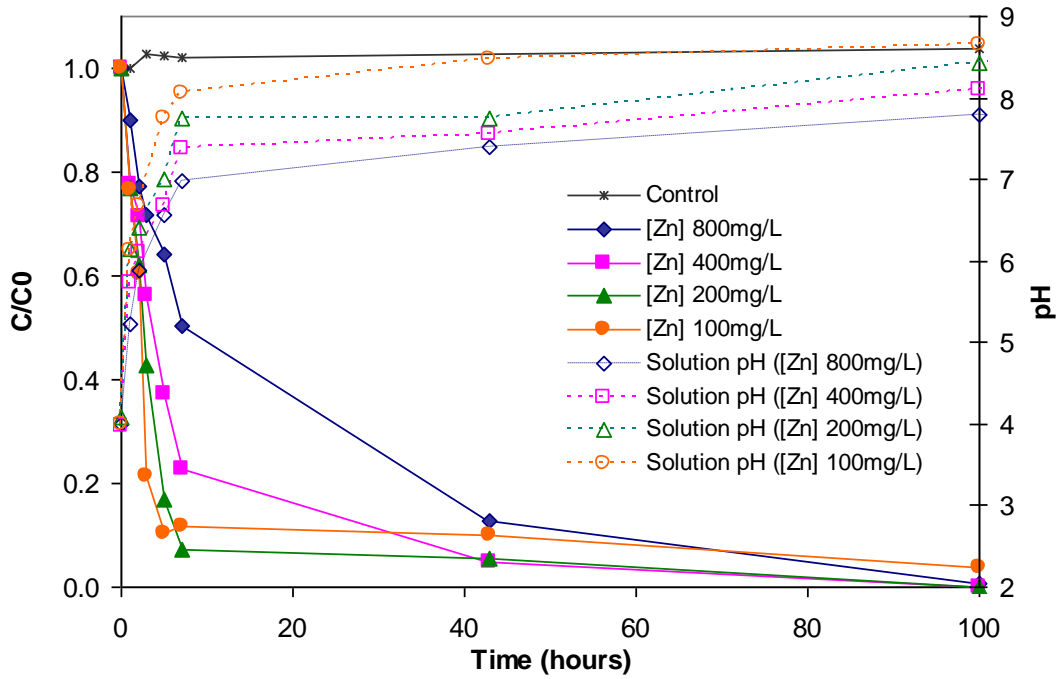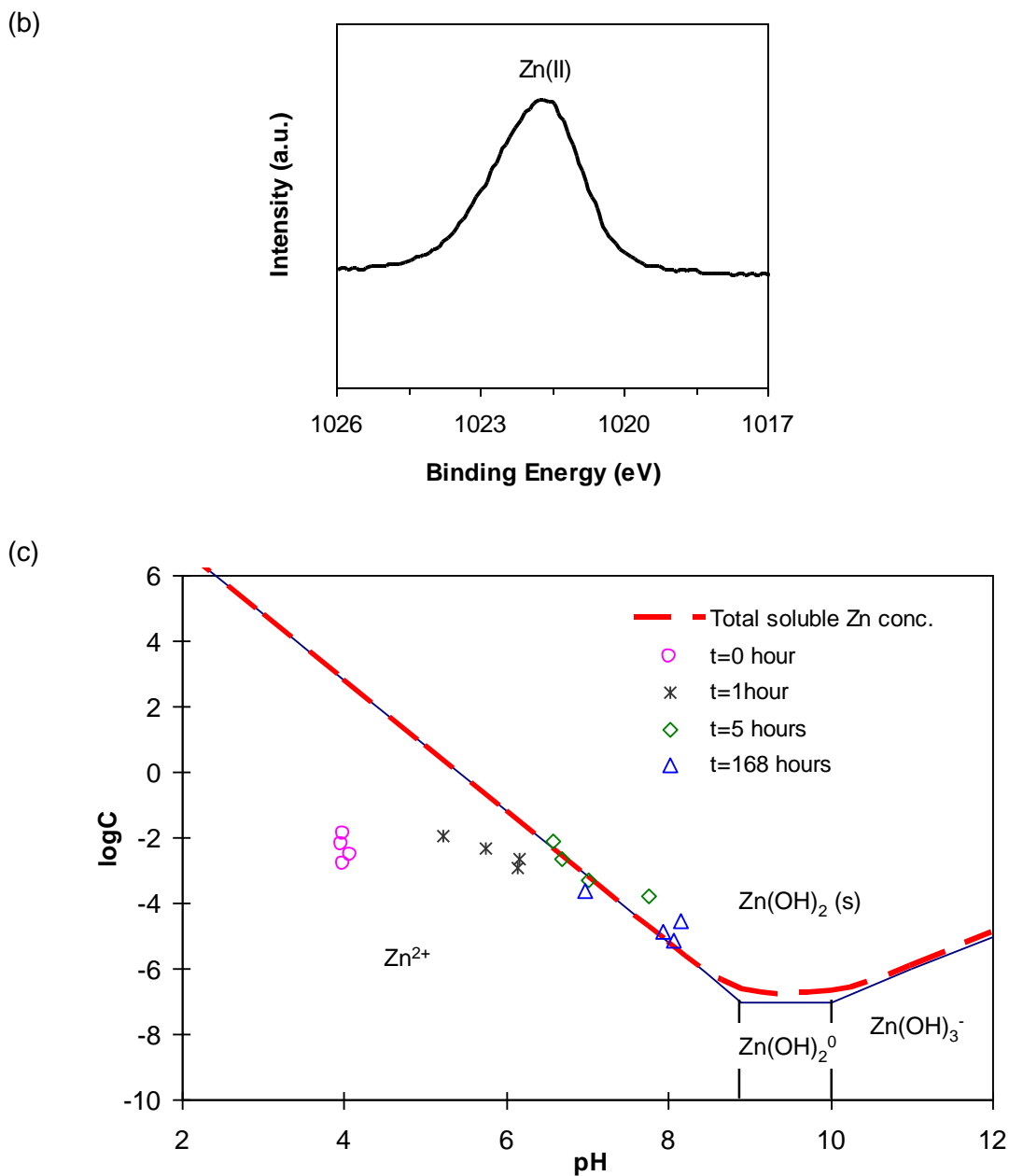
Figure 6.5 (a) Zn(II) removal from solutions at various initial concentrations (nZVI loading was 2g/L) and the corresponding changes in solution pH. (b) Zn2p XPS spectrum of nZVI reacted with Zn(II) for 3 hours. (c) Overlay of aqueous Zn(II) concentrations and solution pH recorded at different reaction times on a theoretical Zn(II) predominance diagram.

6.3.4 Sorption and surface mineralization - Sequestration of H₂S

Hydrogen sulfide (H_2S) is a major sulfur-containing compound contributing to nuisance odors in wastewater and municipal solid wastes (Li *et al*., 2007). H_2S sequestration with nZVI is studied here to exploit the strong iron-sulfur interactions (Figure 6.6). Figure 6.6a illustrates the concentrations of hydrogen sulfide in the head space of the reaction vials upon the addition of nZVI particles. Control experiment showed less than 10% loss of hydrogen sulfide over the entire sampling period. Doping nZVI into the solutions resulted in rapid uptake of hydrogen sulfide. For all doses of nZVI studied (varying from 0.5 to 5 g/L), effectively all hydrogen sulfide (>99%) was removed within 15 minutes.

A high-resolution XPS spectrum in the S2p region of the reacted nZVI particles is shown in Figure 6.6b. The spectrum was curve-fitted using the same full-width-half-maximum (FWHM) for $2p_{3/2}$ and $2p_{1/2}$ doublets and setting $2p_{1/2}$ peak area to be half that of $2p_{3/2}$ peak with a fixed spin-orbit splitting of 1.2 eV (Cantrell *et al*., 2003; Mullet *et al*., 2002). The first doublet with $2p_{3/2}$ component at 160.7 eV is attributed to monosulfide (S^{2-}). The doublet with $2p_{3/2}$ component at 161.5 eV corresponds to disulfide (S_2^{2-}). The peak assignments are based on the binding energies reported in the literature for FeS and FeS_2 (Boursiquot *et al*., 2002; Mullet *et al*., 2002). The low-rise tail at higher binding energies is thought to arise from a polysulfide (S_n^{2-}) or elemental sulfur (S_n^0) component, however its contribution is markedly smaller in comparison to the S^{2-} and S_2^{2-} components.

(a)
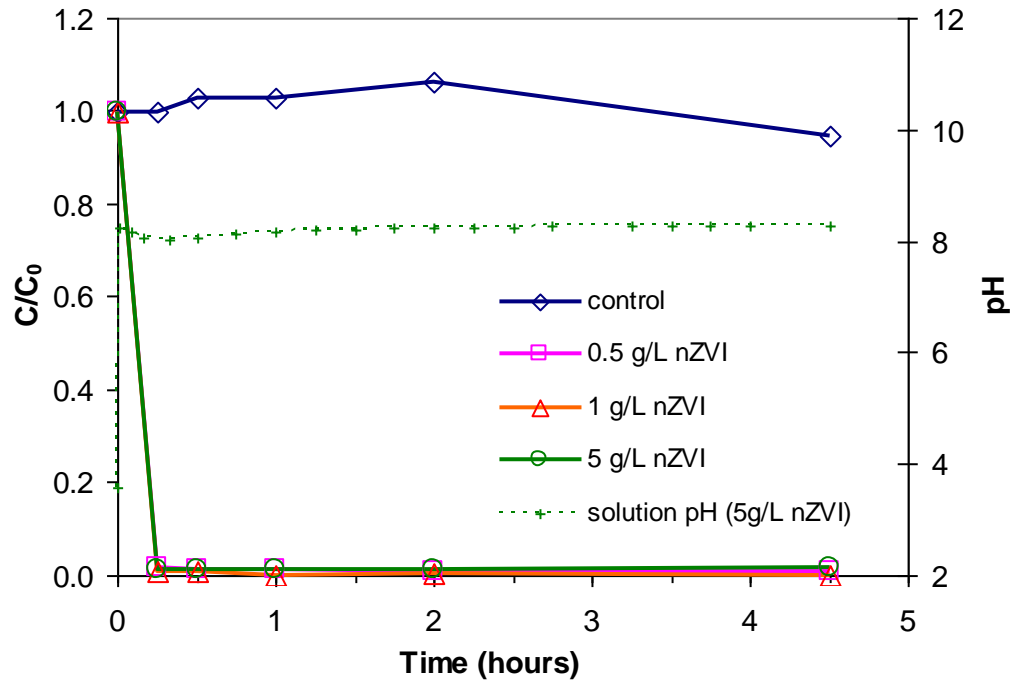
(b)
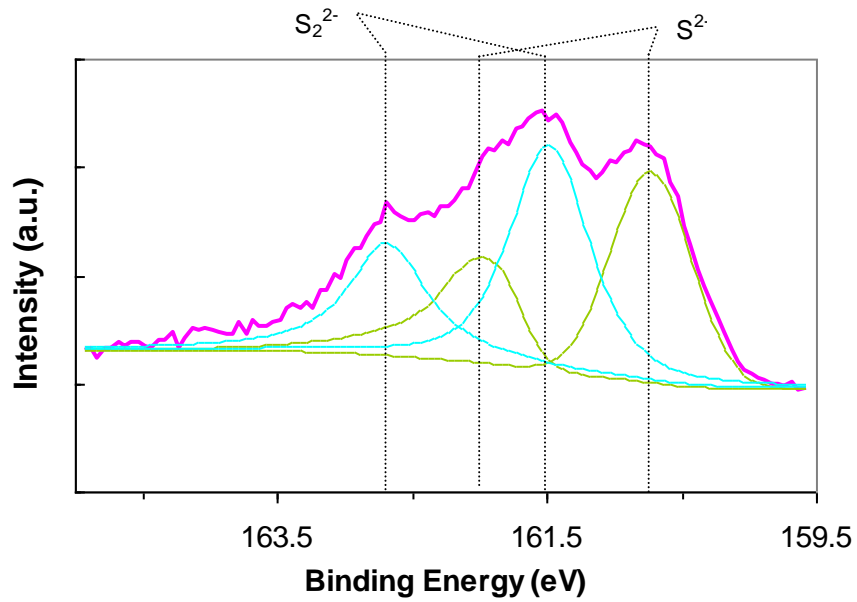
(c)
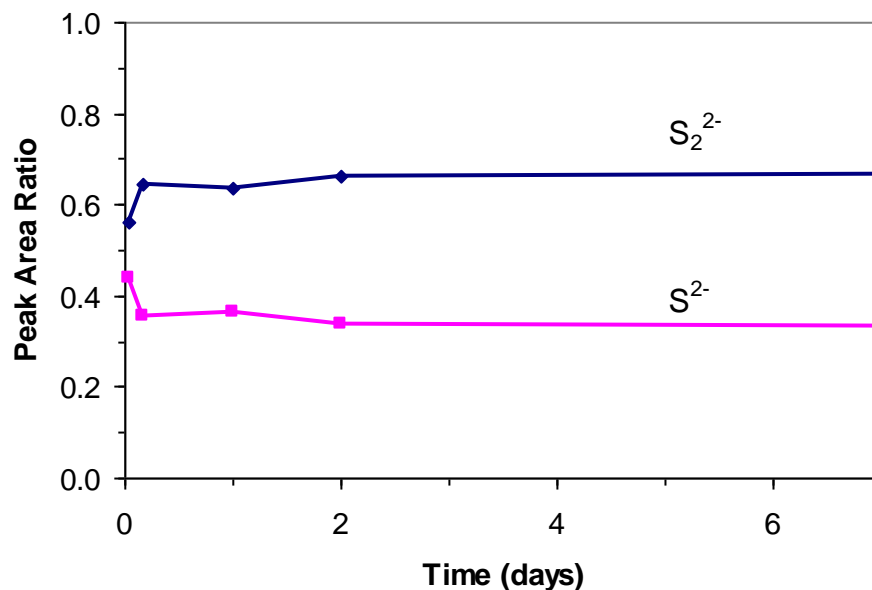
Figure 6.6 (a) H_2S concentrations in the headspace of solutions containing various doses of nZVI ($C_{H2S, initial}$= 1000 mg/L). (b) S2p XPS spectrum of nZVI reacted with hydrogen sulfide for 1 hour. (c) XPS peak area ratios of S^{2-} and S_2^{2-} to total sulfur content.

The same cure-fitting procedure was applied to other S 2p spectra taken at different reaction times. Figure 6.6c shows the relative distribution of the two major sulfur species at various reaction times. At 1 hour, 44% of total sulfur was in the form of S^{2-}. After 4 hours, there was a slight decrease in S^{2-} abundance to 36% accompanied by a corresponding increase in S_2^{2-} fraction, indicating S^{2-} is being converted to S_2^{2-}. The relative abundances of the two species only varied very slightly after this point.

FeS may be produced when hydrogen sulfide reacts directly with the zerovalent iron (Wieckowska, 1995):

$$Fe^0 + H_2S \rightarrow FeS + H_2(g) \tag{6.4}$$
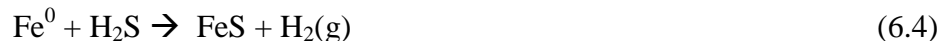
H_2S can also react with the oxyhydroxide shell of the nanoparticles (FeOOH) via Eq. 6.5 (Cantrell *et al.*, 2003):

$$2FeOOH + 3H_2S \rightarrow 2FeS + 1/8S_8 + 4H_2O \tag{6.5}$$
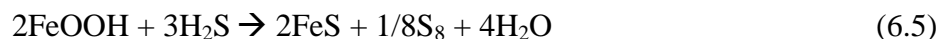
It should be noted that, during the course of the H_2S sequestration experiments, the pH rose rapidly after nZVI introduction and was stable thereafter at pH 8 (Figure 6.6a). Under this condition, H_2S exists primarily in the deprotonated form (HS^-). The isoelectric point of nZVI in aqueous solution is reported to be similar to iron oxide (*c.a.* pH 8.3) (Sun *et al.*, 2006). Hence, in the reaction medium it is electrostatically favorable for HS^- to attach to the iron particles, where it undergoes further reactions. The FeS formed is metastable and it is readily oxidized by the elemental sulfur to form iron disulfide (FeS_2) (Lennie *et al.*, 1997; Luther, 1991; Mullet *et al.*, 2002):

$$FeS + 1/8S_8 \rightarrow FeS_2 \tag{6.6}$$

The net reaction of Eq. 6.5 and 6.6 is therefore:

$$2FeOOH + 3H_2S \rightarrow FeS + FeS_2 + 4H_2O \tag{6.7}$$

It has been suggested that FeS_2 may also be produced from reaction between FeS and H_2S, where H_2S in its protonated form acts as an electrophile (Rickard and Luther, 2007). This particular pathway was unlikely to play a significant role in the present case due to the prevalent existence of hydrogen sulfide as HS^- and the rapid depletion of H_2S upon the addition of nZVI. The relative contributions of the two reactive pathways, *i.e.* Eq. 6.4 & 6.7, can be inferred from the measured product distribution. Eq. 6.7 suggests an atomic ratio of monosufide to disulfide of 1:2. The actual abundance of the two species, estimated after 2 days as indicated in Figure 6.6c, is approximately 1:1.9. The close match between these two ratios implies that H_2S sequestration took place predominately via reactions with the oxide shell (i.e., via Eq. 6.5-6.7). In comparison, the pathway involving metallic iron (via Eq. 6.4) only contributed a minor part to sulfide mineralization. However the indirect role of metallic iron should not be overlooked in the overall process, since iron corrosion creates a strongly reducing environment with mild alkalinity, conditions that stabilize the sulfide species in the solution phase and potentially promote sulfide binding to the nZVI surface.

6.4 Conclusion

Previous microscopic characterizations and XPS analyses provide unequivocal evidence of a core-shell structure for the nZVI material, where a Fe(0) core is encapsulated by a thin layer of amorphous iron oxide. This particular structure and the nature of the oxide layer allow the particle to possess the reductive character of metallic iron and the

sorptive and coordinative properties of iron oxide. Solution experiments involving Hg(II), Zn(II) and hydrogen sulfide and subsequent surface product analysis with HR-XPS reveal that nZVI is capable of enacting distinctive reactive pathways for specific contaminants, and typically more than one mechanism is involved in the respective sequestration processes. The mechanisms observed in the present work and from our previous study on Ni(II) removal (Li & Zhang, 2006) are thus consistent with the core-shell model illustrated in Figure 6.1. The multiple functionality imparted by the core-shell structure of nZVI has not been examined in the prior studies, which focused chiefly on the reductant role of nZVI in degrading halogenated organic compounds and inorganic contaminants. The results presented here imply that nZVI is potentially applicable to a broader spectrum of contaminants amenable to reduction, surface sorption, precipitation, or indeed combinations of the above. It is worth noting that the core-shell structure is an important feature of nZVI owing to the reactive, nanometer-scale oxide layer and its significant proportion relative to the metal component. The reactivity of nZVI observed here may not manifest in bulk-sized ZVI materials due to a much smaller surface-to-volume ratio and the more passivating nature of its oxide layer.

References

1. Baer, D. R.; Gaspar, D. J.; Nachimuthu, P.; Techane, S. D.; Castner, D. G., Application of surface chemical analysis tools for characterization of

nanoparticles. *Anal. Bioanal. Chem.* **2010,** *396* (3), 983-1002.

2.   Balko, B. A.; Tratnyek, P. G., Photoeffects on the reduction of carbon tetrachloride by zero-valent iron. *J. Phys. Chem. B* **1998,** *102* (8), 1459-1465.

3.   Behra, P.; Bonnissel-Gissinger, P.; Alnot, M.; Revel, R.; Ehrhardt, J. J., XPS and XAS study of the sorption of Hg(II) onto pyrite. *Langmuir* **2001,** *17* (13), 3970-3979.

4.   Boursiquot, S.; Mullet, M.; Ehrhardt, J. J., XPS study of the reaction of chromium (VI) with mackinawite (FeS). *Surf. Interface Anal.* **2002,** *34* (1), 293-297.

5.   Cantrell, K. J.; Yabusaki, S. B.; Engelhard, M. H.; Mitroshkov, A. V.; Thornton, E. C., Oxidation of H2S by iron oxides in unsaturated conditions. *Environ. Sci. Technol.* **2003,** *37* (10), 2192-2199.

6.   Cao, J. S.; Elliott, D.; Zhang, W. X., Perchlorate reduction by nanoscale iron particles. *J. Nanopart. Res.* **2005,** *7* (4-5), 499-506.

7.   Carpenter, E. E.; Calvin, S.; Stroud, R. M.; Harris, V. G., Passivated iron as core-shell nanoparticles. *Chem. Mater.* **2003,** *15* (17), 3245-3246.

8.   Ehrhardt, J. J.; Behra, P.; Bonnissel-Gissinger, P.; Alnot, M., XPS study of the sorption of Hg(II) onto pyrite FeS$_2$. *Surf. Interface Anal.* **2000,** *30* (1), 269-272.

9.   Farley, K. J.; Dzombak, D. A.; Morel, F. M. M., A surface precipitation model for the sorption of cations on metal oxides. *J. Colloid Interface Sci.* **1985,** *106* (1), 226-242.

10.   Herbert, R. B., Zinc immobilization by zerovalent Fe: surface chemistry and

mineralogy of reaction products. *Mineralogical Magazine* **2003,** *67* (6), 1285-1298.

11. Herzing, A. A.; Watanabe, M.; Edwards, J. K.; Conte, M.; Tang, Z. R.; Hutchings, G. J.; Kiely, C. J., Energy dispersive X-ray spectroscopy of bimetallic nanoparticles in an aberration corrected scanning transmission electron microscope. *Faraday Discuss.* **2008,** *138*, 337-351.

12. Kanel, S. R.; Manning, B.; Charlet, L.; Choi, H., Removal of arsenic(III) from groundwater by nanoscale zero-valent iron. *Environ. Sci. Technol.* **2005,** *39* (5), 1291-1298.

13. Karn, B.; Kuiken, T.; Otto, M., Nanotechnology and in Situ Remediation: A Review of the Benefits and Potential Risks. *Environ. Health Persp.* **2009,** *117* (12), 1823-1831.

14. Huttenloch, P.; Roehl, K. E.; Czurda, K., Use of copper shavings to remove mercury from contaminated groundwater or wastewater by amalgamation. *Environ. Sci. Technol.* **2003,** *37* (18), 4269-4273.

15. Lalonde, J. D.; Amyot, M.; Orvoine, J.; Morel, F. M. M.; Auclair, J. C.; Ariya, P. A., Photoinduced oxidation of Hg-0 (aq) in the waters from the St. Lawrence estuary. *Environ. Sci. Technol.* **2004,** *38* (2), 508-514.

16. Lennie, A. R.; Redfern, S. A. T.; Champness, P. E.; Stoddart, C. P.; Schofield, P. F.; Vaughan, D. J., Transformation of mackinawite to greigite: An in situ X-ray powder diffraction and transmission electron microscope study. *American*

Mineralogist **1997,** *82* (3-4), 302-309.

17. Li, X. Q.; Brown, D. G.; Zhang, W. X., Stabilization of biosolids with nanoscale zero-valent iron (nZVI). *J. Nanopart. Res.* **2007,** *9* (2), 233-243.

18. Li, X. Q.; Elliott, D. W.; Zhang, W. X., Zero-valent iron nanoparticles for abatement of environmental pollutants: Materials and engineering aspects. *Crit. Rev. Sol. State Mater. Sci.* **2006,** *31* (4), 111-122.

19. Li, X. Q.; Zhang, W. X., Iron nanoparticles: the core-shell structure and unique properties for Ni(II) sequestration. *Langmuir* **2006,** *22* (10), 4638-4642.

20. Li, X. Q.; Zhang, W. X., Sequestration of metal cations with zerovalent iron nanoparticles - A study with high resolution X-ray photoelectron spectroscopy (HR-XPS). *J. Phys. Chem. C* **2007,** *111* (19), 6939-6946.

21. Lowry, G. V.; Johnson, K. M., Congener-specific dechlorination of dissolved PCBs by microscale and nanoscale zerovalent iron in a water/methanol solution. *Environ. Sci. Technol.* **2004,** *38* (19), 5208-5216.

22. Luther, G. W., Pyrite synthesis via polysulfide compounds. *Geochim. Cosmochim. Acta* **1991,** *55* (10), 2839-2849.

23. Martin, J. E.; Herzing, A. A.; Yan, W. L.; Li, X. Q.; Koel, B. E.; Kiely, C. J.; Zhang, W. X., Determination of the oxide layer thickness in core-shell zerovalent iron nanoparticles. *Langmuir* **2008,** *24* (8), 4329-4334.

24. Mullet, M.; Boursiquot, S.; Abdelmoula, M.; Genin, J. M.; Ehrhardt, J. J., Surface chemistry and structural properties of mackinawite prepared by reaction of sulfide

ions with metallic iron. *Geochim. Cosmochim. Acta* **2002,** *66* (5), 829-836.

25. Nurmi, J. T.; Tratnyek, P. G.; Sarathy, V.; Baer, D. R.; Amonette, J. E.; Pecher, K.; Wang, C. M.; Linehan, J. C.; Matson, D. W.; Penn, R. L.; Driessen, M. D., Characterization and properties of metallic iron nanoparticles: Spectroscopy, electrochemistry, and kinetics. *Environ. Sci. Technol.* **2005,** *39* (5), 1221-1230.

26. O'Loughlin, E. J.; Kelly, S. D.; Kemner, K. M.; Csencsits, R.; Cook, R. E., Reduction of Ag-I, Au-III, Cu-II, and Hg-II by Fe-II/Fe-III hydroxysulfate green rust. *Chemosphere* **2003,** *53* (5), 437-446.

27. Ponder, S. M.; Darab, J. G.; Mallouk, T. E., Remediation of Cr(VI) and Pb(II) aqueous solutions using supported, nanoscale zero-valent iron. *Environ. Sci. Technol.* **2000,** *34* (12), 2564-2569.

28. Ponder, S. M.; Darab, J. G.; Bucher, J.; Caulder, D.; Craig, I.; Davis, L.; Edelstein, N.; Lukens, W.; Nitsche, H.; Rao, L. F.; Shuh, D. K.; Mallouk, T. E., Surface chemistry and electrochemistry of supported zerovalent iron nanoparticles in the remediation of aqueous metal contaminants. *Chem. Mater.* **2001,** *13* (2), 479-486.

29. Reardon, E. J., Anaerobic corrosion of granular iron - Measurement and interpretation of hydogen evolution rates. *Environ. Sci. Technol.* **1995,** *29* (12), 2936-2945.

30. Rickard, D.; Luther, G. W., Chemistry of iron sulfides. *Chem. Rev.* **2007,** *107* (2), 514-562.

31. Shokes, T. E.; Moller, G., Removal of dissolved heavy metals from acid rock

drainage using iron metal. *Environ. Sci. Technol.* **1999,** *33* (2), 282-287.

32. Siciliano, S. D.; O'Driscoll, N. J.; Lean, D. R. S., Microbial reduction and oxidation of mercury in freshwater lakes. *Environ. Sci. Technol.* **2002,** *36* (14), 3064-3068.

33. Signorini, L.; Pasquini, L.; Savini, L.; Carboni, R.; Boscherini, F.; Bonetti, E.; Giglia, A.; Pedio, M.; Mahne, N.; Nannarone, S., Size-dependent oxidation in iron/iron oxide core-shell nanoparticles. *Phys. Rev. B* **2003,** *68* (19), 195423.

34. Smith, E. H., Uptake of heavy metals in batch systems by a recycled iron-bearing material. *Water Res.* **1996,** *30* (10), 2424-2434.

35. Stumm, W., Chemistry of the solid-water interface: processes at the mineral-water and particle-water interface in natural systems. John Wiley & Sons, New York, 1992.

36. Bard, A.J., Parsons, R., Jordan, J. (Eds.), Standard Potentials in Aqueous Solution. M. Dekker, New York, 1985.

37. Sun, Y. P.; Li, X. Q.; Cao, J. S.; Zhang, W. X.; Wang, H. P., Characterization of zero-valent iron nanoparticles. *Adv. Colloid Interface Sci.* **2006,** *120* (1-3), 47-56.

38. Tee, Y. H.; Grulke, E., Bhattacharyya, D., Role of Ni/Fe nanoparticle composition on the degradation of trichloroethylene from water. *Ind. Eng. Chem. Res.* **2005**, *44*, 7062-7070.

39. Tratnyek, P. G.; Johnson, R. L., Nanotechnologies for environmental cleanup. *Nano Today* **2006,** *1* (2), 44-48.

40. Wang, C. M.; Baer, D. R.; Amonette, J. E.; Engelhard, M. H.; Antony, J.; Qiang, Y., Morphology and Electronic Structure of the Oxide Shell on the Surface of Iron Nanoparticles. *J. Am. Chem. Soc.* **2009,** *131* (25), 8824-8832.

41. Wang, Q.; Lee, S.; Choi, H., Aging Study on the Structure of Fe-0-Nanoparticles: Stabilization, Characterization, and Reactivity. *J. Phys. Chem. C* **2010,** *114* (5), 2027-2033.

42. Watanabe, M.; Ackland, D. W.; Burrows, A.; Kiely, C. J.; Williams, D. B.; Krivanek, O. L.; Dellby, N.; Murfitt, M. F.; Szilagyi, Z., Improvements in the X-ray analytical capabilities of a scanning transmission electron microscope by spherical-aberration correction. *Microsc. Microanal.* 2006, *12* (6), 515-526.

43. Wieckowska, J., Catalytic and adsorptive desulfurization of gases. *Catal. Today* **1995,** *24* (4), 405-465.

Chapter 7

Reactions of Arsenic with nZVI : A Dual Redox Functionality Enabled by the Core-shell Structure

7.0 Abstract

Nanoscale zerovalent iron (nZVI) has shown a high efficacy for removing arsenite (As(III)), which is one of the the most highly concerned contaminants in groundwater. However, mechanistic details underlying arsenite sequstration are only partially understood, and reactions on the the solid phase are inferred predominantly from indirect aqueous phase analyses. This study investigates the reactions between nZVI and arsenite using high resolution X-ray photoelectron spectroscopy (HR-XPS), which offers new insights into the chemical states and spatial loci of arsenic inside nZVI particles. Highly efficient arsenite removal from water followed by a series of redox reactions on the surface of nZVI were observed, resulting in multiple arsenic valence states (i.e., As(0), As(III) and As(V)) in the solid phase. The parallel arsenite oxidation (to As(V)) and reduction (to As(0)) manifests a dual redox reactivity of nZVI that has not been reported prior to this study. To understand this novel functionality, time-dependent and multiline XPS analyses were employed to resolve the spatial and temporal changes of arsenic species in the nanoparticles. As(III) was rapidly oxidized to As(V) within 10 min at the particle surface, and the oxidized arsenic reverted to As(III)

at a slower rate in the presence of Fe(0). Meanwhile, infiltration of arsenite through the oxide layer resulted in As(0) formation near the Fe(0) interface. The relative extents of these reactions and the resultant arsenic speciation and spatial distribution are strongly dependent on the amount of nZVI present. When a small dose of nZVI was used (0.4 or 1 g/L), extensive Fe(0) corrosion results in arsenite being captured as a mixture of As(III) and As(V) in the corrosion products. In the presence of a relatively large dose of nZVI (5 g/L), layered distributions in the order of As(V) > As(III) > As(0) were established from the surface to the iron metal interface. In both cases, nZVI serves as a sink for arsenic with the contaminant being embedded in the solid phase on a small time scale. These attributes suggests nZVI a potentially more capacious and versatile arsenic abatement material than conventional arsenic adsorbent materials.

7.1 Introduction

High levels of arsenic in groundwater pose a serious health threat to millions of people around the world (Nordstrom, 2002; Smedley & Kinniburgh, 2002). The situation is of particular concern in rural areas of developing countries such as Bangladesh, India, Vietnam, and Cambodia, where there is no centralized water treatment facility and the contaminated groundwater is heavily utilized for drinking and irrigation of food crops (Meharg & Rahman, 2003; Dittmar *et al*., 2010). In the United States, groundwater supplies about one-third of the country's drinking water. However, there are many

locations in the southwestern states where groundwater contains arsenic concentrations in excess of the World Health Organization (WHO) guidelines and the U.S. Environmental Protection Agency (USEPA) drinking water standard of 10 µg/L (Welch *et al*., 2000; USEPA, 2003; WHO, 2008). Severe health implications including cancers have been traced to long-term arsenic intake (Mandal & Suzuki, 2002), and on a world-wide scale, it has been estimated that over 137 million people in more than 70 countries are affected by arsenic poisoning of drinking water (Smedley & Kinniburgh, 2002).

Many options have been explored for arsenic removal and these include coagulation, adsorption, ion exchange, and membrane processes (Edwards, 1997; Sarkar *et al*., 2005; Mohan & Pittman, 2007; Hussam & Munir, 2007). Coagulation with alum or ferric chloride is commonly used in large-scale water treatment plants and can be further optimized for arsenic removal (Edwards, 1997), whereas sorbents such as metal oxides or ion-exchange-based filtration units can be tailored for household or small community use and are currently a more practical solution in rural regions of the affected countries (Sarkar *et al*., 2005; Mohan & Pittman, 2007; Hussam & Munir, 2007).

The principal forms of arsenic in natural waters are arsenate [As(V)] and arsenite [As(III)]. Arsenate exists as oxyanions ($H_2AsO_4^-$ or $HAsO_4^{2-}$) in a pH range of 2 to 12, while arsenite remains as neutral undissociated species (H_3AsO_3) below a pH of 9.2 (Manning *et al*., 2002; Kanel *et al*., 2006). As(III) oxidation to As(V) by dissolved oxygen alone is kinetically slow (Smedley & Kinniburgh, 2002; Scott & Morgan, 1995). Amorphous or crystalline iron oxides possess strong affinity for both As(V) and As(III)

189

species. Under neutral or alkaline pH, As(III) adsorbs to a greater extent than As(V) onto iron oxide surfaces via inner-sphere complex formation (Dixit & Hering, 2003; Raven *et al*, 1998; Manning *et al*., 1998) and the molecular structures of arsenic-iron oxide complexes have been characterized by advanced spectroscopic techniques (Manning *et al*., 1998; Manceau, 1995; Goldberg & Johnston, 2001; Ona-Nguema *et al*., 2005). Figure 7.1 depicts the molecular structures of different As(V) surface complexes formed on goethite based on the inter-atomic distances determined from extended X-ray absorption fine structure (EXAFS) spectroscopy (Fendorf *et al*., 1997).
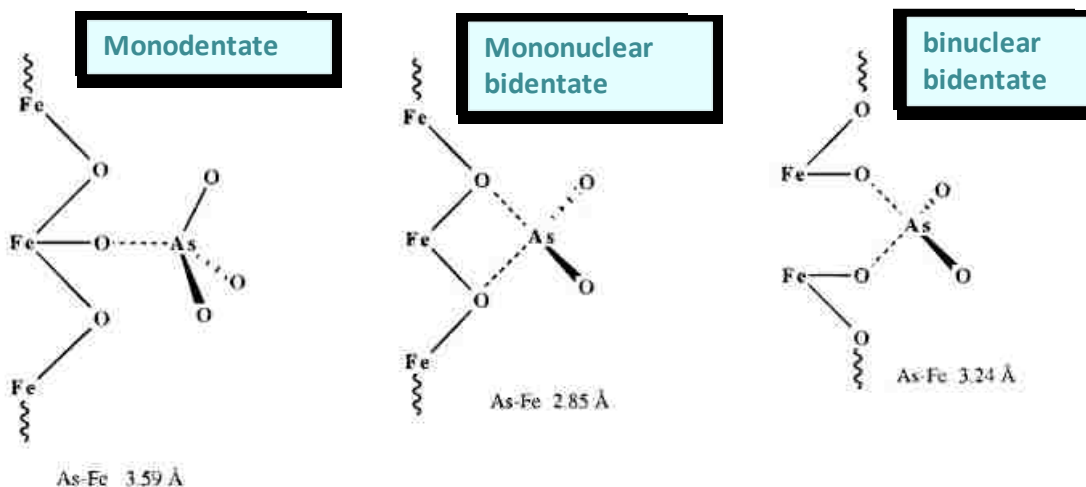
Figure 7.1 Surface complex structure of As(V) on goethite proposed based on EXAFS spectroscopic study (adapted from Fendorf *et al*., 1997).

Recent studies have shown that zero-valent iron is an effective remediation agent for treating arsenic-laden groundwater or drinking water (Lackovic *et al*., 2000; Su & Puls, 2001; Manning, *et al*. 2002; Bang *et al*., 2005; Lien & Wilkin, 2005). It is generally

conceived that As(III) or As(V) is removed by adsorbing to the iron oxide layer on the ZVI particles (Su & Puls, 2001; Manning, *et al.* 2002) or forming co-precipitates with iron hydroxide produced during *in situ* iron corrosion (Lackovic *et al.*, 2000; Lien & Wilkin, 2005). However, spectroscopic investigations of arsenic speciation in ZVI materials reveal that the immobilized arsenic is converted to different oxidation states from their aqueous forms, suggesting arsenic redox transformations have played an active part in the remediation process. X-ray photoelectron spectroscopy (XPS) analysis by Su *et al.* detected no reduction of As(III) by ZVI filings but partial oxidation of As(III) to As(V) (Su & Puls, 2001). Manning *et al.* (2002) reported similar findings with X-ray absorption spectroscopy (XANES and EXAFS) for ZVI powders reacted under aerobic conditions, where they proposed the oxidation of As(III) might be mediated by iron corrosion products such as magnetite/maghemite or lepidocrocite. On the other hand, Bang *et al.* found a fraction of As(III) being reduced to As(0) on an acid-pretreated iron coupon under anoxic conditions (Bang *et al.*, 2005). The variations in the experimental parameters and the limited spectroscopic data sets available make it difficult to interpret these results on a consistent basis.

In recent years, attention has been focused on nanoscale zero-valent iron (nZVI) for its effectiveness in treating halogenated hydrocarbons, hexavalent chromium and other heavy metal species in water (Ponder *et al.*, 2000; Liu *et al.*, 2005; Li & Zhang, 2007). The particles' small size gives rise to an increased surface area, greater remediation capacity, and favorable field injection and transport properties for *in situ* remediation.

While the nanoparticles have shown a remarkable efficacy to immobilize aqueous arsenic species (Kanel *et al*., 2005 & 2006), the reactions involved appear to be more complex than those of iron oxide based sorbents and the bulk-sized ZVI materials. Previous characterization shows nZVI consists of a reactive Fe(0) phase enclosed by a thin layer of amorphous iron oxide averaging ~ 3 nm in thickness (Martin *et al*., 2008). The nanometer scale and the defective nature of the oxide film may increase the rates of charge transfer or mass diffusion processes, thus the nanoparticles exhibit interesting redox behaviors on a relatively small time scale, which may not manifest to an appreciable extent in the bulk iron counterparts. In this context, studying nZVI-arsenic interactions will not only help to reveal the mechanisms underlying nZVI's efficient arsenic sequestration performance, but also shed light on the long-term fate and stability of the immobilized arsenic species.

In this work, high-resolution X-ray photoelectron-spectrometry (HR-XPS) is employed to investigate solid-phase arsenic speciation upon reactions between nZVI and aqueous As(III). High surface sensitivity and the availability of quantitative information on arsenic in different valence states render XPS a powerful tool for the purpose of this study. Specifically, we compared arsenic speciation in reacted nZVI with that in model iron oxide compounds under similar conditions to understand the difference in reactivity of nZVI relative to that of the well-characterized iron oxides. Using XPS multi-line analysis, we show for the first time that different arsenic oxidation states observed on nZVI are enriched in different layers of the nanoparticles, suggesting nZVI

possesses a dual redox functionality enabled by the core-shell structure. We also evaluated the effects of initial As(III) concentration, reaction time, and nZVI dose on the reaction products, which in conjunction with solution phase analysis, allows us to propose a more well-defined reaction model between As(III) and nZVI.

7.2 Materials and methods

Preparation of iron materials. Synthesis of iron nanoparticles (nZVI) follows the procedure described in Chapter 3. Two iron oxides, Fe_3O_4 and Fe_2O_3 (>99%, Fisher Chemical), were used in this study for comparison, whose reactions with As(III) have been extensively studied. XRD characterization shows that the predominant mineral phases for Fe_3O_4 and Fe_2O_3 are magnetite and hematite, respectively (Figure 7.2). The BET surface areas of all iron materials are summarized in Table 7.1.

Batch experiments. As(III) and As(V) solutions were prepared from $NaAsO_2$ and $Na_2HAsO_4 \cdot 7H_2O$ (>98.5%, Fluka), respectively. Batch experiments of As(III) removal were performed in 120-ml serum bottles containing 100 ml of As(III) solution at 100 mg/L. The solution was deoxygenated by sparging with nitrogen (high purity, >99.9%) for 30 minutes immediately before the experiments. Upon adding an appropriate amount of iron material, the bottle was sealed with a screw cap lined with a Teflon-coated septum and placed on a mechanical shaker (250 rpm) at 25°C. After a predetermined reaction time, a batch reactor was sacrificed and the solids were

separated from the solutions by vacuum filtration, dried and stored in a N_2-glovebox before XPS analysis. The solution samples were stored in 40-ml glass vials at 4 ^{o}C prior to analysis. Samples were analyzed within 48 hours of preparation.
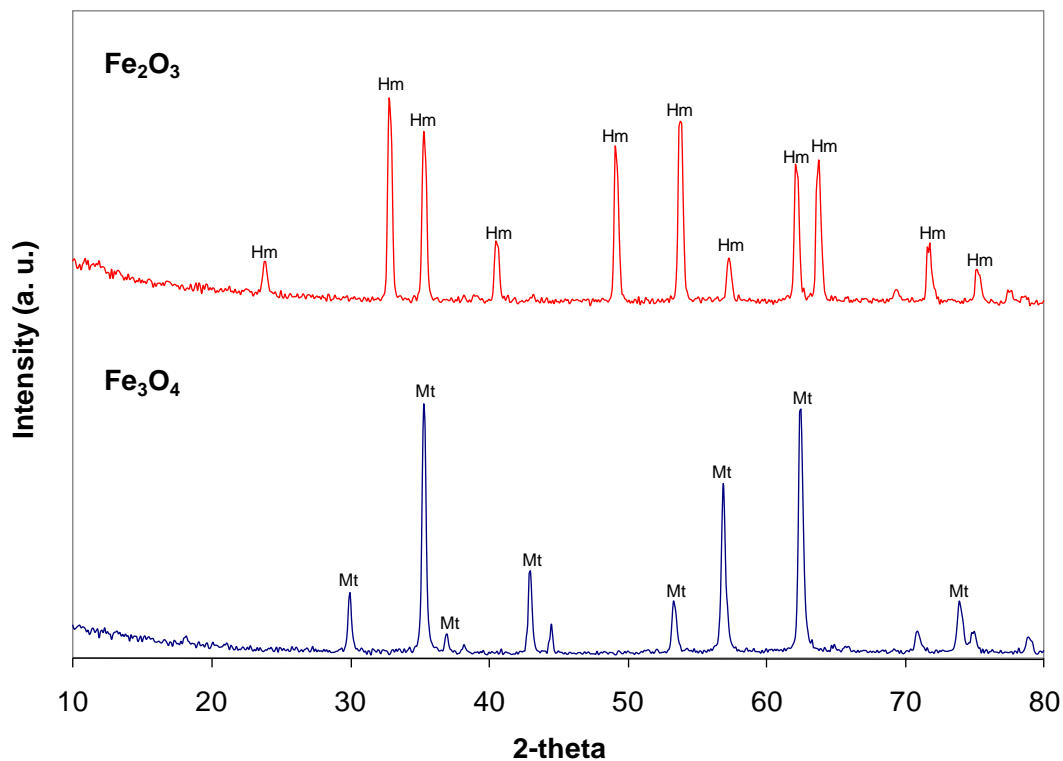
Figure 7.2 X-ray diffractograms of the iron oxides (Fe_2O_3 and Fe_3O_4) used in this study, which are characteristic of hematite (Hm) and magnetite (Mt), respectively.

Table 7.1: Characteristics of iron-based materials used in this work.

Iron material	Source	Mean diameter, nm	BET specific surface area, m^2/g	Crystalline phase
nZVI	This work (refer to ref (*4*) for preparation procedure)	60 [a]	29	Polycrystalline *bcc* Fe(0) [b]
Fe_3O_4	Fisher®, laboratory grade	n/a	30	Magnetite [c]
Fe_2O_3	Fisher®, certified >99% purity	n/a	42	Hematite [c]

[a] determined by acoustic spectrometry (Sun *et al.*, 2006)
[b] determined by selected area electron diffraction (SAED) pattern
[c] determined by XRD analysis

Aqueous phase analysis. Arsenic and iron concentrations in the solution phase were determined by inductively-coupled plasma-optical emission spectroscopy (ICP-OES; Perkin Elmer Optima 2100 DV), which has a detection limit of 50 µg/L and 10 µg/L for arsenic and iron, respectively. The pH and E_h values of the solutions after reactions were measured, respectively, with a pH probe (Orion) and an ORP probe with a Ag/AgCl reference electrode (Cole-Parmer). The reported E_h values are referenced to the standard hydrogen electrode (SHE).

Solid phase analysis. Dried samples of nZVI, after reaction with As(III) or As(V) solutions, were characterized using High Resolution X-ray Photoelectron Spectroscopy (HR-XPS) performed on a Scienta ESCA 300 spectrometer. Analysis procedure and

instrument parameters are available in Chapter 3. The full-width-at-half-maximum (FWHM) of each component peak was set to 1.2 eV, 1.6 eV, and 1.3 eV for As3d, As2p$_{3/2}$ and O1s spectra, respectively. The As3d$_{5/2}$ and As3d$_{3/2}$ components of the As3d spin orbit-split doublet peak were fixed at a constant intensity ratio of 3:2 and at a fixed separation of 0.70 eV.

7.3 Results and discussion

7.3.1 Aqueous phase analysis

Effective aresnic removal involves the transfer of As(III) species from the aqueous phase to the surface of nZVI particles. Although the focus of this study is on reactions at the solid phase, aqueous phase analyses were necessary in order to quantify the amounts of arsenic captured by nZVI at different reaction stages. To afford direct examination of arsenic reactions in the solid phase, arsenic concentrations higher than those found in natural environmental settings (< 1000 µg/L) are needed to ensure adequate arsenic presence in the solids for accurate speciation analysis. For XPS analysis using the high-intensity Scienta ESCA 300, a minimal aqueous concentration of 10 mg/L is needed to generate a convenient amount of arsenic (> 0.1 at.%) in nZVI. Samples prepared at lower arsenic concentrations (10-1000 µg/L) require a scan time orders of magnitude longer than a typical As 3d or As2p$_{3/2}$ analysis (in the order of min) to obtain a reasonable signal-to-noise ratio, which may cause chemical shifts due to X-

ray irradiation and is therefore not used in this study. For most experiments presented in this work, an initial As(III) concentration of 100 mg/L was used for the HR-XPS analysis.

Figure 7.3 compares the rate of As(III) removal by nZVI and Fe_3O_4 at a mass dose of 5 g/L. Rapid loss of aqueous As(III) from the solution phase was observed upon addition of nZVI. The total aqueous arsenic concentration decreased to 106 μg/L (corresponding to ~ 99.9% removal) at 10 min and it was below the detection limit after 1 h of mixing. Since the nZVI samples for XPS analysis were collected after at least 10 min of reaction, rapid loss of arsenic in the solution phase suggests that changes in arsenic speciation observed by XPS were resulted from solid-phase reactions instead of sorption of homogenous reaction products.

Similar experiments using Fe_3O_4 (at the same mass dose of 5 g/L) resulted in sequestration of only 13% of the aqueous As(III). A large difference in As(III) retention capacity between nZVI and the iron oxides can be clearly seen in the inset of Figure 7.3, which compares final As(III) removal after 24 hrs by various doses (0.4 – 5 g/L) of nZVI, Fe_3O_4, and Fe_2O_3. Despite a relatively high initial concentration (100 mg/L), nearly complete removal of As(III) was obtained with a nZVI dose as low as 1 g/L, whereas the removal efficiency remained below 20% even at the highest dose (5 g/L) of Fe_3O_4 and Fe_2O_3. Since the BET specific surface areas of nZVI and the two oxides are comparable (Table 7.1), direct comparison of mass-normalized As(III) removal capacity
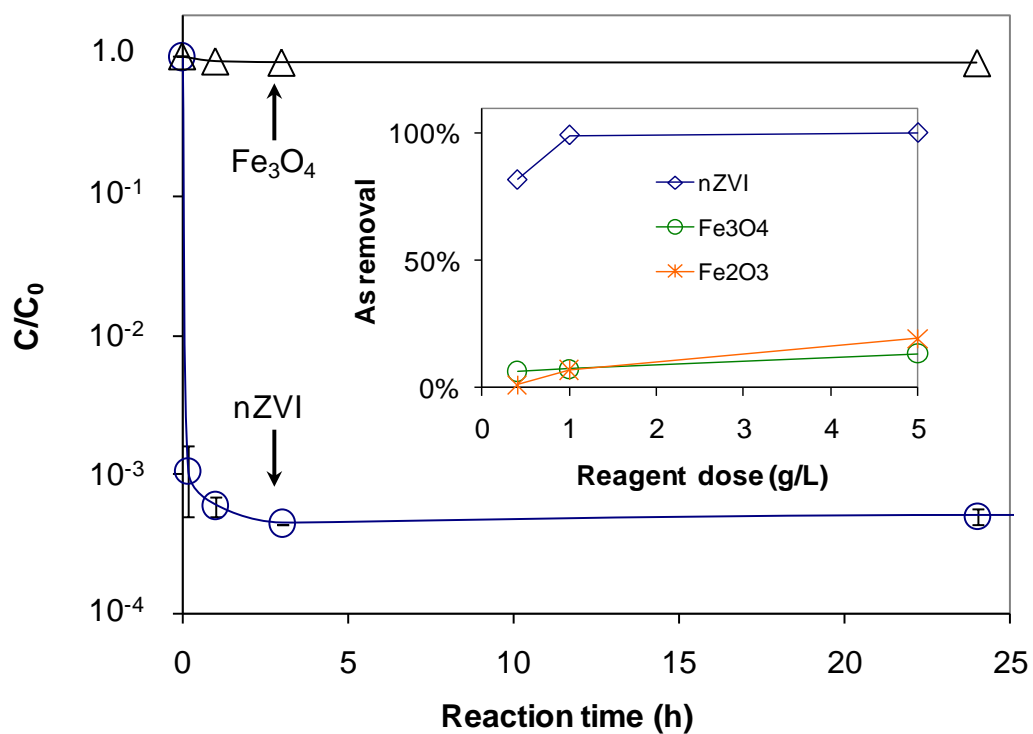
Figure 7.3 Change in aqueous arsenic concentration with time. Initial As(III) concentration (C_0) was 100 mg/L; nZVI or iron oxide dose was 5 g/L. Inset: percentage As(III) removal at various dose of iron materials after 24 hours.

can be made. For nZVI, the maximum As(III) loading capacity is 2.2 mM As/g, while the value of the oxides is no more than 0.17 mM As/g. Applying a surface complexation model in which the average adsorption site density of an iron oxide surface is ~3 sites/nm^2 (Dixit & Hering, 2003), we can estimate a maximum As(III) adsorption of ~ 0.2 mM As/g, which is consistent with the observed capacities of the iron oxides. On the other hand, the arsenite loading capacity of nZVI is well in excess of the total surface adsorption sites available, which suggests arsenite is captured in more than a

mere surface layer. Previous studies have attributed similar results to As(III) forming

co-precipitates with ferric ions (Lackovic *et al*., 2000; Lien & Wilkin, 2005) and the

continuous production of iron corrosion products supplying additional surface sites for

As(III) uptake (Manning *et al*., 2002; Bang *et al*., 2005). Although arsenite oxidation

(Su & Puls, 2001; Katsoyiannis *et al*., 2008) and reduction (Bang *et al*., 2005) were

observed in the presence of ZVI, the mechanisms of these redox exchanges and the

implications for arsenic abatement applications have not been explicitly discussed.

7.3.2 Arsenic speciation on the solid phase

For all samples analyzed by XPS, spectra of major elements such as Fe, O, and As were

collected and analyzed. Composition as atomic percent for each element *i* was

calculated according to Eq. (7.1)

$$C_i = \frac{A_i / S_i}{\sum_i A_i / S_i} \qquad (7.1)$$

where A_i is the measured peak area and S_i is the relative sensitivity factor (RSF). These

latter values were taken from literature (Fairley & Carrick, 2005) as: S(C1s)=1.0,

S(O1s)=2.93, S(Fe2p)=16.4, and S(As3d)=1.82. The value of S(As2p) was determined

empirically from a pure As_2O_3 sample to be 31.5. The atomic percentages obtained as

such are apparent concentrations because of the inherent assumption in the calculation

that each element is distributed homogeneously throughout the probe depth. The results

are tabulated in Table 7.2 together with the pH and E_h readings of the solutions in equilibrium with these samples.

Figure 7.4 displays XPS spectra of the As3d region of nZVI before (a) and after reactions with As(V) (b) and As(III) (c) species, respectively. The XPS peak positions were assigned by comparison to As3d$_{5/2}$binding energies reported in the literature (Moulder *et al.*, 1992). No arsenic was detected on pristine nZVI, but As peaks were clearly detected on reacted nZVI. The XPS spectra reveal the presence of multiple arsenic valence states, *viz.*, As(V), As(III), and As(0) on the nZVI surfaces. As3d peak for each chemical state has two unresolved components due to spin-orbit splitting corresponding to the As3d$_{3/2}$ (at higher BE) and As3d$_{5/2}$ (at lower BE) peaks separated by 0.7 eV.

As shown in Figure 7.4b, when 5 g/L nZVI was added to 100-mg/L arsenate [As(V)] solution, significant amounts of As(III) and As(0) were detected on the nZVI surface in 24 hours, establishing As(V) reduction to As(III) and As(0). The numbers indicated in Figure 7.4 are the proportions of the respective arsenic species as percentages of the total arsenic detected. It should be noted that each of these spectra were not affected by increasing the X-ray irradiation time by a factor of six under the instrument conditions used in this study, *i.e.*, XPS analysis had no observable effect on the arsenic valence state within the prescribed scan-time used in this study (~ 10 min).

Earlier studies reported the reduction of arsenate to arsenite species by iron fillings or nanoscale ZVI , but the kinetics were considerably slow (e.g., >30 days before As(III) was detected). The predominant mechanism for As(V) uptake is generally thought to be surface sorption and precipitation (Lackovic *et al*., 2000; Su & Puls, 2001). Results presented in Figure 7.4 clearly show that nZVI is capable of reducing As(V) with reasonably fast kinetics and reduction to elemental arsenic is a feasible mechanistic step. As will be discussed later herein, the variances in environmental conditions, in particular arsenic concentration and solution pH, and the properties of iron materials play crucial roles in determining the final arsenic speciation.

Analysis of nZVI reacted with 100 mg/L arsenite [As(III)] solution (Figure 7.4c) shows 51 % of the surface-bound arsenic remained as As(III). Meanwhile, 14% and 35% of the total arsenic emerged as As(V) and As(0), respectively, indicating that both As(III) oxidation and reduction had occurred to significant extents. While As(III) oxidation by ZVI was noticed in prior studies (Manning *et al*., 2002; Su & Puls, 2001; Katsoyiannis *et al*, 2008), the concomitant observation of oxidation and reduction of arsenic (III) has not been reported before. This behavior implies that the nanoparticles used here have a more complex character than being a monofunctional reductant as widely acknowledged.

Table 7.2: Solution pH and E_h conditions and surface composition analyzed by XPS. *

Initial As species	Iron material	Reaction time	Solid phase						Solution	
			As(V)^ (rel. %)	As(III)^ (rel. %)	As(0)^ (rel. %)	Total As (at. %)	Total Fe (at. %)	Total O (at. %)	Final pH	Final Eh (mV)
Figure 7.4										
As(III)	5 g/L nZVI	24 h	14	51	35	1.4	16.8	67.2	8.9	-49
As(V)	5 g/L nZVI	24 h	76	11%	13	3.0	18.4	78.6	9.3	115
Nil	5g/L nZVI	24 h	0	0	0	0	13.3	86.7	-	-
Figure 7.6										
Pure NaAsO$_2$	-	-	100	0	0	18.3	0	42.4	-	-
As(III)	5 g/L Fe$_2$O$_3$	24 h	40	60	0	2.0	21.7	49.5	10.0	306
As(III)	5 g/L Fe$_3$O$_4$	24 h	38	62	0	2.3	21.7	53.9	9.9	279
As(III)	5 g/L nZVI	24 h	16	44	40	1.4	19.6	62.8	9.2	-90
Figure 7.10										
As(III) 50 mg/L	5 g/L nZVI	24 h	25	30	45	1.4	21.2	77.3	8.5	-198
100 mg/L	5 g/L nZVI	24 h	14	51	35	1.4	16.8	67.2	8.9	-49
500 mg/L	5 g/L nZVI	24 h	33	67	0	4.8	16.0	79.3	10.8	152
1000 mg/L	5 g/L nZVI	24 h	25	75	0	5.9	15.0	78.0	11.0	158
Figure 7.13										
As(III)	5 g/L nZVI	10 min	40	45	15	2.2	15.8	69.8	-	-
As(III)	5 g/L nZVI	1 h	23	51	26	1.5	16.0	67.5	9.1	-44
As(III)	5 g/L nZVI	4 h	21	51	28	1.2	17.6	66.6	9.0	-48
As(III)	5 g/L nZVI	24 h	14	51	35	1.4	16.8	67.2	8.9	-49
As(III)	5 g/L nZVI	15 d	21	49	30	1.8	14.9	61.1	8.7	-44

Table 7.2 Continued

Initial As species	Iron material	Reaction time	Solid phase						Solution	
			*As(V)^* *(rel. %)*	*As(III)^* *(rel. %)*	*As(0)^* *(rel. %)*	Total As (at. %)	Total Fe (at. %)	Total O (at. %)	Final pH	Final Eh (mV)
Figure 7.14										
As(III)	0.4 g/L nZVI	24 h	45	55	0	3.8	10.4	56.1	9.5	199
As(III)	1 g/L nZVI	24 h	27	73	0	6.6	8.0	44.1	9.9	157
As(III)	5 g/L nZVI	24 h	14	51	35	1.4	16.8	67.2	8.9	-49

*Surface compositions reported as atomic percent, as calculated from XPS spectra using the measured peak areas and appropriate relative sensitivity factors. The calculations assume a homogeneous distribution of elements in the sample.

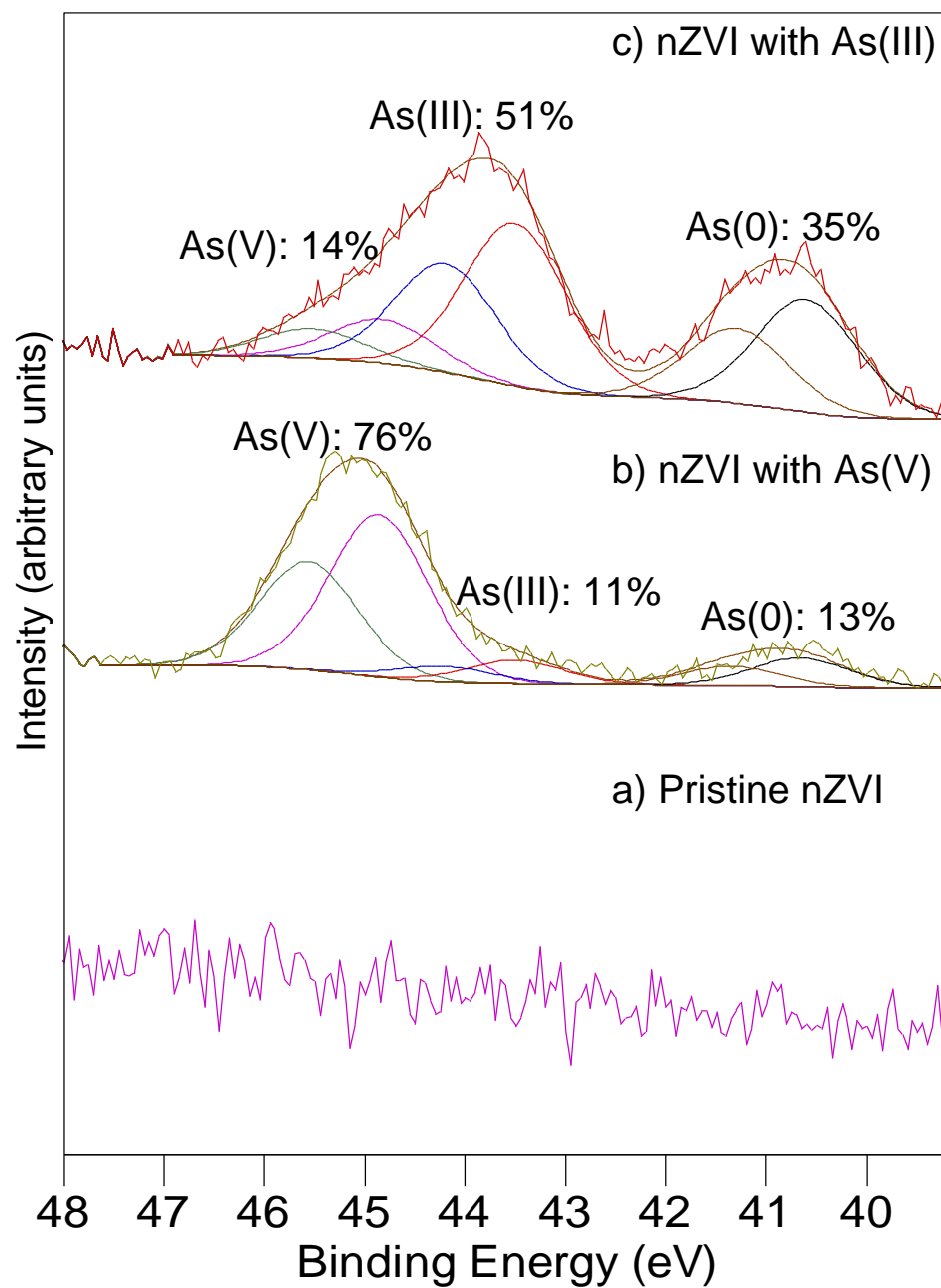^ Refer to relative abundances of arsenic in different oxidation states as estimated from As3d spectra.

Figure 7.4 As3d HR-XPS spectra of (a) fresh nZVI and (b) nZVI reacted with 100 mg/L As(V), and (c) nZVI reacted with 100 mg/L As(III). The nZVI loading in (b) and (c) was 5 g/L. The proportions of the respective species as percentages of the total As detected are annotated on the spectra. The intensity scale varies for each curve.

To understand the properties of nZVI, the material constituents present in individual nZVI particles were characterized with TEM. A bright field-TEM image shows a composite layered structure comprised of a dense metallic center enclosed by a thin layer of iron-oxide material (Figure 7.5a). Phase-contrast TEM imaging did not reveal periodic lattice-fringes in the oxide layer (Figure 7.5b), which suggests that the oxide is largely amorphous in agreement with prior characterizations (Chapter 4). The oxide outer-shell measures on average approximately 3 nm in thickness and has an apparent composition of FeOOH as determined previously from Fe2p and O1s XPS spectra (Martin *et al*., 2008). The oxide layer is thought to form instantaneously upon nZVI synthesis to passivate the highly reactive Fe^0 core and it may be practically viewed as an inherent part of the nanoparticle. The very fine dimension and disordered nature of the oxide layer support earlier notions that the oxide phase is capable of electron passage via tunneling effects or defect sites (Nurmi *et al*., 2005; Li & Zhang, 2006), thereby conserving the reducing characteristics of Fe^0 and accounting for As(III) reduction. On the other hand, iron oxides are known to possess strong adsorptive ability for both As(III) and As(V) species, and certain iron oxides formed from Fe^0 corrosion are able to cause As(III) oxidation to As(V) (Manning & Goldberg, 1997; Manning *et al*., 2002). In our studies, as the nanoparticles are comprised of Fe^0 nuclei encapsulated by an thin layer of iron oxide, we hypothesize this core-shell configuration would permit each component to exert its distinctive reactivity without significant kinetic constraints. The composite particles therefore possess dual properties of the two

components and this leads to unconventional chemical behavior such as the concurrent oxidation, reduction and sorption of As(III) illustrated in Figure 7.4c.
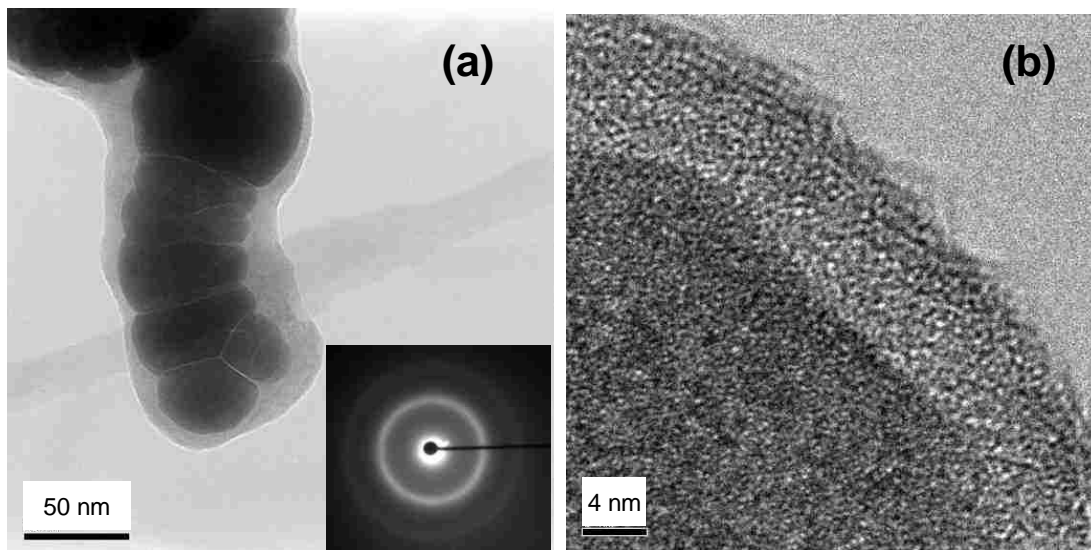
Figure 7.5 (a) Bright field-TEM micrograph of nZVI nanoparticles showing a core-shell structure comprised of a dense metallic center and a thin, continuous oxide skin. The inset shows the electron diffraction pattern of the metallic core, which suggests a polycrystalline *bcc* structure. (b) HR-TEM micrograph of a single nZVI nanoparticle. The lack of long-range periodic lattice fringes in the oxide layer suggests that it is amorphous in character.

7.3.3 Depth-dependent distribution of arsenic in nZVI

7.3.3.1 XPS multiline analysis

Insights into the dual reductive and oxidative properties manifested by nZVI in As(III) systems may be obtained if arsenic speciation and their spatial distributions in the solid

phase can be carefully resolved. In this section, we investigate the reactions between nZVI and arsenite using XPS multiline analysis, wherein HR-XPS spectra for two arsenic core-levels widely separated in binding energy (BE), As2p$_{3/2}$ (~1326 eV BE) and As3d (~44 eV BE), were collected. Due to the large BE differences in these core levels, the photoelectrons analyzed in these spectra have markedly different kinetic energies and thus "escape depths" (3λ, where λ is the attenuation length or mean free path for inelastic scattering at the respective kinetic energy), which are estimated to be 1.4 nm and 6.8 nm, respectively, in FeOOH based on the semi-empirical CS2 equation (Cumpson & Seah, 1997). The different surface sensitivity of each of these As2p$_{3/2}$ and As3d spectra enables us to resolve the distribution of arsenic species within a ~7-nm thick surface region. This depth-dependent information cannot be obtained by bulk analysis or less surface sensitive methods such as X-ray energy absorption techniques (e.g. EXAFS) (Manning *et al.*, 1998; Manceau, 1995), while other depth-profiling techniques, such as angle-resolved XPS measurements, are especially complicated by the spherical geometry and size distribution of the nanoparticles.

Figure 7.6a-b show As2p$_{3/2}$ and As3d spectra of different iron materials that have been reacted with As(III) solutions for 24 hours. Each arsenic oxidation state gives rise to two peaks in the As3d spectra (Figure 7.6b), due to the spin orbit-split As3d$_{5/2}$ and As3d$_{3/2}$ components, and a single peak in the As2p$_{3/2}$ spectra (Figure 7.6a). For Fe$_2$O$_3$ and Fe$_3$O$_4$ particles, approximately 40 at.% of the original As(III) was found to be oxidized to As(V). All solutions were sparged with pure N$_2$ for 30 minutes immediately

before the introduction of iron materials, so direct oxidation of As(III) by dissolved oxygen was effectively avoided. Prior studies have reported As(III) oxidation in the presence of hematite and surfaces with mixed valent Fe(II)-Fe(III) species (Manning et al., 2002; Amstaetter et al., 2010), which may account for the As(V) species observed here for Fe_2O_3 and Fe_3O_4 samples.

HR-XPS spectra of the nZVI sample in Figure 7.6 reveal the presence of As(0), As(III) and As(V), respectively, although the aqueous phase initially contained 100% As(III) only. The observation of multiple arsenic valence states in the solid residues confirms that nZVI exhibits a combination of adsorptive, reductive and oxidative abilities towards As(III) as previously noted (refer to Section 7.3.2). However, deconvolution of the spectra shows that the apparent proportions of arsenic species at different oxidation states differ significantly in the $As2p_{3/2}$ and As3d spectra. Specifically, As(0) constitutes 40 at.% of the total arsenic in the As3d spectrum, while it contributes only 16 at.% in the $As2p_{3/2}$ spectrum. The opposite trend is observed for As(V) species. Clearly, these arsenic species are distributed at varying depths of the nanoparticles.

209
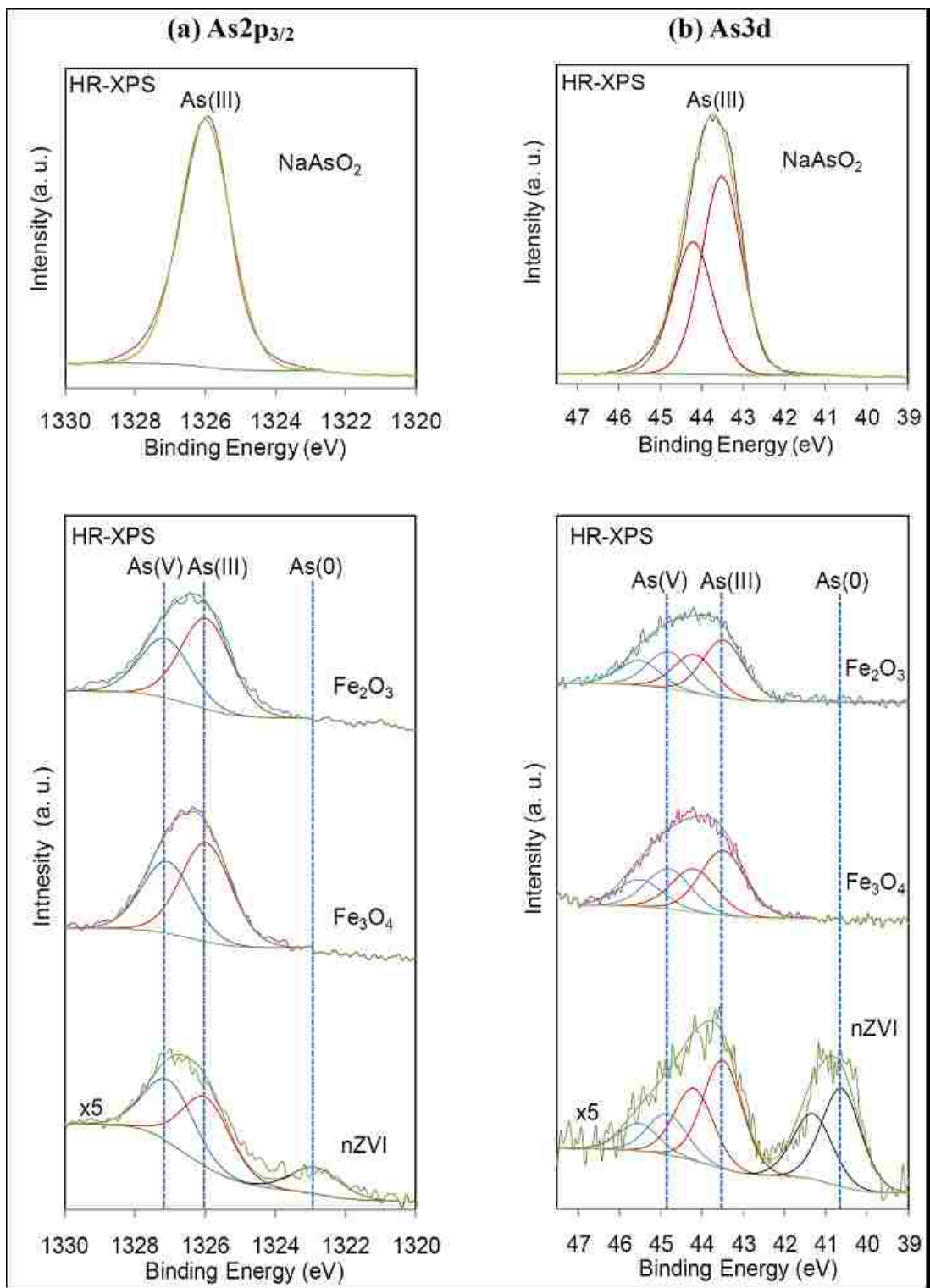
Figure 7.6 (previous page) HR-XPS spectra of (a) As2p$_{3/2}$ and (b) As3d regions of various Fe materials reacted with As(III) solutions. These two core-levels were chosen because of their difference in surface sensitivity. The top spectrum of each column is that of pure sodium arsenite (NaAsO$_2$), which was used to prepare the As(III) solutions used in these experiments. The vertical scale of the two spectra from the nZVI sample is enlarged five-fold.

To delineate the depth-dependent distributions of arsenic species, we evaluated the ratio of the As2p$_{3/2}$ to As3d peak areas in Figure 7.6, after correcting each by a relative sensitivity factor (RSF) to account for the difference in ionization cross-sections and instrument-dependent response functions (Moulder *et al*., 1992). The result, referred to as the normalized As2p$_{3/2}$ and As3d intensity ratio (or simply 'the ratio'), tells much information about the depth range within which the species of interest is located, as illustrated in Figure 7.7.
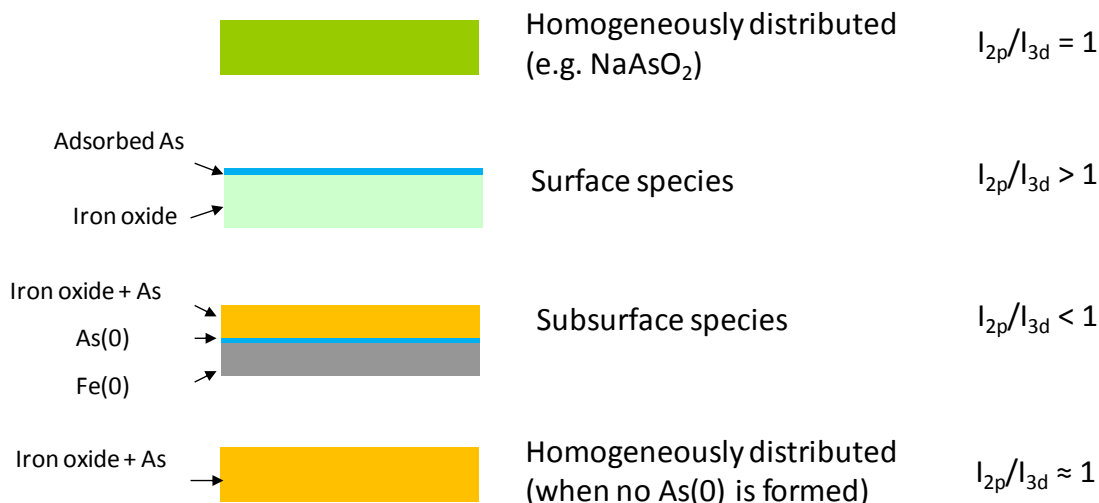
Figure 7.7 Inference of depth-dependent distributions of arsenic species from the normalized As2p$_{3/2}$ and As3d intensity ratio.

Figure 7.7 suggests that arsenic species that are homogeneously distributed in the surface region should have an As2p$_{3/2}$/As3d intensity ratio close to unity. Arsenic species that are more concentrated at the surface will have an As2p$_{3/2}$/As3d ratio greater than one, and conversely, arsenic species enriched in subsurface layers will have a ratio less than one.

7.3.3.2 Arsenic distribution in iron oxide materials

The normalized intensity ratios of the samples shown in Figure 7.6 are plotted in Figure 7.8. A pure homogeneous solid sample, NaAsO$_2$, which is the precursor of As(III) used in the experiments, is included in the figure to verify this approach. As expected, this reference material shows a ratio close to unity (Figure 7.8), thus confirming the relationship depicted in Figure 7.7.

For the Fe$_2$O$_3$ sample, the As2p$_{3/2}$/As3d ratios of As(III) and As(V) equal to 2.2. This value, much greater than one, implies that both species are present predominantly in a surface overlayer. Assuming the overlayer thickness is d, the relationship between the intensity of As2p$_{3/2}$ line and d can be expressed quantitatively as (Mohai, 1995):

$$I_{As2p} = I_{As2p}^{\infty}(1 - \exp(-\frac{d}{\lambda_{As2p}\cos\theta})) \tag{7.2}$$

Where I^∞_{As2p} is the intensity of As2p$_{3/2}$ photoelectrons generated from a pure homogeneous arsenic specimen, and λ_{As2p} is the inelastic mean-free path (IMFP) of As2p$_{3/2}$ photoelectrons.

A similar equation can be written for As3d line (Eq. 7.3):

$$I_{As3d} = I^\infty_{As3d}(1 - \exp(-\frac{d}{\lambda_{As3d}\cos\theta}))$$
(7.3)

Where I^∞_{As3d} is the intensity of As3d photoelectrons generated from a pure homogeneous arsenic specimen, and λ_{As3d} is the inelastic mean-free path (IMFP) of As2p$_{3/2}$ photoelectrons.

Take the ratio of Eq. 7.2 over Eq. 7.3, cancel out the cosine terms (due to normal take-off angle), and replace the terms I^∞_{As2p} and I^∞_{As3d} by their respective sensitivity factors yield the following relationship:

$$\frac{I_{As2p}/S_{As2p}}{I_{As3d}/S_{As3d}} = \frac{1 - \exp(-d/\lambda_{As2p})}{1 - \exp(-d/\lambda_{As3d})}$$
(7.4)

The left-hand-side of Eq. 7.4 is equivalent to the normalized intensity ratio of As2p$_{3/2}$ and As3d signals. Plugging in the ratio measured from the Fe$_2$O$_3$ sample (=2.2), the calculated thickness of the arsenic-laden layer (d) is approximately 0.7 nm. This value is considerably close to the monolayer thickness of arsenic-iron oxide surface complexes derived from X-ray absorption studies (Manceau, 1995;

212

Manning *et al*., 1998), confirming that As(III) and As(V) are essentially bound as a surface complex layer on the Fe_2O_3 particles. For Fe_3O_4, a similar spatial distribution profile is obtained, except that As(III) is distributed in a slightly thicker layer than As(V), a probable result of short-range diffusion of As(III) into the Fe_3O_4 particles via micropores or defect sites (Axe & Trivedi, 2002).
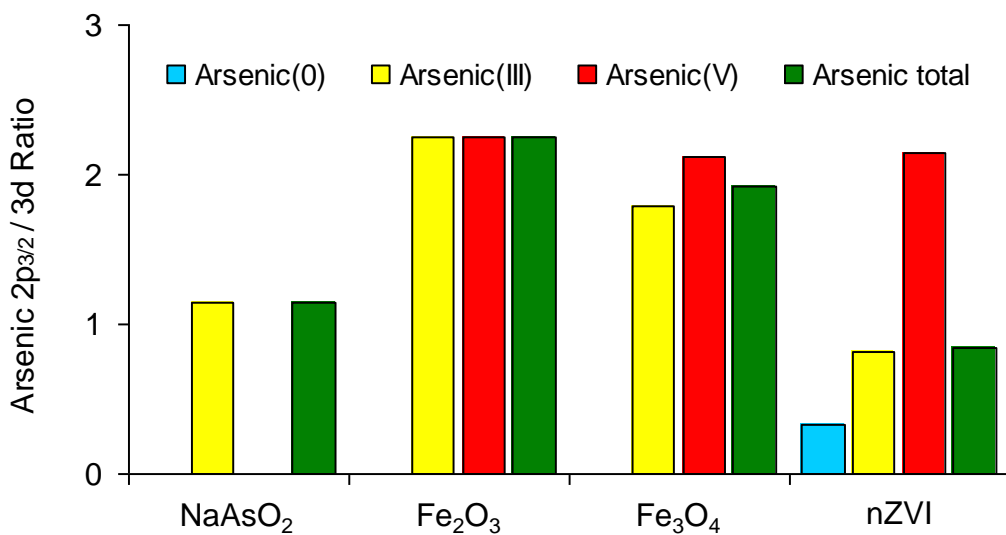
Figure 7.8 Normalized intensity ratios of the $As2p_{3/2}$ to As3d peaks in HR-XPS spectra.
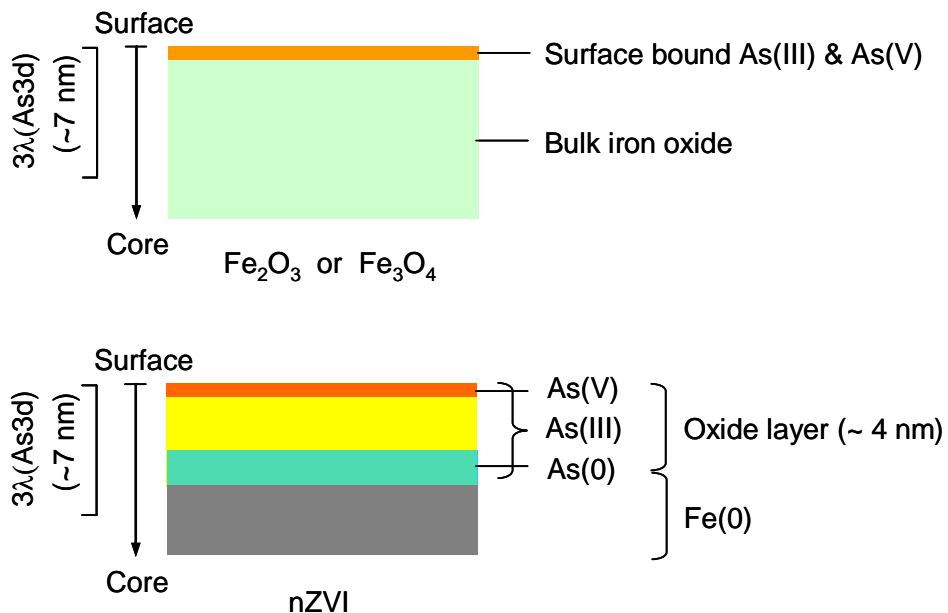
Figure 7.9 Schematic illustrations of the depth distribution of arsenic species in iron oxides and nZVI. The left-hand scale bars indicate the escape depth (3λ) of As3d photoelectrons in iron oxide. The thickness of the surface oxide layer for nZVI is calculated from the relative intensities of metallic and oxidized iron contributions in the Fe2p spectrum.

7.3.3.3 Arsenic distribution in nZVI

In contrast to iron oxides, arsenic species detected in the nZVI sample display a marked disparity in the $As2p_{3/2}$/As3d intensity ratios. As(V) species, with a normalized intensity ratio of 2.1, is clearly enriched at the surface. As(III), with a ratio of 0.82, has a fairly uniform presence across the sampling depth, and As(0) (ratio = 0.34) is localized in a subsurface region. Examination of the Fe2p XPS spectrum of this sample showed a small peak at 707.0 eV corresponding to Fe^0 (spectrum not shown). Following our previous approach to quantifying the oxide layer thickness from the relative intensity of

the metallic and oxidized iron peaks and applying XPS Multiquant with topographic corrections (Martin *et al.*, 2008; Mohai, 2005), we estimate that the average oxide thickness of this nZVI sample is ~ 4 nm. Across this oxide layer, the $As2p_{3/2}$ photoelectrons are strongly attenuated while the As3d photoelectrons are not as much. It is therefore reasonable to infer that the As(0) signals emanate mainly from a region close to the core-shell interface. This is illustrated in Figure 7.9, which provides a schematic of the depth distribution of arsenic based on the present analysis.

The stratified concentration profiles of arsenic species in nZVI expose several novel aspects of the reactions between As(III) and nZVI. The results offer clear evidence of a dual redox functionality exhibited by the nanoparticles. The distinct layers where As(V) and As(0) reside imply As(III) oxidation and reduction are enabled by different components of the nanoparticles. Surface enrichment of As(V) is consistent with an adsorption/oxidation model in which As(III) attaches to the surface coordination sites of the oxide shell and subsequent oxidation is facilitated by the oxide surface and the rearrangement of H_2O or OH^- ligands (Scott & Morgan, 1995; Amstaetter *et al.*, 2010). On the other hand, As(0) residing predominantly in a subsurface region implies that the reduction is enabled by the metallic core. This would entail inward diffusion of As(III) species and migration of reductants from the core region, which can be facilitated by the defect sites (e.g. vacancies or impurites) present in the disordered oxide layer (Wang *et al.*, 2009). This charge and mass transpot processes may cause As(III) reduction to be more kinetically limiting

than its surface oxidation, and further study to evelute nZVI samples reacted with arsenite for different lengths of time is needed (to be discussed in Section 7.3.5).

Figure 7.8 shows that the $As2p_{3/2}$/As3d ratio for the total arsenic detected in nZVI, obtained by summing together all of the different arsenic species present, has a value of 0.8. This implies that the solid-bound arsenic exists mostly underneath the surface. The ability to impregnate arsenic into the solid phase renders nZVI a potentially more voluminous sink for arsenic compared to the widely used iron oxides, whose capacities are limited by the available surface coordinative sites and are subject to competition from co-existing anions in the water (Yavuz *et al*., 2006; Hug *et al*., 2008). This attribute of nZVI explains in part the much higher efficacy of nZVI for As(III) removal relative to that of the iron oxides as observed in our solution experiments, considering that the surface areas of these materials are comparable (Figure 7.3). Furthermore, infiltration of arsenic induced by reactions with Fe^0 may offer an engineering methodology to encapsulate arsenic for remediation and waste disposal applications. In this context, continuing studies to evaluate the performance of nZVI for arsenite treatment in a broad spectrum of environmental conditions are warranted.

7.3.4 Effect of As(III) initial concentrations

Figure 7.10 presents results following reaction of nZVI with arsenite at different initial As(III) concentrations. The initial As(III) concentration in the solution was in the range of 50-1,000 mg/L. The relative abundance of arsenic chemical states is vastly affected by the initial As(III) concentration. As clearly can be seen in Figure 7.10, the relative amount of As(0) formed is the greatest at the lowest initial concentration of As(III) (50mg/L), with approximately one-half of the total arsenic present as As(0). The proportion decreased to 17% when the initial As (III) concentration was increased to 100 mg/L, and no As(0) was detected when As(III) concentration was increased to 500 and 1,000 mg/L.

The solution conditions measured at the end of the experiments (tabulated in Table 7.2) offer a clue to the strong dependence of arsenite reduction on its initial aqueous concentration. Figure 7.12 plots the changes in initial and equilibrium pH values as a function of the As(III) aqueous concentrations. The initial pH readings showed an increasing trend as the As(III) initial concentration increased, due to arsenite hydrolysis and the release of hydroxyl ions ($AsO_2^- + H_2O \rightarrow H_3AsO_3/ H_2AsO_2^- + OH^-$). The equilibrium pH follows a close trend by increasing from circumneutral (pH 8.5) to alkaline (pH 11) as the As(III) concentration increased from 50 to 1,000 mg/L. The alkaline condition associated with high Ar(III) concentrations promotes ferric ion precipitation, which may act as barriers altering the surface properties of the nanoparticles.
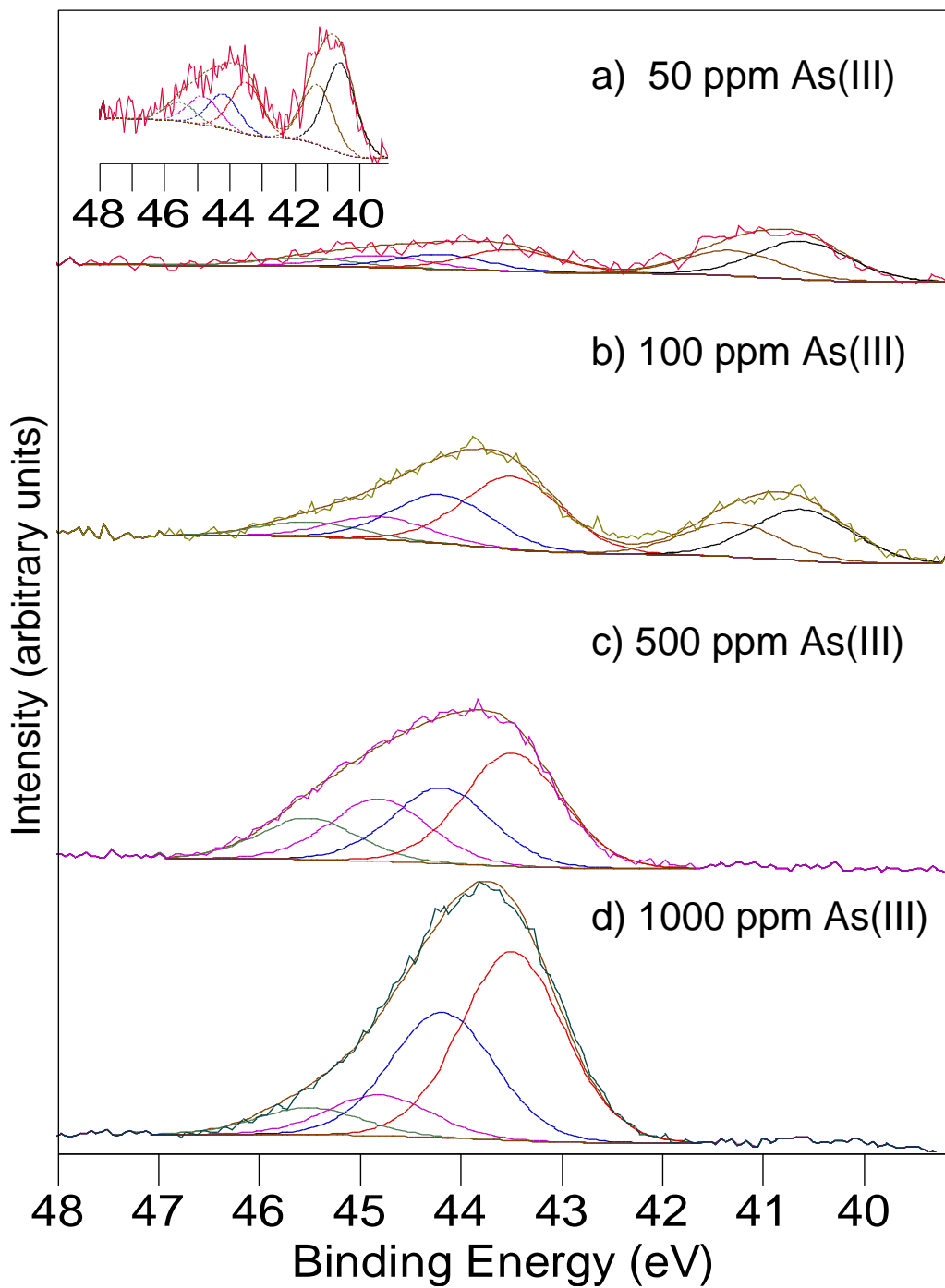
Figure 7.10 As3d HR-XPS spectra from nZVI particles exposed to different initial concentrations of As(III). The nZVI loading was 5g/L in all cases. The inset of (a) and (b) are vertically expanded views of the respective spectrum.

The purported precipitation of ferric hydroxide in solutions containing relatively high concentrations of As(III) is supported by two lines of evidence. One is from the O1s XPS spectra of the reacted sample (Figure 7.11). The curves can be decomposed into different oxygen species, namely, H_2O at 531.8 eV, OH^- at 530.7 eV, and O^{2-} at 529.5 eV (Grosvenor *et al*., 2004). The higher concentration samples (Figure 7.11c-d) reflect a marked increase in OH^- component, indicating growth of hydroxide precipitates in addition to surface sorbed hydroxide species on the sample surfaces. Another piece of evidence comes from SEM images of the reacted particles (shown in Figure 7.12 bottom). Particles after reactions with 100 mg/L of As(III) retained spherical morphology with a noticeable amount of loose, flaky materials scattered across the particle surface. The sample after reaction with 1000 mg/L As(III), in comparison, exhibited more pronounced platelet formation resembling typical formations of iron corrosion. The large amounts of oxidation products effectively form an interconnected matrix burying the nanoparticles inside and rendering them barely discernable. The E_h values in Table 7.2 confirms the build-up of corrosion products in the more concentrated As(III) solutions. Specifically, the E_h potentials registered a sharp increase with As(III) concentration at 500 and 1000 mg/L (Table 7.2), suggesting the prevalence of iron oxidation products observed in O1s HR-XPS and SEM at those high concentrations forms a barrier layer on top of metallic iron and diminishes Fe^0 reducing capability.
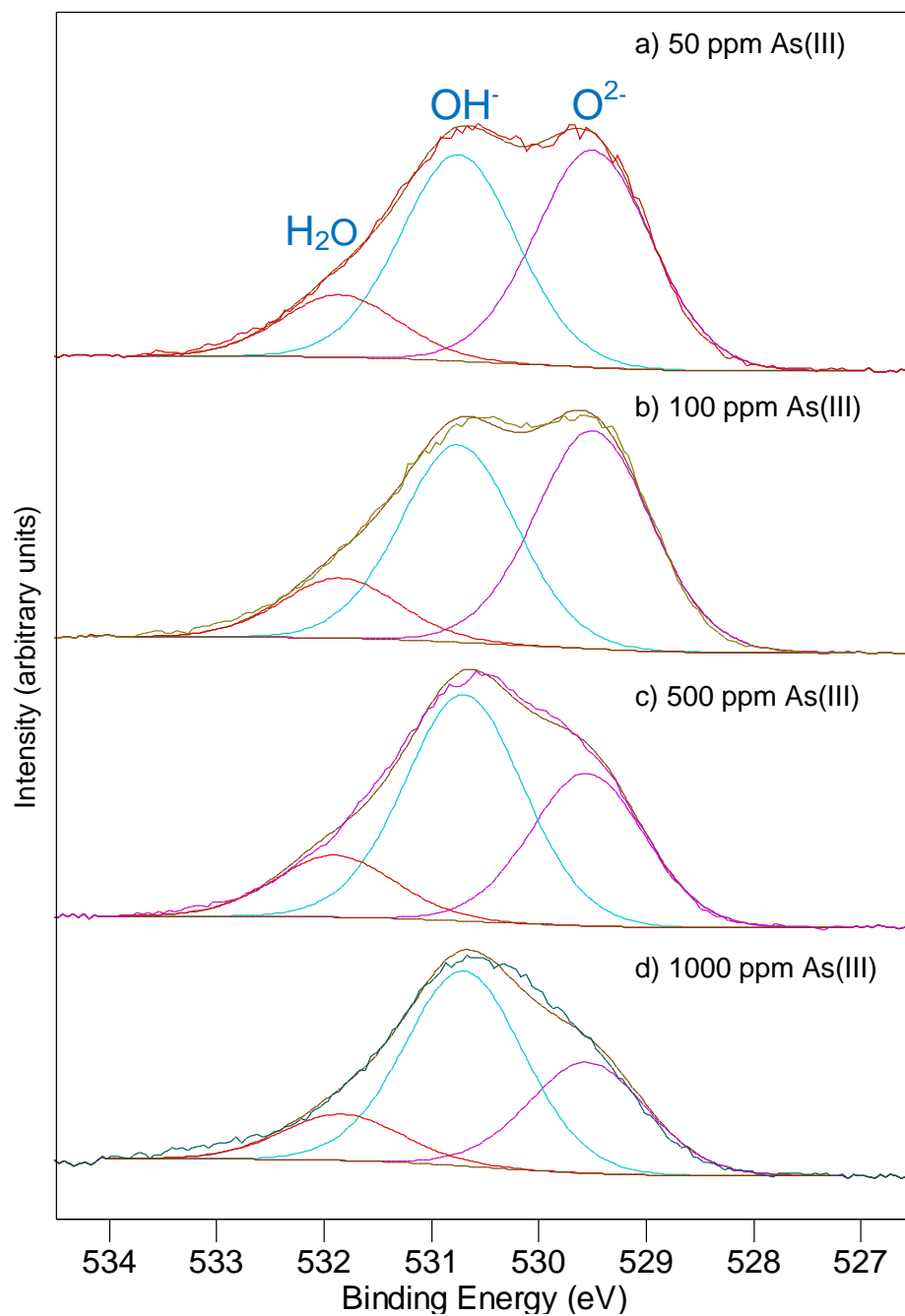
Figure 7.11 O1s XPS spectra of samples shown in Figure 7.10, where the initial As(III) concentration was varied. The different forms of oxygen are indicated in the top spectrum: H_2O at 531.8 eV, OH$^-$ at 530.7 eV, and O^{2-} at 529.5 eV. The prominent increase in OH$^-$ at the two highest As(III) concentrations indicates substantial iron hydroxide formation at the solid surface.

No As(III)   w/ 100 mg/L As(III)   w/ 1000 mg/L As(III)
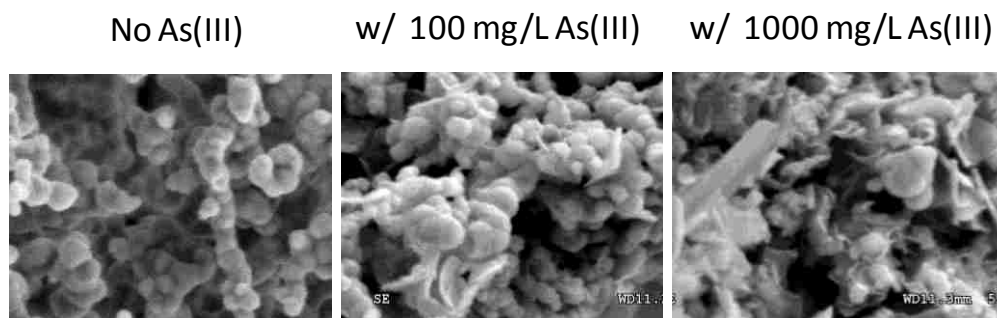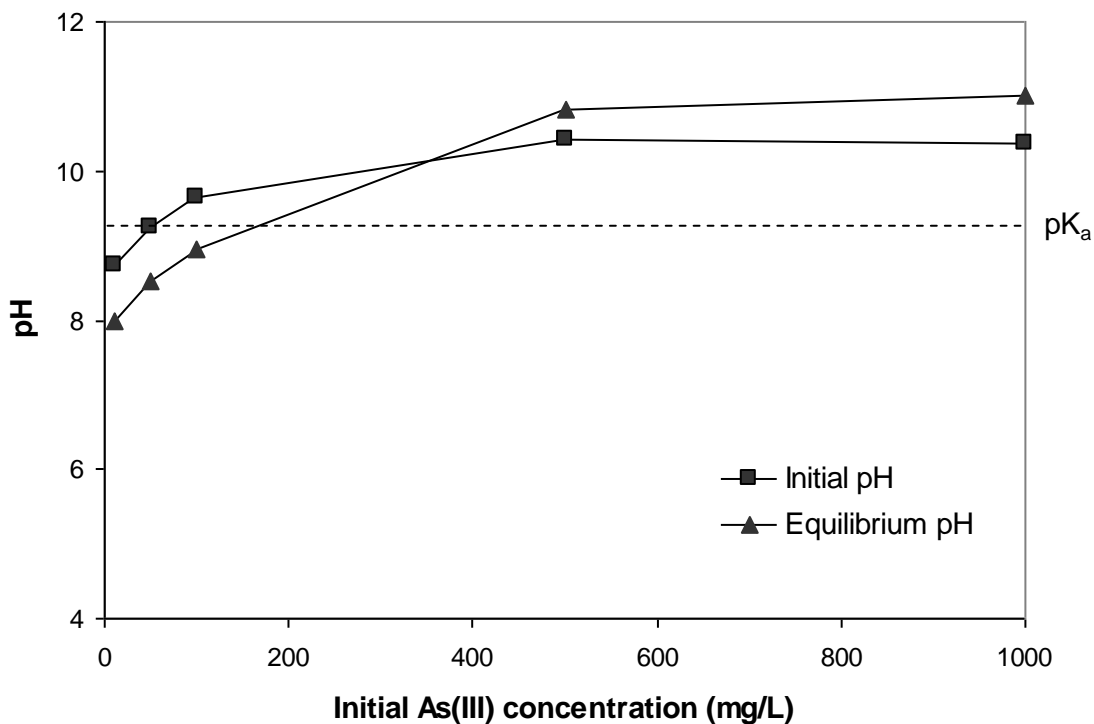
Figure 7.12 Initial and final solution pH at various initial As(III) concentrations. nZVI loading was fixed at 5 g/L. Initial pH was measured before nZVI loading. Equilibrium pH was obtained after a reaction time of 24 hours. The dashed line corresponds to the pK_a value (pH 9.2) of H_3AsO_3, which dissociates to $H_2AsO_3^-$ at pH $> pK_a$.

Bottom row from left to right: SEM images of fresh nZVI, nZVI reacted with 100 mg/L As(III) for 24 hours, and those reacted with 1000 mg/L As(III) for 24 hours. All images were taken at 60k magnification.

In summary, As(III) concentration exerts a pronounced effect on As(III) reduction by controlling solution chemistry and influencing the nZVI surface conditions. Formation of As(0) was more evident at lower concentrations and it was absent at above 100 mg/L due to substantial iron oxidation and precipitate formation. Although the concentration range evaluated here is higher than arsenic occurrence in natural waters (typical range 1-5000 μg/L) (Smedley & Kinniburgh, 2002), the trend revealed in Figure 7.10 strongly implies that reduction of arsenite at trace levels such as in natural waters is likely to occur in the presence of nZVI. As(0) not being observed in previous studies (e.g., Su & Puls, 2001; Manning *et al*., 2002; Lien & Wilkin, 2005) may be attributed to instrumental limitations and the specific reaction conditions used. In those studies, relatively high As(III) concentrations were used since conventional XPS analysis requires a significant amount of arsenic deposited on the particle surfaces to be detected. Under those conditions, As(0) formation is not favored for the reasons just mentioned above, and surface saturation with adsorbed arsenic species may attenuate the already weak As(0) signal. In the present HR-XPS study, we used a Scienta ESCA 300 instrument, which has an intense rotating anode X-ray source and enhanced signal detection utilizing a 300-mm radius hemispherical analyzer and position-sensitive detector, thereby greatly lowering the arsenic detection limit and improving the energy resolution.   This enables us to study nZVI reactions with arsenic at lower initial concentrations, which are conditions more relevant to the natural systems.

Compared to reduction of As(III) to As(0), oxidation of As(III) to As(V) is less sensitive to the initial As(III) concentration (Figure 7.10). In all cases, As(V) formation was observed, but to a moderate extent accounting for less than one third of the total sequestered arsenic. As(III) oxidation by nZVI has been reported in previous studies, although the exact mechanism remains uncertain. It is conceived that there may exist more than one oxidant, including peroxide or radical species generated from Fe^0 corrosion, hydroxide species, and iron oxides (Manning & Goldberg, 1997; Joo *et al*., 2004; Katsoyiannis *et al*., 2008). Peroxide or oxygen-containing radical generation requires dissolved O_2 in acidic medium (Joo *et al*., 2004; Katsoyiannis *et al*., 2008), thus they are not likely to be involved considering our reaction conditions. As(III) oxidation in aqueous phase by hydroxyl ions is plausible (Manning & Goldberg, 1997), but the resultant As(V) species in the solution phase is unlikely to re-attach to the nZVI surface due to surface charge repulsion between As(V) and the oxide layer at neutral to alkaline pH. It is more likely that As(III) was oxidized by iron oxide, which was proceeded via formation of iron oxide-As(III) surface complexes (Manning *et al*., 2002; Amstaetter *et al*., 2010). The lack of a distinct trend for As(III) oxidation within the concentration range studied is probably a result of several interacting effects, since the affinity of As(III) for iron oxides, the amount of iron oxides available as adsorptive sites, and the oxidation potential of iron oxides are intricately affected by pH.

7.3.5 Effect of reaction time

The evidence for the simultaneous occurrence of oxidation, reduction and adsorption of As(III) on nZVI surface suggest that the two components of nZVI are able to bring about different reactions in parallel, which by itself is a novel property that has not been reported before. The progressive transformation of arsenic species in nZVI was investigated by analyzing the reaction products at various times between 10 min to 15 days (Figure 7.13).

Solution phase analysis confirms that 99.9% of the aqueous As(III) was captured by nZVI within 10 min (Figure 7.3), and therefore the total amount of arsenic present in the solid phase was effectively constant during the monitoring period. As shown in Figure 7.13, the maximum formation of As(V) (~ 40% of the total arsenic intensity) was observed at 10 min, and As(V) then gradually declined with time over 24 h. The opposite trend can be noted for As(0), which contributes 15% of the total As intensity at 10 min, and rises steadily to 35% after 24 h. The data indicate arsenite oxidation is a rapid reaction that is completed on a time scale of minutes upon loading nZVI into the solution. Facile As(III) oxidation has been reported in the presence of Fe(II)-adsorbed goethite and other mineral surfaces (Amstaetter et al., 2010), where these surfaces catalyze oxidation reactions of adsorbed As(III). This surface-mediated oxidation model is also consistent with our prior finding that As(V) exists at the outer surface of the nanoparticles (refer to Section 7.3.3).
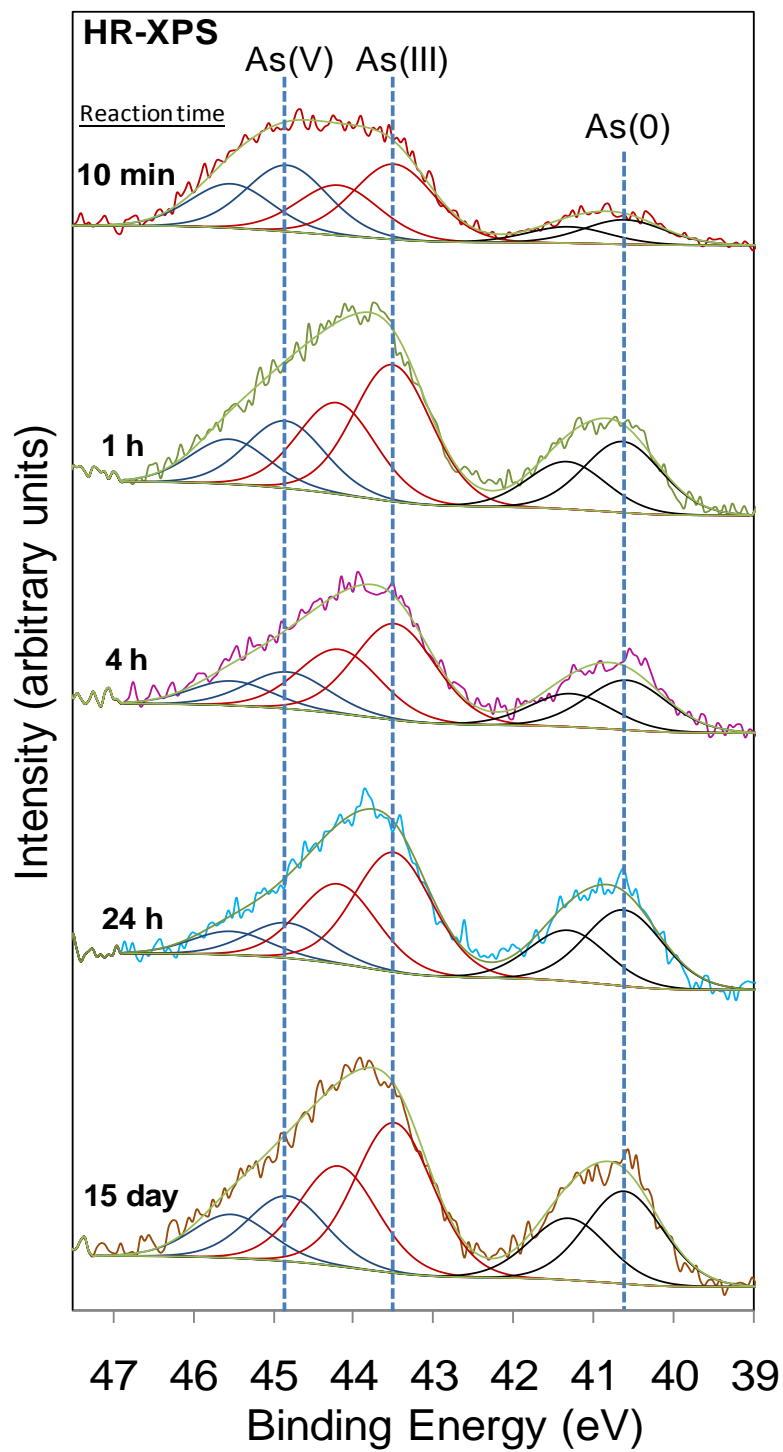
Figure 7.13 As3d HR-XPS spectra of nZVI reacted with As(III) for different times. Initial As(III) concentration was 100 mg/L; nZVI loading was 5 g/L.

The gradual loss of As(V) after the first 10 min in Figure 7.13 indicates As(III) conversion to As(V) is reversible. A similar finding, i.e., rapid initial As(III) oxidation followed by a slower transformation in the opposite direction, has been noted in the As(III)-Fe(II)-goethite system (Amstaetter et al., 2010). On the other hand, the relatively slow emergence of As(0) corroborates with As(0) being formed at the Fe(0) interface, because this would entail arsenite to migrate through the oxide layer, which would likely be a rate-limiting step. Sample reacted for 15 days (Figure 7.13) shows that there were no significant changes compared to the 24 hrs data, suggesting that the reduced arsenic encapsulated by the oxide layer will persist for a substantial amount of time in anoxic conditions.

7.3.6 Effect of nZVI dose

Figure 7.14 shows As3d XPS spectra of samples reacted with As(III) solutions at different nZVI doses. The formation of As(0) was observed at the highest dose of nZVI (5 g/L), but not in lower dose samples. The accompanying Fe2p XPS spectra (Figure 7.15) suggest an apparent association between the presence of As(0) and Fe(0). Notably, an Fe(0) $2p_{3/2}$ component at 707.0 eV BE is present in the 5 g/L sample (Figure 7.15), whereas the solids contain only oxidized iron species in the 0.4 and 1 g/L samples. The concomitant appearance of As(0) and Fe(0) in XPS is consistent with As(0) residing at the Fe(0)-oxide interface as previously noted. Considering the XPS probe depth for

Fe2p photoelectrons is ~ 6 nm, absence of a metallic iron signal in the low dose samples indicates the nanoparticles underwent substantial corrosion, resulting in deposition of oxidation products on the surface. Extensive surface passivation may also be inferred from the solution phase E_h values shown in Table 7.2, where the final E_h values in 0.4 and 1 g/L nZVI systems are higher than that of a freely corroding iron surface (Melitas *et al*., 2002).

Additionally, it is noticed that the proportion of As(V) increased with decreasing nZVI dose. Based on the previous analysis of nZVI reacted for different amounts of time, it is conceived that the amount of As(V) present was controlled by the relatively fast As(V) formation and a slower reaction in the reverse direction. Severe corrosion or depletion of Fe(0) when only a small amount of nZVI was added may effectively quench the reverse reaction and result in more As(V) in the solid phase.

As described in Section 7.3.3, information regarding the depth-dependent distributions of arsenic species within the nanoparticles can be gleaned from the intensities of As3d and As2p$_{3/2}$ XPS spectra (Figure 7.7). Figure 7.16 plots the intensity ratios of individual arsenic valence states and the total arsenic detected in samples shown in Figure 7.14 and 7.15. The ratio of a pure homogeneous arsenic material (sodium arsenite) is denoted on the figure, thus ratios greater or smaller than this benchmark value imply surface or deep-lying species, respectively. For the 5g/L nZVI sample, a stratified (or layered) distribution of different arsenic species is implied by the widely staggered ratios for

different valent states, as noted previously. These layers are predominated by As(V), As(III), and As(0), respectively, in the order from surface towards interior.

At lower nZVI doses (0.4 g/L or 1 g/L), only As(III) and As(V) were detected. Their intensity ratios are close to that of a homogeneous sample, suggesting As(III) and As(V) are intermixed along the depth as opposed to the layered formation seen in the 5 g/L sample. This is somewhat expected because the near surface regions of these low dose samples are made entirely of iron oxides and no metallic iron. Without a strong reducing source to drive electron passage and the reduction reaction, As(III) or As(V) are expected to persist in these samples. In all cases, the As2p3/2 and As3d intensity ratios of the total arsenic are less than one, and this implies the bulk of the sequestered arsenic was embedded below the surface, gradually overlayed by the oxide phase formed through on-going corrosion of iron in the aqueous solution.
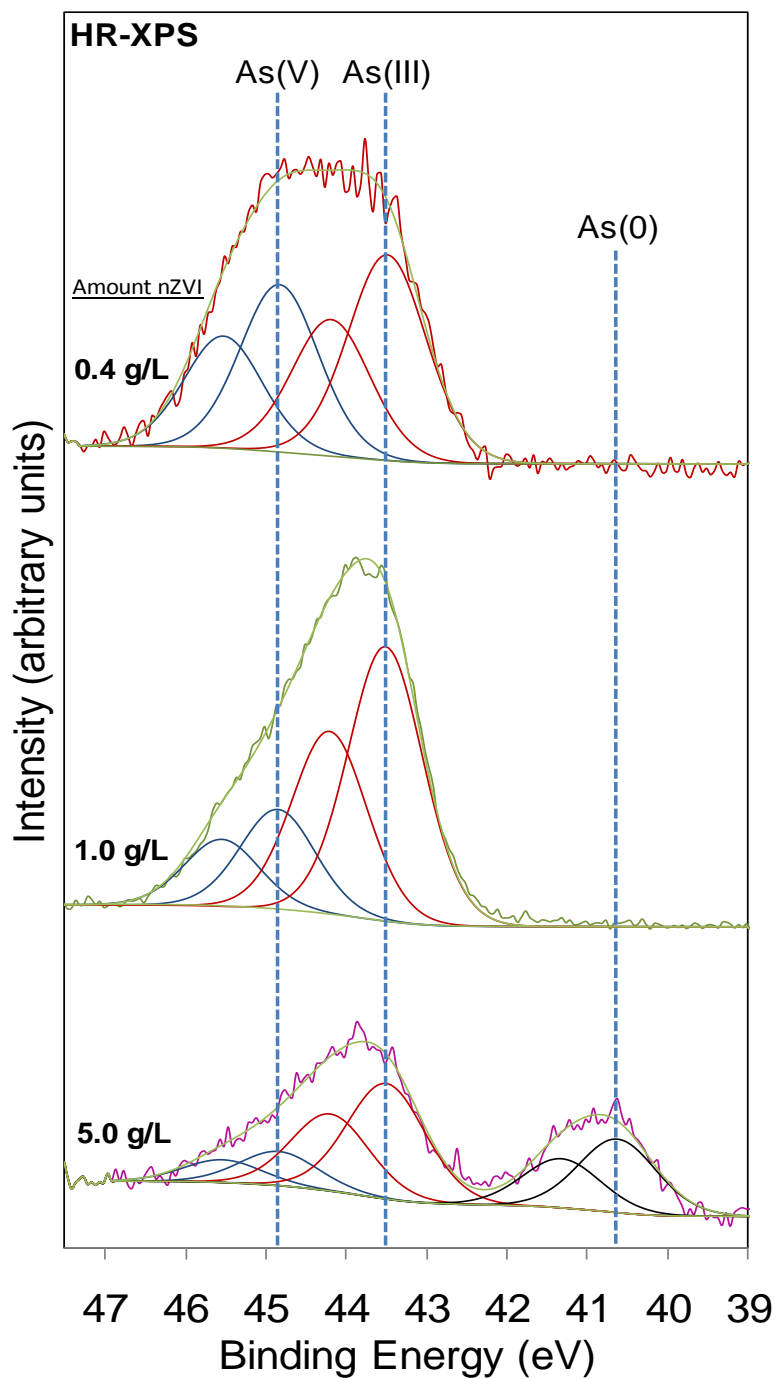
Figure 7.14 As3d HR-XPS spectra of varying dose of nZVI reacted with 100 mg/L As(III) for 24 hours.
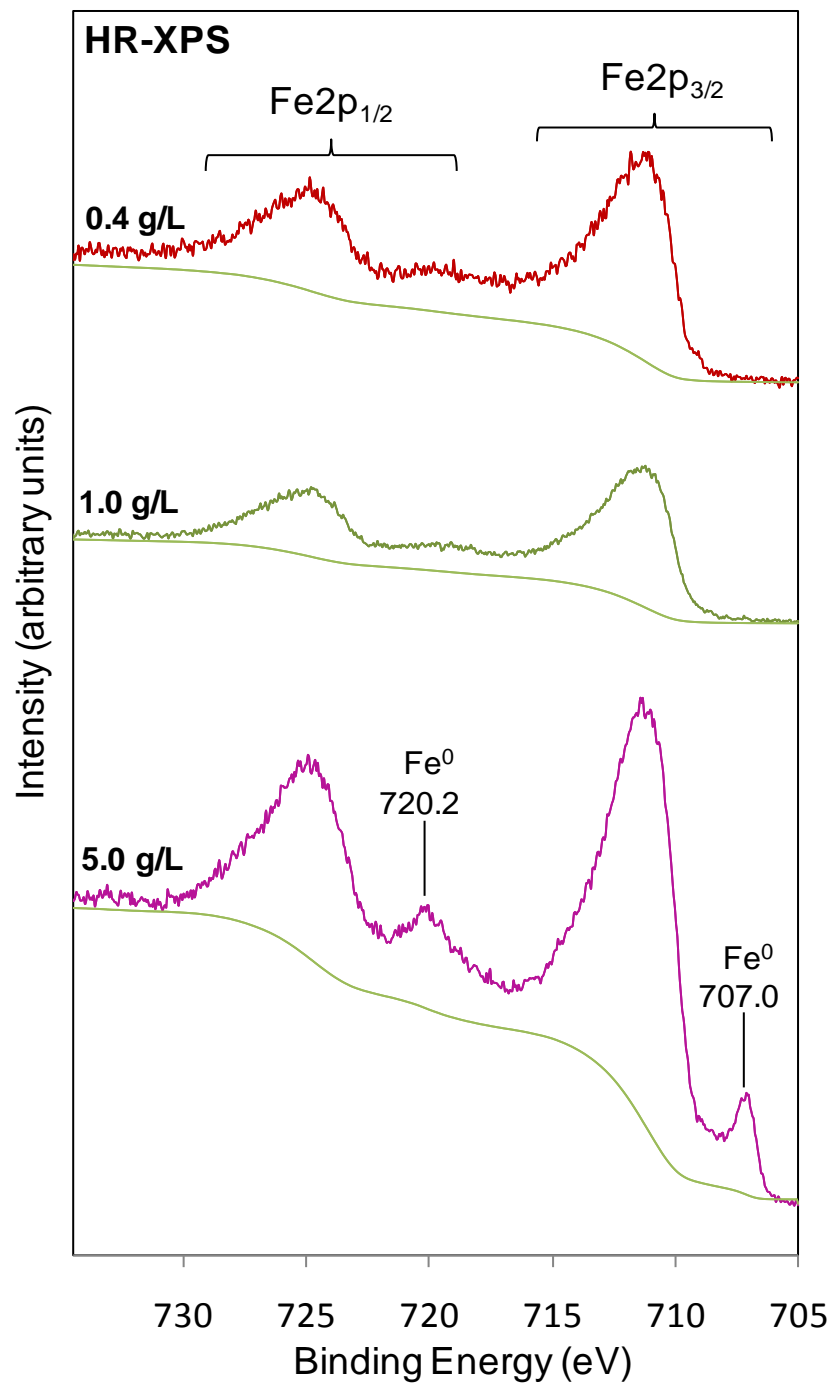
Figure 7.15 Fe2p XPS spectra of varying dose of nZVI reacted with As(III) solutions. Initial As(III) concentration was 100 mg/L; reaction time was 24 hours.
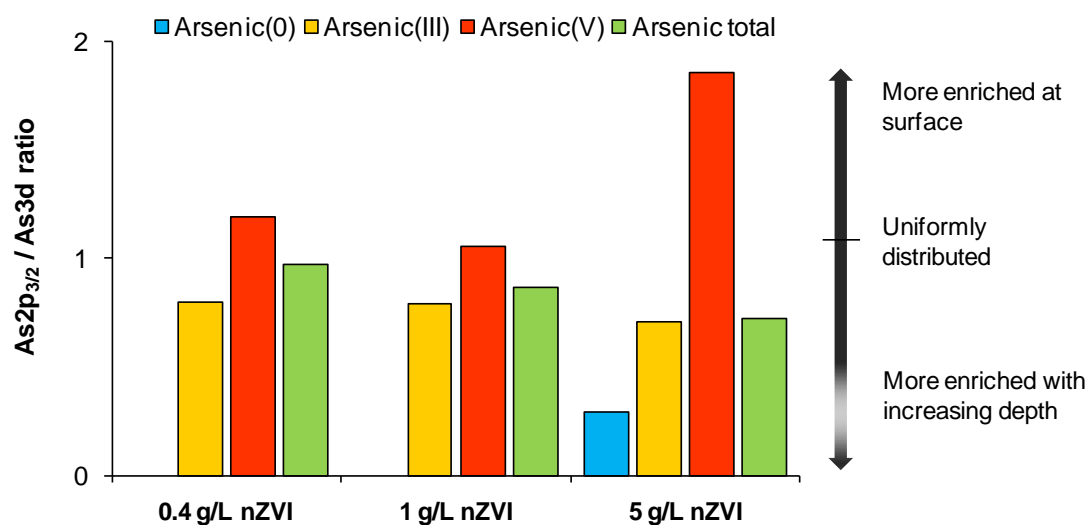
Figure 7.16 Intensity ratios of the As2p$_{3/2}$ and As3d XPS spectra for the three samples in Figure 7.14 & 7.15. The raw intensities have been corrected by the relative sensitivity factors (S): S$_{As2p}$= 31.5 and S$_{As3d}$= 1.82. The value of S$_{As2p}$ was determined empirically (section 7.3.3) and S$_{As3d}$ was from literature (Fairley & Carrick, 2005). Using sodium arsenite (NaAsO$_2$) as a standard, we determined the intensity ratio of uniformly distributed arsenic species is 1.1 as indicated on the figure.

7.3.7 Reaction model and practical implications

Evidence from solid and aqueous phase analyses can be used to establish that sequestered arsenite undergoes a series of redox transformations enabled by the oxide shell and metallic core of the nanoparticles, which results in arsenic being captured in multiple chemical states. Time-dependent and multiline analyses of the reacted solids using HR-XPS reveals the relative time scales of individual reactions and the distribution of arsenic valence states in the products, as depicted schematically in Figure 7.17. The relative importance of each reaction shifts with time and the changing

composition of nZVI during on-going corrosion. This stresses the importance of viewing the arsenic-nZVI system as dynamic instead of as a static, equilibrium-controlled system. Previous studies of reaction kinetics between iron materials and water contaminants rely largely on measurements of contaminant concentrations in bulk solutions. The temporal and spatial variations of arsenic speciation in nZVI observed in this study suggest more attention may be given to the kinetics of solid-phase redox reactions so as to obtain a more complete understanding of the reaction mechanisms. The redox interactions reported here have significant implications on nZVI remediation performance as well as arsenic speciation and distribution in the final products. A distinct feature of nZVI relative to conventional adsorbents is that a large proportion of arsenic is embedded within the oxide structure instead of being retained as surface adsorbed species. Continuous iron corrosion in this case, not only serves to encapsulate the sequestered arsenic, but also supplies a continuous source of reactive sites for arsenic abatement. As such, nZVI exhibits much larger arsenic removal capacities than iron oxides on a mass or surface area basis, and the retained arsenic is potentially less susceptible to leaching caused by pH changes (Dixit & Hering, 2003; Raven *et al.*, 1998) and competing anions (e.g., phosphate) (Korte & Fernando, 1991; Hug *et al.*, 2008). Compared to bulk ZVI materials, nZVI is capable of both arsenite oxidation and reduction, and this results in heterogeneous spatial distributions of arsenic valence states in the solids that represents a new form of arsenic sequestration product previously not discussed. From application point of view, the removal kinetics and arsenic loading per

232

unit mass of nZVI are expected to be significantly higher than those of bulk ZVI materials owing to its larger reactive surface and a greater "volume" participated in the solid-phase redox exchanges. These virtues render nZVI a good candidate for *in situ* applications in underground source zones and for use in centralized water treatment facilities. Since nZVI is a reactive and consumable material, the evolution of these nanoparticles and the stability of sequestered arsenic over long time periods (on the order of months or longer) in environmentally relevant conditions need to be systematically evaluated for these applications.

Figure 7.17 Schematic diagram summarizing processes responsible for arsenic removal in As(III)-nZVI system in anoxic conditions. The relative scale of the core and shell components of nZVI are for illustration only and do not reflect actual dimensions. As(III) may be taken up from the aqueous phase by adsorption or co-precipitation. The solid-bound As(III) is oxidized rapidly at the oxide surface, and the As(V) formed may be reverted to As(III) at a slower rate. Some As(III) diffuses towards Fe(0) core and is reduced to elemental arsenic (As(0)) near the oxide/Fe(0) interface.

References

1. Nordstrom, D. K., Public health - Worldwide occurrences of arsenic in ground water. *Science* **2002,** *296*, 2143-2145.

2. Smedley, P. L.; Kinniburgh, D. G., A review of the source, behaviour and distribution of arsenic in natural waters. *Appl. Geochem.* **2002,** *17*, 517-568.

3.   Meharg, A. A.; Rahman, M., Arsenic contamination of Bangladesh paddy field soils: Implications for rice contribution to arsenic consumption. *Environ. Sci. Technol.* **2003,** *37*, 229-234.

4.   Dittmar, J.; Voegelin, A.; Roberts, L. C.; Hug, S. J.; Saha, G. C.; Ali, M. A.; Badruzzaman, A. B. M.; Kretzschmar, R., Arsenic Accumulation in a Paddy Field in Bangladesh: Seasonal Dynamics and Trends over a Three-Year Monitoring Period. *Environ. Sci. Technol.* **2010,** *44*, 2925-2931.

5.   Mandal, B. K.; Suzuki, K. T., Arsenic round the world: a review. *Talanta* **2002,** *58*, 201-235.

6.   WHO guidelines for drinking-water quality, 3rd edition, 2008.

        (http://www.who.int/water_sanitation_health/dwq/gdwq3rev/en/index.html)

7.   Edwards, M., Chemistry of arsenic removal during coagulation and Fe-Mn oxidation. *J. Am. Water Works Assn.* **1994,** *86*, 64-78.

8.   Sarkar, S.; Gupta, A.; Biswas, R. K.; Deb, A. K.; Greenleaf, J. E.; SenGupta, A. K., Well-head arsenic removal units in remote villages of Indian subcontinent: Field results and performance evaluation. *Water Res.* **2005**, *39*, 2196-2206.

9.   Mohan, D.; Pittman, C. U., Arsenic removal from water/wastewater using adsorbents - A critical review. *J. Hazard. Mater.* **2007,** *142*, 1-53.

10.   Hussam, A.; Munir, A. K. M., A simple and effective arsenic filter based on composite iron matrix: Development and deployment studies for groundwater of Bangladesh. *J. Environ. Sci. Health. Part A Toxic/Hazard. Subst. Environ. Eng.*

2007, *42*, 1869-1878.

11. Dixit, S.; Hering, J. G., Comparison of arsenic(V) and arsenic(III) sorption onto iron oxide minerals: Implications for arsenic mobility. *Environ. Sci. Technol.* **2003,** *37*, 4182-4189.

12. Korte, N. E.; Fernando, Q., A review of Arsenc(III) in groundwater. *Crit. Rev. Env. Control* **1991,** *21*, 1-39.

13. Raven, K. P.; Jain, A.; Loeppert, R. H., Arsenite and arsenate adsorption on ferrihydrite: Kinetics, equilibrium, and adsorption envelopes. *Environ. Sci. Technol.* **1998,** *32*, 344-349.

14. Manning, B. A.; Fendorf, S. E.; Goldberg, S., Surface structures and stability of arsenic(III) on goethite: Spectroscopic evidence for inner-sphere complexes. *Environ. Sci. Technol.* **1998,** *32*, 2383-2388.

15. Manceau, A., The mechanism of anion adsorption on iron-oxides - Evidence for the bonding of arsenate tetrahedra on free Fe(O,OH)(6) edges. *Geochim. Cosmochim. Acta* **1995,** *59*, 3647-3653.

16. Goldberg, S.; Johnston, C. T., Mechanisms of arsenic adsorption on amorphous oxides evaluated using macroscopic measurements, vibrational spectroscopy, and surface complexation modeling. *J. Colloid Interface Sci.* **2001,** *234*, 204-216.

17. Ona-Nguema, G.; Morin, G.; Juillot, F.; Calas, G.; Brown, G. E., EXAFS analysis of arsenite adsorption onto two-line ferrihydrite, hematite, goethite, and lepidocrocite. *Environ. Sci. Technol.* **2005,** *39*, 9147-9155.

236

18. Su, C. M.; Puls, R. W., Arsenate and arsenite removal by zerovalent iron: Kinetics, redox transformation, and implications for *in situ* groundwater remediation. *Environ. Sci. Technol.* **2001,** *35*, 1487-1492.

19. Lackovic, J. A.; Nikolaidis, N. P.; Dobbs, G. M., Inorganic arsenic removal by zero-valent iron. *Environ. Eng. Sci.* **2000,** *17*, 29-39.

20. Manning, B. A.; Hunt, M. L.; Amrhein, C.; Yarmoff, J. A., Arsenic(III) and Arsenic(V) reactions with zerovalent iron corrosion products. *Environ. Sci. Technol.* **2002,** *36*, 5455-5461.

21. Bang, S.; Johnson, M. D.; Korfiatis, G. P.; Meng, X. G., Chemical reactions between arsenic and zero-valent iron in water. *Water Res.* **2005,** *39*, 763-770.

22. Lien, H. L.; Wilkin, R. T., High-level arsenite removal from groundwater by zero-valent iron. *Chemosphere* **2005,** *59*, 377-386.

23. Ponder, S. M.; Darab, J. G.; Mallouk, T. E., Remediation of Cr(VI) and Pb(II) aqueous solutions using supported, nanoscale zero-valent iron. *Environ. Sci. Technol.* **2000,** *34*, 2564-2569.

24. Liu, Y. Q.; Choi, H.; Dionysiou, D.; Lowry, G. V., Trichloroethene hydrodechlorination in water by highly disordered monometallic nanoiron. *Chem. Mater.* **2005,** *17*, 5315-5322.

25. Li, X. Q.; Zhang, W. X., Sequestration of metal cations with zerovalent iron nanoparticles - A study with high resolution X-ray photoelectron spectroscopy (HR-XPS). *J. Phys. Chem. C* **2007,** *111*, 6939-6946.

26. Kanel, S. R.; Manning, B.; Charlet, L.; Choi, H., Removal of arsenic(III) from groundwater by nanoscale zero-valent iron. *Environ. Sci. Technol.* **2005,** *39*, 1291-1298.

27. Kanel, S. R.; Greneche, J. M.; Choi, H., Arsenic(V) removal kom groundwater using nano scale zero-valent iron as a colloidal reactive barrier material. *Environ. Sci. Technol.* **2006,** *40*, 2045-2050.

28. Ramos, M. A. V.; Yan, W.; Li, X. Q.; Koel, B. E.; Zhang, W. X., Simultaneous oxidation and reduction of arsenic by zero-valent iron nanoparticles: Understanding the significance of the sore-shell structure. *J. Phys. Chem. C* **2009,** *113*, 14591-14594.

29. Martin, J. E.; Herzing, A. A.; Yan, W. L.; Li, X. Q.; Koel, B. E.; Kiely, C. J.; Zhang, W. X., Determination of the oxide layer thickness in core-shell zerovalent iron nanoparticles. *Langmuir* **2008,** *24*, 4329-4334.

30. Yan, W. L.; Ramos, M. A. V.; Koel, B. E.; Zhang, W. X., Multi-tiered distributions of arsenic in iron nanoparticles: Observation of dual redox functionality enabled by a core-shell structure. *ChemComm*, **2010**, *46*, 6995-6997.

31. Li, X. Q.; Zhang, W. X., Iron nanoparticles: The core-shell structure and unique properties for Ni(II) sequestration. *Langmuir*, **2006**, *22*, 4638-4642.

32. Cao, J. S.; Li, X. Q.; Tavacoli, J.; Zhang, W. X., Temperature programmed reduction for measurement of oxygen content in nanoscale zero-valent iron.

Environ. Sci. Technol. **2008**, *42*, 3780-3785.

33. Katsoyiannis, I. A.; Ruettimann, T.; Hug, S. J., pH dependence of Fenton reagent generation and As(III) oxidation and removal by corrosion of zero valent iron in aerated water. *Environ. Sci. Technol.* **2008,** *42*, 7424-7430.

34. The values shown in the figure are apparent concentrations because of the inherent assumption in the calculation that each element is distributed homogeneously throughout the probe depth.

35. Amstaetter, K.; Borch, T.; Larese-Casanova, P.; Kappler, A., Redox transformation of arsenic by Fe(II)-activated goethite (alpha-FeOOH). *Environ. Sci. Technol.* **2010,** *44*, 102-108.

36. Ona-Nguema, G.; Morin, G.; Wang, Y. H.; Foster, A. L.; Juillot, F.; Galas, G.; Brown, G. E., XANES evidence for rapid arsenic(III) oxidation at magnetite and ferrihydrite surfaces by dissolved O_2 via Fe^{2+}-mediated reactions. *Environ. Sci. Technol.* **2010,** *44*, 5416-5422.

37. Borch, T.; Kretzschmar, R.; Kappler, A.; Van Cappellen, P.; Ginder-Vogel, M.; Voegelin, A.; Campbell, K., Biogeochemical redox processes and their impact on contaminant dynamics. *Environ. Sci. Technol.* **2010,** *44*, 15-23.

38. Wang, C. M.; Baer, D. R.; Amonette, J. E.; Engelhard, M. H.; Antony, J.; Qiang, Y., Morphology and electronic structure of the oxide shell on the surface of iron nanoparticles. *J. Am. Chem. Soc.* **2009,** *131*, 8824-8832.

39. Signorini, L.; Pasquini, L.; Savini, L.; Carboni, R.; Boscherini, F.; Bonetti, E.;

Giglia, A.; Pedio, M.; Mahne, N.; Nannarone, S., Size-dependent oxidation in iron/iron oxide core-shell nanoparticles. *Phys. Rev. B* **2003,** *68*, 195423.

40. Garcia-Barriocanal, J.; Rivera-Calzada, A.; Varela, M.; Sefrioui, Z.; Iborra, E.; Leon, C.; Pennycook, S. J.; Santamaria, J., Colossal ionic conductivity at interfaces of epitaxial $ZrO_2 : Y_2O_3/SrTiO_3$ heterostructures. *Science* **2008**, *321*, 676-680.

41. Kerisit, S.; Rosso, K. M., Charge transfer in FeO: A combined molecular dynamics and ab initio study. *J. Chem. Phys*. **2005**, *123*, 224712.

42. Carpenter, E. E.; Calvin, S.; Stroud, R. M.; Harris, V. G., Passivated iron as core-shell nanoparticles. *Chem. Mater.* **2003,** *15*, 3245-3246.

43. Melitas, N.; Conklin, M.; Farrell, J., Electrochemical study of arsenate and water reduction on iron media used for arsenic removal from potable water. *Environ. Sci. Technol.* **2002,** *36*, 3188-3193.

44. Hug, S. J.; Leupin, O. X.; Berg, M., Bangladesh and Vietnam: Different groundwater compositions require different approaches to arsenic mitigation. *Environ. Sci.* Technol. **2008**, 42, 6318-6323.

45. Fairley, N.; Carrick, A. The Casa Cookbook – Part 1: Recipes for XPS data Processing; Acolyte Science: Cheshire, U.K., 2005.

46. U. S. Environmental Protection Agency, National Primary Drinking Water Standards, EPA 816-F-03-016, 2003.

47. Welch, A. H.; Westjohn, D. B.; Helsel, D. R.; Wanty, R. B. Arsenic in

groundwater of the united states: Occurrence and geochemistry *Ground Water* **2000,** *38*, 589.

48.   Scott, M. J.; Morgan, J. J. Reactions at oxide surfaces. 1. Oxidation of As(III) by synthetic birnessite. *Environ. Sci. Technol.* **1995,** *29*, 1898.

49.   Fendorf, S.; Eick, M. J.; Grossl, P.; Sparks, D. L., Arsenate and chromate retention mechanisms on goethite. 1. Surface Structure. *Environ. Sci. Technol.* **1997, 31**, 315-320.

50.   Moulder, J. F.; Stickle, W. F.; Sobol, P.E.; Bomben, K. D. *Handbook of X-ray Photoelectron Spectroscopy*; Perkin-Elmer Corporation, Eden Prairie, MN, 1992.

51.   Nurmi, J. T.; Tratnyek, P. G.; Sarathy, V.; Baer, D. R.; Amonette, J. E.; Pecher, K.; Wang, C. M.; Linehan, J. C.; Matson, D. W.; Penn, R. L.; Driessen, M. D., Characterization and properties of metallic iron nanoparticles: Spectroscopy, electrochemistry, and kinetics. *Environ. Sci. Technol.* **2005,** *39* (5), 1221-1230.

52.   Manning, B. A.; Goldberg, S., Adsorption and stability of As(III) at the clay mineral-water interface. *Environ. Sci. Technol.* **1997,** *31*, 2005-2011.

53.   Cumpson, P.; Seah, M. Elastic scattering corrections in AES and XPS. 2. Estimating attenuation lengths and conditons required for their valid use in overlayer/substrate experiments. *Surf. Interface Anal.* **1997**, 25, 430-446.

54.   Axe, L.; Trivedi, P., Intraparticle surface diffusion of metal contaminants and their attenuation in microporous amorphous Al, Fe, and Mn oxides. *J. Colloid Interface Sci.* **2002,** *247* (2), 259-265.

55. Yavuz, C. T.; Mayo, J. T.; Yu, W. W.; Prakash, A.; Falkner, J. C.; Yean, S.; Cong, L. L.; Shipley, H. J.; Kan, A.; Tomson, M.; Natelson, D.; Colvin, V. L., Low-field magnetic separation of monodisperse Fe_3O_4 nanocrystals. *Science* **2006,** *314* (5801), 964-967.

56. Grosvenor, A. P.; Kobe, B. A.; McIntyre, N. S., Studies of the oxidation of iron by water vapour using X-ray photoelectron spectroscopy and QUASES (TM). *Surf. Sci.* **2004,** *572* (2-3), 217-227.

57. Joo., S. H.; Feitz, A. J.; Waite, T. D., Oxidative degradation of the carbothioate herbicide, molinate, using nanoscale-zerovalent iron. *Environ. Sci. Technol.* **2005,** *38*, 2242-2247.

58. Mohai, M. *XPS Multiquant Users Manual,* 2005.

Chapter 8

Summary and Future Work

___

8.1 Summary of contributions

nZVI is one of the most extensively studied and applied engineered nanomaterials for environmental remediation. Despite its promising potential for environmental applications, there is limited knowledge about the fundamental properties of nZVI, particularly, its structure, surface composition, and changes in these characteristics in the aqueous media as the nanoparticles interact with the contaminants. As such, the mechanisms of contaminant abatement, reaction kinetics, and long-term effectiveness of nZVI-enabled remediation technology are not well understood. The overarching goal of this research is to understand the microstructure and surface chemistry of nanoscale zero-valent iron (nZVI) and how these properties influence nZVI interactions with water contaminants. The scope of this research calls for a multi-disciplinary approach where tools developed in material science, surface chemistry, and water chemistry are utilized. The key results of the present research can be summarized into the following interrelated topics.

8.1.1 Characterizing the core-shell structure of nZVI

This part of the work investigated the core-shell structure of nZVI with aptly designed experiments using a suite of advanced electron microscopic (SEM, TEM and STEM-XEDS) and spectroscopic tools (XPS). It is found that: 1) freshly-made nZVI adoptes a metal-core-oxide-shell structure, whereby the polycrystalline *bcc* metal iron nuclei were clad by a continuous, thin layer of iron (oxy-hydr)oxide of amorphous nature. This core-shell configuration was directly visualized for the first time with the ultra-high resolution STEM-XEDS elemental mapping technique. 2) the average thickness of the oxide layer is 2-3 nm based on a quantitative analysis of HR-XPS intensities of the Fe2p region with appropriate topographic corrections. This finding is corroborated by chemical redox titration method using Cu(II) as the oxidant. 3) the core-shell structure is not stationary, but evolves with time when nZVI is reacting with contaminants in aqueous solutions.

8.1.2 Role of the core-shell structure in contaminant sequestration

The minuscule dimension of the oxide overlayer, the highly disordered structure, and the abundance of defects such as vacancies and impurities render the oxide layer to be more permeable to mass and electron transport relative to the passivating oxide on the bulk-scale ZVI materials. This implies that nZVI is capable of enacting more diverse remediation pathways than pure Fe(0) or iron oxides. Using a group of well-studied water contaminants as probe molecules, the results showed that, depending on the

244

electrochemical and coordinative properties of the contaminants, nZVI has exhibited the reactivity of the oxide component (e.g. formation of surface adsorption complex with Zn(II)) and that of the Fe(0) core (*e.g.*, reduction of Hg(II) to Hg(0)). In addition, spontaneous reaction of Fe(0) with water created an locally alkaline environment that was conducive for sulfide surface mineralization to iron disulfide and the formation of metal hydroxide precipitates such as zinc hydroxide. Overall, the core-shell structure imparts the nanoparticles with multiple reactive mechanisms for contaminant sequestration, and the nanoparticles may be potentially applicable to remediating a broad variety of inorganic contaminants in addition to halogenated hydrocarbons.

8.1.3 Aging of nZVI in water and implications for reactivity

Spontaneous reaction with water continuouslly modifies the chemical composition and structure of ZVI particles during the course of remediation. This aspect is particularly important for bimetallic nZVI, a type of iron nanoparticles coated with a small amount of catalyst metals (e.g. Pd or Ni) for catalytic degradation of halogenated hydrocarbons. Rapid reactions of nZVI with contaminants and water may lead to fouling of the additive metal surface by iron oxide deposits and potential loss of catalyst to the aqueous phase. In this part of the work, it is reported for the first time that Pd-doped nZVI (Pd mass fraction at 1.5 wt%), one of the most extensively applied bimetallic nZVI, underwent massive structural changes during exposure to water for 24 hours. Using a state-of-the-art STEM-XEDS technique capable of mapping out elemental

245

distribution at 1-nm resolution, it was shown that the structure of the Pd-doped nZVI experienced several stages of transformation. The freshly-synthesized nanoparticles had heterogeneous coverage of Pd on the surface, whereby Pd formed islands of 2-5 nm in diameters decorating the surface of the iron particles. During immersion in an aqueous solution, the surface Pd migrated through the oxide layer and was relocated to the Fe(0)/oxide shell interface. Meantime, corrosion of Fe(0) caused surface deposition of oxide formation, and eventually this led to a hollowed-out structure with Pd being completely buried underneath the extensive oxide matrix. This aqueous aging process translates to a significant decrease in the dechlorination activity towards trichloroethylene. An 80% decrease in apparent reaction rate constant was observed for the particles aged in water for 24 hours. This findings suggest that the activity of Pd is a dynamic function of time and the nanoparticle structure.

8.1.4 Reactions with arsenic

nZVI is a potentially attractive candidate for the treatment of arsenic-laden groundwater because of their diminutive sizes and high surface reactivity, which can translate to higher remediation efficiency, and in the case of *in situ* application, enhanced particle dispersion and transport in the underground environment. However, the mechanisms of arsenic removal with ZVI materials are poorly characterized. Most research in the literature focused on arsenic speciation in the aqueous phase, and there are relatively few studies considering reactions at the iron surface and the chemical states of arsenic

in the final products. HR-XPS in conjunction with solution chemistry analysis were used to conduct the first systematic study of reactions of arsenic at the surface of iron nanoparticles. The results confirm that arsenic sequestration by nZVI involves several redox reactions mediated by the particle surface. One key finding is the simultaneous oxidation and reduction of As(III) upon reacting aqueous As(III) with the nanoparticles. With XPS multiline analysis to resolve the depth distributions of different arsenic valence states in the solid phase, it is shown that the dual redox functionality was enabled by the core-shell structure. Specifically, As(V) was present predominantly at the surface, indicating arsenite oxidation mediated by the oxide layer in the presence of water and hydroxyl ions. The reduced form, As(0), was concentrated at the Fe(0)/oxide interface, suggesting direct As(III) reduction by Fe(0). Time-resolved XPS studies show that As(III) was rapidly oxidized to As(V) in 10 min at the particle surface, and As(V) was reverted to As(III) at a slower rate in the presence of Fe(0). Infiltration of arsenite through the oxide layer and As(0) formation near the Fe(0) interface occurred on a time scale of hours. The relative extents of these reactions and the resultant arsenic speciation and spatial distribution are strongly dependent on the amount of nZVI present. In all conditions studied, arsenic was embedded in the solid phase as opposed to surface retention by iron oxide sorbents. This ability of nZVI may give rise to attributes favorable for in situ treatment applications or for sound disposal of arsenic-rich wastes.

8.2 Recommended future work

Although iron nanoparticles for environmental applications have been actively studied for over a decade, there are few studies focusing on the reactions at the surface or within the nanoparticles. While this work has contributed to an improved understanding of the fundamental properties of nZVI and the mechanisms underlying the particle's remediation capability, many areas pertaining to the long-term effectiveness of the technology in field conditions remain unexplored. The subsequent section lists several topic worth further investigations. In a broader sense, direct characterization of environmental processes at surfaces or interfaces using multidisciplinary methods is a relatively new field. The methodology developed in this work, i.e., combining solution analysis with surface and microscopic analyses, is applicable not only to iron nanoparticles and water contaminants, but also to many other aqueous/solid heterogeneous systems. Of particular interest is the interactions of nanoparticles with geochemical and biological surfaces in the natural environment, since these processes are expected to influence the aggregation state, surface reactive properties, and the long term fate and transport of the nanoparticles.

8.2.1 Effect of NOM and common groundwater solutes on nZVI surface chemistry

As the first systematic attempt to investigate the structure and surface chemistry of nZVI in aqueous environment, experiments in this work were conducted in simple aqueous solutions without amending background constituents such as natural organic

matter (NOM) and common electrolytes (e.g. ferrous, chloride, carbonate, nitrate, sulfate, and phosphate ions). Recent studies have shown that NOM binds with iron nanoparticles through electrostatic and surface complex interactions, thereby affecting the nanoparticle's stability and reactivity (Giasuddin *et al.*, 2007). Groundwater solutes not only may serve as potential oxidants (e.g. nitrate), but also may alter the rate of $Fe(0)$ corrosion and the nature of the oxide formed (e.g. iron green rust formed in the presence of carbonate and sulfate species) (Liu *et al.*, 2007; Reinsch *et al.*, 2010). The presence of phosphate ions will be of particular interest because of its reported strong competition with arsenic species for active sites on the iron oxide surface (Hug *et al.*, 2008). Further studies to evaluate the effects of these constituents on nZVI surface chemistry and colloidal stability, contaminant sequestration efficiency, and the aging behavior of the nanoparticles are necessary. The methods developed in this work can be readily tailored to study these topics, and the results will enlighten the question about how reliably and consistently will nZVI perform in realistic *in situ* conditions.

8.2.2 Three-dimension profiling of contaminant distributions in nZVI

Heterogeneous distribution of inorganic contaminants inside the nanoparticles has been noted in this study, which is conceivably driven by the difference in chemical potential across the metal core and the oxide shell of the nanoparticles. As a result, contaminants with different redox, coordinative and hydrophilic properties are expected to persist at different layers of the nanoparticles, and their spatial distributions may vary with time

as the nanoparticles undergo continuous oxidation in water. This thus results in a three-dimensional contaminant distribution model which is considerably different from conventional adsorbents where contaminants are bound at surfaces only. To delineate the spatial locations of pollutants sequestered by nZVI particles, well-established XPS depth-profiling methods, e.g. multiline, angle-resolved and sputtering-assisted analysis can be used. Additionally, techniques complementary to XPS spectroscopy, including STEM-XEDS chemical mapping technique and electron energy loss spectroscopy (EELS) may be applied to pinpoint the locations as well as chemical speciation of contaminants within an entire nanoparticle. knowledge in this regard will generate fresh insights into the mode of sequestration and the long-term fate of contaminants sequestered by iron-based nanoparticles.

8.2.3 Optimizing the reactivity of bimetallic nZVI

The work on Pd-doped nZVI suggests that particle reactivity and longevity may be improved by optimizing the synthesis route of Pd-nZVI, the Pd loading content, the storage medium, and the application of surfactants as surface modifier. Preliminary studies suggest, for example, that the precursor of Pd has an important effect on the particle's aging history (data not shown). Recent studies also indicate that the presence of silica and other anodic inhibitors in the soil environment may significantly prolong the life-span of nZVI particles (Reardon *et al*., 2008). The application of polymeric surfactants, known to stabilize the nanoparticles via steric effect or charge neutralization

(Hydutsky *et al*., 2007; Phenrat *et al*., 2009), may help to impede the deactivation of particles by protecting the active surface sites from build-up of oxidation products and from being attached by deactivating agents in the aqueous solution such as chloride ions. Because of an extensive interest in bimetallic nZVI for halogenated hydrocarbon remediation, the potential to improve the activity of surface catalysts and to prolong the particle life-span will have immediate practical implications.

8.2.4 *In situ* characterization of reactions at particle surfaces

Most surface and structural characterization methods used in this study are *ex situ* techniques conducted in ultra-high-vacuum conditions. Direct, *in situ* characterization of environmental processes at interfaces has rarely been explored in the past. This, however, can be achieved with vibration spectroscopic tools such as ATR-FTIR and Raman spectroscopy, atomic force spectroscopy (AFM), and X-ray absorption spectroscopy (XAS). IR and Raman spectroscopy probes molecular stretching and vibrations at the solid/water interfaces, while XAS examines the bonding environment of contaminants both at the surfaces and within the bulk of the solids. Complementary information can be obtained by carefully designed experiments using multiple techniques. The information obtained may answer questions such as the kinetics of solid phase reactions, the identity of intermediates formed, and the in-depth mechanisms at molecular level.

References

1. Giasuddin, A. B. M.; Kanel, S. R.; Choi, H., Adsorption of humic acid onto nanoscale zerovalent iron and its effect on arsenic removal. *Environ. Sci. Technol.* **2007,** *41* (6), 2022-2027.

2. Hydutsky, B. W.; Mack, E. J.; Beckerman, B. B.; Skluzacek, J. M.; Mallouk, T. E., Optimization of nano- and microiron transport through sand columns using polyelectrolyte mixtures. *Environ. Sci. Technol.* **2007,** *41* (18), 6418-6424.

3. Liu, Y.; Phenrat, T.; Lowry, G. V., Effect of TCE concentration and dissolved groundwater solutes on NUI-Promoted TCE dechlorination and H-2 evolution. *Environ. Sci. Technol.* **2007,** *41* (22), 7881-7887.

4. Phenrat, T.; Liu, Y. Q.; Tilton, R. D.; Lowry, G. V., Adsorbed Polyelectrolyte Coatings Decrease Fe-0 Nanoparticle Reactivity with TCE in Water: Conceptual Model and Mechanisms. *Environ. Sci. Technol.* **2009,** *43* (5), 1507-1514.

5. Reardon, E. J.; Fagan, R.; Vogan, J. L.; Przepiora, A., Anaerobic corrosion reaction kinetics of nanosized iron. *Environ. Sci. Technol.* 2008, *42* (7), 2420-2425.

6. Reinsch, B. C.; Forsberg, B.; Penn, R. L.; Kim, C. S.; Lowry, G. V., Chemical Transformations during Aging of Zerovalent Iron Nanoparticles in the Presence of Common Groundwater Dissolved Constituents. *Environ. Sci. Technol.* **2010,** *44* (9), 3455-3461.

Vita

Weile Yan was born on 6th of May, 1979 in Shanghai, China to her father Pinya Yan and mother Qiuping Wang. She was married to Jinsong Tan in 2005.

Weile obtained a bachelor degree with first class honors in Environmental Engineering from the National University of Singapore in 2002 with an overseas undergraduate scholarship awarded by the Ministry of Education, Singapore. During her undergraduate study, she actively participated in research by working as a part-time research assistant under Dr. Renbi Bai on the adsorption behaviors of glucosamine-derived polymeric sorbents. She received a master degree in Molecular Engineering of Biological and Chemical Systems from Singapore-MIT Alliance in 2003.

Weile worked as a process engineer at Tech Semiconductor from 2003 to 2005, where she was responsible for controlling and optimizing aqueous etching processes in DRAM fabrication lines. She then joined Creative Technology Asia in 2005 as an environmental compliance engineer overseeing product compliance with international environmental standards and regulations.

At Lehigh University, Weile studied reactions of iron nanoparticles with water pollutants under Dr. Wei-xian Zhang. Working on this cross-disciplinary research topic, she fostered collaborations with researchers in the Departments of Material Science and Engineering (Dr. Chris J. Kiely) and Chemistry (Dr. Bruce E. Koel). She served as a

teaching assistant of Introduction to Environmental Engineering (CEE170) and Engineering Design (CEE275). She was a recipient of the Dean's Fellowship and Rossin Doctoral Fellowship. While at Lehigh, she was also a leader and long-term active member of the Chinese Students and Scholars Association and the volunteer program, Dumplings, for adoptive families with children from China.

Her publications include the following:

Yan, W.; Herzing, A. A.; Kiely, C. J.; Zhang, W. X. Nanoscale zero-valent iron (nZVI): Aspects of the Nanoparticle Structure and Reactions with Inorganic Species in Water. *Journal of Contaminant Hydrology*, 2010, 118, 96-104.

Yan, W. L.; Ramos, M. A. V.; Koel, B. E.; Zhang, W. X. Multi-tiered distributions of arsenic in iron nanoparticles: observation of dual redox functionality enabled by a core-shell structure. *Chemical Communications*, 2010, 46, 6995-6997.

Yan, W. L.; Herzing, A. A.; Li, X. Q.; Kiely, C. J.; Zhang, W. X. Structural evolution of Pd-doped nanoscale zero-valent Iron (nZVI) in aqueous media and implications for particle aging and reactivity. *Environmental Science & Technology*, 2010, 44, 4288-4294.

Li, S. L.; Yan, W. L.; Zhang, W. X.; Solvent-free production of nanoscale zero-valent iron (nZVI) with precision milling. *Green Chemistry*, 2009, 11, 1618-1626.

Ramos, M. A. V.; Yan, W. L.; Li, X. Q.; Koel, B. E.; Zhang, W. X., Simultaneous Oxidation and Reduction of Arsenic by Zero-Valent Iron Nanoparticles: Understanding the Significance of the Core-Shell Structure. *Journal of Physical Chemistry C* 2009, 113, 14591-14594.

Martin, J. E.; Herzing, A. A.; Yan, W. L.; Li, X; Koel, B. E.; Kiely, C. J.; Zhang, W. X . Determination of the Oxide Thickness in Core-Shell Zero-Valent Iron nanoparticles. *Langmuir*, 2008, 24, 4329-4334.

Yan, W. L.; Bai, R.B. Adsorption of Lead and Humic acid on Chitosan Hydrogel Beads. *Water Research,* 2005, 39, 688-698.